Finite-element modeling and patient-specific prediction of aortic aneurysm progression

Joan Dario Laubrie Soto

N° d'ordre NNT: 2021LYSEM036

THÈSE de DOCTORAT DE L'UNIVERSITÉ DE LYON

opérée au sein de

l'École des Mines de Saint-Étienne

École Doctorale N° 488

Sciences, Ingénierie, Santé

Spécialité de doctorat: Mécanique et Ingénierie

Discipline: Mécanique et Ingénierie

Soutenue publiquement/à huis clos le 06/12/2021, par:

Joan D. Laubrie Soto

Finite-element modeling and patient-specific prediction of aortic aneurysm progression

---

Devant le jury composé de:

HAMBLI, Ridha	Professeur	Polytechnic Orléans	Président du Jury
FAMAEY, Nele	Professeure	KU Leuven	Rapporteure
CELENTANO, Diego	Professeur	PUC Santiago	Rapporteur
GARCÍA-HERRERA, Claudio	Professeur	USACH Santiago	Examinateur
GASSER, Christian	Professeur	KTH Stockholm	Examinateur
MOUSAVI, S. Jamaleddin	Docteur	PrediSurge	Examinateur
AVRIL, Stéphane	Professeur	Mines Saint-Étienne	Directeur de thèse

Spécialités doctorales	Responsables :	Spécialités doctorales	Responsables
SCIENCES ET GENIE DES MATERIAUX	K. Wolski Directeur de recherche	MATHEMATIQUES APPLIQUEES	M. Batton-Hubert
MECANIQUE ET INGENIERIE	S. Drapier, professeur	INFORMATIQUE	O. Boissier, Professeur
GENIE DES PROCEDES	P.Grosseau	SCIENCES DES IMAGES ET DES FORMES	JC. Pinoli, Professeur
SCIENCES DE LA TERRE	B. Guy, Directeur de recherche	GENIE INDUSTRIEL	N. Absi, Maitre de recherche
SCIENCES ET GENIE DE L'ENVIRONNEMENT	V.Laforest, Directeur de recherche	MICROELECTRONIQUE	Ph. Lalevée, Professeur

EMSE : Enseignants-chercheurs et chercheurs autorisés à diriger des thèses de doctorat (titulaires d'un doctorat d'État ou d'une HDR)

ABSI	Nabil	MR	Génie industriel	CMP
AUGUSTO	Vincent	MR	Génie industriel	CIS
AVRIL	Stéphane	PR	Mécanique et ingénierie	CIS
BALBO	Flavien	PR	Informatique	FAYOL
BASSEREAU	Jean-François	PR	Sciences et génie des matériaux	SMS
BATTON-HUBERT	Mireille	PR	Mathématiques appliquées	FAYOL
BEIGBEDER	Michel	MA	Informatique	FAYOL
BILAL	Blayac	DR	Sciences et génie de l'environnement	SPIN
BLAYAC	Sylvain	PR	Microélectronique	CMP
BOISSIER	Olivier	PR	Informatique	FAYOL
BONNEFOY	Olivier	PR	Génie des Procédés	SPIN
BORBELY	Andras	DR	Sciences et génie des matériaux	SMS
BOUCHER	Xavier	PR	Génie Industriel	FAYOL
BOUILLOT	Baptiste	MC	Sciences de l'ingénieur	SPIN
BRUCHON	Julien	PR	Mécanique et ingénierie	SMS
CAMEIRAO	Ana	PR	Génie des Procédés	SPIN
CHRISTIEN	Frédéric	PR	Science et génie des matériaux	SMS
DAUZERE-PERES	Stéphane	PR	Génie Industriel	CMP
DEBAYLE	Johan	MR	Sciences des Images et des Formes	SPIN
DEGEORGE	Jean-Michel	MA	Génie industriel	Fayol
DELAFOSSE	David	PR	Sciences et génie des matériaux	SMS
DELORME	Xavier	PR	Génie industriel	FAYOL
DESRAYAUD	Christophe	PR	Mécanique et ingénierie	SMS
DJENIZIAN	Thierry	PR	Science et génie des matériaux	CMP
BERGER-DOUCE	Sandrine	PR	Sciences de gestion	FAYOL
DRAPIER	Sylvain	PR	Mécanique et ingénierie	SMS
DUTERTRE	Jean-Max	PR	Microélectronique	CMP
EL MRABET	Nadia	MA	Microélectronique	CMP
FAUCHEU	Jenny	MA	Sciences et génie des matériaux	SMS
FAVERGEON	Loïc	MR	Génie des Procédés	SPIN
FEILLET	Dominique	PR	Génie Industriel	CMP
FOREST	Valérie	PR	Génie des Procédés	CIS
FRACZKIEWICZ	Anna	DR	Sciences et génie des matériaux	SMS
GANSTER	Patrick	CR	Génie des Procédés	SMS
GAVET	Yann	MA	Sciences des Images et des Formes	SPIN
GERINGER	Jean	MA	Sciences et génie des matériaux	CIS
GONDRAN	Natacha	MA	Sciences et génie de l'environnement	FAYOL
GONZALEZ FELIU	Jesus	MA	Sciences économiques	FAYOL
GRAILLOT	Didier	DR	Sciences et génie de l'environnement	SPIN
GRIMAUD	Frederic	EC	Génie mathématiques et industriel	FAYOL
GROSSEAU	Philippe	DR	Génie des Procédés	SPIN
GRUY	Frédéric	PR	Génie des Procédés	SPIN
HAN	Woo-Suck	MR	Mécanique et ingénierie	SMS
HERRI	Jean Michel	PR	Génie des Procédés	SPIN
IANDOLA	Donata	MAA	Mécanique et ingénierie	CIS
ISMAILOVA	Esma	MC	Microélectronique	CMP
KERMOUCHE	Guillaume	PR	Mécanique et Ingénierie	SMS
KLOCKER	Helmut	DR	Sciences et génie des matériaux	SMS
LAFOREST	Valérie	DR	Sciences et génie de l'environnement	FAYOL
LERICHE	Rodolphe	DR	Mécanique et ingénierie	FAYOL
LIOTIER	Pierre-Jacques	MA	Mécanique et ingénierie	SMS
MEDINI	Khaled	EC	Sciences et génie de l'environnement	FAYOL
MOLIMARD	Jérôme	PR	Mécanique et ingénierie	CIS
MOULIN	Nicolas	MA	Mécanique et ingénierie	SMS
MOUTTE	Jacques	MR	Génie des Procédés	SPIN
NAVARRO	Laurent	MR	Mécanique et ingénierie	CIS
NEUBERT	Gilles	PR	Génie industriel	FAYOL
NIKOLOVSKI	Jean-Pierre	Ingénieur de recherche	Mécanique et ingénierie	CMP
O CONNOR	Rodney Philip	PR	Microélectronique	CMP
PEILLON	Sophie	MA	Sciences de gestion	FAYOL
PICARD	Gauthier	PR	Informatique	FAYOL
PINOLI	Jean Charles	PR	Sciences des Images et des Formes	SPIN
RIGAUD	Jean-Baptiste	MA	Microélectronique	CMP
POURCHEZ	Jérémy	DR	Génie des Procédés	CIS
ROUSSY	Agnès	MA	Microélectronique	CMP
SANAUR	Sébastien	MA	Microélectronique	CMP
SERRIS	Eric	IRD	Génie des Procédés	FAYOL
STOLARZ	Jacques	CR	Sciences et génie des matériaux	SMS
VALDIVIESO	François	PR	Sciences et génie des matériaux	SMS
VIRICELLE	Jean Paul	DR	Génie des Procédés	SPIN
WOLSKI	Krzystof	DR	Sciences et génie des matériaux	SMS
XIE	Xiaolan	PR	Génie industriel	CIS
YUGMA	Gallian	MR	Génie industriel	CMP
ZIMMERMAN	Antoine	EC	Informatique	FAYOL

Mise à jour : 04/02/2021

Introduction Générale en français

L'aorte est la plus grande artère et joue un rôle essentiel dans le système cardiovasculaire grâce à l'effet Windkessel [1]. L'aorte absorbe la colonne de sang éjectée par le ventricule gauche en se déformant élastiquement, puis en se rétractant pour faire avancer le sang dans le système artériel et ainsi fournir de l'oxygène et des nutriments aux organes. Avec le temps, l'aorte peut éventuellement changer de structure comme d'autres tissus vivants. Ces changements ont pour but de maintenir le bon fonctionnement de l'aorte malgré les effets du vieillissement et sont provoqués par la régénération des tissus ou par des changements dans l'environnement de l'aorte. Les adaptations tissulaires sont contrôlées par les cellules qui y sont intégrées et qui sont capables d'exécuter une fonction mécanosensible pour évaluer l'état mécanique de la paroi aortique [2], [3]. Avec l'âge ou une maladie congénitale, les cellules peuvent avoir des difficultés à évaluer leur environnement, ce qui entraîne des inadaptations. Cela peut aboutir au développement de maladies telles que les anévrismes (AA) pouvant conduire à des dissections aortiques (AD) [4], [5].

Les AD sont en fait une cause de mortalité importante dans les pays développés. En effet, 1-2% de la population mondiale est susceptible d'être atteinte par un AA. Les anévrismes dans l'aorte abdominale sont les plus fréquents et leur rupture est responsable de 1-2% des décès dans le monde occidental. En plus, l'incidence des AD se situe entre 2-4/100 000 par an, identifiée après le décès pour plus de 20% des patients [4], [5]. Leurs causes, leur évolution et leur rupture ne sont pas complètement comprises. Cependant, les chercheurs s'accordent à dire que la progression de ces maladies est liée à la dégénérescence de la structure de la paroi aortique et aux difficultés des cellules à maintenir une stabilité mécanobiologique (homéostasie) [2]-[4]. En outre, pour les anévrismes de l'aorte thoracique (TAA), il est impératif de réparer l'aorte thoracique avant la rupture ou la dissection, le critère utilisé pour les prévenir étant la chirurgie à un diamètre de 50-mm à 55-mm. Malheureusement, de nombreux patients peuvent subir une rupture avant ce seuil, ou certains patients peuvent survivre avec des TAA plus grands que ce seuil [5], [6]. Le chirurgien a donc besoin d'un critère mécanique complémentaire qui puisse être adapté à chaque patient.

L'homéostasie de l'aorte est liée à un état préféré du tissu dans lequel les cellules maintiennent la stabilité mécanobiologique de l'aorte [7], [8]. L'état préféré peut être mesuré en termes de quantité mécanique, par exemple, la contrainte. Si un stimulus est donné, la contrainte peut changer, mais les cellules produiront des

molécules pour modifier la structure de la paroi afin de retrouver sa contrainte préférée [2], [3]. Cependant, avec l'âge, les cellules peuvent cibler une mauvaise contrainte préférée, ce qui entraîne la dégénérescence. Un autre problème pourrait être l'impossibilité pour les cellules de maintenir leur environnement en raison de leur difficultés à restructurer la matrice extracellulaire [3], [9].
Afin de modéliser les adaptations des tissus vivants (l'aorte) dans un contexte mécanique, des modèles de croissance et de remodelage (G&R) ont été développés. Généralement, la G&R est utilisée pour analyser le développement des anévrismes dans les artères intracrâniennes [10], [11], l'aorte abdominale [12]-[16] et thoracique [17], [18]. Également ces modèles sont utilisés pour déterminer la contrainte résiduelle dans la paroi artérielle [19]-[21]. Depuis les années 1990, plusieurs modèles G&R ont été proposés, mais ils sont basés sur des hypothèses diverses et présentent des limitations en termes de prédictions et de performance de calcul [22], [23]. Les modèles sont appliqués dans des codes d'éléments finis pour leurs calculs. Les premiers modèles G&R ont été développés pour des membranes axisymétriques [10], [12], [24], [25], d'autres pour des coques tridimensionnelles [15] et finalement pour des modèles tridimensionnels [14], [17], [26]. Néanmoins, les modèles axisymétriques ne permettent pas de simuler des géométries spécifiques au patient comme peuvent le faire les modèles tridimensionnels. Même si les modèles de coque tridimensionnels peuvent simuler une géométrie personnalisée d'artère [15], ils sont moins réalistes en raison des hypothèses de paroi mince et des difficultés liées à la mise en œuvre d'une paroi artérielle multicouche. Car la paroi artérielle est composée de trois couches (l'intima, la media et l'adventice) [1], [4], [5], mais il y a des modèles qui considèrent l'artère comme une couche homogène [12], [24], des modèles qui considèrent les trois couches [16] et des modèles qui considèrent deux couches en négligeant les effets mécaniques de l'intima [17], [26]. Dans la littérature, la G&R est généralement déclenchée par des changements de masse [12], [27], mais il y a quelques cas où la G&R est déclenchée par des changements de chargement dans l'artère, tels que l'hypertension [28], [29].
Étant donné ce contexte, notre travail vise à proposer un modèle pour l'évolution de l'aorte à partir du concept d'homéostasie dans la G&R. Cet modèle devrait à long terme fournir un nouvel outil pour décider si un patient doit être opéré ou non, en se basant sur des quantités mécaniques telles que la contrainte, la rigidité et la déformation de l'aorte. Il est également prévu que le modèle soit capable de prédire les modifications à l'échelle du tissu dans des modèles d'aortes personnalisées.
Afin d'analyser l'évolution des tissus dans les modèles d'aortes spécifiques aux patients, les objectifs de recherche suivants ont été fixés pour ce travail:

- l'implémentation de la G&R dans un code d'éléments finis et sa vérification;
- l'identification de la structure de l'aorte et son application dans les modèles numériques;
- l'analyse de l'homéostasie de l'aorte à travers le modèle G&R;

- l'analyse des effets de la précontrainte sur différents modèles d'aorte;

- l'analyse de l'adaptation mécanobiologique des modèles de l'aorte sous différents stimuli, par exemple la dégradation de masse ou des changements de chargement;

Au début de ce travail, plusieurs difficultés sont apparues lors de l'implémentation du modèle G&R dans un solveur d'éléments finis (EF) tridimensionnel, tel qu'`ABAQUS`. À ce moment-là, il était également difficile de comprendre toute la portée de la G&R en trois dimensions. Il a donc été décidé de travailler dans un code bidimensionnel dans le but de mieux comprendre les effets de la G&R dans les artères en effectuant plusieurs simplifications dans le modèle. Cela a abouti à l'écriture d'un code `FORTRAN` pour les coques axisymétriques. Le développement de ce code a permis de réduire l'analyse des quantités tensorielles à leurs directions principales et de réduire le temps de calcul pour les simulations de G&R dans les artères cylindriques. Après la mise en œuvre réussie du code bidimensionnel, l'étape suivante de ce travail a consisté à développer un solveur d'éléments finis tridimensionnel pour le G&R. Dans ce cas, le modèle G&R a été implémenté dans un solveur EF open-source disponible sur `GitHub` [30].
Pour atteindre les objectifs et de raconter l'histoire de ce recherche, le travail présenté ci-après est divisé en plusieurs chapitres:
Le **chapitre 1** rassemble l'état de l'art en matière d'anatomie et de physiologie de l'aorte, son histologie et ses maladies. En outre, est présenté le concept d'homéostasie appliqué à l'aorte. Vient ensuite une introduction à la mécanique des milieux continus avec les quantités nécessaires à l'analyse du comportement de l'aorte et utilisées ensuite pour établir des modèles de G&R pour les adaptations mécanobiologiques des tissus vivants.
Le **chapitre 2** contient la méthodologie développée pour la résolution du problème mécanique de G&R avec une procédure générale valable pour des solutions analytiques et pour des solutions numériques. Il présente la loi de comportement élastique pour le comportement de l'aorte avec plusieurs consitituants. Nous présentons également le principe des travaux virtuels avec son application à la méthode des éléments finis. Ensuite, le modèle de coque axisymétrique et le modèle épais tridimensionnel sont introduits avec les détails de leur mise en œuvre dans des codes développé *ex nihilo*.
Le **chapitre 3** correspond à un article publié avec les résultats obtenus à partir des simulations effectuées avec le code de coque axisymétrique présenté au chapitre 2. Dans les simulations, la G&R dans l'artère est déclenchée par la dégradation de l'élastine dans la paroi artérielle et par le déploiement d'une endoprothèse.
Le **chapitre 4** correspond à un article soumis (en révision) avec les résultats obtenus à partir des simulations réalisées avec le code tridimensionnel par éléments finis décrit au chapitre 2. Il contient des simulations sur des formes cylindriques et toriques ainsi que des géométries spécifiques aux patients. Les cas toriques et spécifiques aux patients s'avèrent être un défi et les simulations doivent être

effectuées avec la mise en place d'une pré-contrainte non uniforme pour l'état homéostatique de l'aorte.
Le **chapitre 5** contient la formulation développée pour l'étude de l'évolution des tissus après une dissection de l'aorte. Une simulation test est présentée dans ce chapitre pour montrer les capacités du modèle de dissection proposé ici.
Enfin, une conclusion est présentée mettant en évidence les principaux résultats de ce travail avec les contributions et les perspectives. En outre, les limites des modèles G&R et de l'approche développée ici pour la prédiction de la progression des maladies de l'aorte sont présentées.
Ce travail a été financé par le Conseil européen de la recherche avec la subvention ERC-2014-CoG BIOLOCHANICS et par l'*Agencia Nacional de Investigación y Desarrollo* du Chili. Le projet a été réalisé au CIS (Centre Ingénierie et Santé de Mines Saint-Étienne), en particulier au sein du groupe STBio (*Soft Tissue Biomechanics*), dans l'unité mixte de recherche SAINBIOSE.

General Introduction

The aorta is the largest artery and plays an essential role in the cardiovascular system thanks to the Windkessel effect [1]. The aorta absorbes the column of blood pushed by the left ventricle by deforming elastically, and subsequently recoiling to push the blood forward in the system, providing oxigen and nutriments to the organs. With time the aorta could eventually change its structure as other living tissues. Such changes are motivated by the regeneration of tissue or due to changes in the environment of the aorta. The tissue adaptations are modulated by the cells embeded in it. The cells are able to execute a mechano-sensitive function to assess the mechanical state of the aortic wall [2], [3]. Eventually with age or congenital disease the cells can present problems in assessing their environment and consequently leading to maladaptations. This could end up in the development of diseases such as aortic aneurysms (AA) or dissections (AD) [4], [5].

Cardiovascular diseases are one of the main causes of mortality in developed countries. It is estimated that 1-2% of the world's population has an AA. Aneurysms in the abdominal aorta are the most frequent and their rupture is responsible for 1-2% of deaths in the Western world. Moreover, the incidence of the AD is between 2-4/100,000 per year, and it is identified in more than 20% of patients after death [4], [5]. Their causes and evolution are not completely understood. However, researchers agree that the progression of the diseases are related to the degeneration of the aortic wall structure and difficulties of the cells to maintain mechanobiological stability [2]–[4]. In addition, for ascending thoracic aortic aneurysms (TAAs), it is imperative to remove the thoracic aorta before rupture or dissection, with the criterion being surgery at a diameter of 50-mm to 55-mm. Unfortunately, many patients may experience rupture below this threshold, or some patients may survive with TAAs larger than this threshold [5], [6]. Therefore, the surgeon needs a new mechanical criterion that can be customised to each patient.

Homeostasis in the aorta can be related to a preferred state of the tissue in which the cells maintain the mechanobiological stability of the aorta [7], [8]. The preferred state can be measured in terms of a mechanical quantity, for instance, the stress. Eventually if some stimulus alters the stress applied on the aorta, the cells would produce molecules to add new material in the wall or change the structure of the extant material to recover its preferred stress [2], [3]. However with age the cells may experience issues for sensing their environment correctly and consequently target a wrong preferred stress and lead to maladaptations. Another problem could be the impossibility for the cells to maintain their surrounding en-

vironment due to difficulties in producing new molecules and restructuring the extracellular matrix [3], [9].
In order to model the adaptations of living tissues (the aorta) in a mechanical context, Growth and Remodeling (G&R) models have been developed. Typically G&R was used to analyse the development of aneurysms in intracranial arteries [10], [11], abdominal [12]–[16] and thoracic [17], [18] aortas. Moreover, the models are used to determine the residual stress in the arterial wall [19]–[21]. Since the 1990s, several G&R models have been proposed, where they are based on different assumptions and present different limitations with respect to accuracy and computational performance [22], [23]. The models have been applied in finite-element codes for their calculations. The first G&R models were developed for axisymmetric membranes [10], [12], [24], [25], others for three-dimensional shells [15] and ultimately for three-dimensional thick models [14], [17], [26]. Although three-dimensional shell models can simulate patient-specific aortas [15], they are less realistic because of the thin-wall assumptions and difficulties associated with the implementation of a multi-layer arterial wall. Indeed the arterial wall is composed of three layers (intima, media and adventitia) [1], [4], [5]. However, there are models that consider the artery as an homogeneous layer [12], [24], models that consider all three layers [16] and models that consider two layers [17], [26], neglecting the mechanical effects of the intima. In the literature, the G&R is usually triggered by mass density changes [12], [27], but there are few cases in which G&R is triggered by changes in load in the artery, such as hypertension [28], [29].
Given this state of the art, this thesis intends to propose a model for the evolution of the aorta, based on the concept of homeostasis within G&R. This model should in the long term provide a new tool to decide whether a patient needs surgery or not, based on mechanical quantities, such as stress, stiffness and deformation of the aorta. It is also expected that the model is able to predict tissue scale modifications for patient-specific aortas.
In order to analyse the tissue evolution in patient-specific aortas, the following research objectives were set for this work:

- implementation of G&R in a finite element code and its verification;
- identification of the structure of the aorta and its application in computational models;
- analysis of the homeostasis of the aorta throughout the G&R model;
- analysis of the effects of prestress on different models of the aorta;
- analysis of the evolution of the aorta under different stimuli, e.g. mass removal or load changes.

We solved several challenges related to the implementation of the hCM model in a three-dimensional finite-element (FE) solver. We first worked on a two-dimensional code with the aim to embrace the G&R effects in arteries by performing several simplifications in the model. This ended up in writing a `FORTRAN`

code from scratch for the axisymmetric shell elements. The development of this code allowed to reduce the analysis of the tensorial quantities to their principal directions and reduce the computation time for G&R simulations in cylindrical arteries. We also developed a three-dimensional FE solver for G&R. In this case the G&R model was implemented within an open-source FE solver available in `GitHub` [30].

In order to reach the objectives, this thesis is divided in 5 chapters:

Chapter 1 presents the state of the art about the anatomy and physiology of the aorta, its histology and diseases. Moreover we introduce the concept of homeostasis applied to the aorta. Then follows an introduction to continuum mechanics with the quantities needed for the behavior of the aorta and subsequently used to establish G&R models.

Chapter 2 presents extensively the methodology developed in this thesis for solving the mechanical problem of G&R analytically and numerically. It includes the elastic constitutive model for the aortic behavior with several constituents. We also present the principle of virtual work with its application to finite-element analyses in an axisymmetric shell model and a three-dimensional thick-wall model. All details about their implementation in an in-house code are provided.

Chapter 3 corresponds to a published paper about the results obtained with the axisymmetric shell code of Chapter 2. In the simulations, G&R in the artery is triggered by elastin degradation in the arterial wall and by deployment of a stent.

Chapter 4 corresponds to a paper currently in revision, presenting the results obtained with the three-dimensional finite-element code of Chapter 2. It contains simulations in cylindric and toric shapes along with patient-specific geometries. The toric and patient-specific cases prove to be challenging and the simulations have to be carried out with non-uniform prestretch for the homeostatic state of the aorta.

Chapter 5 introduces a formulation for studying tissue evolution after an aortic dissection. A test simulation is presented in this chapter as a proof of concept.

Finally, a conclusion is presented to highlight the main findings of this work with contributions and future work. Moreover, limitations of the G&R models are discussed for the prediction of disease progression in aortas.

This work was funded by the European Research Council with the grant ERC-2014-CoG BIOLOCHANICS and by *Agencia Nacional de Investigación y Desarrollo* of Chile. The project was carried out at CIS (*Centre Ingénierie et Santé* of Mines Saint-Étienne) in particular the STBio (Soft Tissue Biomechanics) group in the SAINBIOSE research unit.

Contents

Introduction Générale en français iii

General Introduction vii

Contents xiv

List of Figures xxii

List of Tables xxiii

1 Background 1

1.1 Résumé du chapitre en français . . . 2
1.2 Summary of the chapter . . . 2
1.3 Arterial System . . . 3
1.4 The aorta . . . 5
1.5 Histology of the aortic wall . . . 6
1.5.1 Tunica intima . . . 6
1.5.2 Tunica media . . . 7
1.5.3 Tunica adventitia . . . 7
1.5.4 Elastin . . . 8
1.5.5 Collagen . . . 8
1.5.6 Smooth muscle cells . . . 8
1.6 Diseases in the aorta . . . 9
1.6.1 Aging . . . 9
1.6.2 Aneurysm . . . 9
1.6.3 Dissections . . . 11
1.7 Homeostasis . . . 13
1.7.1 Mechanical Homeostasis . . . 13
1.7.2 Turnover . . . 13
1.7.3 Prestress or prestretch . . . 14
1.8 Mechanical framework . . . 15
1.8.1 Kinematics . . . 15
1.8.2 Stress . . . 18
1.8.3 Balance principles . . . 19
1.8.4 Strain Energy function . . . 20

1.9 Growth and Remodeling 21
1.9.1 Kinematic Growth models 21
1.9.2 Constrained Mixture models 23
1.9.3 Homogenized Constrained Mixture Model 25
1.10 Overview and objectives 29

2 Materials and Methods **33**
2.1 Résumé du chapitre en français 34
2.2 Abstract 34
2.3 Definition of the mechanical problem 35
2.4 Elastic constitutive model 38
2.5 Principle of virtual work 40
2.5.1 Internal virtual work 41
2.5.2 External virtual work 42
2.6 Axisymmetric shell elements approach 43
2.6.1 Kinematics 43
2.6.2 Virtual work of shell elements 45
2.6.3 Virtual work of external forces in shell 46
2.6.4 Spatial discretization 47
2.6.5 Time integration method 49
2.6.6 Overview of the program 50
2.7 Three-dimensional approach 53
2.7.1 External forces 53
2.7.2 Spatial discretization 54
2.7.3 Time integration method 55
2.7.4 Overview of the program 55
2.8 Verification 56
2.9 Conclusion 59

3 Axisymmetric model **61**
3.1 Résumé du chapitre en français 62
3.2 Abstract of the chapter 62
3.3 Introduction 63
3.4 Material and methods 64
3.4.1 Strain Energy Function 64
3.4.2 Growth and remodeling 66
3.4.3 Adaptation to axisymmetric shell formulation 68
3.4.4 Finite element implementation 70
3.5 Numerical experiments 71
3.5.1 Comparison with an existing G&R model 71
3.5.2 Applications of the model 71
3.6 Results 72
3.6.1 Comparison with an existing G&R model 72
3.6.2 Case I: benchmark case of a bi-layer arterial wall 73

3.6.3 Case II: adaptation after stent implantation 75
3.6.4 Case III: stent implantation after several years of aneurysm development G&R 77
3.6.5 Computational details 80
3.7 Discussion 80
3.8 Conclusions 83

4 Non-uniform prestretch 85
4.1 Résumé du chapitre en français 86
4.2 Abstract of the chapter 86
4.3 Introduction 87
4.4 Materials and methods 88
4.4.1 Background on homogenized constrained mixture mechanics 88
4.4.2 Growth and remodeling based on homogenized constrained mixture models 90
4.4.3 Assigning non uniform initial prestretches 90
4.4.4 Numerical implementation 96
4.4.5 Verification 96
4.4.6 Applications 96
4.5 Results 100
4.5.1 Idealized ATA model 100
4.5.2 Patient-specific ATA model 103
4.6 Discussion 107
4.7 Conclusions 109

5 Extension of the model to chronic aortic dissections 111
5.1 Résumé du chapitre en français 111
5.2 Abstract of the chapter 112
5.3 The mechanical problem 112
5.4 Formulation of the interaction between layers 113
5.5 Implementation 114
5.6 Simulations 116
5.7 Conclusion 118

Conclusion Générale en français 119

General Conclusion 127

A Appendix of the Chapter 2 135
A.1 Reference configuration tensors 135
A.2 Matrices for shell elements formulation 136

B Appendix of the Chapter 3 139

C Appendix of the Chapter 4 **157**
C.1 Theoretical framework 157
C.2 Constitutive Models 159
C.3 Growth and Remodeling 160
C.4 Material properties 161

Bibliography **165**

List of Figures

1.1 Schematic representation of the arteries in the human body with the aorta in the center of the system [1]. 4

1.2 Aortic trunk with the definition of its segments [4]. 5

1.3 Schematic diagram of the arterial wall structure showing the layers and their composition. [1]. 7

1.4 Picture representing the size of young and old aortas [41]. This shows the effects of aging. 10

1.5 The picture shows the different shapes of the types of aortic aneurysms and it compares them against a normal aorta [32]. 11

1.6 Dissection classification. [4] 12

1.7 Stress in a thin-walled tube and prestress generated by the cells. Radial σ_r, circumferential σ_θ and longitudinal σ_z stresses. And the prestress generated by the cell σ_{pre}. [2]. 14

1.8 A configuration or frame represents a state of the body. As the body moves, a new configuration is obtained, dependeing on time t. The reference configuration is also called material or Lagrangian configuration, while the current configuration is also called spatial, deformed or Eulerian configuration. Additionally, the figure defines the material vector $d\boldsymbol{X} = \boldsymbol{X}_P - \boldsymbol{X}_Q$ and spatial vector $d\boldsymbol{x} = \boldsymbol{x}_p - \boldsymbol{x}_q$. 16

1.9 Constrained Mixture versus Kinematic Growth [9]. 23

1.10 Schematic of the hCM model, showing the different configurations. The reference configuration Ω_R at time zero is without external loads and without prestretch $[\boldsymbol{F}^j_{gr}]^{-1}$ in the jth constituent. Fictitious traction-free configuration Ω_{tf} is defined at time t, without external loads and without prestretch. The *in vivo* reference homeostatic configuration at time zero $\Omega_h = \Omega_0$ with homeostatic remodeling and external loads, and the current *in vivo* configuration Ω_t after G&R. The neighborhood $d\boldsymbol{X}$ of an arbitrary point in Ω_R is related to Ω_t by the transformation $d\boldsymbol{x} = \boldsymbol{F}d\boldsymbol{X}$. At time zero is $\Omega_t = \Omega_0$ and $d\boldsymbol{x}_0 = \boldsymbol{F}d\boldsymbol{X}$. Similarly, the relationship between Ω_t and the natural configuration is $d\boldsymbol{x} = \boldsymbol{F}^j_e d\boldsymbol{x}^j_n$, and the natural configuration and Ω_R are related by the inelastic deformation $d\boldsymbol{x}^j_n = \boldsymbol{F}^j_{gr} d\boldsymbol{X}$ where the inelastic deformation evolves with time. The natural configurations can only be defined locally but are not compatible. 27

2.1 A general representation of the equilibrium of a body Ω_t under surface forces $\boldsymbol{t}^*$ and restricted to the displacements $\boldsymbol{u}^*$. 36

2.2 Procedure to obtain the current state of a living tissue with G&R models. First, the initial inelastic conditions are used to define the elastic behavior of the material which is then used to compute its stress. After the equilibrium under the given boundary conditions, an homeostatic stress $\boldsymbol{\sigma}^j_h$ can be obtained as a reference for the inelastic constitutive equations of the hCM models. Second, the inelastic constitutive equations and the reference state are used to define the new elastic behavior of the material, which is again used to compute the stress for the equilibrium under the given boundary conditions. Once the equilibrium is solved, the current state of the living tissue is known at time t. The procedure is run until some time threshold of interest (t_f) is reached. 37

2.3 Schematic diagram representing the kinematic variables of the shell axisymmetric element. Derived from the Reissner-Mindlin plate. . . 44

2.4 Schematic diagram representing the parametrization of the shell axisymmetric element 48

2.5 Tree of the program for shell elements. 51

2.6 Integration along the thickness. 52

2.7 Structure of the python master script for the FE library. 56

2.8 Tree of the program for Kuru. 57

2.9 Assemblage of the program for Kuru. 57

3.1 Schematics representing the kinematic variables of the shell axisymmetric element 69

3.2 Geometrical characteristics of the artery model with symmetric conditions at $Z = 0$ and $Z = L$. L, R, L_s and $\hat{p}$ denote the arterial length, arterial radius, stent length and the internal pressure, respectively. a: Schematic representation of a real stent deployed in an artery with its media and adventitia, and the square shows the domain over which the simulations are performed (assuming symmetries). b: Simple geometrical model and its boundary conditions in a cylindrical coordinate system. 72

3.3 Changes of the radius in the center of arterial wall with maximum elastin degradation rate ($Z = 0$). Solid lines are the results obtained by the shell model and dashed lines are the results of [24]. 73

4.1 Schematic of the hCM model, showing the different configurations. The reference configuration Ω_R is reconstructed from the actual *in vivo* geometry of the artery. The configuration Ω_0 is obtained by applying the initial boundary conditions and by assigning initial prestretches $[\boldsymbol{F}^j_{gr}]^{-1}$ to each constituent of Ω_R. Ω_R and Ω_0 should be the same as there should be equilibrium between the effects of the initial boundary conditions and the effects of the initial prestretches in the reference configuration. However, both are represented separately in the figure as the initial prestretches providing this equilibrium are found iteratively in our approach. The fictitious traction-free configuration Ω_{tf} is defined as a fictitious configuration at time t, without the effects of boundary conditions and of prestretches. The current configuration Ω_t is obtained after equilibrium between the effects of the current boundary conditions and the effects of the updated prestretches obtained after growth and remodeling. The neighborhood $d\boldsymbol{X}$ of an arbitrary point in Ω_R is related to Ω_t by the transformation $d\boldsymbol{x} = \boldsymbol{F}d\boldsymbol{X}$. At time zero, $\Omega_t = \Omega_0$ and $d\boldsymbol{x}_0 = \boldsymbol{F}d\boldsymbol{X}$. Similarly, the relationship between Ω_t and the natural configuration is $d\boldsymbol{x} = \boldsymbol{F}^j_e d\boldsymbol{x}^j_n$, and the natural configuration and Ω_R are related by the inelastic deformation $d\boldsymbol{x}^j_n = \boldsymbol{F}^j_{gr} d\boldsymbol{X}$ where the inelastic deformation evolves with time. The natural configurations $\Omega^i_n(t)$ can only be defined locally but are not compatible. 89

4.2 (a) Lateral view of a cylinder with its diameter d and the cylindrical system $(\boldsymbol{e}_Z, \boldsymbol{e}_R, \boldsymbol{e}_\Theta)$ with $\boldsymbol{e}_\Theta$ perpendicular to the sheet. (b) Lateral and cross-sectional views of the idealized toric ATA model, where the luminal diameter is $d = R_{OC} - R_{IC}$, the arch radius is R (middle curvature) and the total wall thickness is t. IC=inner curvature and OC=outer curvature of the arch; a linear gradient is assigned for the axial ($\lambda^l_{h\Phi}$) and circumferential ($\lambda^l_{h\Theta}$) prestretch of elastin in the reference homeostatic state. The torus is represented with the spherical coordinate system $(\boldsymbol{e}_\Phi, \boldsymbol{e}_R, \boldsymbol{e}_\Theta)$ with $\boldsymbol{e}_\Theta$ perpendicular to the sheet. (c) Schematic of the boundary conditions, with springs at the proximal (k_{pro}) and at the distal (k_{dis}) ends; the circle (with radius L_{dam}) indicates the insult zone where a localized degradation of elastin is applied; the diameter d and the thickness along the same line are used to assess the initial distortions and displacements during the simulations. (d) Reconstructed geometry of the patient-specific aorta from the CT scan. In (a) and (b), the media is filled with north west lines and the adventitia with north east lines, in (c) the media is filled with dots and the adventitia with vertical black thick lines. 93

4.3 Flowchart for the homeostatic prestretch algorithm, showing how the prestretch gradient is found iteratively by solving forward FE problems successively. In the forward FE model, the prestretch gradient is held constant. After each forward analysis, the axial prestretch gradient ($\nabla\lambda^l_{h\Phi}$) is updated if the thickness distortion (δ_t) is larger than the thickness tolerance (ϵ_t), or the circumferential prestretch gradient ($\nabla\lambda^l_{h\Theta}$) is updated if the diameter distortion (δ_d) is larger than the diameter tolerance (ϵ_d) [49]. 95

4.4 Evolution of the maximum radius for the cylinder benchmark case. 4.4a comparison between the radius predicted by our model (solid lines) with the three-dimensional model (dashed lines) of Braeu et al [27]. 4.4b comparison between the radius predicted by our model (solid lines) with the membrane hCM model of Braeu et al [27] . . . 99

4.5 Diameter (a) and thickness (b) evolution in the idealized ATA geometry in response to half-life elastin degradation. Diameter (c) and thickness (d) evolution of the idealized ATA in response to an initial insult (sharp elastin degradation). 102

4.6 Von Mises stress (σ_{VM}) evolution in response to half-life elastin degradation (a) and in response to an initial insult (sharp elastin degradation) (b) for the idealized ATA geometry. Normalized total collagen density (ρ^c) evolution in response to long-term elastin degradation (c) and localized elastin loss (d) for the idealized ATA geometry. Simulations were achieved with $k_\sigma = 0.09/T$ 104

4.7 Diameter (a) and thickness (b) evolution in the patient-specific ATA geometry in response to half-life elastin degradation. Diameter (c) and thickness (d) evolution of the patient-specific ATA in response to an initial insult (sharp elastin degradation). 105

4.8 Von Mises stress (σ_{VM}) evolution in response to half-life elastin degradation (a) and in response to an initial insult (sharp elastin degradation) (b) for the patient-specific ATA geometry. Normalized total collagen density (ρ^c) evolution in response to long-term elastin degradation (c) and localized elastin loss (d) for the patient-specific ATA geometry. Simulations were achieved with $k = 0.09/T$ 106

5.1 The dissection model comprises two continuum bodies Ω_t^M and Ω_t^S, called the master and slave, respectively. Each body can have its own boundary conditions such as, pressure $\boldsymbol{t}^{p*}$, displacement impedance $\boldsymbol{t}^{k*}$ or imposed displacements $\boldsymbol{u}^*$. However, the two bodies share a special condition $\boldsymbol{t}^{c*}$ due to the connectors that keep the structure together. 113

5.2 Connector forces implementation within the Robin boundary conditions. 115

5.3 Connector assembler. 115

5.4 Connector assembler. 116

5.5 View of the XZ plane of the dissected cylinder. 117

5.6 View of the XY plane of the dissected cylinder. 117

B.1 Effects of different penalties on the aneurysm development of arterial wall due to elastin loss. a, b and c are plotted in the center of the arterial wall ($Z = 0$) versus the time. d, e and f are plotted for the last time step (after 199 months) along the arterial axial direction. 140

B.2 Effects of different media-adventitia ratio on the aneurysm development of arterial wall due to elastin loss. a, b and c are plotted in the center of the arterial wall ($Z = 0$) versus the time. d, e and f are plotted for the last time step (after 199 months) along the arterial axial direction. 141

B.3 Effects of gain parameters on the arterial wall G&R due to stent deployment. a, b and c are plotted in the center of the arterial wall ($Z = 0$) versus the time. d, e and f are plotted for the last time step (after 180 months) along the arterial axial direction. 142

B.4 Effects of different penalties on the arterial wall G&R due to stent deployment. a, b and c are plotted in the center of the arterial wall ($Z = 0$) versus the time. d, e and f are plotted for the last time step (after 180 months) along the arterial axial direction. 143

B.5 Effects of media-adventitia ratios on the arterial wall G&R due to stent deployment. a, b and c are plotted in the center of the arterial wall ($Z = 0$) versus the time. d, e and f are plotted for the last time step (after 180 months) along the arterial axial direction. . . . 144

B.6 The effect of the stent stiffness on the G&R of the arterial wall. a, b and c are plotted in the center of the arterial wall ($Z = 0$) versus the time. d, e and f are plotted for the last time step (after 180 months) along the arterial axial direction. 145

B.7 The effect of the stent tangential coefficients on the G&R of the arterial wall. a, b and c are plotted in the center of the arterial wall ($Z = 0$) versus the time. d, e and f are plotted for the last time step (after 180 months) along the arterial axial direction. 146

B.8 The effect of the stent over-sizing and gain parameters on the G&R of the arterial wall. a, b and c are plotted in the center of the arterial wall ($Z = 0$) versus the time. d, e and f are plotted for the last time step (after 180 months) along the arterial axial direction. . 147

B.9 The effect of the stent stiffness and gain parameters on the G&R of the arterial wall. a, b and c are plotted in the center of the arterial wall ($Z = 0$) versus the time. d, e and f are plotted for the last time step (after 180 months) along the arterial axial direction. . . . 148

B.10 The effect of gain parameters on the behavior of the arterial wall before and after stent deployment for an arterial wall undergone several years of G&R. a, b and c are plotted in the center of the arterial wall ($Z = 0$) versus the time. d, e and f are plotted for the instant just before stent deployment (t=80 months) along the arterial axial direction. g, h and i are plotted for the instant just after stent deployment (t=80 months) along the arterial axial direction. j, k and l are plotted after 100 months of the stent deployment along the arterial axial direction. 149

B.11 The effect of different penalties on the behavior of the arterial wall before and after stent deployment for an arterial wall undergone several years of G&R. a, b and c are plotted in the center of the arterial wall ($Z = 0$) versus the time. d, e and f are plotted for the instant just before stent deployment (t=80 months) along the arterial axial direction. g, h and i are plotted for the instant just after stent deployment (t=80 months) along the arterial axial direction. j, k and l are plotted after 100 months of the stent deployment along the arterial axial direction. 150

B.12 The effect of media-adventitia ratios on the behavior of the arterial wall before and after stent deployment for an arterial wall undergone several years of G&R. a, b and c are plotted in the center of the arterial wall ($Z = 0$) versus the time. d, e and f are plotted for the instant just before stent deployment (t=80 months) along the arterial axial direction. g, h and i are plotted for the instant just after stent deployment (t=80 months) along the arterial axial direction. j, k and l are plotted after 100 months of the stent deployment along the arterial axial direction. 151

B.13 The effect of stent over-sizing on the behavior of the arterial wall before and after stent deployment for an arterial wall undergone several years of G&R. a, b and c are plotted in the center of the arterial wall ($Z = 0$) versus the time. d, e and f are plotted for the instant just before stent deployment (t=80 months) along the arterial axial direction. g, h and i are plotted for the instant just after stent deployment (t=80 months) along the arterial axial direction. j, k and l are plotted after 100 months of the stent deployment along the arterial axial direction. 152

B.14 The effect of stent normal coefficient on the behavior of the arterial wall after stent deployment for an arterial wall undergone several years of G&R. a, b and c are plotted in the center of the arterial wall ($Z = 0$) versus the time. d, e and f are plotted for the instant just before stent deployment (t=80 months) along the arterial axial direction. g, h and i are plotted for the instant just after stent deployment (t=80 months) along the arterial axial direction. j, k and l are plotted after 100 months of the stent deployment along the arterial axial direction. 153

B.15 The effect of stent tangential coefficient on the behavior of the arterial wall after stent deployment for an arterial wall undergone several years of G&R. a, b and c are plotted in the center of the arterial wall ($Z = 0$) versus the time. d, e and f are plotted for the instant just before stent deployment (t=80 months) along the arterial axial direction. g, h and i are plotted for the instant just after stent deployment (t=80 months) along the arterial axial direction. j, k and l are plotted after 100 months of the stent deployment along the arterial axial direction. 154

B.16 The effect of gain parameters and stent stiffness on the behavior of the arterial wall after stent deployment for an arterial wall undergone several years of G&R. a, b and c are plotted in the center of the arterial wall ($Z = 0$) versus the time. d, e and f are plotted for the instant just before stent deployment (t=80 months) along the arterial axial direction. g, h and i are plotted for the instant just after stent deployment (t=80 months) along the arterial axial direction. j, k and l are plotted after 100 months of the stent deployment along the arterial axial direction. 155

C.1 FE algorithm of hCM model 162
C.2 Mechanical parameters 163
C.3 Density diagrams 164

List of Tables

1.1 Aortic dimensions and composition [6], [34]–[36]. 6

2.1 Verification of the FE frameworks against the analytical thin-walled tube. Simulations performed with a Neo-Hookean elastic model. . . 58
2.2 Verification of the FE frameworks against the analytical thin-walled tube. Simulations performed with a Fung Quadratic elastic model. . 58

3.1 Sensitivity Analysis 73
3.2 Material parameters 74
3.3 Computational costs time of every simulation. 81

4.1 Mechanical parameters used to verify our model against the results of [27] for the development of an aneurysm in an idealized cylindrical geometry. 97
4.2 Comparison of our results with results from [27] for the development of an aneurysm in an idealized cylindrical geometry following an initial insult (localized elastin degradation). Gain-parameter $k_\sigma = k_\sigma^m = k_\sigma^{c_i}$ and turnover time $T = T^m = T^{c_i}$ from the equation of rate mass degradation and deposition (details in Appendix C, section C.3). 98
4.3 Material parameters used in our models to simulate G&R in an idealized toric aortic arch and in a patient-specific ATA geometry. The parameters are introduced with their respective models in the Appendix C.2. 101

Chapter 1

Background

Table of contents of the chapter

1.1 Résumé du chapitre en français . . . 2
1.2 Summary of the chapter . . . 2
1.3 Arterial System . . . 3
1.4 The aorta . . . 5
1.5 Histology of the aortic wall . . . 6
1.5.1 Tunica intima . . . 6
1.5.2 Tunica media . . . 7
1.5.3 Tunica adventitia . . . 7
1.5.4 Elastin . . . 8
1.5.5 Collagen . . . 8
1.5.6 Smooth muscle cells . . . 8
1.6 Diseases in the aorta . . . 9
1.6.1 Aging . . . 9
1.6.2 Aneurysm . . . 9
1.6.3 Dissections . . . 11
1.7 Homeostasis . . . 13
1.7.1 Mechanical Homeostasis . . . 13
1.7.2 Turnover . . . 13
1.7.3 Prestress or prestretch . . . 14
1.8 Mechanical framework . . . 15
1.8.1 Kinematics . . . 15
1.8.2 Stress . . . 18
1.8.3 Balance principles . . . 19
1.8.4 Strain Energy function . . . 20
1.9 Growth and Remodeling . . . 21
1.9.1 Kinematic Growth models . . . 21
1.9.2 Constrained Mixture models . . . 23

1.9.3 Homogenized Constrained Mixture Model 25
1.9.3.1 Net mass production 26
1.9.3.2 Growth 28
1.9.3.3 Remodeling 29
1.10 Overview and objectives. 29

1.1 Résumé du chapitre en français

L'aorte est le plus gros vaisseau du système cardiovasculaire et sa tâche est de recevoir le sang expulsé du cœur et de l'acheminer vers les artères mineures, pour enfin fournir aux organes du corps du sang oxygéné et des nutriments. Pour que l'aorte satisfasse à de telles fonctions, sa structure est extrêmement importante, car l'aorte subit une expansion élastique pendant la systole et un retour élastique pendant la diastole pour pousser le sang vers l'avant. La structure de l'aorte, comme les autres vaisseaux sanguins, est divisée en trois couches, l'intima, la media et l'adventice. À travers les couches, des cellules évaluent les conditions de l'environnement et synthétisent des protéines et d'autres molécules pour maintenir ou modifier la matrice extracellulaire dans laquelle elles sont intégrées, la matrice extracellulaire fournissant une structure pour les cellules. Malheureusement, cette structure n'est pas exempte de troubles liés à une rupture du tissu due à des charges élevées, au vieillissement du matériau ou à des problèmes des cellules pour sentir et contrôler la cohésion du tissu conjonctif.
Le processus par lequel les cellules maintiennent la structure de la matrice extracellulaire est appelé homéostasie et c'est une activité importante dans les systèmes biologiques pour maintenir leur stabilité. Habituellement, ce processus permet l'élimination et le renouvellement de cellules et de protéines. Mais sous certaines conditions exceptionnelles un nouveau tissu conjonctif peut être créé et produire des cellules qui peuvent migrer pour cibler les nouveaux besoins, conduisant à une adaptation du système ou éventuellement à une inadaptation dans le cas de certaines maladies. Les modèles mathématiques de Croissance et de Remodelage développés depuis les années 90 visent à donner une représentation mathématique et à comprendre les différents aspects et mécanismes de l'homéostasie dans les tissus vivants. Ils sont basés sur les changements de masse ayant lieu à l'échelle du tissu et la modification des liens dans la structure.

1.2 Summary of the chapter

The aorta is the largest vessel in the cardiovascular system and its task is to receive the blood expelled from the heart and deliver it to minor arteries to finally provide the organs of the body with oxigenated blood and nutriments. In order to satisfy

such functions its structure is tremendously important, as the aorta experiences an elastic expansion during systole and an elastic recoil during diastole, permitting to push the blood forward. The structure of the aorta, like other blood vessels, is divided within three layers, intima, media and adventitia. Through the layers there are cells able to assess the conditions of the environment and to synthesize proteins and other molecules to maintain the extracellular matrix in which they are embedded, providing a structure for the cells. Unfortunately, this structure is not free of disorders related with disruption of the tissue due to high loads, aging or problems of the cells to sense and control the cohesion of the connective tissue.
The process in which the cells assess and manage the structure of the extracellular matrix is denominated as homeostasis and it is an important activity in the biological systems to keep their stability. Usually this process is just in charge of the removal and production of cells and proteins. But under exceptional changes or disruption of the structure, the homeostasis can lead to building new connective tissue and to cell migration to target the new requirements. This could end up in adaptations of the system or eventually in maladaptations with disease progression. Growth and Remodeling models developed since the 90s aim to give a mathematical representation and understand the differents aspects and mechanisms of homeostasis in living tissues. Such aspects are based on mass changes taking place at the tissue scale and the modification of the tissue structure.

1.3 Arterial System

The human body is composed of many systems and organs with specific tasks to remain alive. However, the distance between the organs leads to the need of an efficient transport which is provided by the *blood*. The blood is in charge of transporting mass (nutriments, hormons, oxygen, carbon dioxide and wastes), momentum (pressure) and energy (heat) and it moves through a large network of pipes, called *blood vessels*. At the core of this piping system there is a pump generating the potential (pressure), called the *heart*.
The heart is a double pump, one pushing the blood without oxygen to the pulmonary circulation, and the other, pumping the blood rich in oxygen to the body in the systemic circulation through the *aorta*. The heart contracts to push the blood in a process referred to as *systole*, then it has a period of recoil where it fills again, referred to as *diastole* [1]. The heart collects blood from the *veins* and expells the blood through the *arteries* (Fig. 1.1), where the latter are the downstream piping system working at high pressure. Most vessels share the same wall structure to contain the blood inside.
As the heart pumps the blood in a pulsated fashion, the arteries have to be elastic in order to expand and recoil and to push the blood forward continuously, attenuating the pulsating waves. To manage the high pressure at the opening of the aortic valve and the lower pressure at the closed position, arteries are either elastic or muscular. Elastic arteries –rich in elastic fibres– dilate when they receive the

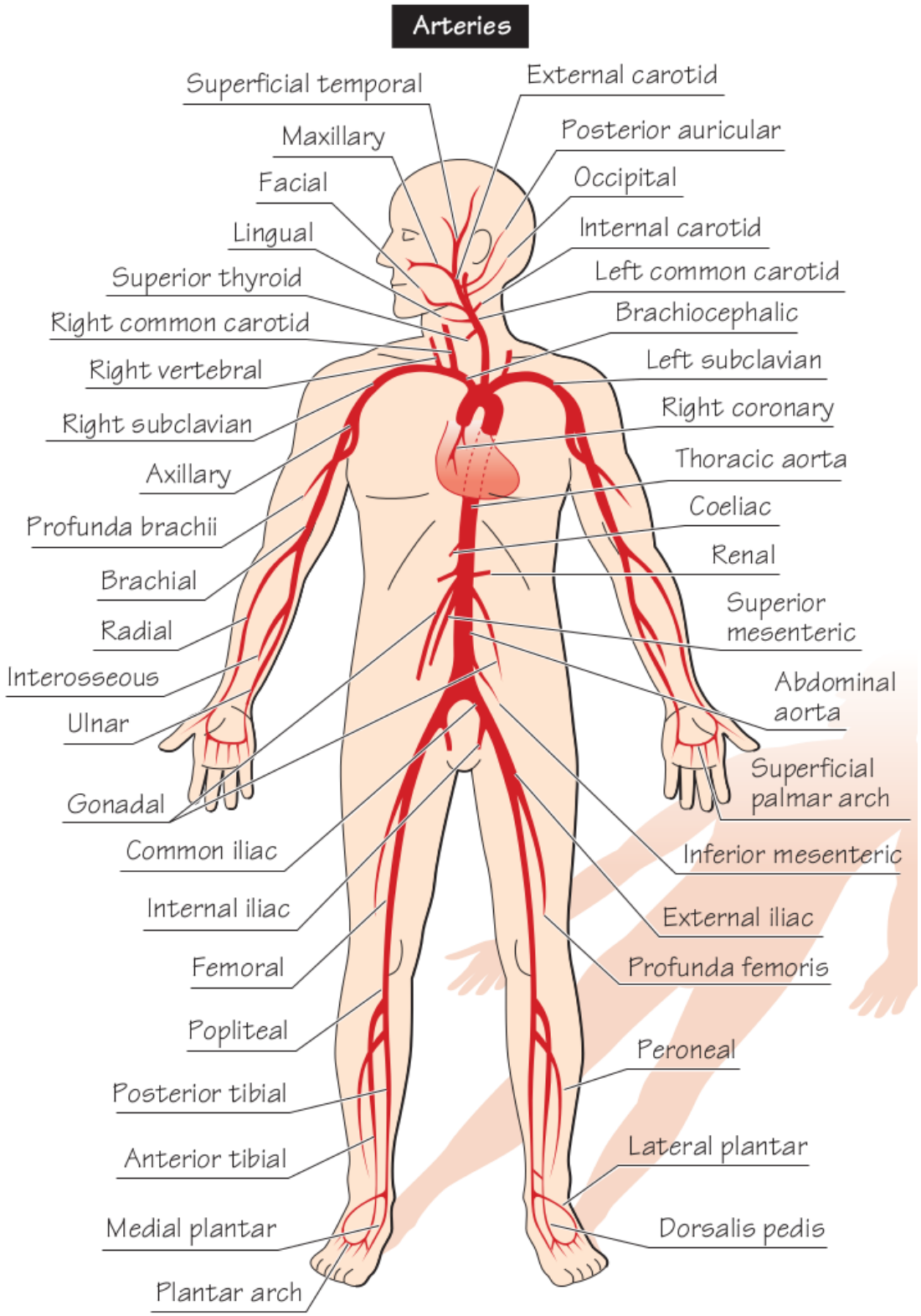

FIGURE 1.1 – Schematic representation of the arteries in the human body with the aorta in the center of the system [1].

blood at systole and recoil at diastole, hence pushing the blood forward. Downstream we find the muscular arteries –having a higher fraction of smooth muscle–. They play an important role with contractions and dilatations managed by the *smooth muscle cells* (SMCs), controlling the flow and guiding the blood to the places of major needs [1], [31].

1.4 The aorta

The aorta was called "the greatest artery" by the ancients [4], it is the largest blood vessel in the human body and it is connected to the heart. It makes its way in the thorax and abdomen. Its branches constitute the major arteries distributing blood to the head, arms, organs and legs. The aorta is cyclically loaded by the pulsed pressures due to the opening and closing of the aortic valve, which reflects in the dilation and contraction of the arterial wall induced by heart beats. During the dilation, energy is stored in an elastic form, which is then released by the recoil of the aorta. This effect helps to maintain a continuous blood flow. This is called the Windkessel effect [1].

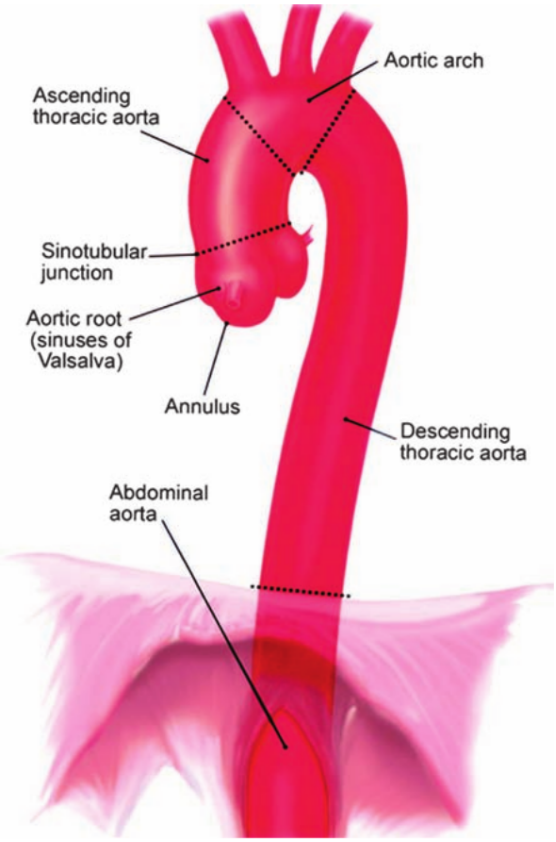

Figure 1.2 – Aortic trunk with the definition of its segments [4].

The thoracic aorta is divided into four segments, Fig. 1.2. The aortic root is the most proximal segment, extending from the annulus of the aortic valve and extending to the sinotubular junction; the aortic root is composed of the right,

left, and noncoronary sinuses of Valsalva. The ascending aorta is tubular and extends from the sinotubular junction to the innominate (brachiocephalic) artery. Both the aortic root and ascending aorta lie within the pericardial space, which means that the ascending aorta can be surrounded by pericardial fluid in the setting of an effusion; it also means that rupture of the ascending thoracic aorta (ATA) can cause cardiac tamponade. The aortic arch extends from the innominate artery to just beyond the left subclavian artery. The aortic arch gives rise to the innominate artery, left common carotid, and left subclavian arteries. The descending aorta begins just after the origin of the left subclavian artery and extends to the aortic bifurcation. At the diaphragm the aorta is divided between the descending thoracic aorta above the diaphragm and the abdominal aorta below [32], Fig. 1.2.

1.5 Histology of the aortic wall

The wall of the aorta is organized in three layers: the *intima*, the *media* and the *adventitia* (Fig. 1.3). This structure comprises cells able to sense the environment, modify the structure, and relax or contract the aorta; such cells are embedded in a viscoelastic structure named the extracellular matrix (ECM) [33]. At the same time, the ECM is maintained by the cells. The ECM supports the stresses induced by the blood pressure. The aorta is abundant in elastic fibres. More details are presented in Table 1.1.

	Thoracic Aorta	Abdominal Aorta
Luminal diameter(mm)	32 – 36	12 – 15
Thickness(mm)	1.6 – 2.3	1.4 – 1.5
Intima/Media/Adventitia(%)	6/76/18	20/47/33
Elastin(%)	22 – 33	23 – 30
Collagen(%)	18 – 31	36 – 45
SMCs(%)	–	≈ 23

TABLE 1.1 – Aortic dimensions and composition [6], [34]–[36].

1.5.1 Tunica intima

The intima is the inner most layer in contact with the blood flow. It consists of a single layer of endothelial cells with no important structural significance. However, this layer modulates the permeability of cells (e.g. lymphocytes) and nutrients from the flow into the wall, it helps to control vasoconstriction through communication with the SMCs of the media, it also facilitates the formation of new blood vessels via angiogenesis. It provides a smooth non-thombogenic surface for blood flow, important in the formation of atherosclerotic plaques [4]. Recent

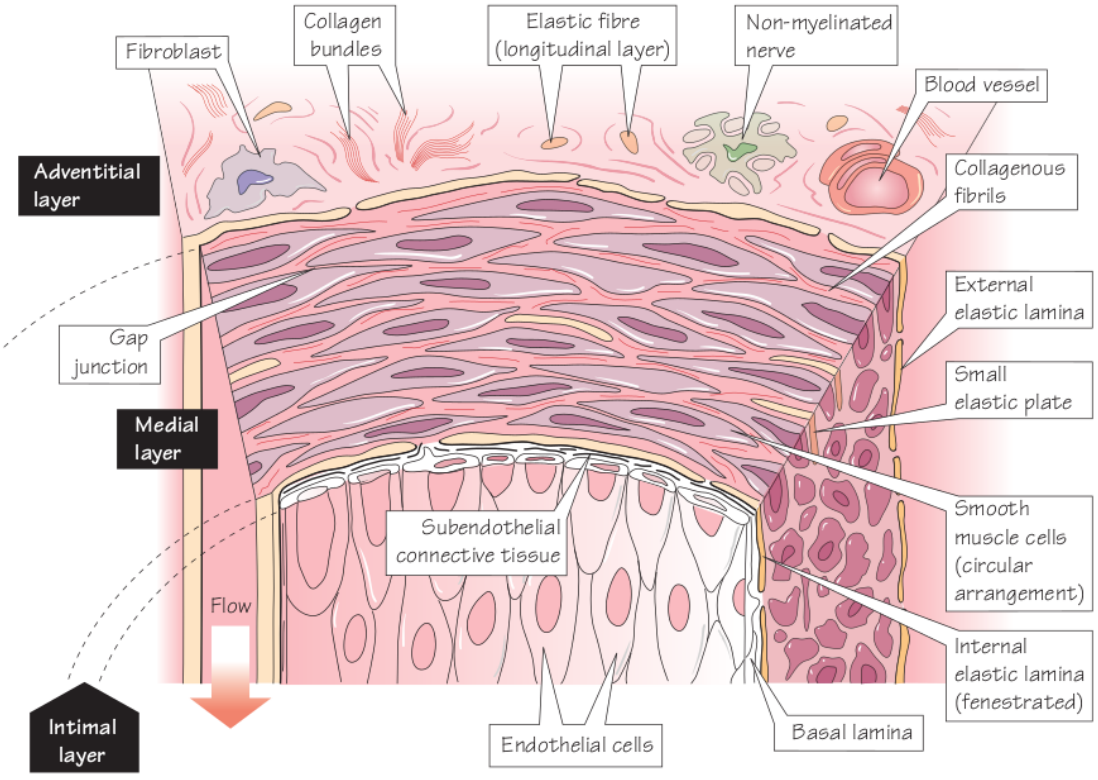

Figure 1.3 – Schematic diagram of the arterial wall structure showing the layers and their composition. [1].

studies showed that the novel COVID-19 disease may affect the functionality of endothelial cells [37].

1.5.2 Tunica media

The media is the middle layer, it contains SMCs circumferentially oriented wrapped in a thin layer of collagen. These concentric arrangements are separated by elastic laminas, composed mainly of *elastin*. It differentiates from the intima and adventitia at the two fenestrated elastic laminas. Due to the abundant elastic fibres, this layer has the important function of storing elastic energy (reservoir) during systole and use it to recoil during diastole to keep the blood flow forward. This function is particularly important for the aorta.

1.5.3 Tunica adventitia

The outer layer is the adventitia, it contains mainly *collagen* supporting fibroblasts and nerves, with some elastin. It provides a mechanical support to the vascular wall, preventing acute overdistention of the more vulnerable elastic fibres and SMCs of the media [3]. It also contains small blood vessels, the vasa vasorum, [1], [3]. The adventitia is around 10% to 50% of the arterial wall for the elastic and muscular kind, respectively [33]

1.5.4 Elastin

Elastin is a protein mainly present in arteries and it is the most abundant in the ECM, being around 50% of the dry weight. It allows arteries to distend elastically during systole and recoil during diastole, which is an essential function of the aorta. It has a half-life in the order of decades. It is mainly produced during the fetal life and infancy period by the SMCs. Elastin is the main constituent of elastic fibres (90% approx). Elastic fibres assemble into the elastic laminas, which are disposed as concentric arrangement with SMCs. With age, calcium may be deposited in the elastic lamina, inducing stiffer properties, which alters the elastic function of large arteries [3], [38]. Elastin is one of the most resistant, both chemically and thermally, of all proteins; it is very distensible, it can withstand up to 150% stretch without breaking [33], [39].

1.5.5 Collagen

Collagen is a fibrous protein present in the three layers of the aorta. At high intraluminal pressures collagen becomes very stiff, limiting vascular distensibility, due to its significant stiffness and strength. The half-life of collagen is in order of only a few weeks or months with a considerable turnover in response to increased mechanical loading. An excessive deposition of collagen may produce fibrosis in the vessel and increase the stiffness. The deposition and removal of collagen is regulated by fibroblasts in the adventitia and by SMCs in the media [1], [3], [38]. Collagen fibres are wavy when they are not stretched. They are oriented helically around the artery [39]. Cross-linking of collagen increases with age, resulting in larger stiffness. The maintenance of collagen relies on a delicate balance between synthesis and degradation. When they are straigthened, collagen fibres can withstand up to 10% stretch without breaking [33].

1.5.6 Smooth muscle cells

Actually, in the arterial wall, there are three different kinds of cells: the endothelial cells in the intima, SMCs in the media and fibroblasts in the adventitia. Although each cell is in charge of the maintenance of the ECM in its respective layer [33], they also share many cross-communication pathways in order to complete this function and to manage the contractions and relaxation of the artery.
Maybe the most important cells in the arterial wall are the SMCs. Their cytoplasm contains dense bodies and bands, which are linked by actin and myosin filaments along the axis of the cell, and by intermediate filaments to form the cytoskeleton (the internal structure that gives the cell shape). The dense bodies interact with the ECM through the integrins, which allow the cells to assess their environment [1], and regulate the production and degradation of proteins and molecules. They exhibit synthetic and contractile functions [3] with the capability to alter the tone of the artery [39]. SMCs have a preferred length of work and their contraction/relaxation depend on the concentration of Ca^{2+} [33].

1.6 Diseases in the aorta

Despite regulations by the cells, the wall of the aorta is not inmune against fatigue or disruption of the structure under perturbations. The difference between adaptation and maladaptation of the tissue lies in the cells ability to sense and maintain the aorta. In this work we are interested by the regulation done by the cells in response to the tissue changes after a perturbation, such as, *age* or an insult related to structural disruptions, geometrical modifications or load variations. Such disturbance in homeostasis of the aorta could end up in the development of diseases such as *aneurysm* and/or *dissection*. Diseases in the aorta are usually related to the degeneration of the media involving SMCs loss or inflammation and elastic fibres fragmentation [40]. Some risk factors that accelerate degeneration of the aortic wall are related to hypertension, smoking and genetic disorders [32].

1.6.1 Aging

Aging is a natural process in the human body since the early life, but it starts to be more significant during adulthood [4]. This is due to the accumulation of load cycles producing diffuse fragmentations of the elastic fibres. As SMCs do not synthesize elastin during adulthood, their lack is compensated by collagen. This replacement produces a loss of elasticity and a stiffness increase, which affects the elastic recoil of the aorta and increases the pulse wave velocity.
The new tissue structure of the arterial wall may produce disproportional dilatation of the artery increasing the lumen diameter and length over 3% and 12% per decade, respectively. This deformation may even produce a tortuous aorta [41]. Between the second and sixth decade, the luminal pressure increases, the inner surface of the aorta doubles, the aortic diameter increases –especially in the ascending aorta and to a lesser extent in the abdominal aorta–[42]. Furthermore with age there is an hyperplasia where the intimal thickness increases due to atherosclerosis. This is related to infiltration of lymphocytes and accumulation of fat, collagen and calcium in the intima [4], [39].

1.6.2 Aneurysm

An aneurysm in an asymptomatic disease that generally develops in major vessels such as the aorta. There are also cases of aneurysms in minor vessels such as the intracranial [10] or carotid arteries [43]. An aneurysm is a localized or diffuse dilatation of the vessel wall with a diameter 1.5 times larger than its normal caliber or greater than 45-mm in the case of the ascending aorta and aortic root. An aneurysm in the aorta primarily involves one segment. Aortic aneurysms are important causes of morbidity and mortality in developed countries where 1–2% of the population is concerned, with a prevalence of 10% in elderly [4], [32]. Aneurysms may be classified by shape in saccular or fusiform. Moreover, they may be classified as true (lined by attenuated media) or false (lined by adjacent

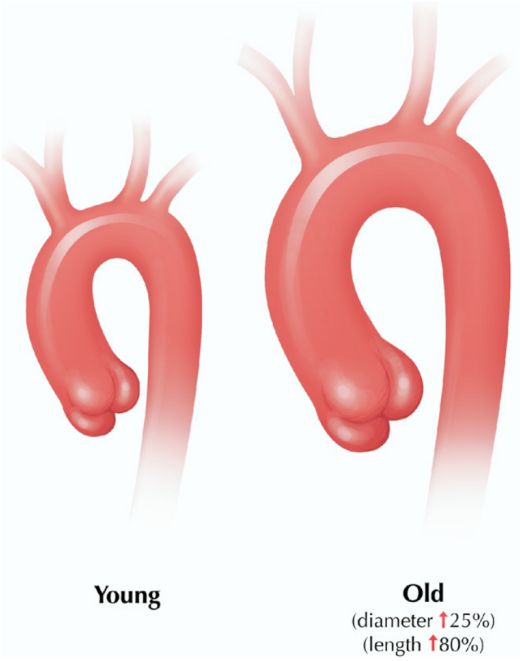

FIGURE 1.4 – Picture representing the size of young and old aortas [41]. This shows the effects of aging.

fibrous tissue) and as dissecting or nondissecting, Fig. 1.5. Abdominal areurysms are more common than thoracic aneurysms [4], [32], [39].

It is widely accepted that the origin of aneurysms is due to disruptions in the media related to death and atrophy of the cells with fragmentation of elastic fibres and accumulation of collagen with proteoglycans [4], [5]. Such medial degeneration may be a consequence of the normal aging process accelerated by conditions such as hypertension and specific genetic conditions. Indeed, Ascending Thoracic Aortic Aneurysms (ATAA) are primarily associated with cystic medial degeneration (CMD) and Abdominal Aortic Aneurysms (AAA) are generally associated with atherosclerosis [4], [5]. CMD is characterized by fragmentation and loss of elastic lamina, pools of proteglycans, appearance of cyst-like structures and necrosis in the media; patients with inherited connective tissue disorders are at greatest risk of CMD. Atherosclerosis produces accumulation of inflammatory cells, which in the long term may produce SMCs atrophy with disruption of elastic fibre translated into attenuation and fragmentation of the media with fibrosis. Atherosclerotic plaques may also exist at the initiation of ATAAs but less often. However, aneurysms may also occur from chronic dissection, trauma, aortic surgery, false aneurysm, noninfectious aortitis, syphylis or other infections [4].

If the aneurysm is left untreated it may lead to aortic dissection or rupture with high mortality risks. The expansion of the aneurysm could be fixed by surgical repair, the latter is indicated for aneurysms diameters larger than 55-mm or fast growing rates (over 0.15cm/year) [44]. Surgical repair can be endovascular for descending thoracic and abdominal aortas. Endovascular aneurysm repair (EVAR) consists in the insertion of a synthetic stent-graft into the aorta where the main

idea is to block or diminish the leak of blood within the aneurysm [4], [39], [45]. On the other hand a complete replacement is advised for ATAAs [32]. The main complications are dissections, degenerative aneurysms, penetrating ulcers, traumatic injuries or leaking [4]. Open surgical repair is the standard of care for treating the thoracic aortic aneurysms (TAAs) but EVAR is an increasingly important technique that is being continually refined [4], [5], [45].

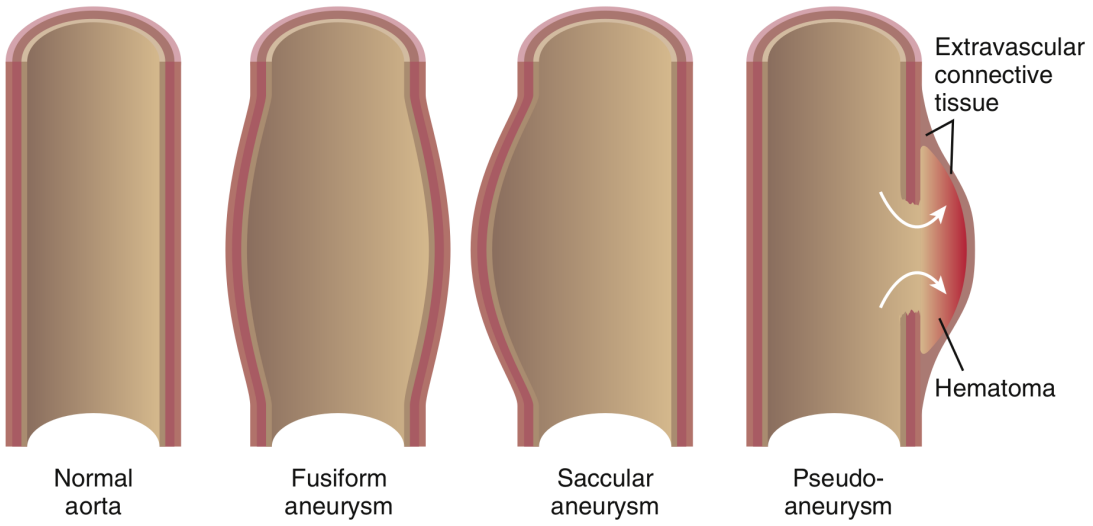

Figure 1.5 – The picture shows the different shapes of the types of aortic aneurysms and it compares them against a normal aorta [32].

1.6.3 Dissections

Aortic dissection is a disease which produces division along the arterial layers leaving a gap for blood invasion. An aortic dissection may be produced by a tear or ulcer in the intima, by the rupture of the vasa vasorum, or even by aortic manipulations [4], [32], [46]. The surface of dissection is usually located between the inner two-third and the outer one-third of the aortic media, or less commonly at the junction between the media and adventitia. This gap within the arterial wall is filled with blood and is denominated false lumen while the original arterial lumen is denominated true lumen. In several cases the false lumen becomes greater than the true lumen. This can induce ischemia in some organs due to the lack of oxygenated blood in the downstream. Actually the main complications are the false lumen rupture and the compression of the true lumen or arterial branches. Moreover aortic dissections have been related to aortic regurgitation and aneurysmal dilatation in the elderly population. Dissections may be produced by other diseases such as the giant cell aortitis, Takayasu and syphilis. Aortic dissections are also six times more common in people with the Turner syndrome than in the general population [4].
Aortic dissections (ADs) are classified into acute and chronic types depending

on the duration of the disease, where the threshold is between two weeks or two months [47], [48]. Moreover there are two classifications depending on the extension of the aorta affected by the dissection, the DeBakey and Stanford systems. The DeBakey system is based upon the site of tear and divides ADs into three major groups: type I dissections, in which the intimal tear is located in the ascending aorta, with dissections extending into the descending aorta; type II dissections, in which the intimal tear is also located in the ascending aorta, but the dissection is limited to the ascending aorta; type III dissections, which differ fundamentally from the other types, because the intimal tear is in the descending or the aortic arch, usually in the distal arch or proximal descending aorta. Type III dissections are further divided into type IIIa –retrograde dissection extending into the ascending aorta– and type IIIb –dissection confined to the aortic arch or the descending aorta–. The Stanford classification is categorized into type A and B. Type A means that the dissection involves the ascending aorta irrespectively of the site of origin, and type B means that the dissection does not involve the ascending aorta and is restricted to the descending aorta. The two types have different clinical implications, as the incidence of in-hospital complications is higher for type A than for type B. Dissections involving the ascending aorta need open surgery and have higher mortality rates than dissection involving just the descending aorta and/or the aortic arch, which can be mitigated with therapy and endovascular interventions [4].

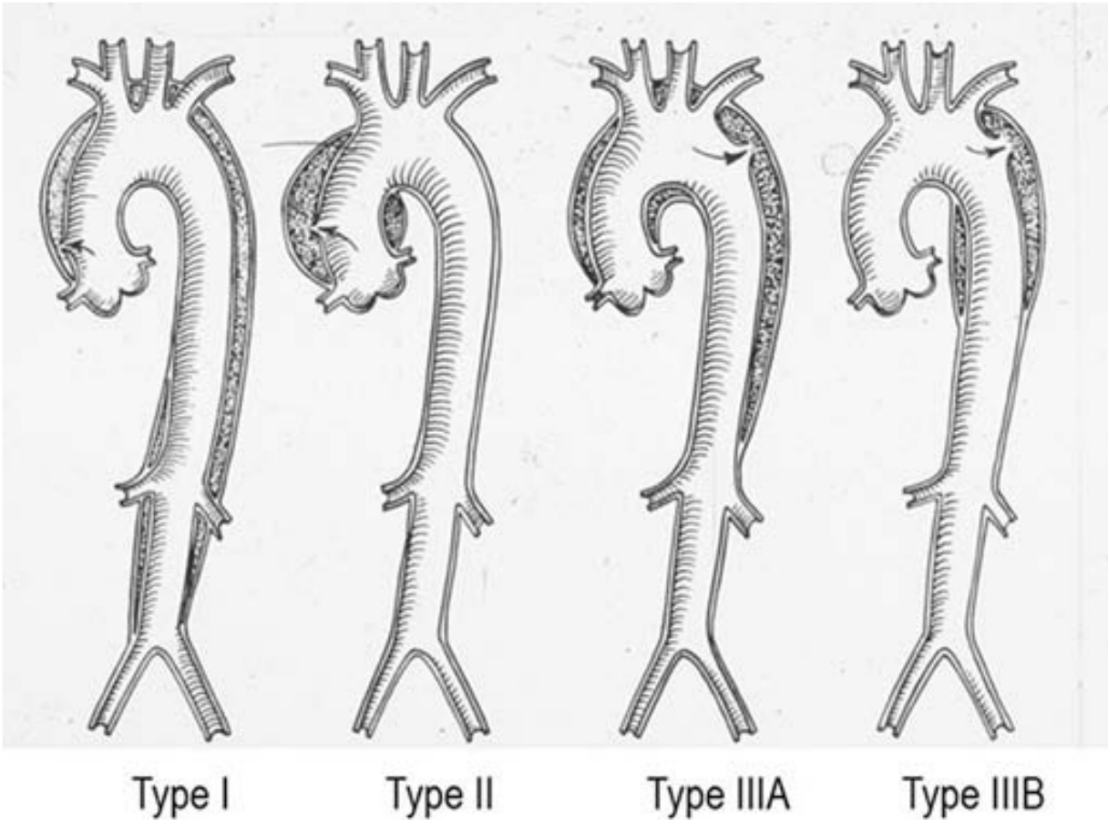

FIGURE 1.6 – Dissection classification. [4]

1.7 Homeostasis

Biological systems have a self-regulating process referred to as homeostasis that tends to maintain stability in the system while adapting to conditions that are optimal for survival [7]. This gives the aorta the natural ability to continually modify its own structure to keep its functionality or adapt under some chemical or mechanical stimuli. Either homeostasis is successful and the aorta does not experience macroscopic changes; or it is unsuccessful and the aorta experiences maladaptation with disease consequences. This depends on the mechano-sensitive and mechano-regulation functions of the cells within the arterial wall, that are in charge to assess the conditions of the ECM to synthesize and reorganize the connective tissue. The mechanical assessment of the ECM relies on the integrins of the cells which connects the cytoskeleton (inside the cell) with the extracellular matrix, Fig. 1.7. As a result, the cells produce proteins and/or molecules to modify the ECM [2], [3], [9]. Eventually, if the cells do not work properly or if they are dead, there is no sufficient maintenance of the cross-links in the ECM and disease may arise in the aorta.

1.7.1 Mechanical Homeostasis

Arteries are able to self-regulate the stress sensed from the aortic wall [2], [3], [8], [28]. The stress is an important measure in biomechanics as it is a force intensity having units of force per unit area (e.g. N/m^2). Therefore, taking into consideration that an artery can be modeled as a straight thin-walled tube, given the inner pressure P and axial load f, the artery will be under the stress state showed in figure 1.7 with radial, circumferential and longitudinal stresses. Moreover under normal conditions of pressure, the circumferential stress in the artery would be approximately between 100-kPa and 150-kPa [2]. In a small portion of the aortic wall, the stress through the ECM is ultimately applied onto the cells (SMCs, fibroblasts and endothelial cells). Additionally it has been observed that the intramural cells target some preferred state of stress, for instance, contractile SMCs generate stresses of 100-kPa approximately and synthetic SMCs with fibroblasts seek stresses between 5-kPa to 10-kPa [2]. Thus, stress variations in the ECM, result in different biological pathways where the cells modify the stiffness of the ECM to restore their preferred stress.

1.7.2 Turnover

Turnover is the mechanism of homeostasis related to the activity of cells in reorganizing the ECM and adapting its stiffness, which incorporates the combined effects of production/removal of structural proteins and the remodeling of tissue. Due to the half-life of the extracellular components and the life-spans of the cells, the stiffness is constantly changing and deviates from the preferred one, making turnover a continuous tissue maintenance process. For instance arterial collagen

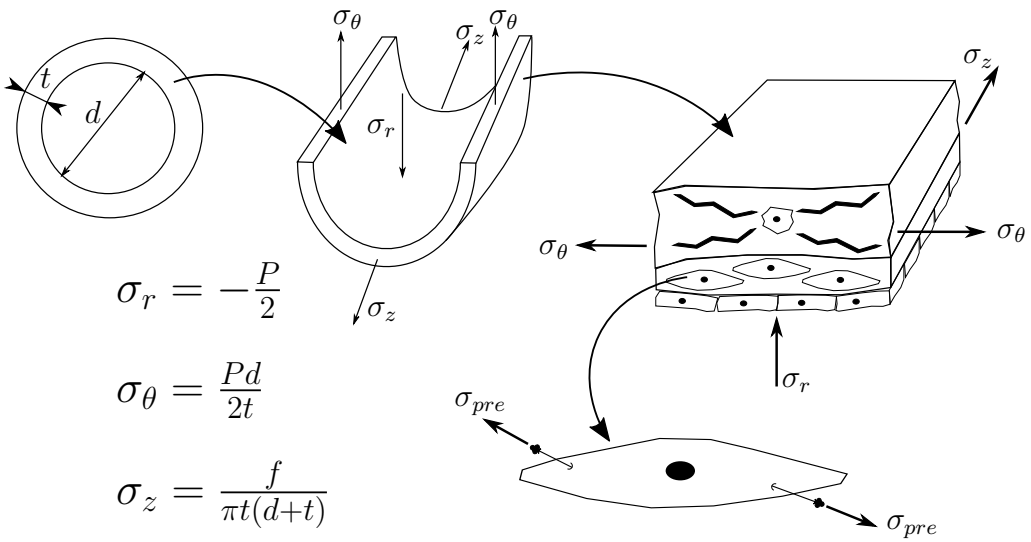

FIGURE 1.7 – Stress in a thin-walled tube and prestress generated by the cells. Radial σ_r, circumferential σ_θ and longitudinal σ_z stresses. And the prestress generated by the cell σ_{pre}. [2].

has a half-life in the order of 60-70 days while arterial elastin has a half-life in the order of 25-70 years. Therefore, compared to the time scale of pulsatile waves this mechanism (growth and remodeling) occurs in long time scales (synthesizing new proteins and cross-linking extant proteins). Eventually, turnover can consist in replacing the cross-links in the connective tissue or creating new cross-links in response to external stimuli. In the latter the artery may undergo maladaptation and facilitate the progression of pathologies, such as fibrosis or atrophy/hypertrophy of the cells [2], [3], [9].

1.7.3 Prestress or prestretch

As indicated before, the intramural cells have a preferred stress and they may produce all the changes needed to recover that mechanical state. Such preferred stress seems essential to generate a prestressed extracellular matrix, as it seems to be the only way to reach the preferred tensional homeostasis. It is achieved through the deposition of prestressed matrix. In other words, the newly deposited and extant fibres, if they were stress-free or under-stressed, would extend until the *in vivo* level of stress [9].

The prestress of the tissue is distributed amongst the cells and the extracellular matrix, with the cells taking only a small part and the matrix schielding them from the largest part of the stress, Fig. 1.7. Nevertheless the stress distribution within the tissue must respect the linear momentum balance, and eventually the prestress can spatially depend on the *in vivo* loads and on the shape of the vessel [21], [49]. Accordingly, the continual prestress incorporation balance the external

loads and reduce the stress directly experienced by the cells. This stress shielding effect seems mechanically favorable for the mechano-sensitive activity of the cells to monitor the turnover and maintain the tissue [9].

1.8 Mechanical framework

Herein the goal is to relate the biological and mechanical aspects of the aortic wall and its homeostasis in a general mathematical framework based on continuum mechanics [50], [51]. Therefore, in this section, we review the mechanical background for modeling mechanical homeostasis in the aorta.

1.8.1 Kinematics

Let us assume that the motion of a continuum body (living tissue) in the Euclidean space can be described by a continuous function $\chi : \Omega_R \times \mathbb{R}^+ \to \mathbb{R}^3$ mapping the displacement of a reference particle P to a current particle p with $\boldsymbol{x}_p = \chi(\boldsymbol{X}_P, t)$, where $\boldsymbol{X}_P$ is a particle in the body $\Omega_R \subset \mathbb{R}^3$ –the *Lagrangian or reference configuration*– and the $\boldsymbol{x}_p$ is a particle in the body $\Omega_t \subset \mathbb{R}^3$ –the *Eulerian or spatial configuration*– at time $t \geq 0$, Fig. 1.8.
The function χ allows to measure the motion of the particles in a body from its reference Ω_R to its current Ω_t frame. For instance, from the function χ we define the following material quantities: *displacement field*, *velocity field* and *acceleration field*,

$$\boldsymbol{U}(\boldsymbol{X}, t) = \boldsymbol{x}(\boldsymbol{X}, t) - \boldsymbol{X}, \tag{1.1}$$

$$\boldsymbol{V}(\boldsymbol{X}, t) = \frac{\partial \chi(\boldsymbol{X}, t)}{\partial t}, \tag{1.2}$$

$$\boldsymbol{A}(\boldsymbol{X}, t) = \frac{\partial^2 \chi(\boldsymbol{X}, t)}{\partial t^2}, \tag{1.3}$$

respectively. If χ is assumed to be a uniquely invertible function, such as $\boldsymbol{X} = \chi^{-1}(\boldsymbol{x}, t)$, it is possible to define the quantities in terms of the spatial coordinates [52],

$$\boldsymbol{u}(\boldsymbol{x}, t) = \boldsymbol{x} - \boldsymbol{X}(\boldsymbol{x}, t), \tag{1.4}$$

$$\boldsymbol{v}(\boldsymbol{x}, t) = \boldsymbol{V}(\chi^{-1}(\boldsymbol{x}, t), t), \tag{1.5}$$

$$\boldsymbol{a}(\boldsymbol{x}, t) = \boldsymbol{A}(\chi^{-1}(\boldsymbol{x}, t), t). \tag{1.6}$$

The function χ describes well the motion of a particle in the body Ω_R. Nevertheless, the motion of the particle might not be enough to describe the behavior of the whole body, because, the reference body Ω_R in motion may deform. Thus, a reference vector $d\boldsymbol{X} = \boldsymbol{X}_Q - \boldsymbol{X}_P$ between the two particles Q and P is mapped by χ to the current vector $d\boldsymbol{x} = \boldsymbol{x}_q - \boldsymbol{x}_p$ to measure the deformation and rotations of the body. When the distance between the particles P and Q becomes

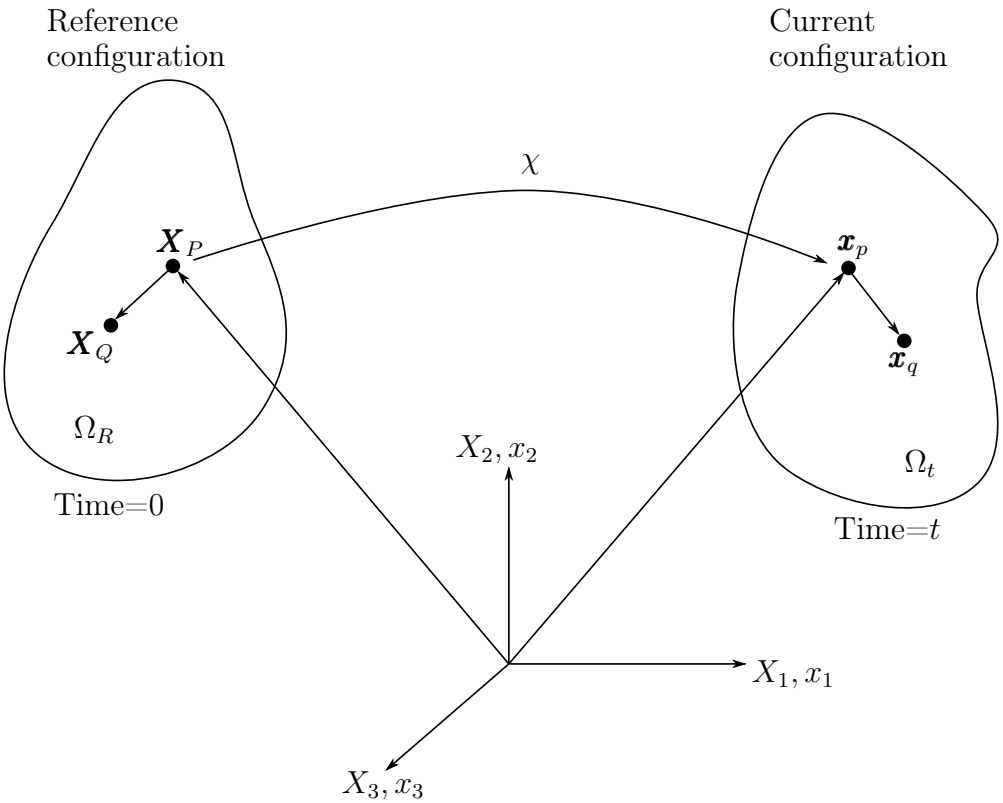

FIGURE 1.8 – A configuration or frame represents a state of the body. As the body moves, a new configuration is obtained, dependeing on time t. The reference configuration is also called material or Lagrangian configuration, while the current configuration is also called spatial, deformed or Eulerian configuration. Additionally, the figure defines the material vector $d\boldsymbol{X} = \boldsymbol{X}_P - \boldsymbol{X}_Q$ and spatial vector $d\boldsymbol{x} = \boldsymbol{x}_p - \boldsymbol{x}_q$.

infinitesimally small the ratio of the spatial and reference coordintes defines the derivative,

$$\boldsymbol{F} = \frac{\partial \chi(\boldsymbol{X}, t)}{\partial \boldsymbol{X}}, \tag{1.7}$$

which is the second-order *deformation gradient* tensor that transforms the Lagrangian vector $d\boldsymbol{X}$ into the Eulerian vector $d\boldsymbol{x}$ by the relation, $d\boldsymbol{x} = \boldsymbol{F}d\boldsymbol{X}$. Then this tensor is a linear transformation from the Lagrangian to the Eulerian configuration. This formulation is possible due to the continuity of the domains Ω_R and Ω_t [51], [53]. That means the bodies are a continuum of particles perfectly assembled.

The deformation gradient can have an unique polar decomposition, such as, one tensor contains the rigid body rotations and the other contains the stretch in the body,

$$\boldsymbol{F} = \boldsymbol{R}\boldsymbol{U} = \boldsymbol{V}\boldsymbol{R}, \tag{1.8}$$

where $\boldsymbol{R}$ is a *rotation* tensor, $\boldsymbol{U}$ is the *right stretch* tensor and $\boldsymbol{V}$ is the *left stretch* tensor, which should not be confused with the material displacements and velocities (Eqs. 1.1 and 1.2). The new tensors have some important properties, for instance, the rotation tensor is orthogonal ($\boldsymbol{R}^T\boldsymbol{R} = \boldsymbol{I}$) and the stretch tensors ($\boldsymbol{U}$ and $\boldsymbol{V}$) are symmetric.

The deformation gradient expresses the change of an infinitesimal volume between its reference (dV) and current (dv) frames by,

$$dv = J(\boldsymbol{X}, t)dV \tag{1.9}$$

with $J = \det(\boldsymbol{F})$. J is known as the volume ratio or Jacobian determinant. If it is assumed that the deformation gradient is invertible, the volume ratio must be strictly positive, $J > 0$. $J = 1$ means the motion of the particles keeps the volume of the body (isochoric deformation).

Additionally, taking the vectors $d\boldsymbol{X}$ and $d\boldsymbol{x}$ in material and deformed frames, respectively, the change of an infinitesimally small material area $d\boldsymbol{A}$ to a deformed area $d\boldsymbol{a}$ can be related through equation 1.9 as,

$$dv = d\boldsymbol{a} \cdot d\boldsymbol{x} = Jd\boldsymbol{A} \cdot d\boldsymbol{X}, \tag{1.10}$$

where $d\boldsymbol{x} = \boldsymbol{F}d\boldsymbol{X}$ gives the relationship between the areas, known as the Nanson's formula [50], [51],

$$d\boldsymbol{a} = J\boldsymbol{F}^{-T}d\boldsymbol{A}. \tag{1.11}$$

Furthermore, the strain of the body can be measured by the difference of the squared lengths of the material and current vectors, with the material length $dX^2 = d\boldsymbol{X}\cdot d\boldsymbol{X}$ and spatial length $dx^2 = d\boldsymbol{x}\cdot d\boldsymbol{x}$, see Fig. 1.8. However there are two possible ways to define the strain either in the reference or current configuration,

$$dx^2 - dX^2 = d\boldsymbol{X} \cdot (\boldsymbol{C} - \boldsymbol{I})d\boldsymbol{X} = 2d\boldsymbol{X} \cdot \boldsymbol{E}d\boldsymbol{X}, \tag{1.12}$$

$$dx^2 - dX^2 = d\boldsymbol{x} \cdot (\boldsymbol{I} - \boldsymbol{b}^{-1})d\boldsymbol{x} = 2d\boldsymbol{x} \cdot \boldsymbol{e}d\boldsymbol{x}. \tag{1.13}$$

From these equations results the *Lagrangian strain* tensor $\boldsymbol{E}$ with its *right Cauchy-Green deformation* tensor $\boldsymbol{C} = \boldsymbol{F}^T\boldsymbol{F}$ and the *Eulerian strain* tensor $\boldsymbol{e}$ with its *left Cauchy-Green deformation* tensor $\boldsymbol{b} = \boldsymbol{F}\boldsymbol{F}^T$. By using the polar decomposition of $\boldsymbol{F}$ (Eq. 1.8), $\boldsymbol{C} = \boldsymbol{U}^2$ and $\boldsymbol{b} = \boldsymbol{V}^2$. Ultimately, the strain tensors are related by the push-forward and pull-back operations [50], [51],

$$\boldsymbol{e} = \boldsymbol{F}^{-T}\boldsymbol{E}\boldsymbol{F}^{-1} \quad , \text{ push-forward,} \tag{1.14}$$

$$\boldsymbol{E} = \boldsymbol{F}^T\boldsymbol{e}\boldsymbol{F} \quad , \text{ pull-back.} \tag{1.15}$$

Given a scalar or tensor of a material quantity $G = G(\boldsymbol{X}, t)$ and of a spatial quantity $g = g(\boldsymbol{x}, t)$, by using the chain rule of derivatives, their material time derivatives are defined as,

$$\dot{G} = \frac{DG(\boldsymbol{X}, t)}{Dt} = \frac{\partial G(\boldsymbol{X}, t)}{\partial t}, \tag{1.16}$$

$$\dot{g} = \frac{Dg(\boldsymbol{x}, t)}{Dt} = \frac{\partial g(\boldsymbol{x}, t)}{\partial t} + \frac{\partial g(\boldsymbol{x}, t)}{\partial \boldsymbol{x}}\frac{\partial \chi(\boldsymbol{X}, t)}{\partial t}, \tag{1.17}$$

where the first term on the right-hand side in equation 1.17 denotes the spatial time derivative and the second term is the convective rate of change of g.
With the latter definition and equation 1.2 it is possible to perform the material time derivative of the deformation gradient, which is a function of the material coordinates,

$$\dot{\boldsymbol{F}} = \frac{\partial}{\partial t}\left(\frac{\partial \chi(\boldsymbol{X}, t)}{\partial \boldsymbol{X}}\right) = \frac{\partial}{\partial \boldsymbol{X}}\left(\frac{\partial \chi(\boldsymbol{X}, t)}{\partial t}\right) = \frac{\partial \boldsymbol{V}(\boldsymbol{X}, t)}{\partial \boldsymbol{X}}. \tag{1.18}$$

If equation 1.5 is used to define the velocity in term of the spatial coordinates in addition to the chain rule, we obtain

$$\dot{\boldsymbol{F}} = \frac{\partial \boldsymbol{v}(\boldsymbol{x}, t)}{\partial \boldsymbol{X}} = \frac{\partial \boldsymbol{v}(\boldsymbol{x}, t)}{\partial \boldsymbol{x}}\frac{\partial \chi(\boldsymbol{X}, t)}{\partial \boldsymbol{X}} = \boldsymbol{L}\boldsymbol{F}, \tag{1.19}$$

where $\boldsymbol{L}$ is the velocity gradient tensor, written as $\boldsymbol{L} = \dot{\boldsymbol{F}}\boldsymbol{F}^{-1}$.
Furthermore, if we apply the material time derivative onto the Lagrangian strain tensor, we obtain the material strain rate tensor, such as

$$\dot{\boldsymbol{E}} = \frac{1}{2}\dot{\boldsymbol{C}} = \frac{1}{2}(\dot{\boldsymbol{F}}^T\boldsymbol{F} + \boldsymbol{F}^T\dot{\boldsymbol{F}}) = \frac{1}{2}\boldsymbol{F}^T(\boldsymbol{L}^T + \boldsymbol{L})\boldsymbol{F} = \boldsymbol{F}^T\boldsymbol{d}\boldsymbol{F}, \tag{1.20}$$

where $\boldsymbol{d}$ is the rate of deformation tensor (Eulerian quantity). Equation 1.20 (compared to the equation 1.15) shows that tensor $\dot{\boldsymbol{E}}$ is the pull-back of $\boldsymbol{d}$ [50], [51].

1.8.2 Stress

As it has been indicated before (section 1.7) the stress is a major quantity in biomechanics as it is the intensity of a force $\boldsymbol{f}$ on an infinitesimal area $d\boldsymbol{a}$ or $d\boldsymbol{A}$, such as,

$$d\boldsymbol{f} = \boldsymbol{\sigma} \cdot d\boldsymbol{a} = \boldsymbol{P} \cdot d\boldsymbol{A} \tag{1.21}$$

where $\boldsymbol{\sigma}$ is the *Cauchy stress* tensor, $\boldsymbol{P}$ is the *first Piola-Kirchhoff stress* tensor and $d\boldsymbol{f}$ is a differential portion of the force applied on the infinitesimal area. Using the relation between the areas (Eq. 1.11) into equation 1.21 results into the next relationship between the stresses,

$$\boldsymbol{P} = J\boldsymbol{\sigma}\boldsymbol{F}^{-T}. \tag{1.22}$$

Another widely used stress tensor is the *Kirchhoff stress* tensor $\boldsymbol{\tau} = J\boldsymbol{\sigma}$. The Cauchy stress tensor is symmetric and measured the stress in the deformed configuration (true stress), however, the first Piola-Kirchhoff is an unsymmetric and two-point tensor (as the deformation gradient) and consequently, it is not completely related to the material configuration. To overcome this problem, we introduce a symmetric and totally material stress tensor, the *second Piola-Kirchhoff stress* tensor,

$$\boldsymbol{S} = J\boldsymbol{F}^{-1}\boldsymbol{\sigma}\boldsymbol{F}^{-T}. \tag{1.23}$$

If a rigid body motion is assumed, in the polar decomposition of $\boldsymbol{F}$ the stretch will be the identity and the deformation gradient becomes $\boldsymbol{F} = \boldsymbol{R}$ with $J = 1$. Thus, the second Piola-Kirchhoff stress can be interpreted as the *co-rotated Cauchy stress* tensor [50], [51],

$$\boldsymbol{\sigma}_R = \boldsymbol{R}^T\boldsymbol{\sigma}\boldsymbol{R}. \tag{1.24}$$

1.8.3 Balance principles

In addition to the mechanical quantities introduced so far, there is a need to examine that the deformations produced by the stresses on the tissue together with tissue adaptations are mechanically possible and consequently such changes do not transgress physical laws as the conservation of mass and of the linear momentum. The full analysis of energy conservation and of dissipation effects (or entropy) is beyond the study of growth and remodeling for now, so they are not mentioned here, but they are well explained in [53], [54].

The *conservation of mass* indicates that the mass variations in the body should produce the same variation in the Lagrangian and Eulerian frames, however, the infinitesimal volume where the mass is contained does not necessarily remain equal. Therefore the mass densities of the reference ($\varrho_R(\boldsymbol{X}, t)$) and current ($\varrho(\boldsymbol{x}, t)$) configurations may evolve in time due to the mass and geometrical changes, where a mass dm of an infinitesimal volume (dV or dv, Eq. 1.9) in the body is,

$$dm = \varrho_R dV = \varrho dv, \tag{1.25}$$

assuming that the reference volume dV does not change. Applying the total time derivative onto Eq. 1.25, using Eq. 1.9 and $\dot{J} = J\mathrm{div}(\boldsymbol{v})$, the equation for the conservation of mass results in [51], [53],

$$\frac{D\varrho_R}{Dt} = \frac{D}{Dt}(J\varrho) \rightarrow \frac{\partial \varrho_R}{\partial t} = J\left(\frac{\partial \varrho}{\partial t} + \mathrm{div}(\varrho \boldsymbol{v})\right). \tag{1.26}$$

The *conservation of the linear momentum* establishes that the forces in the body, either external $\boldsymbol{f}$ (e.g. the gravity, $\boldsymbol{f} = \varrho\boldsymbol{g}$) or internal, would change the inertial state of the body, such as,

$$\frac{D}{Dt}(\varrho\boldsymbol{v}) = \text{div}(\boldsymbol{\sigma}) + \boldsymbol{f}, \tag{1.27}$$

where $\text{div}(\boldsymbol{\sigma})$ is the divergence of the Cauchy stress $\boldsymbol{\sigma}$ related to internal forces and $\varrho\boldsymbol{v}$ is the linear momentum of the body. Additionally, if G&R effects are considered for a living tissue, such adaptation occurs in long time scales (section 1.7) and it can be assumed as a quasi-static equilibrium that shifts the linear momentum variations to zero [27].

1.8.4 Strain Energy function

Living tissues are usually assumed to be hyperelastic materials due to their capability to reach high stretches elastically. It is postulated that an hyperelastic material has a *free-energy function* W and such function must be polyconvex and solely depend on the deformation state ($W = W(\boldsymbol{F}) = W(\boldsymbol{E})$). Additionally, if the material is perfectly elastic, the deformations are reversible and there is not internal dissipation $\mathcal{D}_{int}$ or entropy generation in the material [50], [54],

$$\mathcal{D}_{int} = \boldsymbol{S} : \dot{\boldsymbol{E}} - \dot{W} = \left(\boldsymbol{S} - \frac{\partial W(\boldsymbol{E})}{\partial \boldsymbol{E}}\right) : \dot{\boldsymbol{E}} = 0, \tag{1.28}$$

where : is the double contraction. From equation 1.28 results that the stress-power ($\boldsymbol{S} : \dot{\boldsymbol{E}}$) equals the rate of internal energy of the material if there are no thermal effects (isothermal and isentropic process). Accordingly the second Piola-Kirchhoff stress is defined as,

$$\boldsymbol{S} = \frac{\partial W}{\partial \boldsymbol{E}}. \tag{1.29}$$

Traditionally living tissues are considered to have a non-linear behavior between strain and stress. Therefore, to eventually solve equilibrium for such non-linear problems, it is necessary to linearize the stress,

$$\Delta\boldsymbol{S} = \mathbb{C} : \Delta\boldsymbol{E} \text{ with } \mathbb{C} = \frac{\partial \boldsymbol{S}}{\partial \boldsymbol{E}} = \frac{\partial^2 W}{\partial \boldsymbol{E}^2}. \tag{1.30}$$

In continuum solid mechanics the stress and elasticity tensors are computed in terms of the Lagrangian configuration ($\boldsymbol{S}$,$\mathbb{C}$). Nevertheless, the system of equation 1.27 can be solved in terms of the Lagrangian or Eulerian quantities, the latter introducing the balance principles of this work. Consequently, the stress can be pushed-forward through equation 1.23 and the elasticity tensor through,

$$\mathfrak{c} = \frac{1}{J}\boldsymbol{F}\boldsymbol{F}\mathbb{C}\boldsymbol{F}^T\boldsymbol{F}^T. \tag{1.31}$$

1.9 Growth and Remodeling

Living tissues must be understood as a whole biological system that seeks stability. Consequently, the tissue has the exceptional attribute to adapt under some stimuli. As our goal is to model the aortic wall behavior, its homeostasis may be seen as a process to keep mechanobiological stability by performing changes in the material [8], [28]. Moreover, G&R models have been developed to capture such adaptability in a mechanical framework [22], [23]. G&R models considers inelastic deformations due to mass changes and stress in the material. They are sorted into two major approaches to compute the evolution of mechanical properties and mass in the tissue, Kinematic Growth (KG) models [23] and Constrained Mixture (CM) [22] models.

1.9.1 Kinematic Growth models

KG models for soft tissues were proposed by Rodriguez et al [23]. Those ideas were initially used to understand the residual stresses in the tissue, eventually produced by some permanent inelastic deformation, see Fig 1.9. Accordingly, the deformation gradient is decomposed such as,

$$\boldsymbol{F} = \boldsymbol{F}_e \boldsymbol{F}_g, \tag{1.32}$$

where ($\boldsymbol{F}_e$) is the elastic deformation gradient tensor and ($\boldsymbol{F}_g$) is the inelastic deformation gradient tensor. This is similar to plasticity models for finite deformations [55], [56]. The inelastic deformation is related to the changes in size and shape due to growth. The changes are assumed to take place in a local (infinitesimal volume) stress-free configuration. $\boldsymbol{F}_e$ contains the elastic deformations due to the loads on the body and the elastic deformations needed to assembly all the stress-free infinitesimal volumes.

REMARK: When there is a decomposition of the deformation gradient, an intermediate fictitious configuration is defined and introduced between the reference and current configuration. The intermediate configuration is defined locally and consequently it is not compatible with its neighboring intermediate configurations, and an elastic deformation is needed to assembly it with the other neighboring intemediate configurations. As a result the elastic as well as the inelastic tensors cannot be defined in terms of a derivative like the deformation gradient tensor [51], Eq. 1.7.

The deformation due to growth represents permanent deformation. In other words, the inelastic deformation produces a mechanically irreversible system and the internal dissipation of the material is not zero anymore, see Eq. 1.28. To overcome this problem the strain energy density function of the material must be written

in terms of elastic deformations, which are reversible and produces zero internal dissipation. The strain energy density of the material results in,

$$W(t) = W(\boldsymbol{F}_e(t)). \tag{1.33}$$

Equation 1.33 gives a constitutive model to relate the elastic material behavior with the external forces in the mechanical equilibrium (Eq. 1.27). However, there is still a need to find a constitutive relation for the inelastic behavior of the body. The growth in the tissue can be modeled such as,

$$\boldsymbol{F}_g = \beta(t)\boldsymbol{B} \tag{1.34}$$

where, $\boldsymbol{B}$ is a second order tensor defining the growth directions and β defines the magnitude of growth. The growth direction is often assumed to be isotropic $\boldsymbol{B} = \boldsymbol{I}$ where $\boldsymbol{I}$ is the identity tensor. If anisotropic, the growth may be written such as $\boldsymbol{B} = \boldsymbol{a}^{\perp} \otimes \boldsymbol{a}^{\perp} + (\boldsymbol{I} - \boldsymbol{a}^{\perp} \otimes \boldsymbol{a}^{\perp})$ –where the symbol $\otimes$ denotes the tensor product–. Recalling the homeostasis in living tissues (section 1.7), the growth magnitude β would be measured from the difference of some mechanical quantity, $\boldsymbol{G}$, respect to its value $\boldsymbol{G}_h$ in the preferred state of the tissue, denominated from now on as the *homeostatic state*.
In the KG models, it is often assumed that the Eulerian density remains constant during elastic deformation –due to near incompressiblity– and even during G&R. Taking this into account in the conservation of mass (Eq. 1.26), results into the next relationship for the evolving mass in the body,

$$\dot{\varrho}_R(t) = \varrho \frac{DJ_g}{Dt} \tag{1.35}$$

where it has been assumed that the Eulerian density is homogeneous in the body. $J = J_e J_g = J_g$ is the elastic deformation. $J_e = \det(\boldsymbol{F}_e) = 1$ due to incompressibility. Having in mind that $J_g = \det(\boldsymbol{F}_g)$, $\dot{J}_g = J_g \mathrm{div}(\boldsymbol{v})$ and $\varrho_R = J\varrho$, the relationship for mass density evolution can be established as [23],

$$\dot{\varrho}_R(t) = \varrho_R(t)\boldsymbol{k}_\sigma : (\boldsymbol{G} - \boldsymbol{G}_h), \tag{1.36}$$

where the divergence of the velocity has been related to the deviation of the mechanical quantity $\boldsymbol{G}$ from its homeostatic value, such as, $\mathrm{div}(\boldsymbol{v}) = \boldsymbol{k}_\sigma : \Delta\boldsymbol{G}$, with $\boldsymbol{k}_\sigma$ as gain-type tensor. This is ultimatelly related to β in the equation 1.34. KG models are used for their simplicity and low computational costs, and they are conceptually similar to well-known plasticity models. But they are limited by the arbitrariness of the direction $\boldsymbol{B}$ and magnitude β of growth together with the mechanical quantity $\boldsymbol{G}$ which is usually taken as stress equivalent in the body. Moreover, the models are mechanobiologically limited as they do not capture the *in vivo* stressed configuration of living tissues along with production, removal and remodeling of different constituents at different rates and with different prestresses.

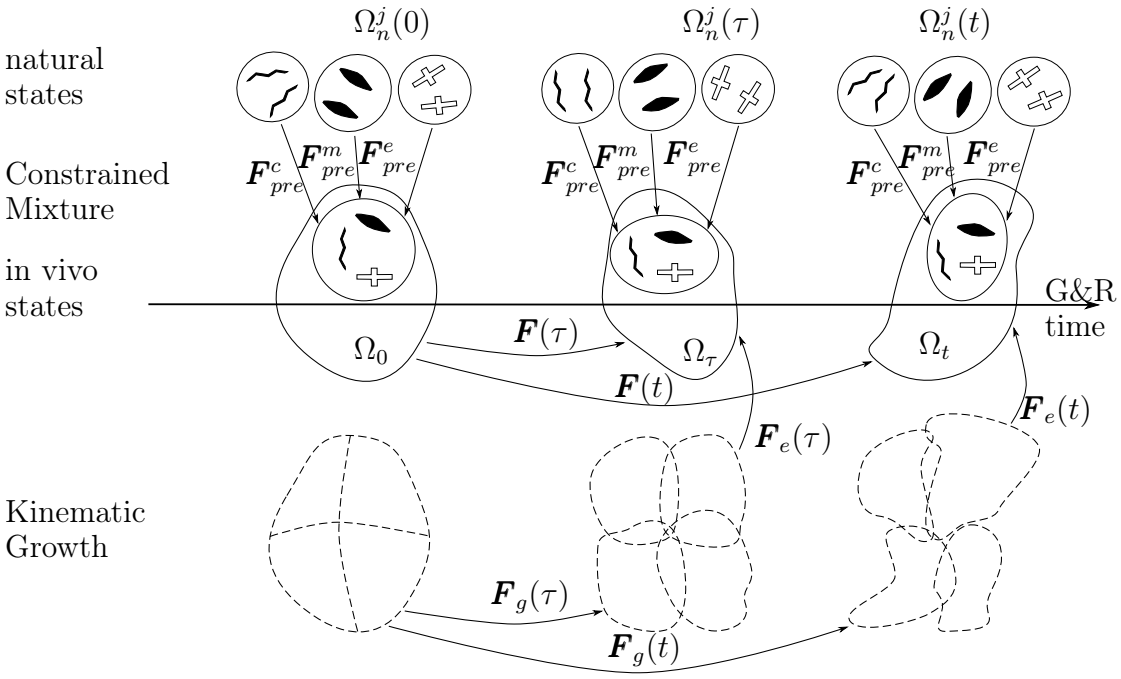

Figure 1.9 – Constrained Mixture versus Kinematic Growth [9].

1.9.2 Constrained Mixture models

Another approach has been proposed for the G&R of soft tissues by Humphrey and Rajagopal [22]. In these models it is assumed that in each infinitesimal volume element there is a mixture of n constituents that are allowed to be deposited within the body at each time $\tau \in [0, t]$, Fig. 1.9. The newly deposited constituent at time τ has its particular natural (stress-free) configuration and yet deforms together with the whole mixture. Moreover, it is incorporated in the extant mixture with an elastic prestretch $\boldsymbol{F}^{j(\tau)}_{pre}$, relative to the stress-free configuration of the mass increment at time τ, see Fig. 1.9. The deformation of the whole mixture from the *in vivo* reference configuration to the time τ is $\boldsymbol{F}(\tau)$ and to the time t is $\boldsymbol{F}(t)$. Then the elastic deformation at time t experienced by a prestressed constituent deposited at time τ is [26],

$$\boldsymbol{F}^{j(\tau)}_{e}(t) = \boldsymbol{F}(t)\boldsymbol{F}^{-1}(\tau)\boldsymbol{F}^{j(\tau)}_{pre}. \tag{1.37}$$

In this model each jth constituent has a mass density $\varrho^j_R(t)$ per unit reference volume and may increase its mass by a mass production rate $\dot{\varrho}^j_{R+}(t) > 0$ per unit reference volume. Additionally the deposited mass has a finite half-life, degrading over time. Thus, the fraction of mass existing at time 0 and still surviving at time t is $Q^j(t) \in [0, 1]$, and the fraction of mass deposited at time τ and still surviving at time t is $q^j(t - \tau)$. Hence, the mass density of the jth constituent in the constrained mixture at time t is [12], [26]

$$\varrho^j_R(t) = \varrho^j_R(0)Q^j(t) + \int_0^t \dot{\varrho}^j_{R+}(\tau)q^j(t - \tau)d\tau \tag{1.38}$$

with survival functions [12],

$$Q^j(t) = \exp\left(-\frac{t}{T^j}\right) \text{ and } q^j(t-\tau) = \exp\left(-\frac{(t-\tau)}{T^j}\right), \tag{1.39}$$

and mass density, $\varrho_R = \sum_j^n \varrho_R^j$ for the whole mixture. In the same way the strain energy for the constrained mixture is the sum of all particular energy functions of the constituents [12], [28],

$$W(t) = \sum_j^n W^j(t) \tag{1.40}$$

and the energy of the jth constituent is [12], [26],

$$W^j(t) = \frac{\varrho_R^j(0)}{\varrho_R(t)} Q^j(t) \Psi^j\left(\boldsymbol{F}_e^{j(0)}(t)\right) + \int_0^s \frac{\dot{\varrho}_{R+}^j(\tau)}{\varrho_R(t)} q^j(t-\tau) \Psi^j\left(\boldsymbol{F}_e^{j(\tau)}(t)\right) d\tau \tag{1.41}$$

with standard energy function $\Psi^j(\boldsymbol{F}_e^{j(\tau)}(t))$ such as neo-Hookean or Fung-type exponentials, depending on the elastic deformations to ensure zero internal dissipation of equation 1.28.
During homeostasis, there are two main cases of net mass production rate, which are the steady replacement of constituent mass due to the half-life time and the deposition/removal of mass due to changes in the stress state of the body. The former would mean that the deposition and removal of mass are equal and are characterized by the half-life time T^j and the extant mass $\varrho_R^j(s)$ of the constituent j [8],

$$\dot{\varrho}_{R-}^j(s) = \dot{\varrho}_{R+}^j(s) = \frac{\varrho_R^j(s)}{T^j}. \tag{1.42}$$

The latter can be produced by some alteration in the loads or material structure of the body which ultimately produces changes in the stress state of the body. Consequently homeostasis will work over the difference of stress between the homeostatic state and the current state at time τ [10], [12],

$$\dot{\varrho}_{R+}^j(\tau) = \varrho_R^j \left[\frac{1}{T^j} + \boldsymbol{k}_\sigma^j : (\boldsymbol{\sigma}(\tau) - \boldsymbol{\sigma}_h)\right]. \tag{1.43}$$

Moreover in CM models the net mass production is understood as the difference between the mass production $\dot{\varrho}_{R+}^j > 0$ and degradation $\dot{\varrho}_{R-}^j > 0$ rates as [8]

$$\dot{\varrho}_R^j = \dot{\varrho}_{R+}^j - \dot{\varrho}_{R-}^j \tag{1.44}$$

and using equations 1.42 and 1.43 along with the assumption of constant mass removal rate, the net mass production rate of the constituent j is [8], [9]

$$\dot{\varrho}_R^j(\tau) = \varrho_R^j \boldsymbol{k}_\sigma^j : (\boldsymbol{\sigma}(\tau) - \boldsymbol{\sigma}_h) \tag{1.45}$$

which is similar to equation 1.36 in the KG models, where the mechanical quantity $\boldsymbol{G} = \boldsymbol{\sigma}$, usually the co-rotated Cauchy stress, Eq. 1.24.

CM models, unlike KG models, account for multiple constituents with different turnover. However, the model has to track the configuration of the constituents at the time of their deposition. This mean high computational costs and implementation efforts, which is the main disadvantage compared to the KG models. As a result, new hybrid models were developed such as the Recruitment Stretch model [57], [58], the homogenized Constrained Mixture (hCM) model [17], [27], [28] and the rate-independent pseudoelastic framework [59], [60]. The approach used further in the developments of this thesis is the hCM model.

1.9.3 Homogenized Constrained Mixture Model

In this work a hybrid approach was developed based on the hCM, with the aim to model continuous mass depositions and changes of structure due to the homeostasis, see section 1.7. This model is selected by its capability to perform tissue changes from a mechanobiological reference and consider the material as a mixture of several constituents with their turnover and arrangement. Despite this, it still requires lower computational efforts and costs than the original CM models due to the homogenization of the temporal deposition of the constituents, see Fig. 1.10. In the hCM model, it is again assumed that a body Ω_R is a mixture of several constituents that deform together, and each constituent has a particular natural (stress-free) configuration. The constituents would update their respective mass in the natural configuration and be remodeled there, see Fig. 1.10. Consequently, there is no an intermediate time state (Ω_τ) where the constituent is deposited, there are just reference and current frames. Instead of depositing/removing mass with different prestretch from different time depositions, each constituent changes its mass and its prestretch at every time.
Furthermore, the deformation gradient of the mixture is decomposed in elastic and inelastic parts as in KG models, but such elastic and inelastic deformation are specific to each constituent. For example, it is similar to a system of parallel springs that deform together but where each spring has its specific stiffness and natural length. Hence, the multiplicative decomposition of the deformation gradient for finite deformations in living tissue is [24],

$$\boldsymbol{F} = \boldsymbol{F}^j_e \boldsymbol{F}^j_{gr}, \tag{1.46}$$

where $\boldsymbol{F}^j_e$ represents the elastic deformations from the assembly of the incompatible local natural configurations ($\Omega^j_n(t)$) and from possible load applied on the body. The inelastic deformation $\boldsymbol{F}^j_{gr}$ relates the traction-free with the jth natural configuration (Fig. 1.10) and captures the turnover of the consituent j (section 1.7), with its rearrangement and deposition in the tissue, e.g. changes in the natural length and stiffness in a spring. Indeed two sub-inelastic deformations are included within the inelastic deformation, such as [27],

$$\boldsymbol{F}^j_{gr} = \boldsymbol{F}^j_r \boldsymbol{F}^j_g. \tag{1.47}$$

The remodeling $\boldsymbol{F}^j_r$ is related to the preferred state of the constituent j and can be interpreted as a prestretch (prestress). It can experience time evolutions depending

on mass addition and change of the stress state. The growth $\boldsymbol{F}_g^j$ is related to the changes in shape and volume of the body –as in KG models– due to the net mass production. Ultimately, variations in the inelastic deformations ($\boldsymbol{F}_{gr}^j$) produce variations in the natural state ($\Omega_n^j(t)$), Fig. 1.10.
As in CM models the density of the mixture is again the sum of the densities of the constituents, $\varrho_R = \sum_j^n \varrho_R^j$, all in terms of reference volume units. And in the same way the strain energy of the mixture (per unit reference volume) is the sum of the strain energy of the constituents, as in equation 1.40,

$$W(t) = \sum_j^n \varrho_R^j \Psi^j(\boldsymbol{C}_e^j(t)) \tag{1.48}$$

where Ψ^j is the strain energy density function of the constituent j, per unit reference mass. $\boldsymbol{C}_e^j$ is the *elastic right Cauchy-Green* tensor for the constituent j,

$$\boldsymbol{C}_e^j = \boldsymbol{F}_e^{jT}\boldsymbol{F}_e^j = \boldsymbol{F}_{gr}^{j\ -T}\boldsymbol{C}\boldsymbol{F}_{gr}^{j\ -1}, \tag{1.49}$$

where $\boldsymbol{C}$ is the right Cauchy-Green tensor of the mixture (Eq. 1.12) and $\boldsymbol{C}_{gr}^j = \boldsymbol{F}_{gr}^{j\ T}\boldsymbol{F}_{gr}^j$ is the *inelastic right Cauchy-Green* tensor. Again the strain energy of each constituent depends only on its specific elastic deformations to ensure zero internal dissipation, see Eq. 1.28. From the energy function of the mixture (Eq. 1.48), the chain rule and equations 1.29 and 1.49, the second Piola-Kirchhoff stress for the mixture is derived such as,

$$\boldsymbol{S} = \sum_j^n \varrho_R^j \frac{\partial \Psi^j(\boldsymbol{C}_e^j)}{\partial \boldsymbol{E}} = 2\sum_j^n \varrho_R^j \frac{\partial \Psi^j(\boldsymbol{C}_e^j)}{\partial \boldsymbol{C}_e^j} : \frac{\partial \boldsymbol{C}_e^j}{\partial \boldsymbol{C}}. \tag{1.50}$$

From equation 1.50 the second Piola-Kirchhoff of the jth constituent may be written such as,

$$\boldsymbol{S}^j = \frac{\varrho_R^j}{\phi^j} \frac{\partial \Psi^j(\boldsymbol{C}_e^j)}{\partial \boldsymbol{E}}. \tag{1.51}$$

with $\boldsymbol{S} = \sum \phi^j \boldsymbol{S}^j$. The push-forward of $\boldsymbol{S}^j$ renders the Cauchy stress of the jth constituent from equation 1.23.
The equilibrium of a body Ω_t under G&R is determined by the conservation of mass (Eq. 1.26) and conservation of linear momentum (Eq. 1.27), without thermal effects. In the former, the assumptions are Lagrangian mass density evolving in time and Eulerian mass density constant and homogeneous, as in KG models. In the latter, the equilibrium can be solved if the energy (Ψ^j), reference mass densities (ϱ_R^j) and inelastic deformations ($\boldsymbol{F}_{gr}^j$) of the constituents are known. The strain energy densities can be neo-Hookean and Fung exponential functions, [51], [53]. The constitutive relations for time evolutions of the mass densities and inelastic deformation are now introduced for this framework.

1.9.3.1 Net mass production

The net mass production (i.e. the difference between mass production and degradation) in each constituent is represented by its rate of mass change $\dot{\varrho}_R^j$. This

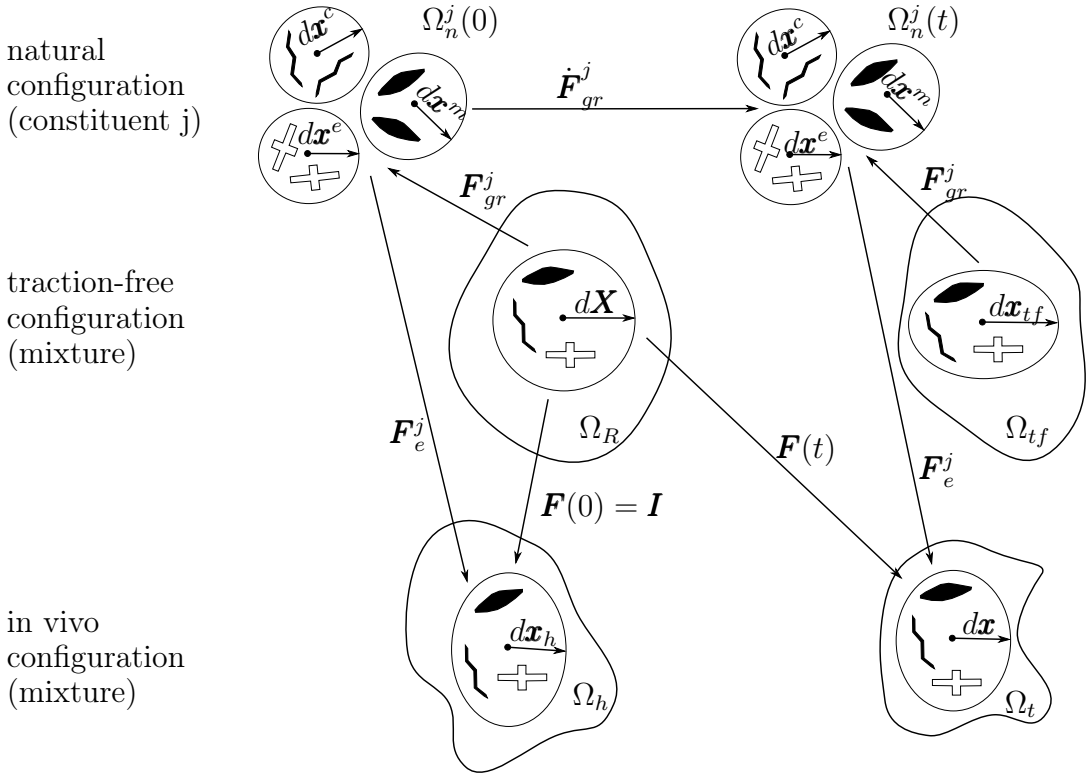

Figure 1.10 – Schematic of the hCM model, showing the different configurations. The reference configuration Ω_R at time zero is without external loads and without prestretch $[\boldsymbol{F}_{gr}^j]^{-1}$ in the jth constituent. Fictitious traction-free configuration Ω_{tf} is defined at time t, without external loads and without prestretch. The *in vivo* reference homeostatic configuration at time zero $\Omega_h = \Omega_0$ with homeostatic remodeling and external loads, and the current *in vivo* configuration Ω_t after G&R. The neighborhood $d\boldsymbol{X}$ of an arbitrary point in Ω_R is related to Ω_t by the transformation $d\boldsymbol{x} = \boldsymbol{F}d\boldsymbol{X}$. At time zero is $\Omega_t = \Omega_0$ and $d\boldsymbol{x}_0 = \boldsymbol{F}d\boldsymbol{X}$. Similarly, the relationship between Ω_t and the natural configuration is $d\boldsymbol{x} = \boldsymbol{F}_e^j d\boldsymbol{x}_n^j$, and the natural configuration and Ω_R are related by the inelastic deformation $d\boldsymbol{x}_n^j = \boldsymbol{F}_{gr}^j d\boldsymbol{X}$ where the inelastic deformation evolves with time. The natural configurations can only be defined locally but are not compatible.

includes mass replacement due to the half-life of each constituent (Eq. 1.42) and mass update due to some alteration that changes the stress state of the mixture (Eq. 1.43). Then the net mass production is again determined by [27],

$$\dot{\varrho}_R^j(t) = \varrho_R^j(t)\boldsymbol{k}_\sigma^j : (\boldsymbol{\sigma}_R^j - \boldsymbol{\sigma}_h^j) + \dot{D}^j(t). \tag{1.52}$$

The term $\boldsymbol{k}_\sigma^j$ is a gain-type second order tensor which can consider normal stress and shear stress, again similar to equation 1.36 –the shear stress is assumed to be irrelevant for the development of this work–. The term $\dot{D}^j$ is a general rate function for additional production or degradation of mass independently of the tensional state. $\boldsymbol{\sigma}_h^j$ is the Cauchy stress in the jth constituent at its preferred state or homeostatic state, section 1.7, and $\boldsymbol{\sigma}_R^j$ is the co-rotated Cauchy stress, Eq. 1.24. Rodriguez et al [23] wrote that a co-rotational form of the Cauchy stress is needed to ensure that both stress quantities need to be expressed in the same frame of reference. Nevertheless, in some articles authors have not used a co-rotated form of the Cauchy stress [8], [24], [28] and in others it is just written that a convenient stress metric is needed [12], [61].
Equation 1.52 can be reduced to a one-dimensional form when it is applied on fibres (the case of SMC and collagen). So, the stress is measured in the direction of the fibre $\boldsymbol{a}_0^j$ and turn the co-rotated stress tensor in a scalar stress in the direction of the fibre ($\sigma^j = \boldsymbol{a}_0^j \cdot \boldsymbol{\sigma}_R^j \boldsymbol{a}_0^j$) and $k_\sigma^j = \sigma_h^j \boldsymbol{a}_0^j \cdot \boldsymbol{k}_\sigma^j \boldsymbol{a}_0^j$. Therefore equation 1.52 can be rewritten as,

$$\dot{\varrho}_R^j(t) = \varrho_R^j(t) k_\sigma^j \frac{\sigma^j - \sigma_h^j}{\sigma_h^j} + \dot{D}^j(t). \tag{1.53}$$

1.9.3.2 Growth

As the mass occupies a space (volume), eventually, a given volume would experience changes due to the deposition or degradation of mass in the mixture. Such volume changes in size and shape are captured by the growth deformation ($\boldsymbol{F}_g^j$). Because all the constituents share an infinitesimal volume in the mixture, the increase of mass in one of them would produce a generalized volume variation in all constituents, resulting in $J_g = J_g^1 = ... = J_g^n$ or $\boldsymbol{F}_g = \boldsymbol{F}_g^1 = ... = \boldsymbol{F}_g^n$.
From the multiplicative decomposition of the gradient deformation (Eqs. 1.46 and 1.47), the Jacobian of the mixture results in the Jacobian of the growth, may be written such as$J = J_e^j J_r^j J_g = J_g$, if the elastic and remodeling deformations are isochoric and assuming that all the constituents experience the same growth. Inserting this relation in the conservation of mass (Eq. 1.26), it is possible to establish that (as in KG models, Eq. 1.35),

$$\dot{\varrho}_R = \varrho \frac{DJ_g}{Dt} \rightarrow \det(\boldsymbol{F}_g) = \frac{\varrho_R(t)}{\varrho_R(0)}, \tag{1.54}$$

where ϱ is the current density, with $\varrho = \varrho_R(0)$. The equation at the right hand side is the integration of the equation at the left hand side.

The direction of growth can be chosen as isotropic,

$$\boldsymbol{F}_g = \left(\frac{\varrho_R(t)}{\varrho_R(0)}\right)^{1/3} \boldsymbol{I} \tag{1.55}$$

or anisotropic, as for instance, in the direction of the thickness $\boldsymbol{a}_0^{\perp}$,

$$\boldsymbol{F}_g = \frac{\varrho_R(t)}{\varrho_R(0)} \boldsymbol{a}_0^{\perp} \otimes \boldsymbol{a}_0^{\perp} + \left(\boldsymbol{I} - \boldsymbol{a}_0^{\perp} \otimes \boldsymbol{a}_0^{\perp}\right). \tag{1.56}$$

1.9.3.3 Remodeling

Remodeling is understood as a modification in the arrangements between the constitutents in the tissue, newly deposited or extant. In the turnover (section 1.7) remodeling is related to the formation of new cross-links in the constituents of the mixture. The cross-links are modified by the cells to achieve a preferred stress state and balance the external loads by changing the stress and stiffness in the mixture. However, the new cross-links provide such changes just if they are deposited with a certain prestress. In hCM models the formation of the new cross-links is modeled by the complete removal of the non cross-linked constituents and the production of the same mass quantity of cross-linked constituent to target the load conditions.

Herein we postulate that within a mixture, the constituents experience a variation of stress ($\dot{\boldsymbol{\sigma}}^j$) due to the deposition of mass ϱ^j_{R+}, where this mass is deposited with a prestress $\boldsymbol{\sigma}^j_{pre}$ in the extant mass ϱ^j_R with stress $\boldsymbol{\sigma}^j$. This process suppose to take place with a constant total deformation and growth deformation, $\boldsymbol{F}, \boldsymbol{F}^j_g = const$, that leads to $\boldsymbol{F}^j_e \boldsymbol{F}^j_r = const$ (Eqs. 1.46 and 1.47). Due to the latter statement, the stress would vary with the rate of the elastic deformations ($\dot{\boldsymbol{C}}^j_e$), such as [24],

$$\frac{\dot{\varrho}^j_{R+}}{\varrho^j_R}\left(\boldsymbol{\sigma}^j - \boldsymbol{\sigma}^j_{pre}\right) = \left(\frac{\partial \boldsymbol{\sigma}^j}{\partial \boldsymbol{C}^j_e} : \left(\boldsymbol{C}^j_e \boldsymbol{L}^j_r + \boldsymbol{L}^{j\,T}_r \boldsymbol{C}^j_e\right)\right)_{\boldsymbol{F}, \boldsymbol{F}^j_g = const}, \tag{1.57}$$

where $\boldsymbol{L}^j_r = \dot{\boldsymbol{F}}^j_r \boldsymbol{F}^{j\,-1}_r$ is the remodeling velocity gradient. Cyron et al [24] proposed the Cauchy and second Piola-Kirchhoff tensors as stress metrics for the remodeling evolution. Additionally, equation 1.57 can be simplified to the one-dimensional fibre case along direction $\boldsymbol{a}^j_0$,

$$\dot{\lambda}^j_r = \frac{\dot{\varrho}^j_{R+}}{\varrho^j_R} \frac{\lambda^j}{(\lambda^j_e)^2} \left(\frac{\partial \sigma^j}{\partial \lambda^j_e}\right)^{-1} \times \left(\sigma^j - \sigma^j_{pre}\right). \tag{1.58}$$

with $\sigma^j = \boldsymbol{a}^j_0 \cdot \boldsymbol{\sigma}^j \boldsymbol{a}^j_0$, $\lambda^j = \sqrt{\boldsymbol{a}^j_0 \cdot \boldsymbol{C} \boldsymbol{a}^j_0}$, $\lambda^j_r = ||\boldsymbol{F}^j_{gr} \boldsymbol{a}^j_0||$ and $\lambda^j_e = \frac{\lambda}{\lambda^j_r}$.

1.10 Overview and objectives

The background presented in this chapter has permitted to review the structure and composition of the aortic wall with its impact in aging or in the development and progression of diseases such as aneurysms and dissections. It has been

observed that the progression of aortic diseases may be induced by tissue degeneration in the media layer. Such degeneration is usually related to elastic fibre disruption, cell death or inflammation. However, the artery, as other biological systems, has the ability to heal by performing a series of changes in the tissue related to cell migration and production of proteins to keep the aortic structure. But due to the impossibility of elastin synthesis after youth, the cells compensate the lack of elastin with collagen –a stiffer material– inducing deformations and stiffening that could end up with altered functions of the aorta or even rupture.
The process in which the aorta modifies its own structure to reach optimal conditions for survival is referred to as homeostasis. Modifications are executed by cells onto the ECM and affect the stiffness, stress and strain of the aortic wall. So the main aspects of the mechanical homeostasis are related to the preferred stress in which the cells execute well their function, to the turnover related to the deposition/removal of mass and to the prestress at which the new mass is deposited in the tissue to protect and ensure normal mechano-sensitive activity in the cells.
With the aim to develop a mechanical model for the adaptations of the aorta throughout age and diseases, it is possible to establish some assumptions for the aorta:

- the deformations are large,
- the tissue is a composite material with several constituents,
- modifications are performed to reach a preferred state,
- there is deposition and removal of mass,
- the new mass is deposited with a prestress or prestretch.

In this work the assumtions and requirements for the tissue adaptations are addressed by the Growth and Remodeling models within the theory of Continuum Mechanics. Within this framework the balance principles are fulfiled: conservation of mass, conservation of linear momentum and zero internal dissipation or entropy production.
Some G&R models were presented to understand the mechanical adaptations taking place in the aortic tissue. KG models comprise a multiplicative decomposition of the deformation between the elastic and growth deformations. This induces that the elastic deformations must keep zero internal dissipation and consequently be modeled by a strain energy density function, while the new growth deformation needs a new constitutive model established throughout the conservation of mass equation. Unfortunately, the KG model considers the existence of one homogeneous material for the aorta. Conversely, the CM models were developed to consider the tissue as a mixture of several constituents to emulate the composition or histology of the aortic wall which is at least composed by elastin, collagen and SMCs. The CM model is an accurate model by considering the survival and deposition of different constituent at different frames of evolution of the mixture.

The price to pay is a heavy computational cost to keep a record of the mass densities and constitutive functions of the different constituents produced at different frames. Finally we showed that a good trade-off is a hybrid model of G&R with a multiplicative decomposition as in the KG model but with a mixture made of several constituents as in the CM model. The use of this approach in this work is justified by the reduced implementation efforts and computational resources consumption and by the accuracy. Eventually such G&R models are able to perform simulations of stable homeostasis and maladaptations leading to disease progression such as, aneurysm, aging and dissection.

Several simulations have been performed under G&R models to analyse the progression of aneurysms in models of intracranial arteries [10], abdominal aorta [12]–[16], [57], [61], [62] and thoracic aorta [17], [18], [21]. Nevertheless, there is a lack of validation with experimental data, such as the diameter and geometry of the diseased arteries. The challenge in this topic is the need of monitoring a cohort of patients for a period of at least 10 years. Mousavi et al [18] have tried to overcome this problem with the use of a statistical model for the evolution of the diameter in aneurysms, but still lack model validation. Moreover, the simulations need to solve the equilibrium several times for each time step when the computational model need to reach convergence. This again lengthens simulations and increases the consumption of computational resources, not mentioning the production of heavy data for postprocessing. With complex meshes –needed for patient-specific geometries– the situation is even more critical. Other limitations lie in the inelastic constitutive equations and the arbitrariness of their choice, where usually the stress is considered as a convenient metric for the evolutions but it could be the stiffness or the strain too. Such constitutive equations have several parameters that need to be calibrated from experiments. This may produce a lack of physical interpretation of some parameters. The way in how the preferred stress is defined as a reference for further adaptations in the aortic tissue is also arbitrary because of the assumptions that have to be taken to define it. Furthermore, it is usually assumed that the progression of aneurysms in arteries is triggered by the degradation of elastin but potential cell death or even dysfunction in the mechanosensitive activity of the cells should also be considered. From a biological point of view it has also been observed that the pressure may change in long periods, which should also be taken into account [18], [63].

The G&R models reviewed in this chapter need the definition of a reference state based on the concepts of mechanical homeostasis. This reference is usually established by assuming normal conditions of pressure [2], [12] for a given artery. The latter is related to the geometry obtained from a picture of the artery. However, there is incertitude on the actual state of the artery in the frame the picture is taken, as there is the possibility the artery is in the development of a disease. The latter means that the assumed homeostatic state for the model could be a non-homeostatic or non-healthy frame of the artery.

This work intends to contribute in the area by proposing an efficient computational implementation of G&R, first with axisymmetric shell elements, and then with full

3D models opening the possibility of non-uniform prestretch for the preferred state and opening the exploration of the G&R in dissected arteries. Three-dimensional implementations bring some new challenges, such as the definition of the tensional homeostasis in the artery. Thus the main novelty of this work will be that prestress or prestretch may not be uniform in the body. Based on this principle, it is intended to apply the G&R models in chronic aortic dissections.

Chapter 2

Materials and Methods

Table of contents of the chapter

2.1 Résumé du chapitre en français. . . . 34
2.2 Abstract . . . 34
2.3 Definition of the mechanical problem . . . 35
2.4 Elastic constitutive model . . . 38
2.5 Principle of virtual work . . . 40
2.5.1 Internal virtual work . . . 41
2.5.2 External virtual work. . . . 42
2.6 Axisymmetric shell elements approach. . . . 43
2.6.1 Kinematics . . . 43
2.6.2 Virtual work of shell elements . . . 45
2.6.3 Virtual work of external forces in shell . . . 46
2.6.4 Spatial discretization . . . 47
2.6.5 Time integration method . . . 49
2.6.6 Overview of the program . . . 50
2.7 Three-dimensional approach . . . 53
2.7.1 External forces . . . 53
2.7.2 Spatial discretization . . . 54
2.7.3 Time integration method . . . 55
2.7.4 Overview of the program . . . 55
2.8 Verification . . . 56
2.9 Conclusion . . . 59

2.1 Résumé du chapitre en français

La croissance et le remodelage (G&R) des tissus vivants impliquent un problème mécanique nécessitant de résoudre les équations d'équilibre présentés dans le chapitre précédent. Cependant, les principes d'équilibre ont été utilisés dans la présentation de G&R pour établir les relations constitutives laissant l'équation de la quantité de mouvement linéaire sans contraintes. La conservation de la quantité de mouvement linéaire est à nouveau présentée dans ce chapitre et elle est abordée comme le problème à résoudre en introduisant des conditions spatiales et temporelles dans l'équation. Il est certain que la résolution du système d'équations différentielles ainsi obtenu, en utilisant des méthodes analytiques, n'est pas une stratégie efficace, et l'application aux aortes personnalisées augmente la complexité du problème mathématique. Nous avons résolu ce problème en introduisant une forme faible de l'équilibre mécanique. Cette formulation faible est basée sur le principe du travail virtuel et peut être utilisée dans des méthodes numériques telles que les éléments finis (EF).
Parce que cette thèse vise à modéliser l'évolution des aortes des patient, nous avons implémenté deux codes EF avec l'approche *Homogenized Constrained Mixture* (hCM). Le premier code est fondé sur des éléments de coque axisymétriques et a été écrit entièrement dans cette thèse. Ce code a permis d'analyser la progression de l'anévrisme dans les artères et le déploiement des endoprothèses. Ce nouvel outil de simulation de G&R est efficace mais limité aux géométries axisymétriques. Le deuxième code est fondé sur un solveur élément-finis open-source, avec des modifications supplémentaires apportées dans cete thèse pour les vaisseaux sanguins et les simulations G&R. Cette nouvelle implémentation est tridimensionnelle, ce qui permet de prendre en compte la progression de l'anévrisme dans les aortes personnalisées. Cette dernière étape ouvre la voie à la configuration d'un outil de calcul robuste capable d'aider à l'analyse de la progression des anévrismes.

2.2 Abstract

Growth and remodeling (G&R) of living tissues implies a mechanical problem in which it is necessary to solve the balance principles presented in the previous chapter. However, the balance principles were used to set the constitutive relationships leaving the equation of linear momentum without constraints. The conservation of linear momentum is again presented in this chapter and it is addressed as the problem to solve by introducing spatial and temporal conditions to the equation. It is not an efficient strategy to solve the resulting system of differential equations by analytical methods, as the application to patient-specific aortas increases the complexity of the mathematical problem. We overcome this issue by introducing a weak form of the mechanical equilibrium. The weak form is based in the principle of virtual work and it can be further used in numerical methods such as the Finite-Element (FE) method.

As this thesis aims to model the evolution of patient-specific aortas, we have implemented two FE codes with the Homogenized Constrained Mixture (hCM) approach. The first code is based on axisymmetric shell elements and it was written from scratch. This code permitted to analyse aneurysm progression in arteries and stent-graft deployment. This new G&R framework is efficient but limited to axisymmetric geometries. The second code is based on an open-source FE solver in which we implemented all the needed routines for blood vessels and G&R simulations. This new implemetation is three-dimensional allowing to consider aneurysm progression in patient-specific aortas. This last step opens the path to a robust computational framework for the prediction of aneurysm progression.

2.3 Definition of the mechanical problem

A body (or artery) Ω_t in the current configuration must satisfy the conservation of mass, linear momentum and energy. The conservation of mass was considered in the growth models introduced at the previous chapter. The analysis of the conservation of energy is usually beyond the studies about G&R for soft tissues. The entropy of the body has been partially analysed to establish the reversibility of the elastic deformations and its relation with the strain energy density function. However, the conservation of linear momentum introduced at equation 1.27 was not solved in the review of the constitutive relationships of G&R and it represents the challenge of this chapter. This equation of mechanical equilibrium can be rewritten such as

$$\operatorname{div}(\boldsymbol{\sigma}) + \boldsymbol{f} = 0 \text{ in } \Omega_t, \tag{2.1}$$

where it is supposed that the equilibrium is quasi-static because the tissue changes take place across long times-scales and the deformations due to mass deposition/removal do not produce major accelerations.
Eventually, the displacements of the body can be constrained to some reference system (a fixed point in the space). The constraints can be given either by a traction field $\boldsymbol{t}$ at the boundaries of the body ($\partial\Omega_t$) or by a displacement field $\boldsymbol{u}$ on the body. These conditions are represented by

$$\boldsymbol{u}(\boldsymbol{x}, t) = \boldsymbol{u}^*(t) \quad \text{on} \quad \partial\Omega_t, \tag{2.2}$$

$$\boldsymbol{t}(\boldsymbol{x}, t) = \boldsymbol{t}^*(t) \quad \text{on} \quad \partial\Omega_t, \tag{2.3}$$

where the quantities $\boldsymbol{u}^*$ and $\boldsymbol{t}^*$ are prescribed displacements and tractions, respectively. Additionally, G&R is a temporal process captured by constitutive equations and inelastic deformations in the homogenized Constrained Mixture (hCM) models. Such constitutive equations are given in terms of the rates of G&R quantities: mass density, remodeling and growth. Consequently, to obtain them for a given time t it is needed to define the initial (or reference) conditions for such quantities,

$$\varrho_R^j(\boldsymbol{x}, t) = \varrho_R^{j\,*}(\boldsymbol{x}) \quad \text{at} \quad t = 0, \tag{2.4}$$

$$\boldsymbol{F}_r^j(\boldsymbol{x}, t) = \boldsymbol{F}_r^{j*}(\boldsymbol{x}) \quad \text{at} \quad t = 0, \tag{2.5}$$

$$\boldsymbol{F}_g^j(\boldsymbol{x}, t) = \boldsymbol{F}_g^{j*}(\boldsymbol{x}) \quad \text{at} \quad t = 0. \tag{2.6}$$

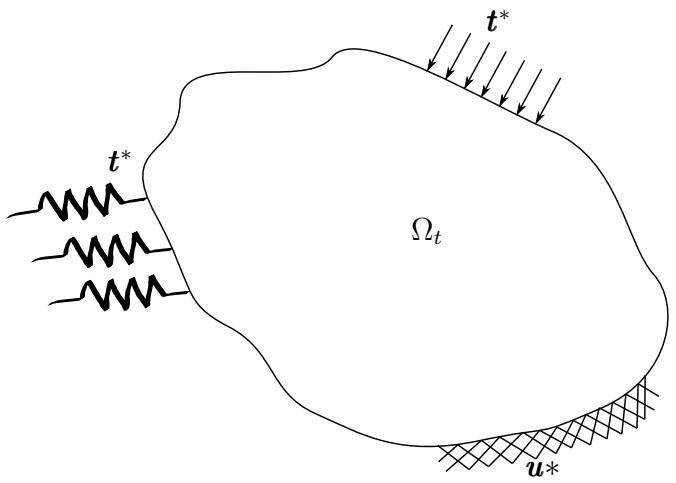

FIGURE 2.1 – A general representation of the equilibrium of a body Ω_t under surface forces $\boldsymbol{t}^*$ and restricted to the displacements $\boldsymbol{u}^*$.

With the definition of the boundary and initial conditions it is now possible to solve the equilibrium (Eq. 2.1) to find the current frame of the body Ω_t at time t within the hCM models. However, in the equilibrium equation (Eq. 2.1) the stress $\boldsymbol{\sigma}$ is related to the tractions applied on the boundaries ($\boldsymbol{t}(\boldsymbol{x}, t)$) and to the elastic behavior of the material of the body. The elastic behavior of the constituents of the material mixture ($W(\boldsymbol{C})$) depends on the inelastic quantities in the current frame at time t, see section 2.4. The inelastic quantities (current natural state of a constituent) of the tissue can be computed through the inelastic constitutive equations provided by the hCM models. As seen in section 1.9 the inelastic constitutive equations depend on the homeostatic state and its stress $\boldsymbol{\sigma}_h^j$. Generally, the homeostatic state is defined by the initial conditions of the inelastic quantities and its stress can be found from the corresponding initial equilibrium. A diagram of this general procedure is introduced in Figure 2.2.

For G&R the definition of the homeostatic state is essential. However it is not completely understood how to measure and choose this reference. Some authors have provided some experimental method to determine the homeostatic state for some constituents in the mixture [64] but always reinforced with numerical methods [12], [65]. With those methods it is assumed that the average stress in normal function (*in vivo*) of the artery may be between 90 to 150-kPa [2], [10], [12]. Additionally, patient-specific arterial geometries are obtained from a scan of the *in vivo* artery, meaning that the obtained geometry is loaded and stressed. Under the assumption of normal pressure (load), and assuming that the homeostatic state corresponds to the stress in the *in vivo* geometry, it is possible to find the inelastic deformations if the displacements of the body Ω_t are near zero ($\boldsymbol{u} \approx 0$), after applying all the conditions [49].

In conclusion, the evolution of a patient-specific artery is given by the solution of the mechanical equilibrium (Eq. 2.1) at time t. However, the equilibrium is a differential equation complicated to solve by analytical methods and a FE strategy is

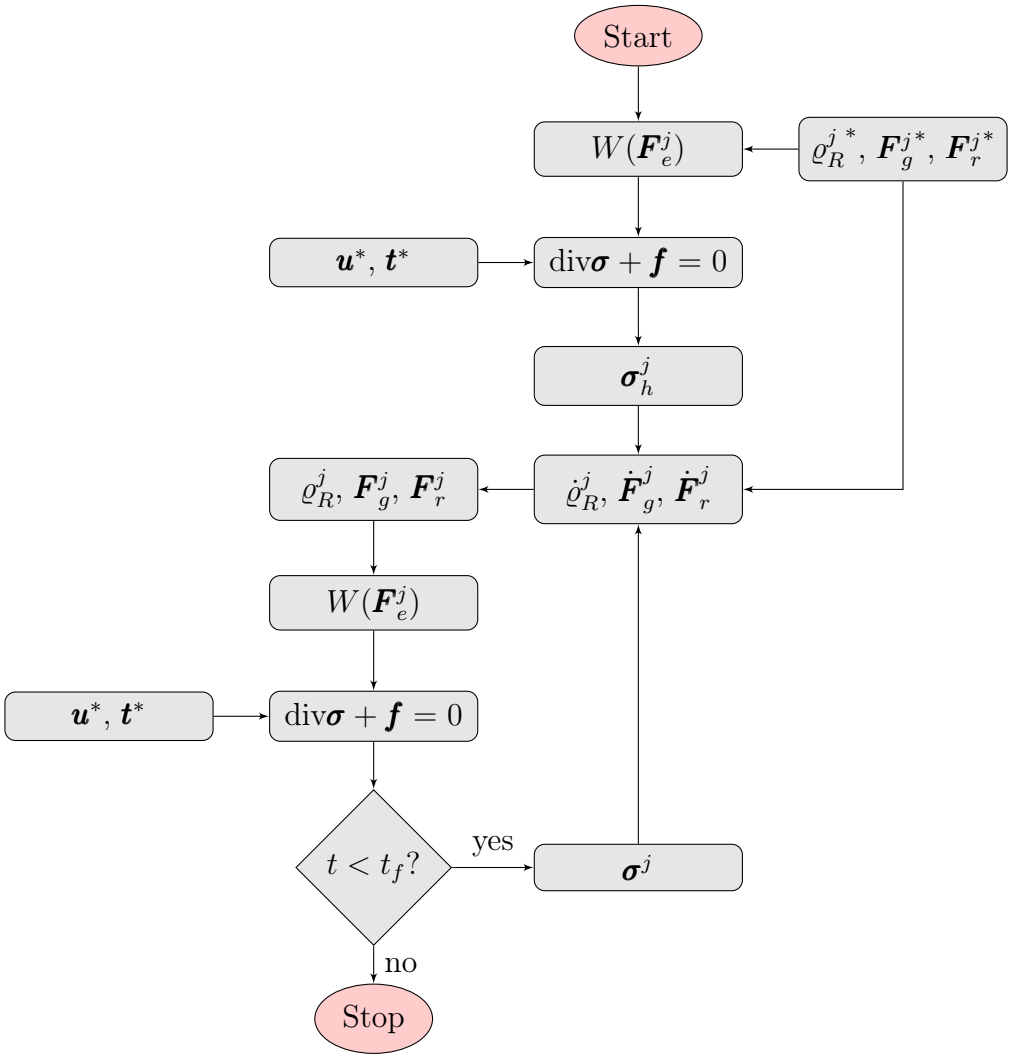

Figure 2.2 – Procedure to obtain the current state of a living tissue with G&R models. First, the initial inelastic conditions are used to define the elastic behavior of the material which is then used to compute its stress. After the equilibrium under the given boundary conditions, an homeostatic stress $\boldsymbol{\sigma}_h^j$ can be obtained as a reference for the inelastic constitutive equations of the hCM models. Second, the inelastic constitutive equations and the reference state are used to define the new elastic behavior of the material, which is again used to compute the stress for the equilibrium under the given boundary conditions. Once the equilibrium is solved, the current state of the living tissue is known at time t. The procedure is run until some time threshold of interest (t_f) is reached.

needed for its solution. Therefore, in this work two FE analyses were implemented to achieve G&R of arteries for aneurysm progression. First, an axisymmetric shell element code was written from scratch to simulate aneurysm progression in cylinders and stent-graft deployment. Second, a three-dimensional analysis of G&R was implemented in a FE solver (Florence, written in C++ and Python) [66], [67]. In the latter it was finally possible to perform simulations of G&R in patient-specific aortas by taking a new approach in the application of the initial conditions (prestretch or initial remodeling). The new 3D FE analysis also permitted the first applications of this G&R model to the evolution of chronic aortic dissections.

2.4 Elastic constitutive model

Figure 2.2 shows our approach to solve the linear momentum. First we need the elastic behavior of the material mixture as it is a fundamental part of the stress $\boldsymbol{\sigma}$. It is remarked that just the elastic deformations are assumed reversible and their dissipation must be zero, as introduced in Eq. 1.28. Therefore, the strain energy $W(\boldsymbol{C})$ of the mixture (per unit reference volume) is the addition of the strain energies $\Psi^j(\boldsymbol{C}_e^j)$ of each constituent (per unit reference mass), such as,

$$W(\boldsymbol{C}) = \varrho_R^e(\Psi_{vol}^e(J_e^e) + \Psi_{iso}^e(\boldsymbol{C}_e^e)) + \varrho_R^m(\Psi_{act}^m(\boldsymbol{C}_e^m) + \Psi_{pas}^m(\boldsymbol{C}_e^m)) + \sum_{i=1}^{4} \varrho_R^{c_i}\Psi^{c_i}(\boldsymbol{C}_e^{c_i}), \tag{2.7}$$

where ϱ_R^j is the reference mass density of the jth constituent within the mixture. Moreover, it is considered that the mixture is composed by three relevant constituents, for instance, elastin (e), smooth muscle cells (m) and four collagen fibres families (c_i) [22], [26]. The smooth muscle cells (SMCs) behavior is further split between passive (Ψ_{pas}^m) and active (Ψ_{act}^m) parts [25], due to the active contractile behavior of the cells. The elastin is included in an isotropic matrix material that can undergo volume changes due to the compressibility. Furthermore, if the mixture is considered incompressible, full incompressibility of the material could produce numerical instabilities in a FE analysis [55]. Therefore, the isotropic material needs to be decomposed into volumetric (Ψ_{vol}^e) and isochoric (Ψ_{iso}^e) parts [27].

In the hCM models the strain energy densities of the constituents are represented as functions of some invariants of the elastic deformation, such as

$$J_e^j = \det(\boldsymbol{F}_e^j) = \sqrt{\det(\boldsymbol{C}_e^j)}\ ,\ I_1^j = \mathrm{tr}(\boldsymbol{C}_e^j)\ ,\ \bar{I}_1^j = \mathrm{tr}(\bar{\boldsymbol{C}}_e^j)\ ,\ I_4^j = \boldsymbol{a}_{gr}^j \cdot \boldsymbol{C}_e^j \boldsymbol{a}_{gr}^j, \tag{2.8}$$

where J_e^j is the invariant related to the volumetric changes due to the elastic deformations; I_1^j is the first invariant of the deformation; $\bar{I}_1^j$ is the modified first invariant for isochoric elastic deformations with $\bar{\boldsymbol{C}}_e^j = {J_e^j}^{-2/3}\boldsymbol{C}_e^j$ that produces $\det(\bar{\boldsymbol{C}}_e^j) = 1$ [51]; and the fourth invariant is actually the square of the elastic stretch ($I_4^j = {\lambda_e^j}^2$) in the direction of the inelastic deformed intermediate configuration $\boldsymbol{a}_{gr}^j = \boldsymbol{F}_{gr}^j\boldsymbol{a}_0^j/||\boldsymbol{F}_{gr}^j\boldsymbol{a}_0^j||$ with $\boldsymbol{a}_0^j$ the direction of the fibre in the reference configuration.

The strain energy densities of the constituents in terms of the invariants are introduced as,

$$\Psi^e_{vol}(J^e_e) = \frac{1}{2}\kappa^e(J^e_e - 1)^2 \tag{2.9}$$

$$\Psi^e_{iso}(\boldsymbol{C}^e_e) = \frac{1}{2}\mu^e(\mathrm{tr}(\bar{\boldsymbol{C}}^e_e) - 3) \tag{2.10}$$

$$\Psi^m_{pas}(\boldsymbol{C}^m_e) = \frac{k^m_1}{2k^m_2}(\exp(k^m_2(\lambda^{m2}_e - 1)^2) - 1) \tag{2.11}$$

$$\Psi^m_{act}(\boldsymbol{C}^m_e) = \frac{\sigma_{actmax}}{\varrho_R(0)}\left(\lambda_{act} + \frac{(\lambda_m - \lambda_{act})^3}{3(\lambda_m - \lambda_0)^2}\right) \tag{2.12}$$

$$\Psi^{c_i}(\boldsymbol{C}^{c_i}_e) = \frac{k^{c_i}_1}{2k^{c_i}_2}(\exp(k^{c_i}_2(\lambda^{c_i 2}_e - 1)^2) - 1) \tag{2.13}$$

where κ^e is the bulk modulus related to the compressibility of the material; μ^e is the shear stiffness of the elastin; k^m_1 with k^m_2 are stress-like and dimensionless material parameters of the SMCs, respectively; σ_{actmax} is the maximal active Cauchy stress, λ_{act} is the active stretch in the fibre direction, λ_0 and λ_{max} are the zero and maximum active stretches, respectively; in the collagen $k^{c_i}_1$ with $k^{c_i}_2$ are stress-like and dimensionless material parameters, respectively.

The Cauchy stress tensor $\boldsymbol{\sigma}$ is determined from the push-forward operation (Eq. 1.23) onto the second Piola-Kirchhoff stress tensor, as introduced in Eq. 1.50. The derivation of the second Piola-Kirchhoff stress is presented in the appendix A.1. The Cauchy stress tensor is represented by

$$\boldsymbol{\sigma} = \phi^e(\boldsymbol{\sigma}^e_{vol} + \boldsymbol{\sigma}^e_{iso}) + \phi^m(\boldsymbol{\sigma}^m_{act} + \boldsymbol{\sigma}^m_{pas}) + \sum_{i=1}^{4}\phi^{c_i}\boldsymbol{\sigma}^{c_i}, \tag{2.14}$$

where again the Cauchy stress of the mixture is defined as the addition of the stress of the constituents times the mass per unit volume of the constituent in the mixture, which it is now represented by the volume fraction of the constituent (Eq. 1.51). The Cauchy stresses are more specifically

$$\boldsymbol{\sigma}^e_{vol} = \kappa^e J^e_e(J^e_e - 1)\boldsymbol{I} \tag{2.15}$$

$$\boldsymbol{\sigma}^e_{iso} = \mu^e J^{e-2/3}_e\left(\boldsymbol{b}^e_e - \frac{1}{3}\mathrm{tr}(\boldsymbol{b}^e_e)\boldsymbol{I}\right) \tag{2.16}$$

$$\boldsymbol{\sigma}^m_{pas} = 2k^m_1(\lambda^{m2}_e - 1)\exp(k^m_2(\lambda^{m2}_e - 1)^2)\frac{\boldsymbol{F}\boldsymbol{a}^m_0 \otimes \boldsymbol{F}\boldsymbol{a}^m_0}{||\boldsymbol{F}^m_{gr}\boldsymbol{a}^m_0||^2} \tag{2.17}$$

$$\boldsymbol{\sigma}^m_{act} = \frac{\sigma_{actmax}}{\varrho_R(0)\lambda}\left(1 - \frac{(\lambda_m - \lambda_{act})^2}{(\lambda_m - \lambda_0)^2}\right)\boldsymbol{F}\boldsymbol{a}^m_0 \otimes \boldsymbol{F}\boldsymbol{a}^m_0 \tag{2.18}$$

$$\boldsymbol{\sigma}^{c_i} = 2k^{c_i}_1(\lambda^{c_i 2}_e - 1)\exp(k^{c_i}_2(\lambda^{c_i 2}_e - 1)^2)\frac{\boldsymbol{F}\boldsymbol{a}^{c_i}_0 \otimes \boldsymbol{F}\boldsymbol{a}^{c_i}_0}{||\boldsymbol{F}^{c_i}_{gr}\boldsymbol{a}^{c_i}_0||^2} \tag{2.19}$$

where $\boldsymbol{b}^e_e$ is the elastic left Cauchy-Green stretch tensor.

NOTE: The volumetric stress introduced in equation 2.15 is a penalization approach for nearly incompressible materials to avoid numerical issues such as, locking. This model is suitable for the three-dimensional implementation. However, in the shell analysis we can consider the additional constraint of radial stress nearly zero ($\sigma_r \approx 0$) and assume a full incompressible behavior of the material through the Lagrange multiplier p where the volumetric stress is $\boldsymbol{\sigma}^e_{vol} = p\boldsymbol{I}$. This approach applied in shells does not produce volumetric locking as in a three-dimensional analysis.

To find the stress from the strain energy density functions, we used the derivatives of the invariants and the derivatives of the elastic right Cauchy-Green stretch tensor. Such derivatives are now introduced to understand how the stress quantities are obtained,

$$\frac{\partial \boldsymbol{C}^j_e}{\partial \boldsymbol{C}} = \boldsymbol{F}^{j\ -T}_{gr} \odot \boldsymbol{F}^{j\ -1}_{gr}\ ,\ \frac{\partial J^j_e}{\partial \boldsymbol{C}} = \frac{1}{2} J^j_e \boldsymbol{C}^{-1}\ ,\ \frac{\partial I^j_1}{\partial \boldsymbol{C}} = \boldsymbol{C}^{j\ -1}_{gr}, \tag{2.20}$$

$$\frac{\partial \bar{I}^j_1}{\partial \boldsymbol{C}} = J^{j\ -2/3}_e (\boldsymbol{C}^{j\ -1}_{gr} - \frac{1}{3}\mathrm{tr}(\boldsymbol{C}^j_e)\boldsymbol{C}^{-1})\ ,\ \frac{\partial I^j_4}{\partial \boldsymbol{C}} = \frac{\boldsymbol{a}^j_0 \otimes \boldsymbol{a}^j_0}{||\boldsymbol{F}^j_{gr}\boldsymbol{a}^j_0||^2}. \tag{2.21}$$

The symbol $\odot$ is a special tensor product defined in index notation as

$$(\boldsymbol{A} \odot \boldsymbol{B})_{ijkl} = \frac{1}{2}(\boldsymbol{A}_{ik}\boldsymbol{B}_{jl} + \boldsymbol{A}_{jk}\boldsymbol{B}_{il}). \tag{2.22}$$

Finally, mechanical equilibrium (Eq. 2.1) of the body Ω_t can be solved through the Cauchy stress to find the stretch and stress of the body. Nevertheless, the equation resulting from applying the divergence over the Cauchy stress is nonlinear and tremendously complex. Consequently, it might not be possible to reach static equilibrium (Eq. 2.1) analytically. Consequently, it is necessary to apply an iterative method to find the solution, as for instance, a Newton-Raphson scheme. The obstacle here is to find the equilibrium for all the particles in the body. This is usually overcome by solving the equilibrium just in some particles of interest. This can be achieved in the strong form (directly from equation 2.1) or by the weak form through the principle of virtual work.

2.5 Principle of virtual work

The deformation that satisfies static equilibrium (Eq. 2.1) of the body Ω_t is usually found after writing the weak formulation of the equation. The weak formulation is produced by the multiplication of the static equilibrium equation with an arbitrary virtual displacement $\delta\boldsymbol{u}$. This produces a virtual work per unit volume, which after integration of all infinitesimal volume elements dv results in the virtual work of the whole body Ω_t, such as

$$\delta\mathcal{W}(\boldsymbol{x}, \delta\boldsymbol{u}) = \int_{\Omega_t} (\mathrm{div}(\boldsymbol{\sigma}) + \boldsymbol{f}) \cdot \delta\boldsymbol{u} dv = 0. \tag{2.23}$$

By considering the divergence of vector $\boldsymbol{\sigma}\delta\boldsymbol{u}$

$$\mathrm{div}(\boldsymbol{\sigma}\delta\boldsymbol{u}) = \mathrm{div}(\boldsymbol{\sigma}) \cdot \delta\boldsymbol{u} + \boldsymbol{\sigma} : \mathrm{grad}(\delta\boldsymbol{u}), \tag{2.24}$$

and by using the divergence theorem

$$\int_{\Omega_t} \mathrm{div}(\boldsymbol{\sigma}\delta\boldsymbol{u})dv = \int_{\partial\Omega_t} \boldsymbol{n} \cdot \boldsymbol{\sigma}\delta\boldsymbol{u}da, \tag{2.25}$$

the relation between the gradient of the virtual displacement, the virtual Eulerian strain (Eq. 1.13)

$$\delta\boldsymbol{e} = \frac{1}{2}(\mathrm{grad}^T\delta\boldsymbol{u} + \mathrm{grad}\delta\boldsymbol{u}), \tag{2.26}$$

and the tension vector $\boldsymbol{t} = \boldsymbol{\sigma}\boldsymbol{n}$, the total virtual work (Eq. 2.23) may be written

$$\delta\mathcal{W}(\boldsymbol{x}, \delta\boldsymbol{u}) = \underbrace{\int_{\Omega_t} \boldsymbol{\sigma} : \delta\boldsymbol{e}dv}_{\delta\mathcal{W}_{int}} \underbrace{- \int_{\Omega_t} \boldsymbol{f} \cdot \delta\boldsymbol{u}dv - \int_{\partial\Omega_t} \boldsymbol{t} \cdot \delta\boldsymbol{u}da}_{\delta\mathcal{W}_{ext}} = 0 \tag{2.27}$$

where the first term is the internal virtual work performed by the material $\delta\mathcal{W}_{int}$. The second term is the virtual work of external forces and the third term is the virtual work of tractions on the boundary. Their sum is the external virtual work of the forces working on the body $\delta\mathcal{W}_{ext}$.
Unfortunatelly, the virtual work principle still provides a non-linear equation for the mechanical equilibrium. Consequently to find the displacements that solves the virtual work (Eq. 2.27) with the Newton-Raphson iterative method, we had to linearize the virtual work equation. Making the variation or linearization in terms of the displacement field of the particles of the body we obtained,

$$\Delta\delta\mathcal{W}(\boldsymbol{x}, \delta\boldsymbol{u}) \cdot \Delta\boldsymbol{u} + \delta\mathcal{W}(\boldsymbol{x}, \delta\boldsymbol{u}) \approx 0. \tag{2.28}$$

In the next subsections we present the linearization of the internal and external virtual work.

2.5.1 Internal virtual work

When the internal virtual work is linearized, increments in displacements, in stress and in strain need to be considered. Such considerations end up in a linearization of the internal work with an elastic stiffness from the elastic behavior of the material and a geometric stiffness due to the virtual strain increments, such as

$$\Delta\delta\mathcal{W}_{int}(\boldsymbol{x}, \delta\boldsymbol{u}) \cdot \Delta\boldsymbol{u} = \int_{\Omega} \delta\boldsymbol{e} : \mathfrak{c} : \Delta\boldsymbol{e}dv + \int_{\Omega} \boldsymbol{\sigma} : \Delta\delta\boldsymbol{e}dv \tag{2.29}$$

The geometric stiffness appears due to the finite deformations in the body that allows increments in the virtual Eulerian strain,

$$\Delta\delta\boldsymbol{e} = \frac{1}{2}\left(\mathrm{grad}^T\delta\boldsymbol{u}\ \mathrm{grad}\Delta\boldsymbol{u} + \mathrm{grad}\delta\boldsymbol{u}\ \mathrm{grad}^T\Delta\boldsymbol{u}\right), \tag{2.30}$$

while the elastic stiffness is produced by the increments of stress due to increments in strain, $\Delta\boldsymbol{\sigma} = \mathfrak{c} : \Delta\boldsymbol{e}$. The elasticity tensor $\mathfrak{c}$ in the current configuration is the push-forward of the elasticity tensor $\mathbb{C}$ of the reference configuration, where the latter is the derivative of the second Piola-Kirchhoff stress tensor with respect to the Lagrangian strain, as shown in Eq. 1.30. Then the current elasticity tensors for the constituents in the mixture are

$$\mathfrak{c} = \phi^e(\mathfrak{c}^e_{vol} + \mathfrak{c}^e_{iso}) + \phi^m(\mathfrak{c}^m_{act} + \mathfrak{c}^m_{pas}) + \sum_{i=1}^{4} \phi^{c_i}\mathfrak{c}^{c_i} \tag{2.31}$$

$$\mathfrak{c}^e_{vol} = \kappa^e J^e_e((2J^e_e - 1)\boldsymbol{I} \otimes \boldsymbol{I} - 2(J^e_e - 1)\boldsymbol{I} \odot \boldsymbol{I}) \tag{2.32}$$

$$\mathfrak{c}^e_{iso} = \frac{2}{3}\mu^e J_e^{e-2/3}\left(\mathrm{tr}(\boldsymbol{b}^e_e)\boldsymbol{I} \odot \boldsymbol{I} + \frac{1}{3}\mathrm{tr}(\boldsymbol{b}^e_e)\boldsymbol{I} \otimes \boldsymbol{I} - \boldsymbol{b}^e_e \otimes \boldsymbol{I} - \boldsymbol{I} \otimes \boldsymbol{b}^e_e\right) \tag{2.33}$$

$$\mathfrak{c}^m_{pas} = 4k^m_1(1 + 2k^m_2(\lambda^{m2}_e - 1)^2)\exp(k^m_2(\lambda^{m2}_e - 1)^2)\frac{\boldsymbol{F}\boldsymbol{a}^m_0 \otimes \boldsymbol{F}\boldsymbol{a}^m_0 \otimes \boldsymbol{F}\boldsymbol{a}^m_0 \otimes \boldsymbol{F}\boldsymbol{a}^m_0}{||\boldsymbol{F}^m_{gr}\boldsymbol{a}^m_0||^4} \tag{2.34}$$

$$\mathfrak{c}^m_{act} = \frac{-2\sigma_{actmax}}{\varrho_R(0)\lambda^2}\left(1 - \frac{(\lambda_m - \lambda_{act})^2}{(\lambda_m - \lambda_0)^2}\right)\boldsymbol{F}\boldsymbol{a}^m_0 \otimes \boldsymbol{F}\boldsymbol{a}^m_0 \otimes \boldsymbol{F}\boldsymbol{a}^m_0 \otimes \boldsymbol{F}\boldsymbol{a}^m_0 \tag{2.35}$$

$$\mathfrak{c}^{c_i} = 4k^{c_i}_1(1+2k^{c_i}_2(\lambda^{c_i 2}_e - 1)^2)\exp(k^{c_i}_2(\lambda^{c_i 2}_e - 1)^2)\frac{\boldsymbol{F}\boldsymbol{a}^{c_i}_0 \otimes \boldsymbol{F}\boldsymbol{a}^{c_i}_0 \otimes \boldsymbol{F}\boldsymbol{a}^{c_i}_0 \otimes \boldsymbol{F}\boldsymbol{a}^{c_i}_0}{||\boldsymbol{F}^{c_i}_{gr}\boldsymbol{a}^{c_i}_0||^4} \tag{2.36}$$

The computation of the material elasticity tensor $\mathbb{C}$ used to obtain the current elasticity tensor $\mathfrak{c}$ is detailed in appendix A.1.

2.5.2 External virtual work

Usually the external forces are not linearized because they do not experience increments with the displacement increments, such is the case of the Neumann boundary conditions, which represent an imposed traction $\boldsymbol{t}^*$ with constant direction and magnitude. However, in the analysis of blood vessels the forces in the surface may depend of the displacement of the body Ω_t, such is the case of the lumen pressure and the elastic resistance of the surroundings of the vessel. These deformation-dependent loads are denominated as Robin boundary conditions with the tractions changing with the displacements, such as

$$\boldsymbol{t} = p\boldsymbol{n} + k\boldsymbol{u}, \tag{2.37}$$

where p is a pressure applied on a surface with normal vector $\boldsymbol{n}$ and k is the stiffness of the elastic boundary. Note that viscoelastic boundary conditions are not considered in the scope of this work. By multiplying the traction vector $\boldsymbol{t}$ with the virtual displacements and integrating on the surface of the body Ω_t we obtain the virtual work of the external forces due to the Robin boundary conditions, such as

$$\delta\mathcal{W}^R_{ext}(\boldsymbol{x}, \delta\boldsymbol{u}) = \underbrace{\int_{\partial\Omega_t} \delta\boldsymbol{u} \cdot p\boldsymbol{n}da}_{\delta\mathcal{W}^p_{ext}} + \underbrace{\int_{\partial\Omega_t} \delta\boldsymbol{u} \cdot k\boldsymbol{u}da}_{\delta\mathcal{W}^k_{ext}}. \tag{2.38}$$

In the elastic force the dependence to the displacement $\boldsymbol{u}$ is explicit but in the pressure the dependence is less evident. The current normal vector $\boldsymbol{n}$ to the surface may change direction due to the displacements. In both cases the differential surface da depend on the spatial coordinates. Thus, the forces may experience increments when the displacement increments are applied to the body,

$$\Delta\delta\mathcal{W}^R_{ext}(\boldsymbol{x},\delta\boldsymbol{u})\cdot\Delta\boldsymbol{u} = \underbrace{\int_{\partial\Omega_t}\delta\boldsymbol{u}\cdot\Delta(p\boldsymbol{n}da)}_{\Delta\delta\mathcal{W}^p_{ext}} + \underbrace{\int_{\partial\Omega_t}\delta\boldsymbol{u}\cdot k\Delta\boldsymbol{u}da}_{\Delta\delta\mathcal{W}^k_{ext}}. \tag{2.39}$$

In $\Delta(p\boldsymbol{n}da)$ the pressure is constant and it can be pulled-out from the increment, leaving just the differential surface to vary in direction and size. The elastic force experiences variations due to the incremental displacements.
The virtual work of the residual forces (internal minus external forces) vary pointwisely within the body Ω_t. Thus, the analysis of G&R in the tissue would be represented by some points of interest, due to the difficulties to reproduce a displacement function across the whole domain. This obstacle is overcome in the finite-element (FE) method, which provides a discretization of the body of interest Ω_t. Thus, in the next sections two FE approaches are reviewed and adapted to the specific case of G&R in arteries.

2.6 Axisymmetric shell elements approach

We employed shell elements because they eventually produce simplifications for arteries in the resolution of mechanical equilibrium and of their evolution due to the tissue changes. Despite the simplifications in the implementation of this kind of elements, this approach is limited by the bending locking and by the axisymmetric constraints that only allow simulations in axisymmetric shapes. Complementary information about shell elements can be found in the books of Wriggers [55], Zienkiewicz [68] and out article [69].
In this section we introduce the whole mathematical background of the axisymmetric shell element code. This documentation may facilitate further work or development in the code available in GitHub [70].

2.6.1 Kinematics

Before developing the discretized approach based on shell elements we established kinematics measures for continuous shell bodies. This begins with a reduction of the coordinates to a plane.
The shell is assumed to be a thin layer and it is relevant for bodies where the thickness changes are negligible compared to the displacements of the body. For this reason we considered coordinates related to the position of the neutral axis of the shell, represented by $\boldsymbol{X}_M$ in the reference configuration and by $\boldsymbol{x}_M$ in the deformed configuration. The neutral axis is also denominated as the shell mid–surface. An arbitrary point in the shell will be described by the $\boldsymbol{X}$ and by $\boldsymbol{x}$ in

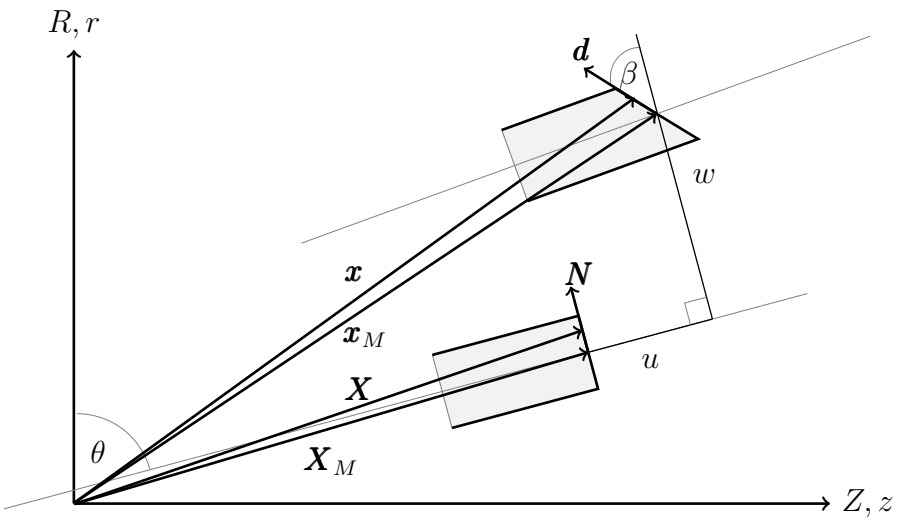

FIGURE 2.3 – Schematic diagram representing the kinematic variables of the shell axisymmetric element. Derived from the Reissner-Mindlin plate.

reference and deformed coordinates, respectively. Such vectors are written as

$$\boldsymbol{X} = \underbrace{\begin{bmatrix} Z \\ R \end{bmatrix}}_{\boldsymbol{X}_M} + \xi \underbrace{\begin{bmatrix} -\cos\theta \\ \sin\theta \end{bmatrix}}_{\boldsymbol{N}} \tag{2.40}$$

$$\boldsymbol{x} = \underbrace{\begin{bmatrix} Z + u\sin\theta - w\cos\theta \\ R + u\cos\theta + w\sin\theta \end{bmatrix}}_{\boldsymbol{x}_M} + \xi \underbrace{\begin{bmatrix} -\cos(\theta-\beta) \\ \sin(\theta-\beta) \end{bmatrix}}_{\boldsymbol{d}} \tag{2.41}$$

where $\boldsymbol{N}$ is a unit normal vector in the reference configuration and $\boldsymbol{d}$ is a vector describing the rotation of the cross section with respect to the mid–surface. The parameter ξ provides a local thickness coordinate and its domain is $[-h_0/2, h_0/2]$, where h_0 is the thickness of the shell, as shown in Fig. 2.3.
By application of Eq. Eq. 1.12 for Lagrangian strains, with $dX^2 = d\boldsymbol{X} \cdot d\boldsymbol{X}$ and $dx^2 = d\boldsymbol{x} \cdot d\boldsymbol{x}$, and by assuming θ as the direction of the mid–surface reference vector, $Z = s\sin\theta$ and $R = s\cos\theta$, we defined the Lagrangian strains in the shell in terms of the arch-length (s) and thickness (ξ) parametrization (second order terms in the thickness are neglected),

$$dx^2 - dX^2 = 2E_z ds^2 + 2E_{zr} ds d\xi, \tag{2.42}$$

where E_z is the Lagrangian strain in the arch-length direction s of the shell and E_{zr} is the shear strain between the s and r directions, such as

$$E_z = u_{,s} + \frac{1}{2}(u_{,s}^2 + w_{,s}^2) - \xi((1 + u_{,s})\cos\beta + w_{,s}\sin\beta)\beta_{,s} \tag{2.43}$$

$$E_{zr} = -(1 + u_{,s})\sin\beta + w_{,s}\cos\beta. \tag{2.44}$$

The notation $(\bullet)_{,s}$ represents the derivative $d(\bullet)/ds$. Herein the displacements u and w are expressed with respect to the local coordinate system and β is the rotation angle which describes the rotation of the normal vector $\boldsymbol{d}$ in the plane. An extra relation is needed to constraint the displacement to an axial symmetry. Thus, by taking the radial components of the reference (X_r) and current (x_r) vectors of the shell we defined the axisymmetric constraint with the tangential strain E_θ (direction perpendicular to the sheet), such as

$$E_\theta = \frac{x_r^2 - X_r^2}{2R^2} = e_\theta + \frac{1}{2}e_\theta^2 + \xi\frac{1}{R}((1+e_\theta)\sin(\theta-\beta) - \sin\theta) \tag{2.45}$$

Moreover, by using equation 1.12 for the relation between the stretch tensor and the strain tensor $(E = (\lambda^2 - 1)/2)$ we defined the stretches of the shell such as,

$$\lambda_z = \sqrt{(1+u_{,s})^2 + w_{,s}^2 - 2\xi((1+u_{,s})\cos\beta + w_{,s}\sin\beta)\beta_{,s}} \tag{2.46}$$

$$\lambda_\theta = \sqrt{(1+e_\theta)^2 + 2\xi((1+e_\theta)\sin(\theta-\beta) - \sin\theta)\frac{1}{R}}, \tag{2.47}$$

where the stretches are expressed in the principal axes of the shell and the deformation gradient is then a diagonal second-order tensor, by assuming the shear strain is zero $(E_{zr} = 0)$. Moreover, the plane stress assumption was considered due to the negligible stress in the radial direction $(\sigma_r = S_r \approx 0)$. Accordingly,

$$\boldsymbol{F} = \begin{bmatrix} F_{zz} & F_{z\theta} \\ F_{\theta z} & F_{\theta\theta} \end{bmatrix} = \begin{bmatrix} \lambda_z & 0 \\ 0 & \lambda_\theta \end{bmatrix}. \tag{2.48}$$

The current thickness is such,

$$h = \frac{h_0}{\lambda_z\lambda_\theta}. \tag{2.49}$$

We assumed a fully incompressible behavior and used the Lagrange multiplier approach. Moreover, we applied the Voigt's notation [55] to reduce the stress, strain and elasticity tensors to

$$\boldsymbol{S} = \begin{bmatrix} S_z \\ S_\theta \end{bmatrix}, \boldsymbol{E} = \begin{bmatrix} E_z \\ E_\theta \end{bmatrix}, \mathbb{C} = \begin{bmatrix} C_{zz} & C_{z\theta} \\ C_{\theta z} & C_{\theta\theta} \end{bmatrix} \tag{2.50}$$

$$S_z = 2\frac{\partial W}{\partial {\lambda_z}^2} + p{\lambda_z}^{-2}\ ,\ S_\theta = 2\frac{\partial W}{\partial {\lambda_\theta}^2} + p{\lambda_\theta}^{-2}\ ,\ S_r = 2\frac{\partial W}{\partial {\lambda_r}^2} + p{\lambda_r}^{-2} \tag{2.51}$$

2.6.2 Virtual work of shell elements

An special approach was taken for the thickness of the shell here. It was further divided in two layers representing, for example, the media and the adventitia. Accordingly, the thickness of the inner layer is $\xi \in [-h_0/2, h^*]$ and the thickness of the outer layer is $\xi \in]h^*, h_0/2]$, where ξ is the thickness paremeter varying in

$[-h_0/2, h_0/2]$. Additionally, if the shell has a total arch-length L and the geometry has axial symmetry, the internal virtual work of the body is

$$\delta\mathcal{W}_{int}(\boldsymbol{x}, \delta\boldsymbol{u}) = 2\pi \int_L \left(\int_{-h_0/2}^{h^*} \boldsymbol{S} \cdot \delta\boldsymbol{E} R d\xi + \int_{h^*}^{h_0/2} \boldsymbol{S} \cdot \delta\boldsymbol{E} R d\xi + \epsilon h_0 E_{zr} \delta E_{zr} R \right) ds, \tag{2.52}$$

where the differential reference volume is $dV = 2\pi R d\xi ds$. Moreover, the third term is a penalty to constraint the shear strain in the shell ($E_{zr} = 0$ assumption) and ensure the continuity of the displacements in the domain [71].
The internal virtual work was further linearized to apply an iterative method and find the displacement that satisfies equilibrium of the body,

$$\begin{aligned} \Delta\delta\mathcal{W}_{int}(\boldsymbol{x}, \delta\boldsymbol{u}) \cdot \Delta\boldsymbol{u} = \; & 2\pi \int_L \left(\int_{-h_0/2}^{h^*} \left(\delta\boldsymbol{E} \cdot \mathbb{C} \cdot \Delta\boldsymbol{E} + \boldsymbol{S} \cdot \Delta\delta\boldsymbol{E} \right) R d\xi \right. \\ & + \int_{h^*}^{h_0/2} \left(\delta\boldsymbol{E} \cdot \mathbb{C} \cdot \Delta\boldsymbol{E} + \boldsymbol{S} \cdot \Delta\delta\boldsymbol{E} \right) R d\xi \\ & \left. + \epsilon h_0 \left(\delta E_{zr} \Delta E_{zr} + E_{zr} \Delta\delta E_{zr} \right) R \right) ds. \end{aligned} \tag{2.53}$$

2.6.3 Virtual work of external forces in shell

We considered just the pressure from the Robin boundary conditions. This was jutified as all displacement-dependent forces were applied perpendicularly to the surface of the shell. Therefore, the inner pressure in a blood vessel and the elastic load performed by a stent can be modeled similarly here. The load of the stent is then a pressure applied on the arterial wall depending on the stiffness of the stent and the displacement from the original radius of the stent. The "stent pressure" may produce increments in the pressure with the displacement increments. The virtual work of the external force corresponding to the Robin boundary conditions is then,

$$\delta\mathcal{W}^R_{ext}(\boldsymbol{x}, \delta\boldsymbol{u}) = 2\pi \int_L \delta\boldsymbol{u} \cdot p(-\boldsymbol{e}_\theta \times \boldsymbol{x}_{,s}) r ds, \tag{2.54}$$

and its respective linearization for the iterative method of solution is

$$\begin{aligned} \Delta\delta\mathcal{W}^R_{ext}(\boldsymbol{u}, \delta\boldsymbol{u}) \cdot \Delta\boldsymbol{u} = \; & 2\pi \int_L \delta\boldsymbol{u} \cdot \left(\Delta p(-\boldsymbol{e}_\theta \times \boldsymbol{x}_{,s}) r - p(\boldsymbol{e}_\theta \times \Delta\boldsymbol{u}_{,s}) r \right. \\ & \left. - p(\boldsymbol{e}_\theta \times \boldsymbol{x}_{,s}) \Delta w \right) ds. \end{aligned} \tag{2.55}$$

In equations 2.54 and 2.55 we used the deformed surface $da = 2\pi || -\boldsymbol{e}_\theta \times \boldsymbol{x}_{,s} || r ds$ and the normal vector,

$$\boldsymbol{n} = \frac{-\boldsymbol{e}_\theta \times \boldsymbol{x}_{,s}}{|| -\boldsymbol{e}_\theta \times \boldsymbol{x}_{,s} ||} \text{ with } \boldsymbol{e}_\theta \times \boldsymbol{x}_{,s} = \begin{bmatrix} r_{,s} \\ z_{,s} \end{bmatrix} \tag{2.56}$$

where eventually the normal vector and the pressure are updated incrementally such as,

$$\boldsymbol{e}_\theta \times \Delta\boldsymbol{u}_{,s} = \begin{bmatrix} \Delta w_{,s} \\ \Delta u_{,s} \end{bmatrix} \text{ and } \Delta p = p_{,u}\, \Delta u + p_{,w}\, \Delta w. \tag{2.57}$$

The increments of the normal vector are related to rotations around the vector perpendicularly to the sheet. And the pressure increments are related to increments in the longitudinal and normal displacements of the shell. However, in the case of the luminal pressure $\hat{p}$ there are no increments and in the case of stent pressure there are increments just in the normal direction,

$$p = \begin{cases} \hat{p} & \Rightarrow \quad \Delta p = 0 & \text{if pressure,} \\ C_N(d-w) & \Rightarrow \quad \Delta p = -C_N \Delta w & \text{if stent} \end{cases} . \tag{2.58}$$

The stent is modeled by springs with stiffness C_N and natural length (or original radius) d which is the oversizing of the stent respect to the radius of the vessel.

2.6.4 Spatial discretization

After establishing the kinematics and the virtual work for the shells, the next step is to discretize the domain of the body Ω_t or Ω_R (current and reference configurations, respectively). Herein, a formulation for the elements resulting from the splitting of the geometry is proposed. The quantities in the domain will be further interpolated with linear functions between the points resulting from the discretization. For example, the displacements ($\boldsymbol{u} = [u, w, \beta]^T$) in a shell element (Fig. 2.4) can be interpolated by the functions N_a,

$$\boldsymbol{u} = \sum_{a=1}^{2} N_a \boldsymbol{u}_a \text{ and } \boldsymbol{u}_{,s} = \sum_{a=1}^{2} N_{a,s}\, \boldsymbol{u}_a, \tag{2.59}$$

with $\boldsymbol{u}_{,s}$ the derivative of the displacements, as the displacement suppose to be continuous in the domain. Additionally, the functions have to satisfy the condition of $\boldsymbol{u} = \boldsymbol{u}_1$ in the local node 1 and $\boldsymbol{u} = \boldsymbol{u}_2$ in the local node 2. The local linear interpolation functions that satisfy such conditions are

$$N_1 = \frac{1-\zeta}{2} \text{ and } N_2 = \frac{1+\zeta}{2}, \tag{2.60}$$

where ζ is the local parameter in the arch length of the element, $\zeta \in [-1, 1]$. So its parametrization respect to the arch length s is

$$\zeta = \frac{2}{L_e}(s - s_1) - 1 \text{ and } \zeta_{,s} = \frac{2}{L_e} \tag{2.61}$$

where s_1 is the arch length at the local node 1 of the element, L_e is the length of the element. Moreover, the derivatives of the quantities in the domain can be derived respect to the arch length parameter (Eq. 2.59(b)) through the interpolation functions by the chain rule,

$$N_{1,\zeta} = -\frac{1}{2} \text{ and } N_{2,\zeta} = \frac{1}{2} \text{ and } N_{a,s} = N_{a,\zeta}\, \zeta_{,s} \tag{2.62}$$

By applying the new interpolation function in the displacements and subsequently in the strain vector (Eqs. 2.50(b) with 2.43 and 2.45) and in the shear strain (Eq.

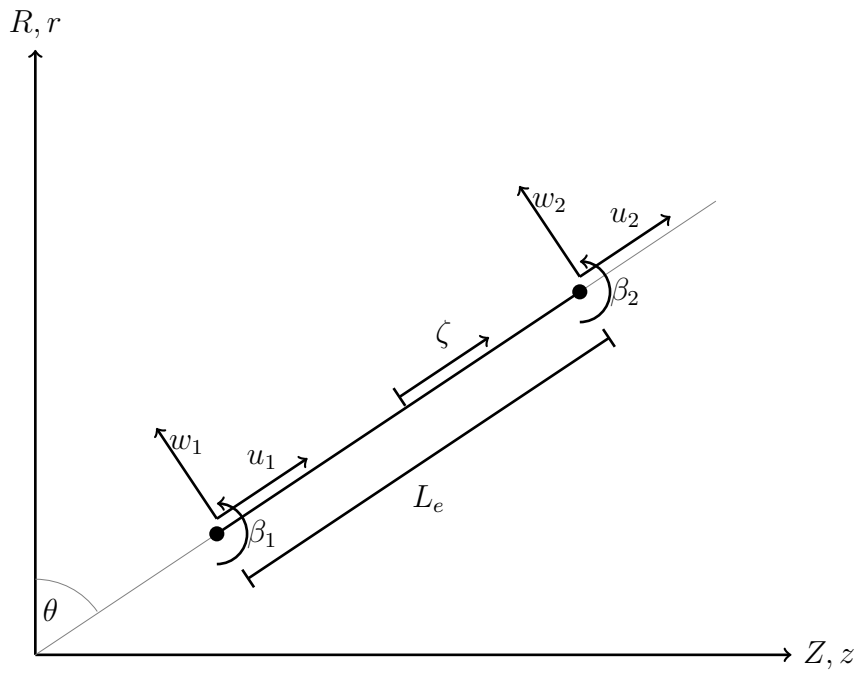

FIGURE 2.4 – Schematic diagram representing the parametrization of the shell axisymmetric element

2.44) we can obtaine the discretization of the virtual strains,

$$\delta \boldsymbol{E} = \sum_{a=1}^{2} \boldsymbol{B}_a^{mb} \delta \boldsymbol{u}_a \ , \ \delta E_{zr} = \sum_{a=1}^{2} \boldsymbol{B}_a^{pen} \delta \boldsymbol{u}_a. \tag{2.63}$$

where the matrices $\boldsymbol{B}_a^{mb}$ and $\boldsymbol{B}_a^{pen}$ are membrane-bending and penalization interpolation of the virtual displacements of the node a, respectively. The components of these matrices are introduced in the appendix A.2.
If the discretized virtual strains are replaced in the internal virtual work (Eq. 2.52) can be obtained a discretized internal virtual work for the element e,

$$\delta \mathcal{W}_{int}^{e}(\boldsymbol{x}, \delta \boldsymbol{u}) = 2\pi \sum_{a=1}^{2} \delta \boldsymbol{u}_a^T \int_{-1}^{+1} \int_{-1}^{+1} \left(\boldsymbol{B}_a^{mbT} \boldsymbol{S} + \epsilon \boldsymbol{B}_a^{penT} E_{zr} \right) R \frac{L_e}{2} \frac{h_0}{2} d\hat{\xi} d\zeta. \tag{2.64}$$

And applying the same concepts of discretization to the displacement increments are obtained the incremental strain and incremental virtual strains are obtained,

$$\Delta \boldsymbol{E} = \sum_{a=1}^{2} \boldsymbol{B}_a^{mb} \Delta \boldsymbol{u}_a \quad \Delta \delta E_z = \sum_{a=1}^{2} \sum_{b=1}^{2} \delta \boldsymbol{u}_a^T \boldsymbol{G}_{ab}^{z} \Delta \boldsymbol{u}_b \tag{2.65}$$

$$\Delta \delta E_\theta = \sum_{a=1}^{2} \sum_{b=1}^{2} \delta \boldsymbol{u}_a^T \boldsymbol{G}_{ab}^{\theta} \Delta \boldsymbol{u}_b \quad \Delta \delta E_{zr} = \sum_{a=1}^{2} \sum_{b=1}^{2} \delta \boldsymbol{u}_a^T \boldsymbol{G}_{ab}^{pen} \Delta \boldsymbol{u}_b \tag{2.66}$$

By using the increments just defined in the linearization of the internal virtual

work,

$$\Delta\delta\mathcal{W}^{e}_{int}(\boldsymbol{x},\delta\boldsymbol{u})\cdot\Delta\boldsymbol{u} = 2\pi\sum_{a=1}^{2}\sum_{b=1}^{2}\delta\boldsymbol{u}_a^T\int_{-1}^{+1}\int_{-1}^{+1}\Big(\boldsymbol{B}_a^{mbT}\mathbb{C}\boldsymbol{B}_b^{mb}+S_z\boldsymbol{G}^z_{ab}+S_\theta\boldsymbol{G}^\theta_{ab} + \epsilon(\boldsymbol{B}_a^{penT}\boldsymbol{B}_b^{pen}+E_{zr}\boldsymbol{G}^{pen}_{ab})\Big)R\frac{L_e}{2}\frac{h_0}{2}d\hat{\xi}d\zeta\Delta\boldsymbol{u}_a \quad (2.67)$$

Eventually, the virtual work of the pressure can be discretized too and it is represented as,

$$\delta\mathcal{W}^{p}_{ext}(\boldsymbol{x},\delta\boldsymbol{u}) = \frac{\pi}{6}\begin{bmatrix} r_1-r_2 \\ z_2-z_1\end{bmatrix}(\delta\boldsymbol{u}_1(3p_1r_1+p_1r_2+p_2r_1+p_2r_2) +\delta\boldsymbol{u}_2(p_1r_1+p_1r_2+p_2r_1+3p_2r_2)) \quad (2.68)$$

and its linearized form due to the dependece on the displacements is

$$\Delta\delta\mathcal{W}^{p}_{ext}(\boldsymbol{x},\delta\boldsymbol{u})\cdot\Delta\boldsymbol{u} = \frac{\pi}{6}(\delta\boldsymbol{u}_1\boldsymbol{K}^p_{11}\Delta\boldsymbol{u}_1+\delta\boldsymbol{u}_1\boldsymbol{K}^p_{12}\Delta\boldsymbol{u}_2 +\delta\boldsymbol{u}_2\boldsymbol{K}^p_{21}\Delta\boldsymbol{u}_1+\delta\boldsymbol{u}_2\boldsymbol{K}^p_{22}\Delta\boldsymbol{u}_2) \quad (2.69)$$

In this work, the shell finite element formulation is made from the work developed by Wagner (1990) [71].

2.6.5 Time integration method

After finding the displacement that satisfy the mechanical equilibrium and obtain the current stress state (homeostatic state in the reference step) there is the need to define the inelastic quantities for the time of interest $(t+\Delta t)$ from the inelastic constitutive equations given by the hCM model, Eqs. 1.53, 1.58, 1.54. As the law for the mass density, remodeling and growth are given in rates it is needed to use a time integration scheme, and in this work is used the forward Euler method. Remark, stability issues in this integration method are avoided by using $\Delta t \approx T^j/10$, where T^j is the smallest turnover time of any constituent. Therefore, the G&R quantities at time $t+\Delta t$ are determined by their constitutive model and the integration as

$$\varrho^j_{R(t+\Delta t)} = \varrho^j_{R(t)} + \dot{\varrho}^j_R(\varrho^j_R,t)\Delta t \quad (2.70)$$

$$\lambda^j_{r(t+\Delta t)} = \lambda^j_{r(t)} + \dot{\lambda}^j_r(\lambda^j_r,t)\Delta t \quad (2.71)$$

$$\det(\boldsymbol{F}_g)_{(t+\Delta t)} = \frac{\varrho_{R(t+\Delta t)}}{\varrho_{R(0)}} \quad (2.72)$$

Moreover, if we consider an anisotropic growth and more specifically in the thickness direction, the thickness would be now defined by the deformation (Eq. 2.49) in the shell and by the growth (Eq. 2.72),

$$h = \frac{h_0}{\lambda_z\lambda_\theta}\frac{\varrho_{R(t+\Delta t)}}{\varrho_{R(0)}}. \quad (2.73)$$

2.6.6 Overview of the program

The shell elements were implemented in a Fortran 90 code to solve the G&R problem for axisymmetric geometries (e.g. cylinders or cones). A tree of the program structure for shell elements is presented in the figure 2.5:

- `main.f90` is he main script. It calls the routines `openfi`, `datainp`, `initial_comp_0` and `computation`.
- `openfi` is the routine to open the input file with the necessary data for the simulation.
- `datainp` read all the block of the input file for the control, mesh, materials, sections and the time steps with its boundary conditions and loads.
- `initial_comp_0` initialize the variables to be use during computation, allocate memory and pointers and store the reference configuration of the shell.
- `computation` is the heart of the code, it is where the G&R computations are performed in a time loop until arrives to the end of the interval of study. Within this routine the total displacements of the body are updated according to the boundary conditions or loads in `initial_comp_t`.
- `gauscheb` compute the interpolation fuctions, their derivatives and the Gauss points for integration.
- `iteration` apply the Newthon-Raphson method to find the displacements that satisfy the equilibrium.
- `gauss_to_nodes` interpolate or extrapolate the values in the Gauss point back to the nodes to prepare the data for the `output` which organize the data in matrices that can be wirtten in VTK format for paraview.

To perform the iterations the `assembler` routine perform the assembly of the local element stiffness matrices (`shell2d_elem` and `loads_elem`) into a global stiffness matrix. Moreover, the quadrature rule within the element is set at the `gauscheb` routine, the quadrature rules provide the interpolation functions and the quadrature points (Gauss points) for space integration. Then, at each Gauss point is computed the stretch and the matrices needed for the formulation, additionally, the elastic and inelastic constitutive relation are computed in `constitutive` routine.
The bi-layer approach for the arterial wall is implemented within the routine `shell2d_elem` where additional Gauss points are used in the thickness. More Gauss point in the thickness allow to use an interpolation function for each layer of the artery. With this expansion in integration points it is possible to configure two groups of points for a further selection of layer (`'MEDIA'` and `'ADVEN'`). This last selection permit to model each layer independently and use different constitutive relations in each of them, Fig. 2.6.

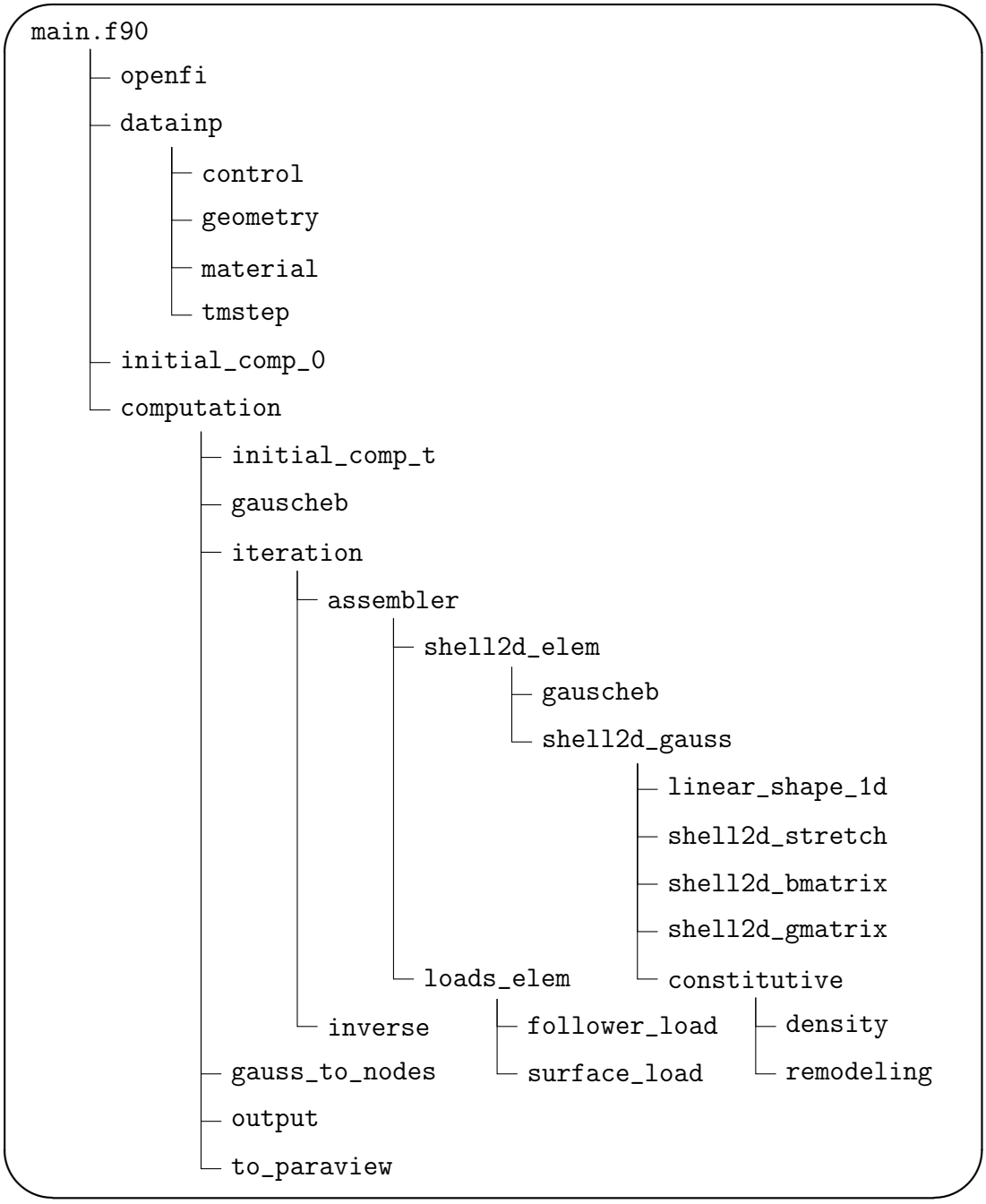

Figure 2.5 – Tree of the program for shell elements.

```
MODULE shell2d_mod
 ...
 CONTAINS
 SUBROUTINE shell2d_elem(...)
  ...
  DO igaus=1,ngaus !Gauss integration along element
   !Gauss integration along thickness MEDIA/ADVENTITIA
   DO jgaus=1,2*ngaus
    IF (jgaus>ngaus) THEN
     jgaux = jgaus - ngaus
    ELSE
     jgaux = jgaus
    END IF
    CALL shell2d_gauss(...)
    ....
   END DO !along thickness MADIA/ADVENTITIA
   ....
  END DO !along element
 END SUBROUTINE shell2d_elem

 SUBROUTINE shell2d_gauss(...)
  ...
  !Select layer
  IF (jgaus>ngaus) THEN
   LAYER = 'ADVEN'
   zet = (hA0/2.d0)*(zeta+h0/hA0-1.d0)
   Dthick = hA0/2.d0
  ELSE
   LAYER = 'MEDIA'
   zet = (hM0/2.d0)*(zeta-h0/hM0+1.d0)
   Dthick = hM0/2.d0
  END IF
  ...
 END SUBROUTINE shell2d_gauss
 ...
END MODULE shell2d_mod
```

FIGURE 2.6 – Integration along the thickness.

2.7 Three-dimensional approach

Furthermore, a three-dimensional framework is needed to eventually perform G&R simulations in non-symmetric geometries, for example, patient-specific geometries obtained from CT scans. For this reason we selected a three-dimensional FE open-source library available for python [66], [67]. Within the library further modifications were made in the code to adapt it for blood vessels simulations, as for instance the addition of deformation-dependent loads due to the pressure, for example. The most significative modification for this work was the addition of a G&R routine in the code for the simulations of adaptations in living tissues, based on the homogenized constrained mixture model. Additionally, we implemented a multiphase (or multiset) approach to consider a bi-layer model as in the shell implementation.
The mathematical presentation of the virtual work of external forces and its discretization are presented in this chapter to facilitate further development in the three-dimensional code, available in GitHub [30], [72].

2.7.1 External forces

In the FE library, Dirichlet and Neumann boundary conditions are already well implemented. However Robin boundary conditions are not considered there, so an extension of the code is developed to include the loads from the Robin conditions. Following the equation 2.38, two forces produce work. First, the pressure,

$$\delta \mathcal{W}^{p}_{ext}(\boldsymbol{x}, \delta \boldsymbol{u}) = \int_{A_\xi} p \delta \boldsymbol{u} \cdot \left(\frac{\partial \boldsymbol{x}}{\partial \xi} \times \frac{\partial \boldsymbol{x}}{\partial \eta} \right) d\xi d\eta \tag{2.74}$$

where ξ and η are the parametrization of the surface where the pressure is applied. The derivative of the current position respect to the parameters gives two tangential vectors in the surface da and their cross product produces the normal to the surface,

$$\boldsymbol{n} = \frac{\frac{\partial \boldsymbol{x}}{\partial \xi} \times \frac{\partial \boldsymbol{x}}{\partial \eta}}{\left|\left| \frac{\partial \boldsymbol{x}}{\partial \xi} \times \frac{\partial \boldsymbol{x}}{\partial \eta} \right|\right|} \text{ with } da = \left|\left| \frac{\partial \boldsymbol{x}}{\partial \xi} \times \frac{\partial \boldsymbol{x}}{\partial \eta} \right|\right| d\xi d\eta. \tag{2.75}$$

A detailed presentation of the virtual work of pressure can be found in [51]. Second, the elastic forces in the boundary

$$\delta \mathcal{W}^{k}_{ext}(\boldsymbol{x}, \delta \boldsymbol{u}) = \int_{\partial \Omega_t} \delta \boldsymbol{u} \cdot k \boldsymbol{u} da, \tag{2.76}$$

where k is the elastic stiffness of the boundary. Furthermore, the forces represented here are displacement-depenedent and consequently experience increments due to displacement increments. Thus, the virtual work of the Robin boundary conditions must be linearized in order to add its incremental form to the iterative method

for solution,

$$\begin{aligned}\Delta\delta\mathcal{W}^{p}_{ext}(\boldsymbol{x},\delta\boldsymbol{u})\cdot\Delta\boldsymbol{u} = \quad & \frac{1}{2}\int_{A_\xi} p\frac{\partial\boldsymbol{x}}{\partial\xi}\cdot\left(\frac{\partial\delta\boldsymbol{u}}{\partial\eta}\times\Delta\boldsymbol{u}-\delta\boldsymbol{u}\times\frac{\partial\Delta\boldsymbol{u}}{\partial\eta}\right)d\xi d\eta \\ & -\frac{1}{2}\int_{A_\xi} p\frac{\partial\boldsymbol{x}}{\partial\eta}\cdot\left(\frac{\partial\delta\boldsymbol{u}}{\partial\xi}\times\Delta\boldsymbol{u}-\delta\boldsymbol{u}\times\frac{\partial\Delta\boldsymbol{u}}{\partial\xi}\right)d\xi d\eta \quad (2.77)\end{aligned}$$

$$\Delta\delta\mathcal{W}^{k}_{ext}(\boldsymbol{x},\delta\boldsymbol{u})\cdot\Delta\boldsymbol{u} = \int_{\partial\Omega_t}\delta\boldsymbol{u}\cdot k\Delta\boldsymbol{u}da \quad (2.78)$$

The reason the area da is not linearized for the elastic boundary conditions will be given in the discretization section.

2.7.2 Spatial discretization

In the FE library it is possible to use high order interpolation function for the displacements and coordinates. Therefore, the interpolation functions are presented in a general way, as they can be linear, quadratic or more, and the functions can be applied to tetrahedra or hexahedra elements, with several n nodes. So the interpolated coordinates and displacement in the element are

$$\boldsymbol{x}=\sum_{a=1}^{n}N_a\boldsymbol{x}_a\ ,\ \boldsymbol{u}=\sum_{a=1}^{n}N_a\boldsymbol{u}_a, \quad (2.79)$$

where N_a is the interpolation function in the node a. By applying the new interpolations within the virtual work for Robin conditions (Eq. 2.74 and 2.76), we obtain

$$\delta\mathcal{W}^{pe}_{ext}(\boldsymbol{x},\delta\boldsymbol{u})=\delta\boldsymbol{u}_a\cdot\int_{A_\xi}pN_a\left(\frac{\partial\boldsymbol{x}}{\partial\xi}\times\frac{\partial\boldsymbol{x}}{\partial\eta}\right)d\eta d\xi, \quad (2.80)$$

$$\delta\mathcal{W}^{k}_{ext}(\boldsymbol{x},\delta\boldsymbol{u})=\sum_{a}\delta\boldsymbol{u}_a\cdot k\boldsymbol{u}, \quad (2.81)$$

and subsequently applying the interpolation functions to the linearization of the external virtual work of the Robin conditions (Eq. 2.77 and 2.78), it results,

$$\Delta\delta\mathcal{W}^{pe}_{ext}(\boldsymbol{x},\delta\boldsymbol{u})\cdot\Delta\boldsymbol{u}=(\delta\boldsymbol{u}_a\times\Delta\boldsymbol{u}_b)\cdot\boldsymbol{K}^{p}_{ab}, \quad (2.82)$$

$$\begin{aligned}\boldsymbol{K}^{p}_{ab} = \quad & \frac{1}{2}\int_{A_\xi}p\frac{\partial\boldsymbol{x}}{\partial\xi}\left(\frac{\partial N_a}{\partial\eta}N_b-N_a\frac{\partial N_b}{\partial\eta}\right)d\xi d\eta \\ & -\frac{1}{2}\int_{A_\xi}p\frac{\partial\boldsymbol{x}}{\partial\eta}\left(\frac{\partial N_a}{\partial\xi}N_b-N_a\frac{\partial N_b}{\partial\xi}\right)d\xi d\eta, \quad (2.83)\end{aligned}$$

$$\Delta\delta\mathcal{W}^{k}_{ext}(\boldsymbol{x},\delta\boldsymbol{u})\cdot\Delta\boldsymbol{u}=\sum_{a,b}\delta\boldsymbol{u}_a\cdot\boldsymbol{K}^{k}_{ab}\Delta\boldsymbol{u}_b, \quad (2.84)$$

$$\boldsymbol{K}^{k}_{ab}=k, \quad (2.85)$$

where the elastic forces are applied in the nodes of the discretized body. This means that its surface integral is replaced by the sum of the elastic forces applied to the nodes of the constrained surface.

2.7.3 Time integration method

Again as indicated by the mechanical problem, the inelastic quantities are computed after finding the equilibrium. The computation of the density, remodeling and growth is obtained through the inelastic constitutive relations provided by the hCM model which are presented in a rate form. Then, for density and remodeling is applied the forward Euler method to obtain the quantities at time $t + \Delta t$ from the time t, the growth is obtained from the addition of the constituent densities into the total density of the mixture,

$$\varrho^j_{R(t+\Delta t)} = \varrho^j_{R(t)} + \dot{\varrho}^j_R(\varrho^j_R, t)\Delta t, \tag{2.86}$$

$$\lambda^j_{r(t+\Delta t)} = \lambda^j_{r(t)} + \dot{\lambda}^j_r(\lambda^j_r, t)\Delta t, \tag{2.87}$$

$$\boldsymbol{F}^j_{g(t+\Delta t)} = \frac{\varrho_{R(t+\Delta t)}}{\varrho_{R(0)}}\boldsymbol{a}_0^{\perp} \otimes \boldsymbol{a}_0^{\perp} + (\boldsymbol{I} - \boldsymbol{a}_0^{\perp} \otimes \boldsymbol{a}_0^{\perp}), \tag{2.88}$$

The remodeling is again simplified to the fibre direction because the elastin is not pruduced anymore and there is remodeling just in the fibres (collagen and SMCs). Additionally, the growth is related to the tensor $\boldsymbol{a}_0^{\perp}$, a vector in the thickness direction, because the growth is assumed anisotropic, having place in the thickness direction.

2.7.4 Overview of the program

A simulation in with the FE library is managed by a master python script where some basic instances are declared to perform G&R simulations:

- `Mesh` contains the geometry, nodes and elements to be used in the simulation.
- `BoundaryCondition` sets the conditions for the nodes in the boundaries according to the kind of conditions, either Dirichlet, Neumann or Robin.
- `Material` initializes the appropiate elastic constitutive model with its parameters
- `GrowthRemodeling` establishes the G&R parameters and prepares the time integration scheme for the inelastic quantities.
- `Formulation` calls the variational principle with the interpolation function and quadrature rules.
- `FEMSolver` carries out the simulation which in first place sets the iterative criteria and controls.

Moreover, in the master script we difined the functions `Sets` and `Directions` for multiphase materials and for anisotropic fibre directions, respectively (Fig. 2.7). The instance `FEMSolver` runs the simulations by its function `Solve`, Fig. 2.8. Indeed that function computes the displacements needed to solve the equilibrium

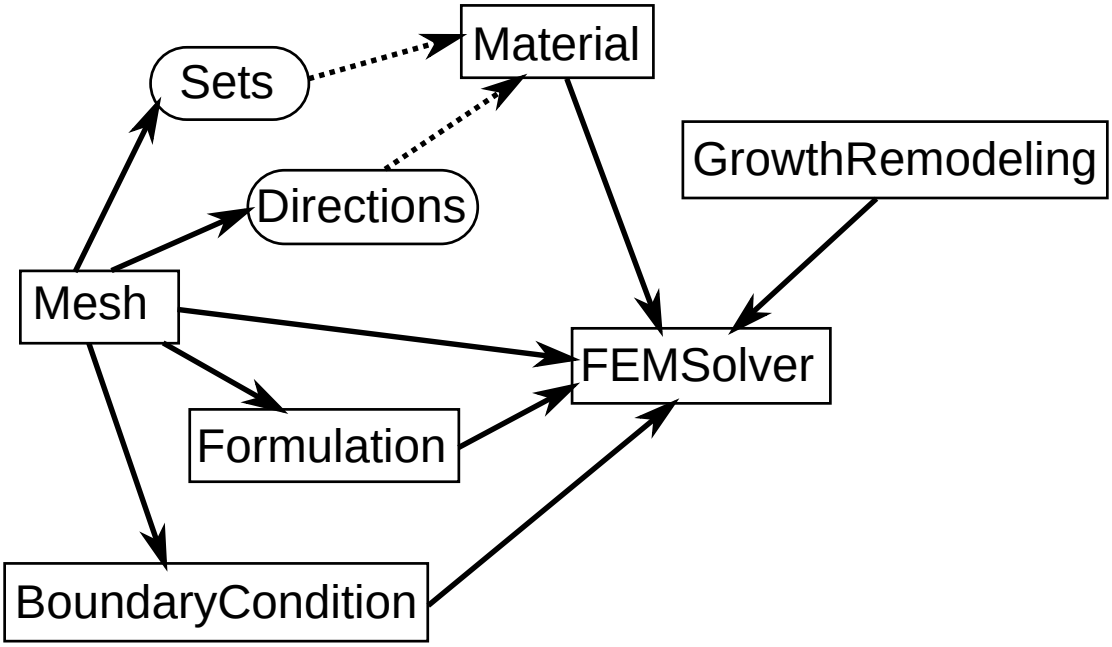

FIGURE 2.7 – Structure of the python master script for the FE library.

equation. For this purpose it is checked that all the data is correctly initialized, after the boundary conditions are computed with the first assembly of the stiffness matrix, Fig. 2.9. Just after this first assembly the incremental method is called for the simulation. Where the incremental method can be either time-independent or time-dependent. The time-independent increments are used to calibrate the homeostatic state. While G&R works under time-dependent increments, within these increments the inelastic constitutive relations, the Robin forces, the quantities needed for the hCM model, are computed and updated in the iterative scheme.
In figures 2.8 and 2.9, the routines in gray boxes were created originally in this thesis and the routines surrounded by a black border are routines modified from the original code. The other routines remain without changes from the original `Florence` code to the modified `Kuru` code.

2.8 Verification

The codes developed in this work are further tested. The test is over a benchmark case of a cylinder with internal pressure. The test aims to compare the results given by the codes implemented here against the analytical solution of a thin-walled tube. In this manner we seek to measure the error produced by the FE framework and conclude if the code gives realistic results. Consequently, some test are performed over the same problem with different elastic materials and we register their results, Tables 2.1 and 2.2.
In this section is also noted that the analytical response and the axisymmetric code are under incompressibility assumptions. However, the three-dimensional code use the penalization approach for nearly incompressible materials, where the

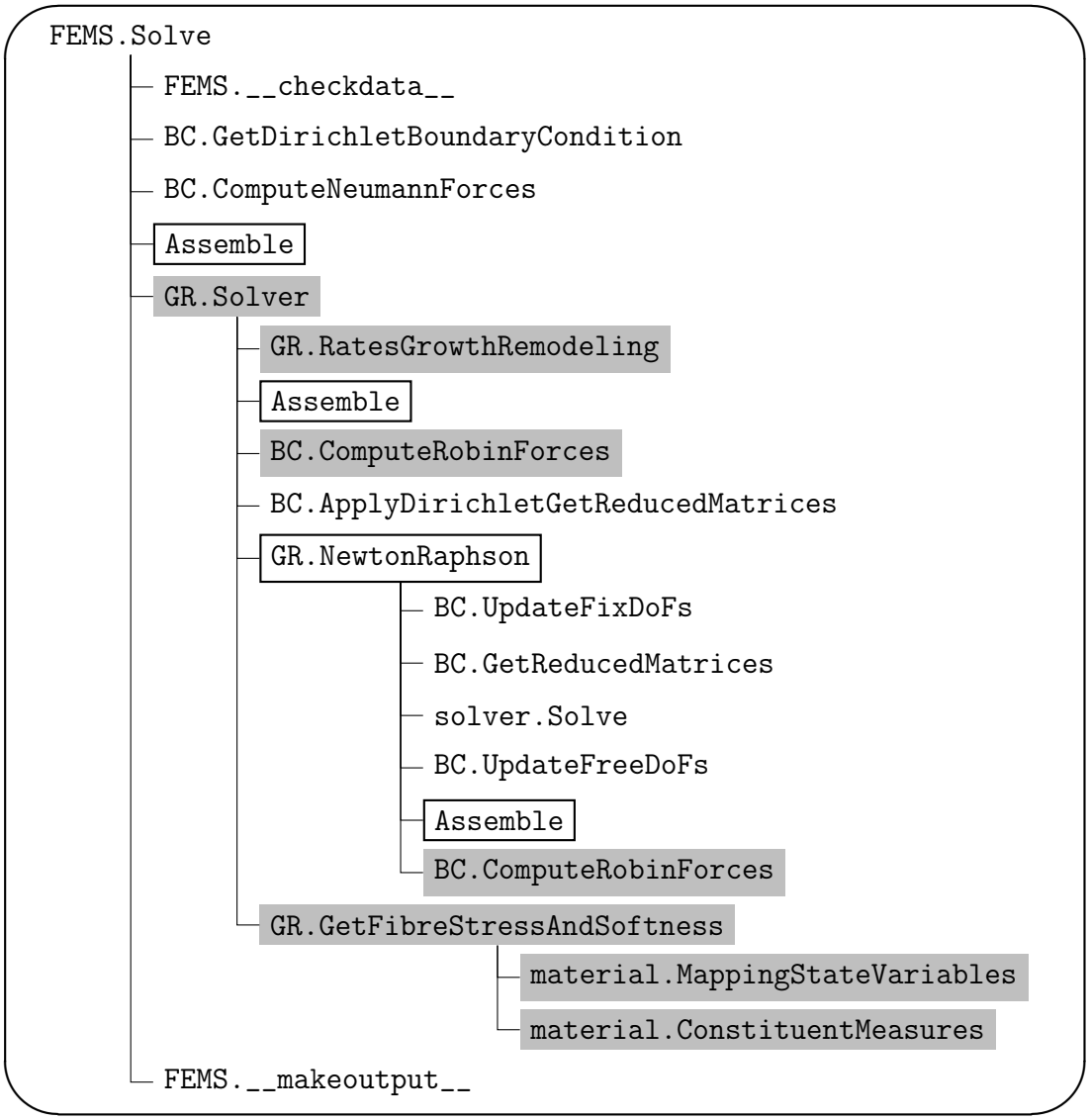

Figure 2.8 – Tree of the program for Kuru.

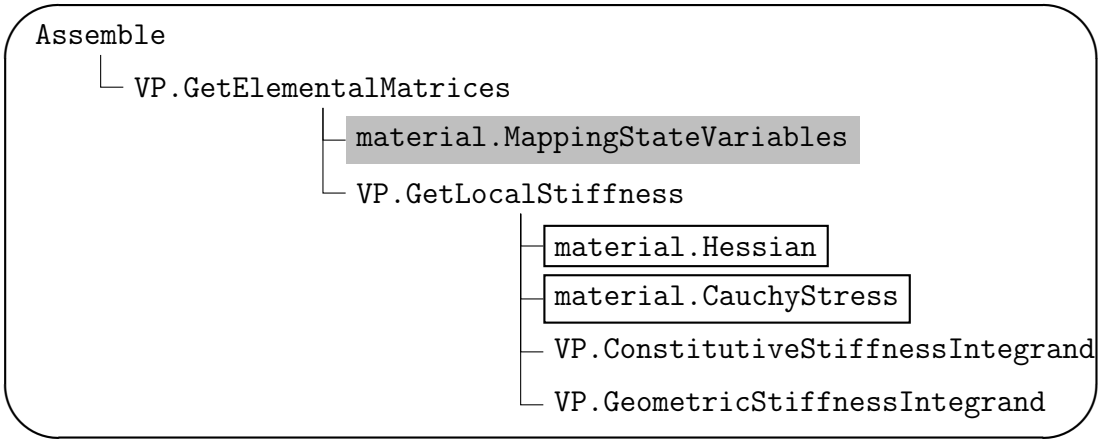

Figure 2.9 – Assemblage of the program for Kuru.

bulk modulus κ, the shear stiffness μ and the Poisson's ratio ν are related by

$$\kappa = \mu \frac{2}{3} \left(\frac{1+\nu}{1-2\nu} \right), \tag{2.89}$$

where ν=0.5 is a singular value for the equation and also means incompressible behavior of the material. It is remarked that the bulk modulus does not apply for incompressible behavior.
The first test (Table 2.1) is performed in a body made of a homogeneous material modeled by the Neo-Hookean elastic law, where μ=151.2-kPa,

$$W(\boldsymbol{C}) = \frac{1}{2}\kappa(J-1)^2 + \frac{\mu}{2}(\bar{I}_1 - 3). \tag{2.90}$$

Platform	Displacement[mm]	Error (abs)	Error (%)	Compressibility
Analytical	2.781	-	-	Incompressible
Axisymmetric	2.781	9.005×10^{-4}	0.032	Incompressible
Florence	2.887	1.050×10^{-1}	3.774	$\nu = 0.485$
Florence	2.801	1.950×10^{-2}	0.701	$\nu = 0.495$

TABLE 2.1 – Verification of the FE frameworks against the analytical thin-walled tube. Simulations performed with a Neo-Hookean elastic model.

The second test (Table 2.2) is also focus in the analysis of the new anisotropic model implemented in the three-dimensional code. The anisotropic model taken is the Fung-quadratic elastic law

$$W(\boldsymbol{C}) = \frac{1}{2}\kappa(J-1)^2 + \frac{\mu}{2}(\bar{I}_1 - 3) + \sum^{2} \frac{k_1}{2k_2} \left[\exp(k_2(I_4 - 1)^2) - 1 \right] \tag{2.91}$$

where μ=37.8-kPa, k_1=298.2-kPa, k_2=11.2 and the material behavior include two fibre families in diagonal direction $\{-\frac{\pi}{4}, \frac{\pi}{4}\}$.

Platform	Displacement[mm]	Error (abs)	Error (%)	Compressibility
Analitical	1.111	-	-	Incompressible
Axisymmetric	1.109	1.997×10^{-3}	0.180	Incompressible
Florence	1.099	1.188×10^{-2}	1.069	$\nu = 0.485$
Florence	1.098	1.240×10^{-2}	1.116	$\nu = 0.495$

TABLE 2.2 – Verification of the FE frameworks against the analytical thin-walled tube. Simulations performed with a Fung Quadratic elastic model.

Finally, the low error given by the simulations executed within the codes written in this thesis allow to conclude their good perfomance for isotropic and anisotropic materials with the application of Robin boundary conditions in the body (internal pressure). Furthermore, this establish the FE workbenches needed for the development of this work and it is now possible to use a material mixture approach for the material and perform further G&R simulations with the confidence that the codes give realistic results.

2.9 Conclusion

As most of the balance principles are used in the construction of the constitutive relationships, only the linear momentum remains to be solved in G&R. The challenge was the complexity of the system of differential equations produced by equation 2.1. With the goal to solve the equilibrium of a body Ω_t and follow its evolution during G&R, we developed two FE workbenches ables to simulate aneurysm progression in arteries. The results given by the codes have been compared against the response of a thin-walled tube with errors low enough to conclude the positive reliability of the new frameworks. The axisymmetric shell code permitted to simulate aneurysm growing in cylinders from mass degradation and to simulate stent-graft deployment. The three-dimensional framework permitted to introduce patient-specific aortas in the G&R simulations and predict aneurysm progression after mass degradation in the arterial model.
The results achieved with the FE frameworks developed in this chapter are presented in the following chapters. The next chapter shows simulations of aneurysm progression and stent-graft deployment in axisymmetric arterial models. The subsequent chapter introduce simulations of aneurysm progression in three-dimensional idealized and patient-specific arterial models.

Chapter 3

Axisymmetric model

Table of contents of the chapter

3.1 Résumé du chapitre en français. . . . 62
3.2 Abstract of the chapter . . . 62
3.3 Introduction . . . 63
3.4 Material and methods. . . . 64
3.4.1 Strain Energy Function . . . 64
3.4.2 Growth and remodeling . . . 66
3.4.3 Adaptation to axisymmetric shell formulation . . . 68
3.4.4 Finite element implementation . . . 70
3.5 Numerical experiments . . . 71
3.5.1 Comparison with an existing G&R model . . . 71
3.5.2 Applications of the model . . . 71
3.6 Results . . . 72
3.6.1 Comparison with an existing G&R model . . . 72
3.6.2 Case I: benchmark case of a bi-layer arterial wall . . . 73
3.6.3 Case II: adaptation after stent implantation . . . 75
3.6.4 Case III: stent implantation after several years of aneurysm development G&R . . . 77
3.6.5 Computational details . . . 80
3.7 Discussion. . . . 80
3.8 Conclusions . . . 83

3.1 Résumé du chapitre en français

L'objectif de cet article est d'étudier numériquement comment les vaisseaux sanguins s'adaptent lorsqu'ils sont exposés à un stimulus mécanobiologique, à savoir un changement soudain de leurs conditions biomécaniques comme des blessures protéolytiques ou une implantation. L'adaptation se produit par la croissance et le remodelage (G&R), consistant en la production ou l'élimination de protéines structurelles, telles que le collagène, jusqu'au rétablissement des conditions biomécaniques homéostatiques initiales. Dans certaines circonstances, les artères évoluent vers des conditions pathologiques instables, comme les anévrismes, qui sont responsables d'une morbidité et d'une mortalité importantes. Par conséquent, les prédictions numériques de G&R dans différentes circonstances peuvent être utiles pour comprendre fondamentalement comment les pathologies artérielles évoluent. Pour cela, nous avons développé un modèle de coque axisymétrique 2D par éléments finis (FEM) à faible coût et open-source de la paroi artérielle. Les lois de comportement et la réponse G&R sont exprimées dans le cadre de la théorie des mélanges homogénéisés contraints. L'originalité est d'intégrer dans le modèle le comportement spécifique des deux couches artérielles (média et adventice). En considérant différentes stimuli mécanobiologiques, nos résultats montrent que la dilatation artérielle résultante est fortement corrélée à l'épaisseur de la média. La simulation de l'implantation d'endoprothèses est particulièrement intéressante. Un oversizing du stent trop grand peut provoquer une dilatation définitive alors que la dilatation se stabilise après une période transitoire pour des rapports d'oversizing plus modérés. Nous montrons également que l'implantation d'une endoprothèse induit une réponse différente dans un anévrisme ou dans une artère saine, cette dernière donnant lieu à une G&R plus instable. En résumé, notre modèle G&R peut prédire efficacement, avec un coût de calcul très faible, les aspects fondamentaux de l'adaptation artérielle induite par les procédures cliniques.

3.2 Abstract of the chapter

The goal of this paper is to study computationally how blood vessels adapt when they are exposed to a mechanobiological insult, namely a sudden change of their biomechanical conditions such as proteolytic injuries or implantation. Adaptation occurs through growth and remodeling (G&R), consisting in mass production or removal of structural proteins, such as collagen, until restoring the initial homeostatic biomechanical conditions. In some circumstances, the initial conditions can never be recovered and arteries evolve towards unstable pathological conditions, such as aneurysms, which are responsible for significant morbidity and mortality. Therefore, computational predictions of G&R under different circumstances can be helpful in understanding fundamentally how arterial pathologies progress. For that we have developed a low-cost open-source finite-element 2D axisymmetric shell model (FEM) of the arterial wall. The constitutive equations for static

equilibrium used to model the stress-strain behavior and the G&R response are expressed within the homogenized constrained mixture theory. The originality is to integrate the layer-specific behavior of both arterial layers (media and adventitia) into the model. Considering different mechanobiological insults, our results show that the resulting arterial dilatation is strongly correlated with the media thickness. The adaptation to stent implantation is particularly interesting. For large stent over-sizing ratios, the artery cannot recover from the mechanobiological insult and dilates forever, whereas dilatation stabilizes after a transient period for more moderate oversizing ratios. We also show that stent implantation induces a different response in an aneurysm or in a healthy artery, the latter yielding more unstable G&R. Finally, our G&R model can efficiently predict, with very low computational cost, fundamental aspects of arterial adaptation induced by clinical procedures.

3.3 Introduction

Vascular tissues, as other biological tissues, commonly maintain homeostatic conditions during routine function and therefore, they continually adapt to any mechanical and biochemical alteration in their surrounding. Any factor disturbing the preferred homeostatic state of arterial wall, such as permanent hypertension or disruption of elastin fibers [73], may induce vascular growth and remodeling (G&R) which is a vital process to maintain vessel function. At the tissue scale, this manifests through continuous mass changes of the existent components in the extracellular matrix (ECM) such as collagen, elastin and proteoglycans [22], [24]. When the arterial wall is unable to recover its homeostatic conditions through G&R, arterial dysfunction may arise and end up with, for instance, an aneurysm, which is a permanent, degenerative and localized expansion of the arterial diameter. An aneurysm can lead to a wall dissection and rupture and potentially be a life-threatening condition.

In the past two decades, different computational approaches were developed to model G&R of load–bearing soft tissues. These methods can be grouped in two major mathematical theories: a constrained mixture theory (CMT) determining the rates of mass removal and production of individual constituents within stressed configurations or a kinematic theory specifying an evolution equation for the stress-free configuration of the tissue as a whole. Although the latter is popular and conceptually more simple, it relies largely on heuristic definitions of growth [24]. Kinematic growth theories commonly split multiplicatively the total deformation gradient into elastic and inelastic parts, where the inelastic one is related to growth [23]. This theory has been widely used for single-constituent solid continuum [74], [75] as well as for homogenized [24], [27] and non–homogenized [14], [26], [76], [77] constrained mixture models (CMMs). For example, Valentín et al [26], [78] modelled arterial wall adaptation and maladaptation to different cases, such as loss of smooth muscle cells (SMCs), elastin degradation and changes in fiber

orientations and quantities. Watton et al [13], [57] quantified the interaction between collagen microstructure and mechanical stretch to model the growth of an abdominal aortic aneurysm (AAA). They introduced variables for the recruitment of collagen fibers to account for microstructural changes leading to the formation of an aneurysm. Watton et al [57] introduced the first bi-layered G&R approach using a membrane model. Cyron et al [28] employed the CMT to capture G&R of soft tissues due to altered mechanobiological stimuli. Moreover, Wilson et al [61] investigated the effects of collagen turnover and elastin loss on the formation of AAAs in a parametric study. Their results showed that a number of variables play a substantial role on radial dilatation and axial expansion of AAAs, including wall thickness, fiber stretch, maximum wall stress and evolving material properties.
Despite extensive endeavor to establish G&R models, significant efforts are still needed to develop reliable models of aneurysm evolution. Moreover, adaptation after endovascular aneurysm repair has never been modelled so far. Therefore, there is still an important potential for G&R models to understand the adaptation of arteries before or after different clinical treatments.
In this work, our contribution was twofold. First, it was computational: we implemented an original layer-specific homogenized CMT-based finite element (FE) shell model to study transient G&R effects of different clinically-relevant cases related to aneurysm growth and repair. Second it was physiological: we predicted the adaptation of an artery after stent implantation and showed the major effect of oversizing on the post-surgery outcomes.

3.4 Material and methods

3.4.1 Strain Energy Function

The homogenized CMT was employed as an hybrid approach to consider G&R in the arterial wall [22]. Let us assume a material point of a mixture in the Ω^{r} domain, represented by its position vector $\mathbf{X}$ in the reference configuration and by its position vector $\mathbf{x} = \chi(\mathbf{X})$ in the deformed configuration. The total deformation gradient tensor can be defined by

$$\boldsymbol{F} = \nabla \boldsymbol{x} \tag{3.1}$$

where ∇ is the gradient operator. For a bi-layered shell element without any shear in cylindrical coordinates the total deformation gradient can be written as $\mathbf{F} = \mathrm{diag}[\lambda_z\, \lambda_\theta\, \lambda_r]$. Noting that λ_z, λ_θ and λ_r are the total stretches in axial, circumferential and radial directions, respectively.
Based on the CMT, we split the strain energy function of the wall, W, into contributions of elastin, collagen fiber families and SMCs. We assumed that SMCs are present only in the media layer and are aligned along the circumferential direction. They have both an active, $(\bullet)_{act}$, and a passive, $(\bullet)_{pas}$, behavior. We modeled the collagen by four fiber families aligned in circumferential, longitudinal and two diagonal directions respectively. We assumed the same strain energy functions for

each constituent in the media and in the adventitia while their mass fraction were different in each layer and even between each collagen fiber family. Assuming Ψ^j, $j \in \{e, m, c_i\}$, is the **strain energy density function per unit mass** of each constituent, the **total strain energy density function per unit reference volume** in the media, W_M, and in the adventitia, W_A, layers were respectively calculated by

$$W_M = \varrho_R(t)(\phi_M^e \Psi^e + \phi_M^m(\Psi_{pas}^m + \Psi_{act}^m) + \sum_{i=1}^{4} \phi_M^{c_i} \Psi^{c_i}) \tag{3.2}$$

$$W_A = \varrho_R(t)(\phi_A^e \Psi^e + \phi_A^m(\Psi_{pas}^m + \Psi_{act}^m) + \sum_{i=1}^{4} \phi_A^{c_i} \Psi^{c_i}) \tag{3.3}$$

where $\varrho_R(t)$ is the total density and ϕ_M^j and ϕ_A^j denote mass fractions of each jth constituent in the media and in the adventitia, respectively. For each component, we assumed a strain energy density function to represent the corresponding hyperelastic behavior. We modeled the elastin behavior with a Neo-Hookean hyperelastic model as in [65], [79]

$$\Psi^e = \frac{C^e}{2}\left(\lambda_z^{e2} + \lambda_\theta^{e2} + \lambda_r^{e2} - 3\right) \tag{3.4}$$

where C^e is a stress-like material parameter while λ_z^e, λ_θ^e and λ_r^e are stretches of the elastin component in axial, circumferential and radial directions, respectively. In the CMT, these stretches are calculated by considering the elastin deposition stretch, $\boldsymbol{G}_h^e = \text{diag}[G_{hz}^e\, G_{h\theta}^e\, G_{hr}^e]$, such as [65], [79]

$$\lambda_z^e = G_{hz}^e \lambda_z \ , \ \lambda_\theta^e = G_{h\theta}^e \lambda_\theta \ , \ \lambda_r^e = G_{hr}^e \lambda_r \tag{3.5}$$

we modeled the Collagen fiber families by an anisotropic exponential function [50] such as

$$\Psi^{c_i} = \frac{C_1^{c_i}}{4C_2^{c_i}}\left(\exp(C_2^{c_i}(\lambda_e^{c_i 2} - 1)^2) - 1\right) \tag{3.6}$$

where $C_1^{c_i}$ and $C_2^{c_i}$ are a stress–like and dimensionless material parameters, respectively, while $\lambda_e^{c_i}$ is the elastic contribution of the collagen fiber stretch obtained as

$$\lambda_e^{c_i} = \frac{\lambda^{c_i}}{\lambda_r^{c_i}} \text{ with } \lambda^{c_i} = G_h^{c_i}\sqrt{\lambda_z^2 \cos^2\alpha^{c_i} + \lambda_\theta^2 \sin^2\alpha^{c_i}} \tag{3.7}$$

where λ^{c_i}, $\lambda_r^{c_i}$, $G_h^{c_i}$ and α^{c_i} are the total stretch, remodeling stretch (cf. 4.1), deposition stretches and orientation angles of the different collagen fiber families, respectively. We also modeled the passive behavior of SMCs by an anisotropic exponential function [50] such as

$$\Psi_{pas}^m = \frac{C_1^m}{4C_2^m}\left(\exp(C_2^m(\lambda_e^{m2} - 1)^2) - 1\right) \tag{3.8}$$

while we modeled its active behavior according to Braeu et al [27],

$$\Psi_{act}^m = \frac{\sigma_{actmax}}{\varrho_R(0)}\left(\lambda_{act} + \frac{(\lambda_{max}^m - \lambda_{act})^3}{3(\lambda_{max}^m - \lambda_0^m)^2}\right) \tag{3.9}$$

where C_1^m and C_2^m are stress–like and dimension–less material parameters, respectively, σ_{actmax} is the maximal active Cauchy stress, λ_{act} is the active stretch in the fiber direction, λ_0^m and λ_{max}^m are the zero and maximum active stretches and $\varrho_R(0)$ denotes the total mixture density in the reference configuration; λ_e^m is the elastic contribution of SMCs calculated such as

$$\lambda_e^m = \frac{\lambda^m}{\lambda_r^m} \text{ with } \lambda^m = G_h^m \sqrt{\lambda_z^2 \cos^2 \alpha^m + \lambda_\theta^2 \sin^2 \alpha^m} \tag{3.10}$$

where λ^m, λ_r^m and G_h^m are the total stretch, remodeling stretch (cf. 4.1), deposition stretch and orientation angle of SMCs, respectively.
Given the strain energy function, the second Piola-Kirchoff stress tensor and the fourth order elasticity tensor of the mixture were obtained as

$$\boldsymbol{S} = 2\frac{\partial W}{\partial \boldsymbol{C}} = \boldsymbol{S}^e + \boldsymbol{S}_{pas}^m + \boldsymbol{S}_{act}^m + \sum_{i=1}^{4} \boldsymbol{S}^{c_i} \tag{3.11}$$

$$\mathbb{C} = 2\frac{\partial \boldsymbol{S}}{\partial \boldsymbol{C}} = \mathbb{C}^e + \mathbb{C}_{pas}^m + \mathbb{C}_{act}^m + \sum_{i=1}^{4} \mathbb{C}^{c_i} \tag{3.12}$$

where we included the penalty term of incompressibility into the expressions of stress and elasticity tensor of elastin. We considered a bi-layer arterial wall assuming that the media is mainly occupied by elastin and SMCs while the adventitia is mainly composed of collagen fibers.

3.4.2 Growth and remodeling

Similarly to classical G&R studies [23], [24], we split the total deformation gradient of each constituent into an elastic $\boldsymbol{F}_e^j$ and an inelastic $\boldsymbol{F}_{gr}^j$ contribution such as

$$\boldsymbol{F}^j = \boldsymbol{F}_e^j \boldsymbol{F}_{gr}^j. \tag{3.13}$$

The idea of the homogenized CMT is to pool all the sequential mass additions within one single constituent using temporal homogenization. To do so, three assumptions are made: (i) the mechanical properties are changed by G&R, (ii) survival mass (mass turnover) functions are exponential and (iii) inelastic deformations, $\boldsymbol{F}_{gr}^j = \boldsymbol{F}_g^j \boldsymbol{F}_r^j$, are in turn decomposed into growth-related, $\boldsymbol{F}_g^j$, and remodeling-related (turnover-related), $\boldsymbol{F}_r^j$, contributions. In this model, a single average inelastic deformation gradient $\boldsymbol{F}_{gr}^j$ is defined. The growth-based part captures the changes of the differential volume element due to mass variations. The model can handle isotropic or anisotropic growth, the latter being more relevant for arteries and manifesting with thickening or thinning effects [80].
We assumed that G&R is a stress mediated process which tends to minimize deviations between the current stresses and a reference stress metrics named homeostatic stress. Therefore, the rate of mass degradation and deposition at time t for the jth constituent were expressed as

$$\dot{\varrho}_R^j(t) = \varrho_R^j(t) k_\sigma^j \frac{\sigma_t^j - \sigma_h^j}{\sigma_h^j} + \dot{D}^j \tag{3.14}$$

where $\varrho_R^j(t)$ is the mass density of the jth constituent at time t and k_σ^j denotes a growth parameter while σ_t^j and σ_h^j ($\sigma_h^j = (\boldsymbol{a}_0^j \otimes \boldsymbol{a}_0^j) : \boldsymbol{\sigma}_h^j$) are the current and homeostatic stresses, respectively. $\dot{D}^j$ includes any additional mass deposition or degradation governed by non-mechanical effects (for instance effect of a drug). A more general form of this equation is presented by Braeu et al [27], using a tensorial representation and possibly considering wall shear stress stimuli [25], [81]. The wall shear stress effects induced by the blood flow are neglected in our work here. Therefore, due to continuous mass deposition and removal, the traction–free configuration changed during G&R, even if there is a balance between mass deposition and removal ($\dot{\varrho}_R^j(t) = 0$). Mass deposition or removal occurred with a prestress which is different from the current stress at which mass is removed. Altogether this leads to changes of tissue microstructure referred as remodeling. Therefore, assuming that remodeling occurs at a constant volume, the evolution of the inelastic remodeling deformation gradient of the jth constituent at time t was expressed such as [24]

$$\left(\frac{\dot{\varrho}_R^j(t)}{\varrho_R^j(t)} + \frac{1}{T^j}\right)\left(\boldsymbol{S}^j(t) - \boldsymbol{S}_{pre}^j\right) = \left(\frac{\partial \boldsymbol{S}^j}{\partial \boldsymbol{C}_e^j} : \left(\boldsymbol{C}_e^j \boldsymbol{L}_r^j + \boldsymbol{L}_r^{jT} \boldsymbol{C}_e^j\right)\right) \tag{3.15}$$

where $\boldsymbol{L}_r^j = \dot{\boldsymbol{F}}_r^j \boldsymbol{F}_r^{j-1}$ and $\boldsymbol{S}^j$ is the second Piola–Kirchhoff while subscript "pre" indicates prestress. $\boldsymbol{L}_r^j$ denotes the remodeling velocity gradient and T^j is the average turnover time during which old mass increment is degraded and replaced by a new mass increment. Prestress σ_{pre}^i is equal to the homeostatic stress σ_h^i, according to proposition 1 from Cyron and Humphrey [8]. On the other hand, the growth deformation gradient captures any local change of volume induced by mass variations of each constituent. Following Braeu et al [27], we assumed that all components of the mixture shared the same growth deformation gradient: $\boldsymbol{F}_g^j = \boldsymbol{F}_g$ obtained by summing the growth rate of each constituent: $\dot{\boldsymbol{G}} = \sum_{j=1}^n \dot{\boldsymbol{G}}^j$, where n is number of constituents in the mixture. Following [27] the mass density in the current spatial configuration was related to the mass density in the reference configuration by

$$\det(\boldsymbol{F}_g) = \frac{\varrho_R(t)}{\varrho_R(0)} \tag{3.16}$$

Differentiating both sides and recalling that $J = \det(\boldsymbol{F}) = \det(\boldsymbol{F}_e^j)\det(\boldsymbol{F}_r^j)\det(\boldsymbol{F}_g^j) = \det(\boldsymbol{F}_g^j)$, after some arrangement the rate of the growth deformation gradient for the jth constituent was obtained by

$$\dot{\boldsymbol{G}}^j = \frac{\dot{\varrho}_R^j(t)}{\varrho_R(t)\boldsymbol{F}_g^{j-T} : \boldsymbol{B}^j}\boldsymbol{B}^j \tag{3.17}$$

where the second-order tensor $\boldsymbol{B}^j$ defines the growth direction and it is normalized such that $tr(\boldsymbol{B}^j) = 1$.

Note here that $\boldsymbol{G}^j$ is the growth rate tensor and it should not be confused with $\boldsymbol{G}_h^j$ which is the deposition stretch tensor.

Assuming anisotropic growth normal to the arterial wall and to fibers (thinning

or thickening effects, $\boldsymbol{B}^j = \boldsymbol{a}_0^\perp \otimes \boldsymbol{a}_0^\perp$) and considering the through-thickness homogenization ($J = \lambda_z \lambda_\theta \lambda_r$, with $\lambda_r = \frac{h}{h_0}$), the current thickness (h) was derived as

$$h = \frac{h_0}{\lambda_\theta \lambda_z} \frac{\varrho_R(t)}{\varrho_R(0)} \tag{3.18}$$

where h_0 is the initial thickness, λ_θ and λ_z are the circumferential and axial stretches, $\varrho_R(t)$ and $\varrho_R(0)$ are the time density and the initial density. Also we simplified the equations for remodeling 3.15 and growth 3.17 to the following expressions

$$\dot{\lambda}_r^j = \left(\frac{\dot{\varrho}_R^j(t)}{\varrho_R^j(t)} + \frac{1}{T^j} \right) \frac{\lambda^j}{(\lambda_e^j)^2} \frac{1}{\varrho_R(t)\phi^j} \left(\frac{\partial \Psi^j}{\partial \lambda_e^j} + \lambda_e^j \frac{\partial^2 \Psi^j}{(\partial \lambda_e^j)^2} \right)^{-1} \times \left(\sigma_t^j - \sigma_{pre}^j \right) \tag{3.19}$$

$$\dot{G}_r^j = \frac{\dot{\varrho}_R^j(t)}{\varrho_R(t)} \tag{3.20}$$

where the remodeling stretch (λ_r^j) was along the fiber direction ($\boldsymbol{a}_0^j$), growth ($\dot{\boldsymbol{G}}^j$) is along the thickness direction ($\boldsymbol{e}_r$), and σ^j is the Cauchy stress. Then, we wrote the following expressions for inelastic deformation gradients $\boldsymbol{F}_r^j$ and $\boldsymbol{F}_g^j$,

$$\boldsymbol{F}_r^j = \lambda_r^j \boldsymbol{a}_0^j \otimes \boldsymbol{a}_0^j + \frac{1}{\sqrt{\lambda_r^j}} (\boldsymbol{I} - \boldsymbol{a}_0^j \otimes \boldsymbol{a}_0^j) \tag{3.21}$$

$$\boldsymbol{F}_g^j = \boldsymbol{I} + \frac{\varrho_R(t)}{\varrho_R(0)} \boldsymbol{a}_0^\perp \otimes \boldsymbol{a}_0^\perp - \boldsymbol{a}_0^\perp \otimes \boldsymbol{a}_0^\perp \tag{3.22}$$

where $\boldsymbol{I}$ is the identity second order tensor, $\boldsymbol{a}_0^j$ are vectors of the fiber directions and $\boldsymbol{a}_0^{j\perp}$ are the vectors normal to the fibers (thickness direction). Finally, the inelastic deformation gradient was derived from 3.21 and 3.22, yielding

$$\boldsymbol{F}_{gr}^j = \lambda_r^j \boldsymbol{a}_0^j \otimes \boldsymbol{a}_0^j + \frac{1}{\sqrt{\lambda_r^j}} (\boldsymbol{I} - \boldsymbol{a}_0^j \otimes \boldsymbol{a}_0^j + \frac{\varrho_R(t)}{\varrho_R(0)} \boldsymbol{a}_0^\perp \otimes \boldsymbol{a}_0^\perp - \boldsymbol{a}_0^\perp \otimes \boldsymbol{a}_0^\perp) \Longrightarrow \boldsymbol{F}_{gr}^j \cdot \boldsymbol{a}_0^j = \lambda_r^j \boldsymbol{a}_0^j \tag{3.23}$$

To calculate the G&R deformation gradient over time we solved the system composed of Eqs. 3.14, 3.15 and 3.17 by performing explicit temporal integration. It was assumed that elastin cannot be produced during adulthood, it even undergoes a slow degradation with a half–life time of several decades. Therefore, elastin evolution was basically calculated based on its degradation rate. Moreover, it was assumed that SMCs do not experience any mass turnover, however they undergo remodeling due to collagen and elastin mass evolutions.

3.4.3 Adaptation to axisymmetric shell formulation

In the current work, we implemented the G&R model described in the previous subsection in axisymmetric shell elements. This subsection introduces the axisymmetric shell element with an overview of its kinematics and of the principle of virtual work (for more details we suggest [55], [68]).

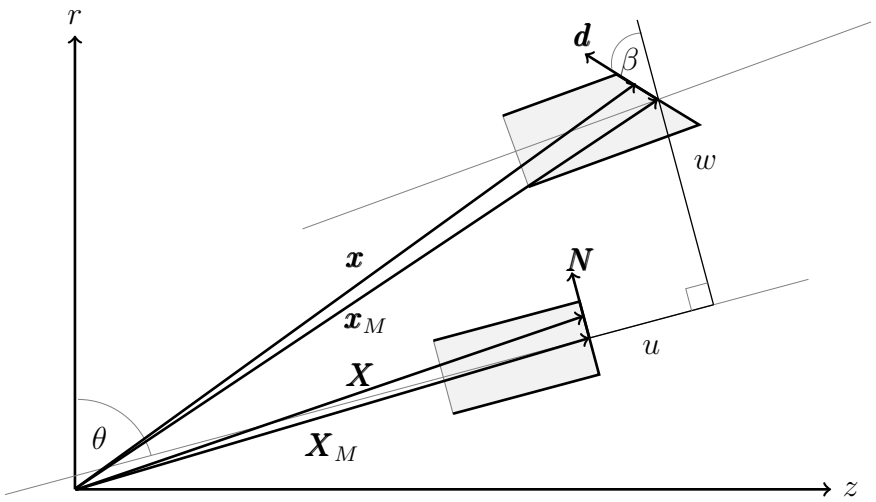

Figure 3.1 – Schematics representing the kinematic variables of the shell axisymmetric element

Consistently with the kinematics of axisymmetric shell elements, we assumed that coordinates of a material point in the reference configuraton, denoted $\boldsymbol{X}$ in the shell space, can be expressed by the position of the shell mid–surface, $\boldsymbol{X}_M$, and by their local thickness parametric coordinate ξ as

$$\boldsymbol{X} = \underbrace{\begin{bmatrix} Z \\ R \end{bmatrix}}_{\boldsymbol{X}_M} + \xi \underbrace{\begin{bmatrix} -\cos\theta \\ \sin\theta \end{bmatrix}}_{\boldsymbol{N}} \tag{3.24}$$

where $\boldsymbol{N}$ is a unit normal vector, Fig. 3.1. Similarly for the position in the deformed configuration, denoted $\boldsymbol{x}$, it can be written

$$\boldsymbol{x} = \underbrace{\begin{bmatrix} Z + u\sin\theta - w\cos\theta \\ R + u\cos\theta + w\sin\theta \end{bmatrix}}_{\boldsymbol{x}_M} + \xi \underbrace{\begin{bmatrix} \cos(\theta-\beta) \\ \sin(\theta-\beta) \end{bmatrix}}_{\boldsymbol{d}} \tag{3.25}$$

with $\boldsymbol{x}_M$ being the position of the deformed shell mid–surface and $\boldsymbol{d}$ being a vector describing the rotation of the cross section with respect to the mid–surface. Assuming plane stress, the deformation gradient is reduced to

$$\boldsymbol{F} = \begin{bmatrix} \lambda_z & 0 \\ 0 & \lambda_\theta \end{bmatrix} \tag{3.26}$$

With the aim to solve the mechanical equilibrium by the principle of virtual work, the work due to the intenal and external forces is developed here. The internal virtual work is split along the shell thickness to define different properties for the media and the adventitia layers (bi-layered arterial wall). Let h_0 and h^* be the total wall thickness and the media thickness, respectively. ξ being the radial position, inequalities $-h_0/2 \leq \xi \leq h^*$ and $h^* \leq \xi \leq h_0/2$ define the media and

the adventitia layers, respectively. The radial integral was derived by applying the principle of virtual work such as

$$\delta\mathcal{W}_{int}(\boldsymbol{u},\delta\boldsymbol{u}) = 2\pi\int_L\left(\int_{-h_0/2}^{h^*}\boldsymbol{S}\cdot\delta\boldsymbol{E}Rd\xi + \int_{h^*}^{h_0/2}\boldsymbol{S}\cdot\delta\boldsymbol{E}Rd\xi + \epsilon h_0 E_{zr}\delta E_{zr}R\right)ds \tag{3.27}$$

Then it is linearized as

$$\begin{aligned}\Delta\delta\mathcal{W}_{int}(\boldsymbol{u},\delta\boldsymbol{u})\cdot\Delta\boldsymbol{u} &= 2\pi\int_L\left(\int_{-h_0/2}^{h^*}\left(\delta\boldsymbol{E}\cdot\mathbb{C}\cdot\Delta\boldsymbol{E}+\boldsymbol{S}\cdot\Delta\delta\boldsymbol{E}\right)Rd\xi\right.\\ &+ \int_{h^*}^{h_0/2}\left(\delta\boldsymbol{E}\cdot\mathbb{C}\cdot\Delta\boldsymbol{E}+\boldsymbol{S}\cdot\Delta\delta\boldsymbol{E}\right)Rd\xi\\ &+ \left.\epsilon h_0\left(\delta E_{zr}\Delta E_{zr}+E_{zr}\Delta\delta E_{zr}\right)R\right)ds\end{aligned} \tag{3.28}$$

where ϵ is a penalty related to the shear strain E_{zr} constraining the rotation of the cross section [71].
The external virtual work comes from a follower load. In this case the load could be an internal pressure due to the blood in the artery or a force due to the stent pushing onto the artery.

$$\delta\mathcal{W}_{ext}(\boldsymbol{u},\delta\boldsymbol{u}) = 2\pi\int_{-1}^{+1}\delta\boldsymbol{u}\cdot\hat{p}(-\boldsymbol{e}_\theta\times\boldsymbol{x}_{,\xi})rd\eta \tag{3.29}$$

Then it is linearized as

$$\Delta\delta\mathcal{W}_{ext}(\boldsymbol{u},\delta\boldsymbol{u})\cdot\Delta\boldsymbol{u} = 2\pi\int_{-1}^{+1}\delta\boldsymbol{u}\cdot\{\Delta\hat{p}(-\boldsymbol{e}_\theta\times\boldsymbol{x}_{,\xi})r-\hat{p}(\boldsymbol{e}_\theta\times\Delta\boldsymbol{u}_{,\xi})r-\hat{p}(\boldsymbol{e}_\theta\times\boldsymbol{x}_{,\xi})\Delta w\}\,d\eta \tag{3.30}$$

where $\hat{p}$ is the load due to an internal pressure $\hat{p}=P_i$ or a stent (Fig. 2) $\hat{p}=C_N\delta$. $\Delta\hat{p}$ is the variation of the load along the element, $\Delta\hat{p}=0$ for blood pressure or $\Delta\hat{p}=-C_N\Delta w$ for the stent. In equation 3.30 we consider the term $\Delta\hat{p}$ for possible variations of the load, in order to incorporate the force of the stent onto the arterial wall.
Finally, the Newton's method is used to solve the mechanical equilibrium, yielding the following system

$$(\Delta\delta\mathcal{W}_{int}-\Delta\delta\mathcal{W}_{ext})\cdot\Delta\boldsymbol{u}+(\delta\mathcal{W}_{int}-\delta\mathcal{W}_{ext})=0 \tag{3.31}$$

Following Voigt's notation [55] we reduced the order of stress, strain and elasticity tensors as below

$$\boldsymbol{S}=\begin{bmatrix}S_z\\S_\theta\end{bmatrix},\ \boldsymbol{E}=\begin{bmatrix}E_z\\E_\theta\end{bmatrix},\ \mathbb{C}=\begin{bmatrix}C_z & C_{z\theta}\\C_{\theta z} & C_\theta\end{bmatrix} \tag{3.32}$$

3.4.4 Finite element implementation

The model was implemented in an in-house code for axisymmetric shell elements (section 2.3) using FORTRAN programming language along with implementation

of the homogenized CMT of G&R. A simplified arterial model was defined as a shell cylinder (thin-walled) of length $L = 100[mm]$, mean radius $R = 10[mm]$ and wall thickness $h_0 = 1.41[mm]$. The cylinder was discretized with 2-node shell elements in 35 elements along the axial direction. A luminal reference pressure $P_i = 100[mm]$ was assigned. In some cases we considered a stent into the artery with length $L_s = 40[mm]$, as shown in Fig. 2. The long time term problem was solved by a forward Euler time integration scheme with a time step of 30 days. The spatial and time discretization was chosen based in a convergence study.

3.5 Numerical experiments

3.5.1 Comparison with an existing G&R model

First we considered an axisymmetric single-layer cylindrical shell wall as previously studied by Cyron et al [24]. Using the algorithm presented by Mousavi and Avril [65], the reference configuration was defined in such a way to ensure that the circumferential component of elastin deposition stretch was mechanically in equilibrium with the reference pressure. Following the first example of Braeu et al [27], the arterial wall underwent elastin degradation varying temporally and spatially across the arterial wall with the following rate:

$$\dot{D}^e(\boldsymbol{X},t) = -\frac{\varrho^e_R(\boldsymbol{X},t)}{T^e} - \frac{D_{max}}{t_{dam}}\varrho^e_R(\boldsymbol{X},0)e^{-0.5\left(\frac{Z}{L_{dam}}\right)^2-\frac{t}{t_{dam}}} \tag{3.33}$$

where t_{dam} and L_{dam} are the temporal and the spatial damage distribution parameters, respectively. Z is the material position in the axial direction of the cylinder and D_{max} is the maximum damage. The first term in Eq. 3.33 refers to a normal elastin degradation by age while the second one is related to a sudden and abnormal local damage starting at $t = 0$ with maximum value at the center of the cylinder ($Z = 0$) and fading at $Z = \frac{L}{2}$. The results obtained with the present model were compared with the corresponding results of Cyron et al [24] for different growth parameters, $k^{c_j}_\sigma$. Material parameters are listed in Table 3.2.

3.5.2 Applications of the model

After verification of the model on a single layer arterial wall, three different G&R cases were considered for a bi-layered cylindrical artery:

1. a benchmark case was considered first with a regional and sharp degradation rate of elastin in the arterial wall to develop an aneurysm (case I).

2. a stent of length L_s was deployed in the artery as shown in Fig. 3.2 and the induced G&R undergone by the artery was predicted (case II).

3. after developing an aneurysm for several months due to elastin degradation (as in the first case), the implantation of a stent graft of length L_s was

modeled and the induced G&R undergone by the artery was predicted (case III).

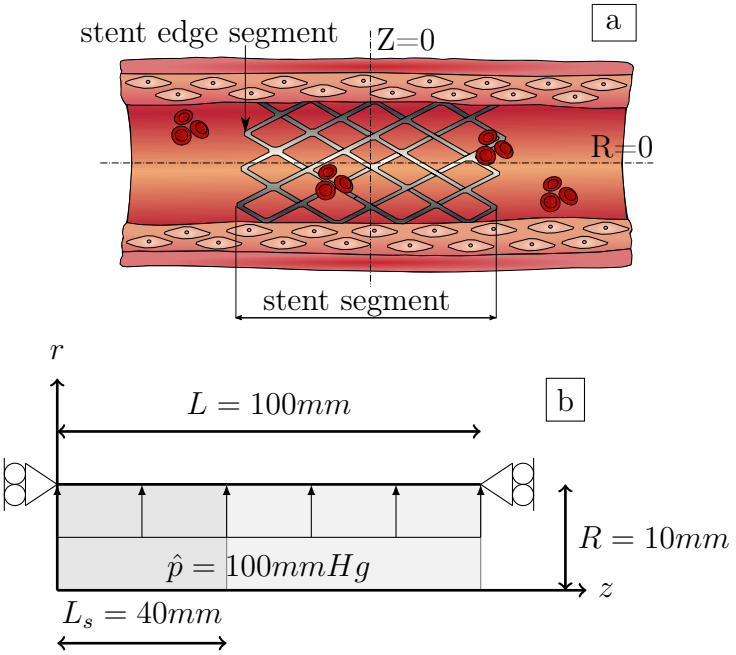

FIGURE 3.2 – Geometrical characteristics of the artery model with symmetric conditions at $Z = 0$ and $Z = L$. L, R, L_s and $\hat{p}$ denote the arterial length, arterial radius, stent length and the internal pressure, respectively. a: Schematic representation of a real stent deployed in an artery with its media and adventitia, and the square shows the domain over which the simulations are performed (assuming symmetries). b: Simple geometrical model and its boundary conditions in a cylindrical coordinate system.

The geometrical characteristics and boundary conditions of the different cases are shown in Fig. 3.2 and material parameters are summarized in Table 3.2. For each case, we performed different sensitivity analyses on parameters such as the effect of the G&R rate, the penalty in the shell element formulation, the media thickness, the stent over-sizing ratio (ratio between the radius of the stent at equilibrium stress-free conditions and the radius of the artery just before stent implantation) and the normal and tangential friction coefficient between the stent and the arterial wall. Those parameters are reported in Table 3.1.

3.6 Results

3.6.1 Comparison with an existing G&R model

Aneurysm growth predicted by our model was compared against the corresponding results from Cyron et al [24] in Fig. 3.3. As expected, the single-layer cylindrical artery underwent excessive and unstable dilatation for small growth parameters

Parameter	Values	Case
Gain parameter	$\{0.01; 0.02; 0.03; 0.04\}$	① ② ③
Over-sizing	$\{5\%; 10\%; 15\%; 20\%\}$	② ③
Media thickness ratio	$\{0.15; 0.50; 0.85\}$	① ② ③
Shell penalty	$\{10^5; 10^7; 10^9\}$	① ② ③
Normal Coefficient	$\{25MPa; 50MPa; 75MPa\}$	② ③

Table 3.1 – Sensitivity Analysis

while it recovered its stability after a transient period of growth for larger growth parameters. Elastin loss is responsible for altering the stress field, leading subsequently to the deposition of new collagen fibers. Therefore, stability (large k_σ^c) or instability (small k_σ^c) of the aneurysm growth is governed by the balance between elastin loss and new collagen production.

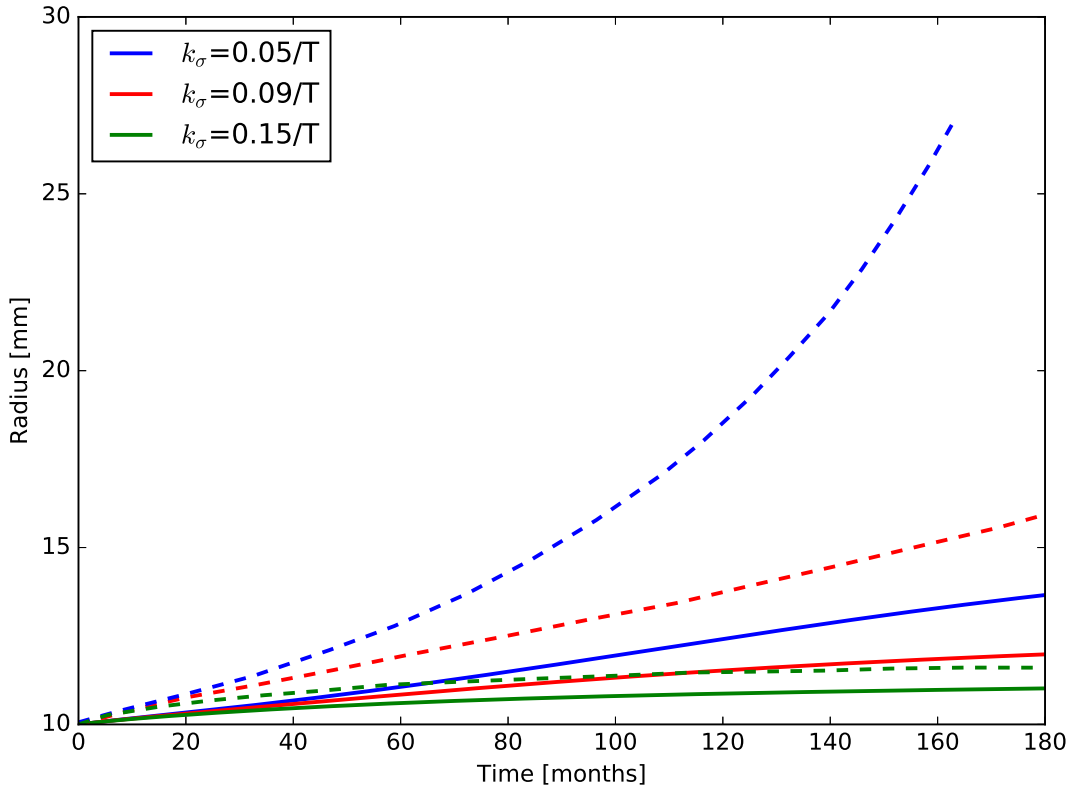

Figure 3.3 – Changes of the radius in the center of arterial wall with maximum elastin degradation rate ($Z = 0$). Solid lines are the results obtained by the shell model and dashed lines are the results of [24].

3.6.2 Case I: benchmark case of a bi-layer arterial wall

The degradation of elastin changed the stiffness at the center ($Z = 0$). From this imbalance, the G&R model predicted an adaptation of the artery by collagen

Material parameters		
C^e	elastin neo-hookean parameter	$72[J/kg]$
$C_1^{c_i}$	Collagen: Fung exponential parameters	$1136[J/kg]$
$C_2^{c_i}$		11.2
C_1^m	Smooth muscle: passive contribution	$15.2[J/kg]$
C_2^m		11.4
S_{actmax}	Smooth muscle: active contribution	$54[kPa]$
λ_0^m		0.8
λ_{max}^m		1.4
λ_{act}		1.0
$\varrho_R(0)$	Total initial density	$1050[kg/m^3]$
Media fraction mass		
ϕ_M^e	Elastin	40%
ϕ_M^m	Smooth muscle	40%
$\phi_M^{c_1}$	Collagen: axial	1%
$\phi_M^{c_4}$	Collagen: circumferential	18%
$\phi_M^{c_2} = \phi_M^{c_3}$	Collagen: diagonal	0.5%
Adventitia fraction mass		
ϕ_A^e	Elastin	5%
ϕ_A^m	Smooth muscle	0%
$\phi_A^{c_1}$	Collagen: axial	10%
$\phi_A^{c_4}$	Collagen: circumferential	5%
$\phi_A^{c_2} = \phi_A^{c_3}$	Collagen: diagonal	40%
Deposition Stretch		
G_{hz}^e	Elastin: axial	1.25
$G_{h\theta}^e$	Elastin: circumferential	1.34
G_h^m	Smooth muscle	1.1
$G_h^{c_i}$	Collagen	1.062
Growth and Remodeling parameters		
$T^{c_i} = T^m$	Collagen/Smooth muscle: turnover time	$101[days]$
T^e	Elastin: mean life time	$101[years]$

Table 3.2 – Material parameters

deposition, until reaching equilibrium again, 3.14. The turnover of collagen was directly proportional to the gain parameter (k_σ^c), so for small gain parameters the arterial wall did not recover homeostasis (stability) and a bulge grew from this instabiblity as shown in Fig. 3.4 and 3.5 a. Herein the simulation with $k_\sigma^c = 0.01/T^c$ lead to a $18.2mm$ radius whereas the simulation with $k_\sigma^c = 0.04/T^c$ lead to a $13.4mm$ radius after 200 months of G&R.

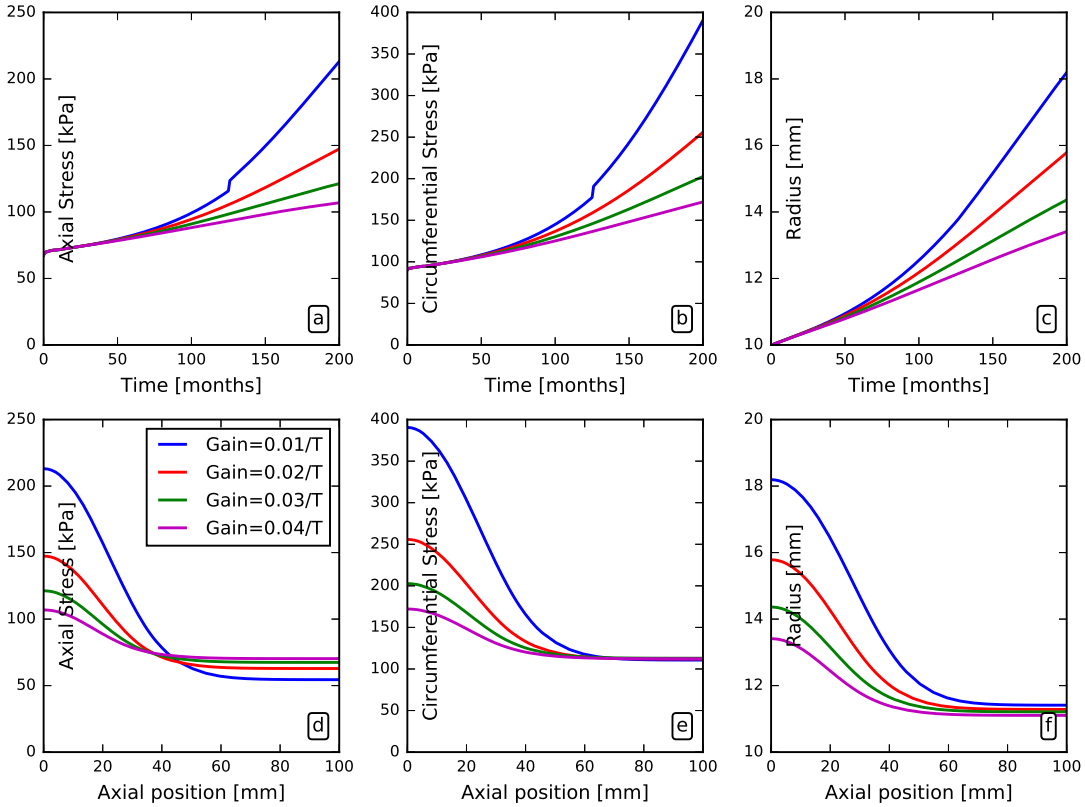

Figure 3.4 – Effects of gain parameters on the aneurysm growth after elastin loss. a, b and c are plotted in the center of the arterial wall ($Z = 0$) versus time. d, e and f are plotted for the last time step (after 199 months) along the arterial axial direction.

The turnover of collagen also depended on the previous amount of collagen as shown in equation 3.14. Then for arteries with less initial collagen, it was difficult to recover homeostasis. A similar effect was observed with arteries having a thick media, see for instance the case with 85% media shown in Fig. 3.5 b. Penalties also had some effect (Fig. 3.5 c) with smaller radius reached for $\epsilon = 1 \times 10^9$ (Fig. B.1 in appendix B).

3.6.3 Case II: adaptation after stent implantation

In this case, the mechanobiological insult applied to the artery was the radial force of a stent. The stent also stretched the artery during its deployment as shown in Fig. 3.6 b, depending on the over-sizing ratio. But the stress decreased quickly

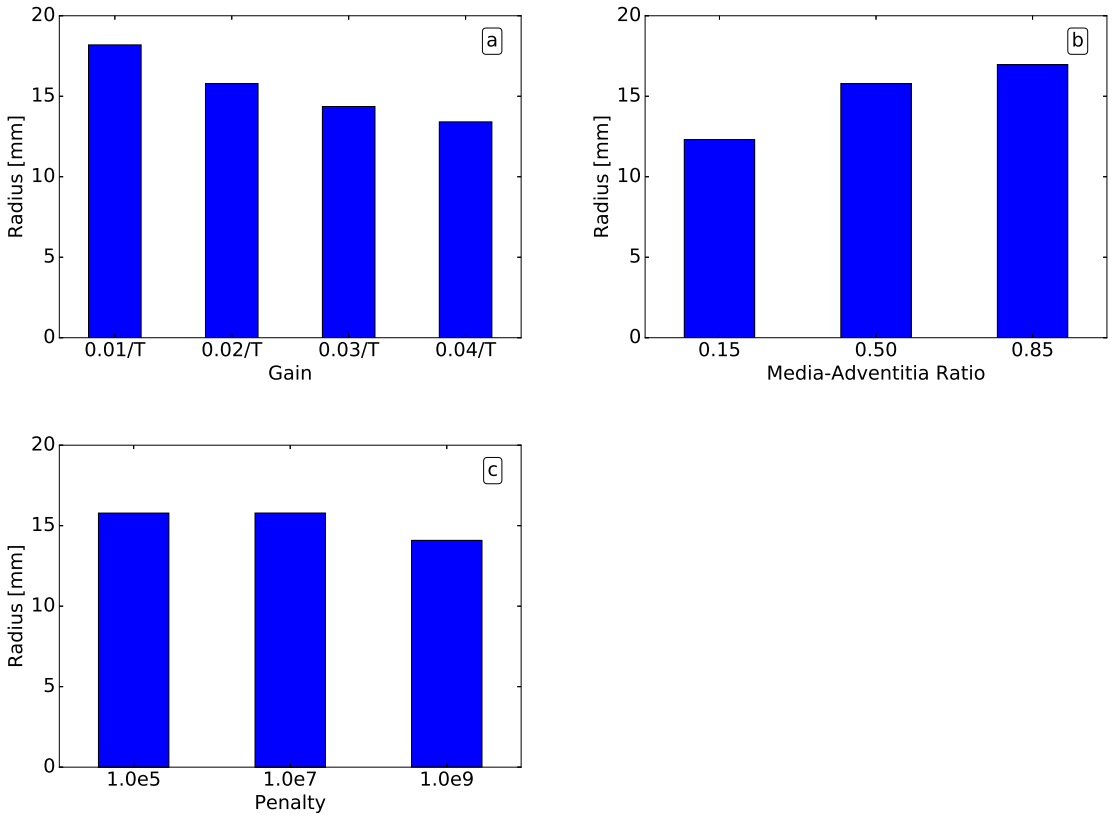

FIGURE 3.5 – Sensitivity analysis on the radius at $Z = 0$ after 200 months of elastin degradation. a: Effect of different gain parameters. b: Effect of the media thickness. c: Effect of the penalty.

during the first 30 months due to G&R, until reaching nearly homeostasis. The time to recover homeostasis was shorter for 5% over-sizing than for 20% over-sizing, $k_\sigma^c = 0.02/T^c$ (Fig. 3.6 c).

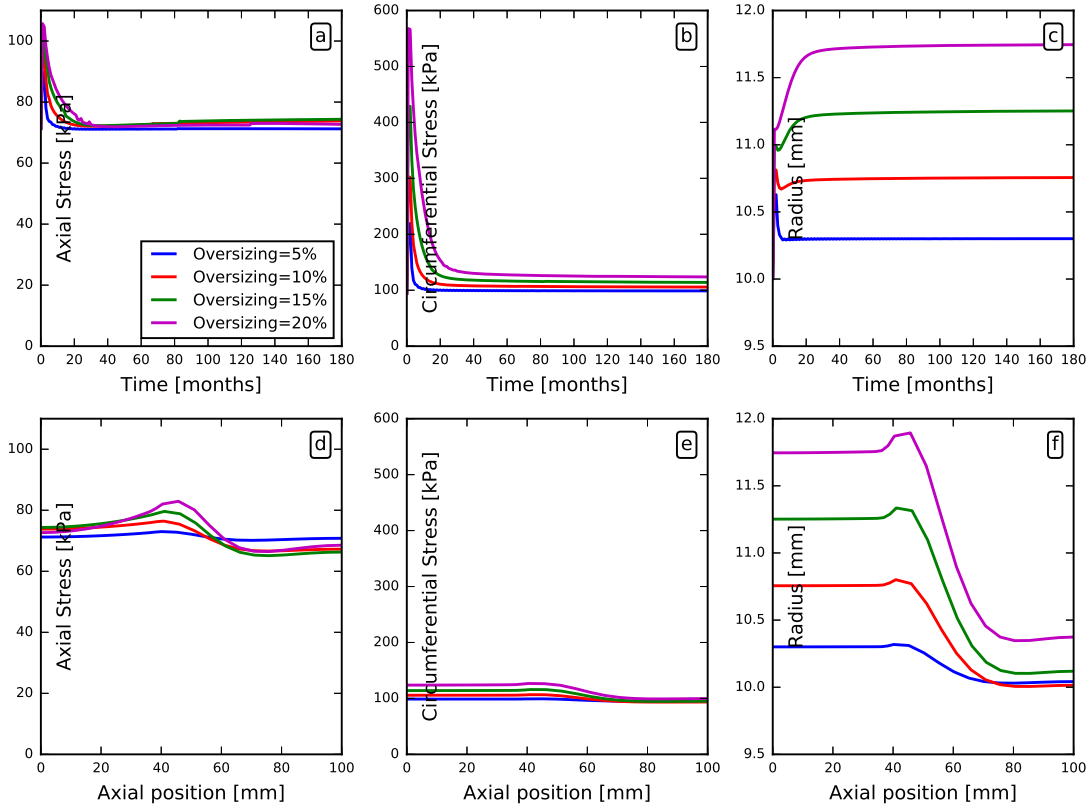

Figure 3.6 – Effect of the stent over-sizing on G&R of the arterial wall. a, b and c are plotted in the center of the arterial wall ($Z = 0$) versus time. d, e and f are plotted for the last time step (after 180 months) along the arterial axial direction.

However, homeostasis was never reached everywhere along the artery. A residual radius increase was systematically obtained at the edge of the stent. This dilatation was bigger for small gain parameters as shown in Fig. B.3 (appendix B), for larger over-sizing ratios, for large stent stiffness (Fig. 3.7) and for thicker media (Fig. B.5).

3.6.4 Case III: stent implantation after several years of aneurysm development G&R

In this case, the central radius obtained after several months of adaptation did not depend either on the gain parameters or on the media thickness (Fig. 3.8 a and b). The stent over-sizing and the stent stiffness had a small but significant effect (Fig. 3.8 c and d).
However the major effects were on the stress obtained in the wall, which depended significantly on the gain parameters as shown in Fig. 3.9 b and c, Fig. B.10. After stent implantation, the artery had a fast adaptation (20 months) in the stent

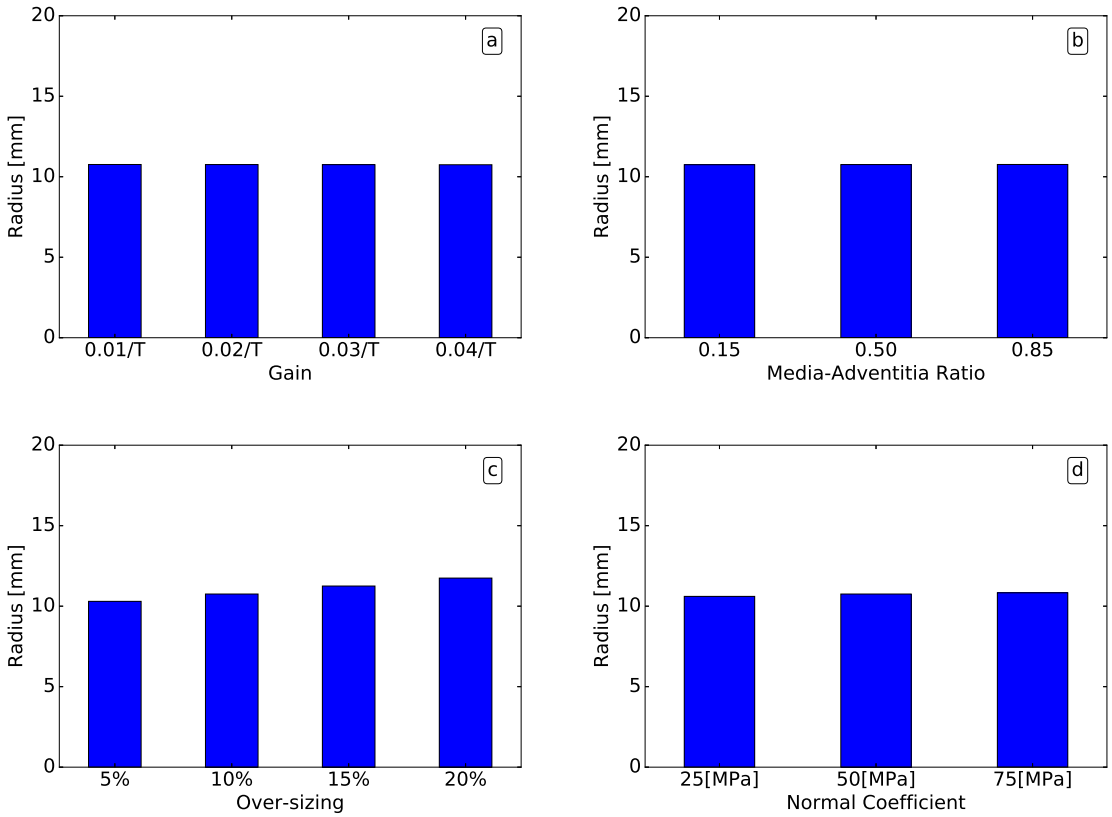

FIGURE 3.7 – Sensitivity analysis on the at $Z = 0$ after 180 months following stent implantation. a: Effect of different gain parameters. b: Effect of the media thickness. c: Effect of stent over-sizing. d: Effect of the stent stiffness.

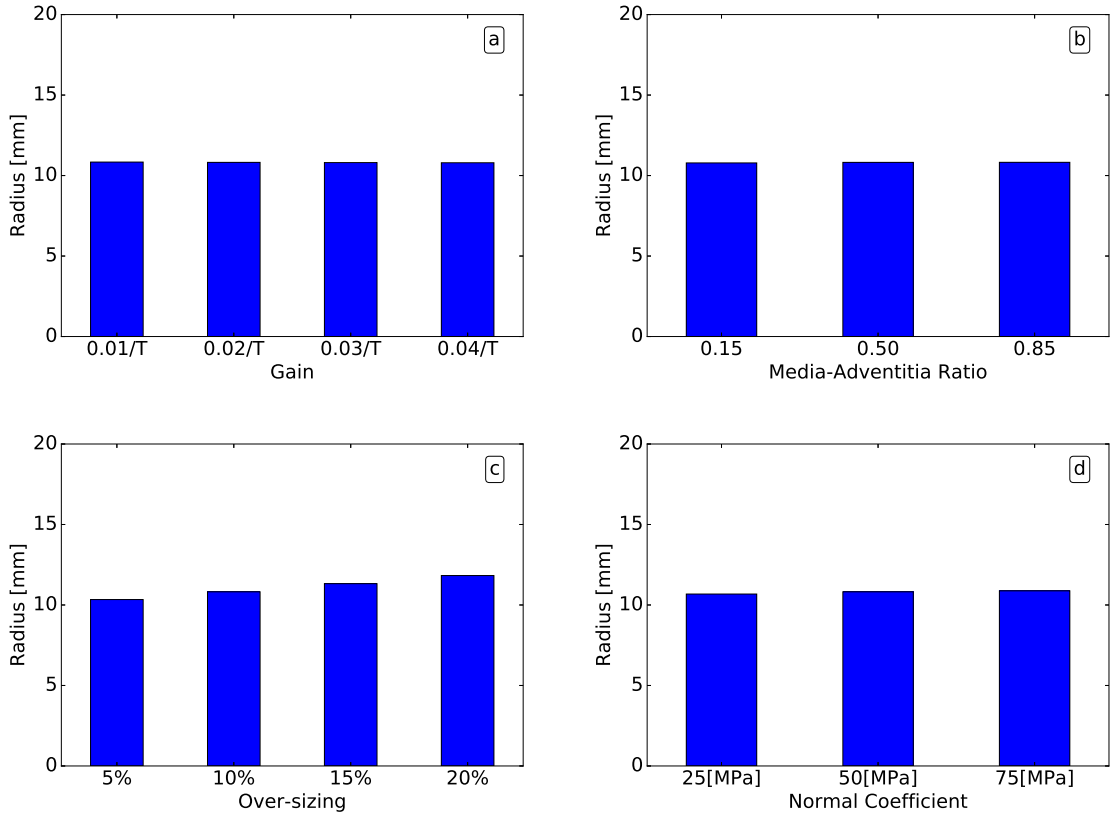

Figure 3.8 – Sensitivity analysis on the radius at $Z = 0$ after 100 months following stent implantation preceded by 80 months of aneurysm growth. a: Effect of different gain parameters. b: Effect of the media thickness. c: Effect of stent over-sizing. d: Effect of the stent stiffness.

segment. As in case II, a residual radius increase developed at the edge of the stent, with significant effects of the gain and of the media thickness (Figs. B.10 and B.12).

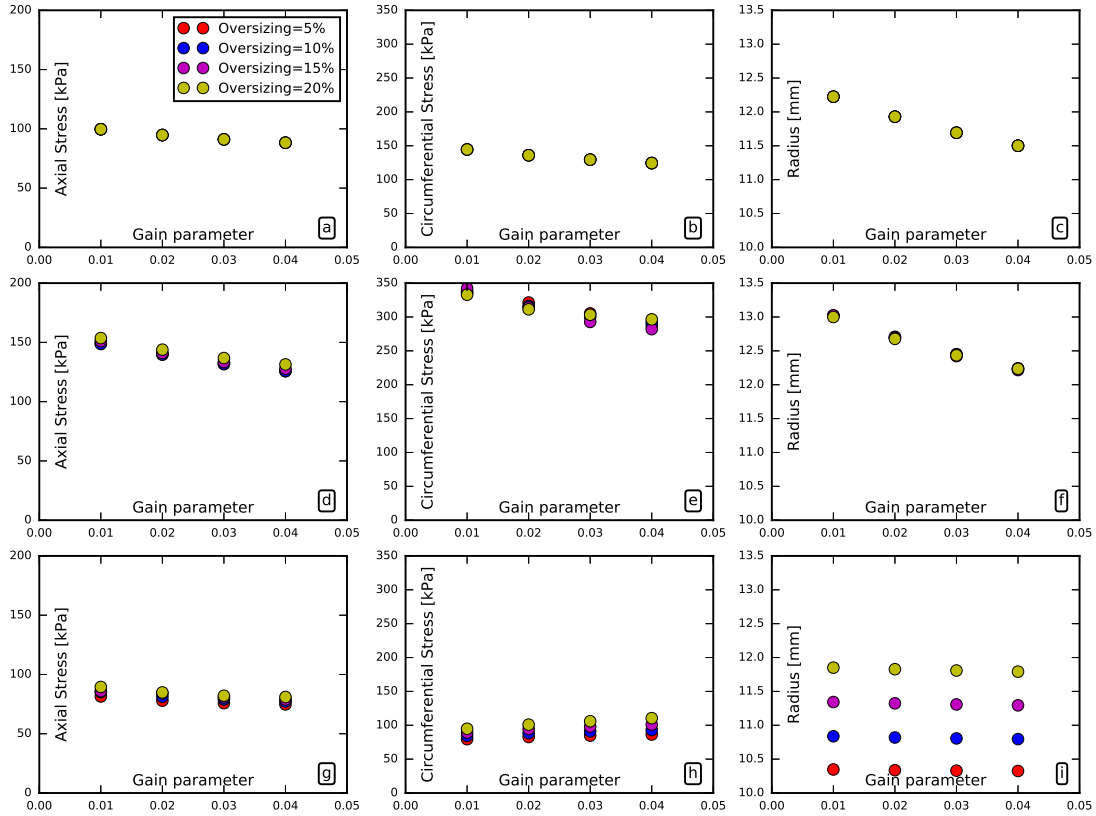

FIGURE 3.9 – Effect of gain parameters and stent over-sizing on the behavior of the arterial wall after stent implantation for an arterial wall undergoing several years of G&R. a, b and c are plotted at the center of the arterial wall ($Z = 0$) versus time. d, e and f are plotted just before stent implantation (t=80 months) along the arterial axial direction. g, h and i are plotted just after stent implantation (t=80 months) along the arterial axial direction. j, k and l are plotted after 100 months following stent implantation along the arterial axial direction.

3.6.5 Computational details

The simulations were performed in a Workstation Dell Precision 3620 (Intel Core i5-7500 3.40GHz, 16.4 GB RAM) with Linux OS. The code was compiled with GNU gfortran compiler on same machine. The time spent by simulation are shown in Table 3.3.

3.7 Discussion

In this work, a new open-source FE model of vascular adaptation, with low computational cost, was introduced and applied to model aneurysm growth and stent

	CPU Time [s]	Clock Time [s]
Case I (200 G&R steps)	0.972	0.977
Case I (180 G&R steps)	0.872	0.877
Case II (180 G&R steps)	0.876	0.885
Case III (80 G&R steps and 100 G&R steps)	1.088	1.108

Table 3.3 – Computational costs time of every simulation.

implantation. We used a layer-specific shell model for the arterial wall. Although previous simulations used membrane models [10], [13], [15], [24], [61] and hexaedra elements [14], [27], shell models appear as very well adapted to modeling the deformations of the aorta and its G&R behavior [13]. Moreover, the ratio between thickness and diameter, which has to be at least of 1 to 10 for a shell, evolves favorably as the aneurysm grows. On top of that, remodeling tends to naturally maintain a uniform stress field across the thickness.

A 2D axisymmetric membrane model has two degrees of freedom (DOF), while a shell model has at least three DOF, depending on the number of extra constraints [55], [68]. In our model, the third DOF is the bending angle where we added the shear strain as an extra constraint. Thanks to the latter, we used a penalty (ϵ) [71] to zero the through-thickness shear strain. Our simulations showed that high penalty coefficients, $\epsilon = 1 \times 10^9$, can affect arterial adaptation and even induce instabilities in G&R due to shear locking effects [55]. We found that the optimal penalty factor was $\epsilon = 1 \times 10^5$, as it permitted a good compromise between shear strains, and displacements. However, after tuning the different parameters, differences remain between our results and the results from Cyron et al [24]. These differences may be attributed to the contribution of the bending behavior in our model, whereas Cyron et al [24] used membrane elements. The main argument for this interpretation is that the differences depend significantly on the penalty factor we use in our model to account for the through-thickness shear stiffness of the shell.

The simplification we have done in the fibre families enforce incompressiblity for elastic and remodeling deformation gradients and reduces the amount of unknowns to be solved at each time step. The assumption of anisotropic growth was shown to be more relevant to model adaptation after elastin degradation [27], [58]. Eriksson [58] even showed that inapropriate growth models could possibly induce counter-expected results such as arterial diameter shrinking.

An interesting feature of our model is the layer-specific implementation which allow to use different mass of constituents (elastin, collagen and SMC) in the mixture by layer and employ the G&R separately. Indeed, there are mechanical differences between the media and the adventitia in the arterial wall due to the amount of constituents in each layer [3]. Then, it was assumed that homeostatic stresses are different in the media and in the adventitia, as they harbor different cell phenotypes (contractile smooth muscle cells in the media and fibroblasts in

the adventitia). For instance, Bellini et al [19] also considered different stress distributions in the media and in the adventitia and showed that their model is well suited to predict the results of open angle experiments. The first bi-layered models of arterial wall in finite elasticity were proposed by Von Maltzahn et al [82] who reported discontinuous circumferential and axial stresses at the interface between the media and the adventitia. Different material parameters for the media and the adventitia permitted to reach nearly uniform, layer-specific circumferential stresses under physiologic conditions of pressure and axial stretch. Latorre and Humphrey [59] proposed a bi-layered model with a time-independent CMT approach. G&R simulations with bi-layered models were performed using time-independent Rachev [83] and time-dependent Taber and Humphrey [20] approach. Both were based on the assumption that circumferential stress should be restored to their normal initial value. Taber and Humphrey [20] suggested that transmural differences in material properties were needed to predict the same opening angles as the ones observed experimentally. Finally this heterogeneity of material properties contributed to reach more uniform transmural distributions of stresses and to account for residual stresses. Herein, we proposed a bi-layered model for time-dependent G&R. We defined layer-specific mass fractions of each constituent. Even if in both layers each constituent has the same strain energy density (per unit mass), each layer has a different strain energy density (per unit volume) due to the different mass fractions.

Following Wilson et al [12] and Braeu et al [27], elastin degradation was assumed to be the mechanobiological insult initiating G&R simulations. Consistently with Wilson et al [61], it appeared that collagen production tends to compensate for the loss of elastin. Results demonstrated that the gain parameter, k_σ, has a key effect on collagen production and expansion rate, (Fig. 3.3) consistently with other studies [10], [24]. Nonetheless, the gain parameter was assumed to be fixed during the evolution of aneurysm in our model, whereas in an actual aneurysms gain may change during aneurysm growth due to pathological changes [15] affecting mechanosensing and mechanotransduction. The simulation showed that $k_\sigma = 0.09$ provides almost a linear growth. With $k_\sigma < 0.05$ the lesion enlarged continuously implying that the stress-mediated collagen turnover was not enough to return to the homeostatic stress. Another important factor in collagen production is the existing mass of collagen [61]. The initial collagen mass related to the initial thickness of adventitia, which has the larger mass fraction of collagen [84]. Simulations showed that only small dilatation were reached in 200 months (16.5 years) for $h_M = 0.15h_0$, whereas large lesions were obtained with $h_M = 0.85h_0$, due to the insufficient collagen turnover.

Aortic aneurysms can be repaired using stent-grafts [32], [85]. The stress distribution obtained after implanting a stent (we neglected the mechanical effect of the graft) in a bi-layer arterial wall has been studied extensively using the finite-element method [86]. However, the further adaptation had never been simulated using the CMT approach. Our results showed that G&R induced an effect on the arterial wall similar to a stress relaxation effect at the long term [24]. This stress

relaxation was dependent on the over-sizing ratio, see Fig. 3.6, with a possible instability occurring at the edge of the stent. The relaxation also affected the radius, see Fig. 3.9(c,f,i) and Fig. 3.6(c). Turnover (gain and existing mass) of collagen had no significant transient effects along the stent segment, see Fig. B.3 and Fig. B.5, but was responsible for the dilatation developed at the stent edge. We also showed in case III that the aneurysm diameter decreased after stent-graft implantation.

Furthermore, clinical evidence suggests the existence of issues after stenting, such as restenosis, stent thrombosis and arterial injuries. Kitahara et al [87] studied the impact of stent oversizing, concluding that aggressive oversizing may not lead to vascular injuries at the stent edge, as arteries with siginificant stent oversizing reach better apposition without increasing the amount of dissection at the stent egde. However, Chamie et al [88] concluded that the overstretching of the arterial wall due to an oversized stent was an important factor of dissection at stent edges. They also observed that the arterial wall responds to the injury through neointimal proliferation and vessel remodeling, then leading to restenosis around the stent. Finally, García-García [89] reported expansive vascular remodeling at the stent edge, which is also in agreement with our model prediction.

Finally, we emphasize that the model considered herein only simulates fusiform aneurysms as proposed by Baek et al [10] and Wilson et al [12]. Other limitations of this work are related to the contact between the artery and the stent, which is simply modeled by springs pushing the shell elements at its nodes. Additionally, intraluminal thrombus [12], [15], which often has an important role in the growth of aortic aneurysm, was neglected in our models. Further extension of our shell formulation to 3D is expected to address these limitations.

3.8 Conclusions

In this work, we implemented a low-cost open-source finite-element 2D axisymmetric shell model (FEM) of the arterial wall for simulating layer-specific growth and remodeling using the homogenized constrained mixture theory. After testing the reliability of the implementation, we used the model to evaluate the long-term mechanobiological adaptation after stent implantation. Two types of regime were found: either the artery recovered its initial homeostatic stress state after some months of adaptation (stable regime), or the artery dilated locally at the edge of the stent without recovering homeostasis (unstable regime). The main results are that the ratio between the media and the adventitia thicknesses and the gain parameters are the major parameters determining the type of adaptation regime undergone by the aorta after stent implantation. It will be essential to estimate their patient-specific values for real patient-specific applications.

Although our model was limited to axisymmetric examples with 2D shell elements, its main advantage was the computational time, which was extremely low, while still capturing the main aspects of G&R. Further extension to 3D geometries of

this shell formulation is expected to address more realistic cases.

Chapter 4

Non-uniform prestretch

Table of contents of the chapter

4.1 Résumé du chapitre en français. . . . 86
4.2 Abstract of the chapter . . . 86
4.3 Introduction. . . . 87
4.4 Materials and methods . . . 88
4.4.1 Background on homogenized constrained mixture mechanics . . 88
4.4.2 Growth and remodeling based on homogenized constrained mixture models . . . 90
4.4.3 Assigning non uniform initial prestretches . . . 90
4.4.3.1 General statements about initial prestretches. . . . 90
4.4.3.2 Assigning $\boldsymbol{F}^l_e(\boldsymbol{X}, t_0)$ in a perfectly cylindrical straight tube . . . 92
4.4.3.3 Assigning $\boldsymbol{F}^l_e(\boldsymbol{X}, t_0)$ in a perfectly toric tube . . . 92
4.4.3.4 Assigning $\boldsymbol{F}^l_e(\boldsymbol{X}, t_0)$ in a patient-specific aortic arch . . 94
4.4.3.5 Time evolutions of $\boldsymbol{F}^j_{gr}(\boldsymbol{X}, t_0)$ . . . 94
4.4.4 Numerical implementation . . . 96
4.4.5 Verification . . . 96
4.4.6 Applications . . . 96
4.4.6.1 Initial insult for G&R . . . 96
4.4.6.2 Idealized ATA model . . . 99
4.4.6.3 Patient-specific ATA model . . . 100
4.5 Results . . . 100
4.5.1 Idealized ATA model . . . 100
4.5.2 Patient-specific ATA model . . . 103
4.6 Discussion. . . . 107
4.7 Conclusions . . . 109

4.1 Résumé du chapitre en français

L'évolution des propriétés mécaniques et structurelles de l'aorte thoracique ascendante est le résultat de processus mécanobiologiques complexes. Dans ce travail, nous relevons certains défis numériques afin d'élaborer des modèles de calcul de ces processus. Pour cela, nous étendons l'état de l'art des modèles de mélange contraint homogénéisé (hCM). Dans ces modèles, des pré-étirements sont appliqués aux constituants du mélange afin d'assurer un équilibre mécanique local au niveau macroscopique, et de maintenir un niveau homéostatique de tension dans les fibres de collagène au niveau microscopique. Bien que les pré-étirements initiaux aient été supposés homogènes dans des tubes droits idéalisés, des distributions de pré-étirement plus élaborées doivent être prises en compte pour les modèles géométriques courbes tels que l'ATA de patients. Par conséquent, nous introduisons des pré-étirements ayant un gradient tridimensionnel à travers la géométrie de l'ATA dans l'état de référence homéostatique. Nous testons différents schémas dans le but de garantir la stabilité des simulations de croissance et de remodelage (G&R) sur des vaisseaux courbes spécifiques aux patients. Dans ces simulations, la progression de l'anévrisme est déclenchée par des changements tissulaires dans les constituants tels que la dégradation massive de l'élastine intramurale. Les résultats montrent que les pré-étirements initiaux ne sont pas seulement critiques pour la stabilité des simulations numériques, mais qu'ils affectent également la réponse G&R. Enfin, nous concluons que les conditions initiales requises pour les simulations G&R doivent être identifiées au niveau local pour garantir des prédictions réalistes de la progression de l'anévrisme, spécifiques au patient.

4.2 Abstract of the chapter

Evolution of mechanical and structural properties in the Ascending Thoracic Aorta (ATA) are the results of complex mechanobiological processes. In this work, we address some numerical challenges in order to elaborate computational models of these processes. For that, we extend the state of the art of Homogenized Constrained Mixture (hCM) models. In these models, prestretches are assigned to the mixed constituents in order to ensure local mechanical equilibrium macroscopically, and to maintain a homeostatic level of tension in collagen fibers microscopically. Although the initial prestretches were assumed as homogeneous in idealized straight tubes, more elaborate prestretch distributions need to be considered for curved geometrical models such as patient-specific ATA. Therefore, we introduce prestretches having a three-dimensional gradient across the ATA geometry in the homeostatic reference state. We test different schemes with the objective to ensure stable growth and remodeling (G&R) simulations on patient-specific curved vessels. In these simulations, aneurysm progression is triggered by tissue changes in the constituents such as mass degradation of intramural elastin. The results show that the initial prestretches are not only critical for the stability of numerical

simulations, but they also affect the G&R response. Eventually, we submit that initial conditions required for G&R simulations need to be identified regionally for ensuring realistic patient-specific predictions of aneurysm progression.

4.3 Introduction

The Ascending Thoracic Aorta (ATA) plays an essential role for the function of the cardiovascular system thanks to the Windkessel effect [33]. Similarly to other biological tissues, the ATA continuously adapts its structure and shape to accommodate aging effects [41] and possible physiopathological changes, which in the long-term can unfortunately lead to diseases such as aneurysms [5].
Such structural changes can be computationally predicted by Growth and Remodeling (G&R) models. These models date back from the mid 1990s when [23] introduced the Kinematics Growth (KG) model, which is based on a multiplicative decomposition of the deformation gradient into elastic and inelastic contributions. Some years after, [22] proposed the Constrained Mixture (CM) model, which is based on the assumption that soft tissues are composite materials. In arteries, the main constituents of this composite material are elastin, collagen and smooth muscle cells (SMCs). Based on CM models, G&R explicitly simulates continuous mass deposition/removal of each constituent. Due to the high implementation efforts and computation resources required by CM models, some authors proposed hybrid models such as the Evolving Recruitment Stretch model [57], [58], the Homogenized Constrained Mixture (hCM) model [17], [27], [28] or the rate-independent pseudoelastic framework [59], [60].
Generally, geometries of organs and tissues that are considered to set-up numerical models are acquired *in vivo* and consequently the reference configuration cannot be assumed as stress-free [19]. A prestretch, *i.e.* a stretch that exists in the reference configuration of the body of interest [49], needs to be introduced. As most G&R computational models rely on the paradigm of tensional homeostasis, which states that a biological system produces and removes mass to reach a target stress metrics [8], [28], the prestretch can contribute significantly to the G&R response of the system. Therefore, inclusion of prestretch is needed in G&R computational models of biological tissues to obtain reasonable predictions of tissue mechanics. In CM models, the prestretch is specific to each constituent [19], [65].
Regional variations of prestretch in G&R models have been rarely investigated as most of previous work about vascular mechanobiology was achieved in quasi-straight patient-specific tubes [15] or in idealized straight arteries representing either the abdominal aorta [12], [16], [25], [26], [69] or brain arteries [10]. Nevertheless, [21] found regionally varying prestretches in a torus –representing an idealized aortic arch– after G&R simulations. More recently, [17] performed G&R simulations in a torus again, and, for the first time ever, in patient-specific ATA geometries. They assigned spatially uniform prestretches for each constituent, named deposition stretches. As uniform prestretches do not guarantee global

equilibrium of the ATA structure, [17] resorted to radial rollers, which were used to assign a supplemental kinematic constraint to each point of the model. Although their G&R simulations showed very realistic predictions of ATA aneurysm progression, the radial rollers represent a limitation as they do not represent a physical reality.
In the current work, we investigate G&R models for patient-specific ATA. As ATA is a curved artery, this makes the task of assigning initial prestretches quite challenging. Previous work on this topic is rather scarce. Therefore, our objective is to find the prestretch conditions permitting G&R simulations in ATA curved geometries without resorting to the radial rollers. In order to accomplish this, we propose to use non-uniform prestretches in order to define the initial homeostatic state within the hCM model.
The manuscript is organized as follows: in section 4.4, we give details about the G&R background, estimation of the prestretch gradient and the numerical implementation of our approach with its respective verification. At the end of section 4.4, in subsection 4.4.6, we describe the numerical tests used to demonstrate the robustness of our G&R implementation. After showing the obtained results in section 4.5, we eventually propose, in section 4.6, a discussion about the significance of prestretches in G&R patient-specific models.

4.4 Materials and methods

4.4.1 Background on homogenized constrained mixture mechanics

Let us consider an unloaded body Ω_R, made of a mixture of several constituents. These constituents are smooth muscle cells (m), extracellular matrix containing collagen fiber families (c_i) and the remaining matrix (l) composed of elastin, fibronectin, laminin, vitronectin and glycosaminoglycans [2], [3]. Each constituent of the mixture is denoted with letter j as in Figure 4.1. When the mixture undergoes a deformation from the reference configuration (Ω_R) to a deformed configuration (Ω_t), all the constituents of the mixture have the same deformation gradient $\boldsymbol{F}$ at a given position. In the hCM model, this deformation gradient is split into an inelastic and an elastic part, both being specific to each constituent. Then, it may be written at any time t,

$$\boldsymbol{F}(\boldsymbol{X},t) = \boldsymbol{F}_e^j(\boldsymbol{X},t)\boldsymbol{F}_{gr}^j(\boldsymbol{X},t), \tag{4.1}$$

where $\boldsymbol{F}_e^j$ is the elastic part of the deformation gradient in the jth constituent and $\boldsymbol{F}_{gr}^j$ is the inelastic part of the deformation gradient in the jth constituent. The stresses, related to the elastic part, satisfy equilibrium equations whereas the inelastic part relates to the permanent deformations resulting from G&R [23], [24], [27] (for more details, see the Appendix C, sections C.1 and C.3).

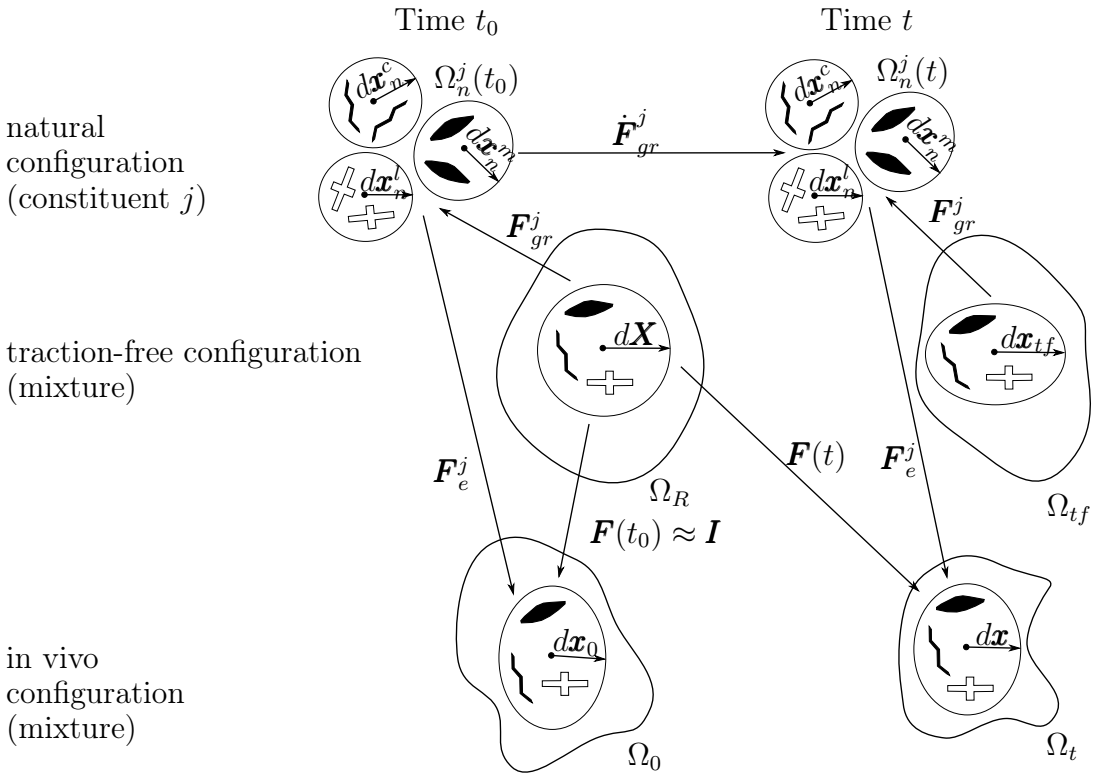

Figure 4.1 – Schematic of the hCM model, showing the different configurations. The reference configuration Ω_R is reconstructed from the actual *in vivo* geometry of the artery. The configuration Ω_0 is obtained by applying the initial boundary conditions and by assigning initial prestretches $[\boldsymbol{F}_{gr}^j]^{-1}$ to each constituent of Ω_R. Ω_R and Ω_0 should be the same as there should be equilibrium between the effects of the initial boundary conditions and the effects of the initial prestretches in the reference configuration. However, both are represented separately in the figure as the initial prestretches providing this equilibrium are found iteratively in our approach. The fictitious traction-free configuration Ω_{tf} is defined as a fictitious configuration at time t, without the effects of boundary conditions and of prestretches. The current configuration Ω_t is obtained after equilibrium between the effects of the current boundary conditions and the effects of the updated prestretches obtained after growth and remodeling. The neighborhood $d\boldsymbol{X}$ of an arbitrary point in Ω_R is related to Ω_t by the transformation $d\boldsymbol{x} = \boldsymbol{F}d\boldsymbol{X}$. At time zero, $\Omega_t = \Omega_0$ and $d\boldsymbol{x}_0 = \boldsymbol{F}d\boldsymbol{X}$. Similarly, the relationship between Ω_t and the natural configuration is $d\boldsymbol{x} = \boldsymbol{F}_e^j d\boldsymbol{x}_n^j$, and the natural configuration and Ω_R are related by the inelastic deformation $d\boldsymbol{x}_n^j = \boldsymbol{F}_{gr}^j d\boldsymbol{X}$ where the inelastic deformation evolves with time. The natural configurations $\Omega_n^i(t)$ can only be defined locally but are not compatible.

The constituents are assumed to be hyperelastic. The strain energy density function W (per unit reference volume) of the mixture of n constituents is defined as

$$W(\boldsymbol{C}) = \sum_{j}^{n} \varrho_R^j \Psi^j(\boldsymbol{C}_e^j) = \sum_{j}^{n} \varrho_R^j \Psi^j \left({\boldsymbol{F}_{gr}^j}^{-T} \boldsymbol{C} \, {\boldsymbol{F}_{gr}^j}^{-1} \right), \tag{4.2}$$

where $\boldsymbol{C} = \boldsymbol{F}^T \boldsymbol{F}$ is the right Cauchy-Green stretch tensor, $\boldsymbol{C}_e^j = \boldsymbol{F}_e^{jT} \boldsymbol{F}_e^j$ is the elastic part of the right Cauchy-Green stretch tensor, Ψ^j is the jth constituent strain energy function (per unit reference mass), which depends only on $\boldsymbol{C}_e^j$, ϱ_R^j is the mass density (per unit reference volume), in the jth constituent. Complete details about of the hyperelastic constitutive models can be found in Appendix C, section C.2. Then we can derive the stress and tangent stiffness tensors, which are needed in our finite-element implementation, and which are written respectively as

$$\boldsymbol{S} = \sum_{j}^{n} \varrho_R^j \frac{\partial \Psi^j(\boldsymbol{C}_e^j)}{\partial \boldsymbol{C}} \text{ and } \mathbb{C} = \sum_{j}^{n} \varrho_R^j \frac{\partial^2 \Psi^j(\boldsymbol{C}_e^j)}{\partial \boldsymbol{C}^2}, \tag{4.3}$$

where $\boldsymbol{S}$ is the second Piola-Kirchhoff and $\mathbb{C}$ is the elasticity tensor for the material stiffness.

4.4.2 Growth and remodeling based on homogenized constrained mixture models

G&R considers temporal evolutions related to the mass changes of the different constituents of the mixture. The idea of the hCM models is to use temporal homogenization in order to pool all the sequential changes within one single inelastic deformation gradient for each constituent (Fig. 4.1). As G&R is a stress mediated process, we assumed that mass can be added or removed to minimize deviations between a convenient stress equivalent in the current state and a reference homeostatic stress value. This requires a continuous update of $\boldsymbol{F}_{gr}^j(\boldsymbol{X}, t)$ in order to account for the changes of tissue microstructure, which are referred as remodeling, and which result from this continuous mass deposition and removal. Indeed, due to the ongoing mass deposition and removal, the natural configuration of each constituent continuously changes during G&R (Fig. 4.1), even when there is a balance between mass deposition and removal ($\dot{\varrho}_R^j = 0$). More details about the numerical implementation of G&R are given in Appendix C, section C.3.

4.4.3 Assigning non uniform initial prestretches

4.4.3.1 General statements about initial prestretches

As shown in Fig. 4.1, we can define the following configurations:

- Ω_R is the reference configuration. Ω_R is reconstructed from the actual *in vivo* geometry of the artery.

- Ω_0 is the configuration obtained by applying the initial boundary conditions and by assigning initial prestretches to each constituent of Ω_R. Ω_R and Ω_0 should be the same as there should be equilibrium between the effects of the initial boundary conditions and the effects of the initial prestretches in the reference configuration. Therefore, all points of the body are at position $\boldsymbol{X}$ at time t_0 and we consider small neighborhoods as $d\boldsymbol{X}$ in this configuration.

- Ω_t is the spatial configuration of the body, defined with positions $\boldsymbol{x}(\boldsymbol{X}, t)$ deformed from the reference coordinates under the effects of the current boundary conditions and the current prestretches. The deformed neighborhood is $d\boldsymbol{x}(\boldsymbol{X}, t) = \boldsymbol{F}(\boldsymbol{X}, t)d\boldsymbol{X}$

- $\Omega_n^j(t)$ are the local natural stress-free configurations of the jth constituents of the mixture, defined with positions $\boldsymbol{x}_n^j(\boldsymbol{X}, t)$ such as the local and incompatible neighborhoods of each constituent are given by $d\boldsymbol{x}_n^j(\boldsymbol{X}, t) = \boldsymbol{F}_{gr}^j(\boldsymbol{X}, t)d\boldsymbol{X}$. Those local neighborhoods can be re-assembled in the spatial configuration by a new deformation such as $d\boldsymbol{x}(\boldsymbol{X}, t) = \boldsymbol{F}_e^j(\boldsymbol{X}, t)d\boldsymbol{x}_n^j(t)$, where the resulting relationship $\boldsymbol{F}_e^j = \boldsymbol{F}[\boldsymbol{F}_{gr}^j]^{-1}$ may be seen as a prestretch and is sometimes called deposition stretch, as collagen fibers or smooth muscle cells are naturally under tension when they are deposited at homeostasis [19].

A major characteristic of hCM models is that, at a chosen reference time t_0, $\boldsymbol{F}_{gr}^j(\boldsymbol{X}, t_0) \neq \boldsymbol{I}$ for each constituent. Assuming homeostatic conditions at t_0, the prestress tensor of collagen fibers and of smooth muscle cells satisfy $\boldsymbol{\sigma}_h^j(\boldsymbol{X}, t_0) = \sigma_h^j \ \boldsymbol{a}_0^j \otimes \boldsymbol{a}_0^j$, where $\boldsymbol{a}_0^j$ is the vector indicating the direction of the main axis of collagen fibers or smooth muscle cells at t_0 [24]. The elastic models for collagen and SMCs are presented in Appendix C, section C.2.
Then, the prestretch tensors of collagen fibers and of smooth muscle cells, $\boldsymbol{F}_e^{c_i}$ and $\boldsymbol{F}_e^m$ respectively, satisfy

$$\boldsymbol{F}_e^j(\boldsymbol{X}, t_0) = \lambda_h^j \boldsymbol{a}_0^j \otimes \boldsymbol{a}_0^j + \frac{1}{\sqrt{\lambda_h^j}}(\boldsymbol{I} - \boldsymbol{a}_0^j \otimes \boldsymbol{a}_0^j), \tag{4.4}$$

where λ_h^j is the prestretch of fibre j at homeostasis. This deposition stretch can be determined experimentaly [19].
The prestretch of the extracellular matrix is partially defined with the collagen prestretch. However, the remaining matrix (composed mainly of elastin but also of a ground substance comprising fibronectin, laminin, or glycosaminoglycans [2], [3]), which is further denoted with letter l, should also be assigned a prestretch tensor $\boldsymbol{F}_e^l$. As Neo-Hookean (Appendix C, section C.2), the Cauchy stress of this constituent should satisfy

$$\boldsymbol{\sigma}^l(\boldsymbol{X}, t_0) = \frac{\rho_R^l}{J}\mu^l \left(J_e^l\right)^{-2/3} \left(\bar{\boldsymbol{b}}_e^l - \frac{1}{3}\mathrm{tr}\left(\bar{\boldsymbol{b}}_e^l\right)\boldsymbol{I}\right) + \frac{\rho_R^l}{J}\kappa^l J_e^l \left(J_e^l - 1\right)\boldsymbol{I}, \tag{4.5}$$

where $\bar{\boldsymbol{b}}_e^l = \bar{\boldsymbol{F}}_e^l \left[\bar{\boldsymbol{F}}_e^l\right]^T$ is the modified left Cauchy-Green stretch tensor and $J_e^l =$

$\det(\boldsymbol{F}_e^l)$. $\bar{\boldsymbol{F}}_e^l$ is the isochoric elastic deformation, its determinant is $\det(\bar{\boldsymbol{F}}_e^l) = 1$ and it is defined as $\bar{\boldsymbol{F}}_e^l = {J_e^l}^{-1/3}\boldsymbol{F}_e^l$.
Unlike collagen and smooth muscle cells, this constituent is not bound to satisfy homeostatic conditions. However, $\boldsymbol{F}_e^l$ should ensure the mechanical equilibrium of the mixture (Appendix C.3) when a external force $\boldsymbol{f}$ is applied on the body, which may be written such as

$$\operatorname{div}\left(\boldsymbol{\sigma}^l + \sum_j^{m,c_i} \sigma_h^j \, \boldsymbol{a}_0^j \otimes \boldsymbol{a}_0^j\right) + \boldsymbol{f} = 0. \tag{4.6}$$

In order to perfectly define the initial conditions, we have to solve Eq. 4.6 and find $\boldsymbol{F}_e^l(t_0)$ (prestretch of the matrix, surrounding collagen fibers and smooth muscle cells) such as,

$$d\boldsymbol{x}_0 = \boldsymbol{F}_e^l d\boldsymbol{x}_n^l = d\boldsymbol{X}. \tag{4.7}$$

The resolution of this problem is only possible if we know the tractions applied on the whole boundary of Ω_0. When Ω_0 is a segment of artery *in vivo*, these tractions are usually unknown at both cross-sectional ends. Indeed if we keep the ends of the segment constrained and free from the external loads (pressure for instance), the obtained configuration will not be stress-free and there will be elastic deformations (cf. Eq. (1) in [24]). We can also imagine to split the body into several small parts, where each part has just one constituent, but their assembly is not necessarily geometrically compatible. As a consequence, it is not possible to use $\boldsymbol{F}_e^l = \partial\boldsymbol{x}_0/\partial\boldsymbol{x}_n^l$ as a valid definition for the prestretch [51].

4.4.3.2 Assigning $\boldsymbol{F}_e^l(\boldsymbol{X}, t_0)$ in a perfectly cylindrical straight tube

The problem can be easily overcome when Ω_R is a perfectly cylindrical straight tube. It can be assumed that the prestretch is a diagonal tensor within the cylindrical ($\boldsymbol{X} = X_1\boldsymbol{e}_Z + X_2\boldsymbol{e}_R + X_3\boldsymbol{e}_\Theta$, Fig. 4.2a) reference frame, such as,

$$\boldsymbol{F}_e^l(\boldsymbol{X}, t_0) = diag\left(\lambda_{hZ}^l, \lambda_{hR}^l, \lambda_{h\Theta}^l\right), \tag{4.8}$$

where $\{\lambda_{hZ}^l, \lambda_{hR}^l, \lambda_{h\Theta}^l\}$ are the elastic prestretches in the radial, circumferential and longitudinal direction, respectively.
Then, $\lambda_{hZ}^l(\boldsymbol{X}, t_0)$ is fixed to an arbitrary value, which is equal to the supposed *in vivo* axial stretch of the artery, denoted λ^{iv} (known averagely for the human aorta [90]) and assumed to be uniform in all directions. Eventually, $\lambda_{h\Theta}^l$ and λ_{hR}^l, which are assumed to be uniform across the cylinder, are directly obtained by solving Eq. 4.6 in the radial and tangential directions and by satisfying the incompressibility condition.

4.4.3.3 Assigning $\boldsymbol{F}_e^l(\boldsymbol{X}, t_0)$ in a perfectly toric tube

Things become more complex for non-cylindrical shapes. We found that, when Ω_R is a perfectly toric tube (torus slice), compatibility equations could still be satisfied if we assumed that $\boldsymbol{F}_e^l(\boldsymbol{X}, t_0)$ is a diagonal tensor within the local toric

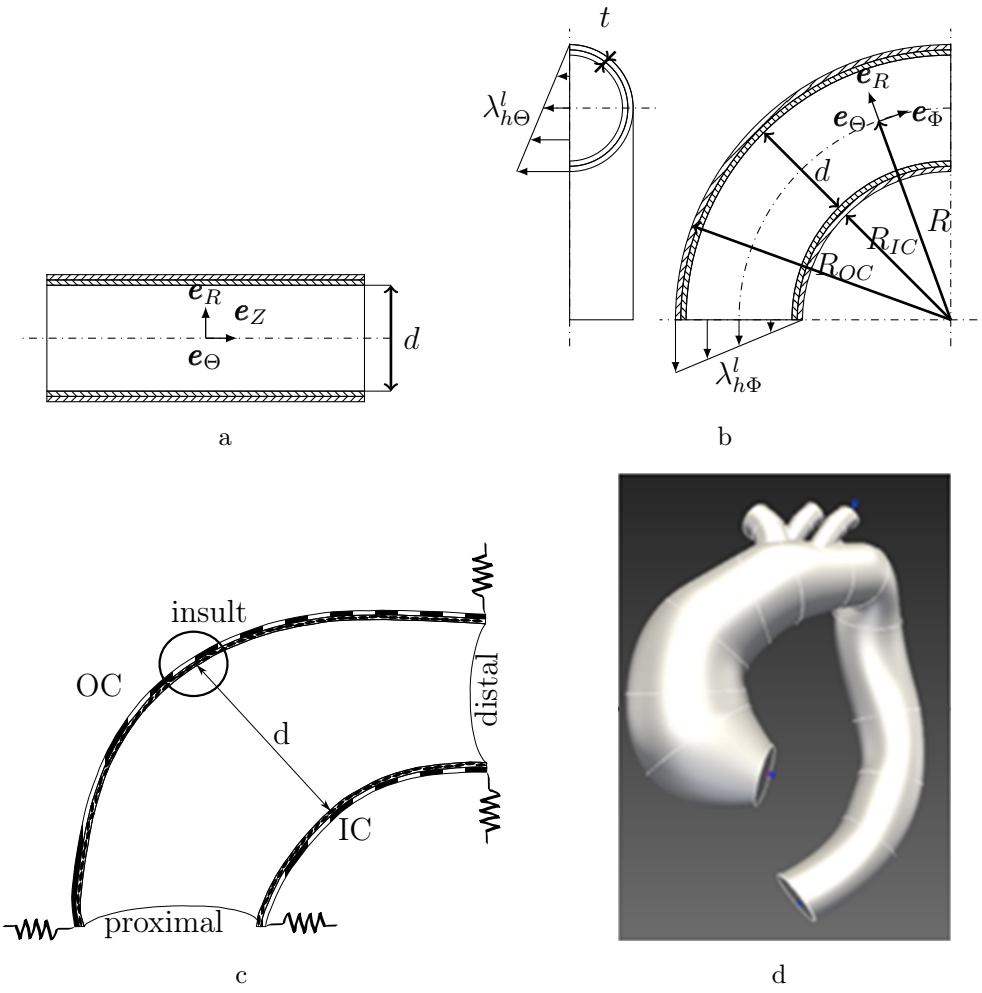

Figure 4.2 – (a) Lateral view of a cylinder with its diameter d and the cylindrical system $(\boldsymbol{e}_Z, \boldsymbol{e}_R, \boldsymbol{e}_\Theta)$ with $\boldsymbol{e}_\Theta$ perpendicular to the sheet. (b) Lateral and cross-sectional views of the idealized toric ATA model, where the luminal diameter is $d = R_{OC} - R_{IC}$, the arch radius is R (middle curvature) and the total wall thickness is t. IC=inner curvature and OC=outer curvature of the arch; a linear gradient is assigned for the axial ($\lambda^l_{h\Phi}$) and circumferential ($\lambda^l_{h\Theta}$) prestretch of elastin in the reference homeostatic state. The torus is represented with the spherical coordinate system $(\boldsymbol{e}_\Phi, \boldsymbol{e}_R, \boldsymbol{e}_\Theta)$ with $\boldsymbol{e}_\Theta$ perpendicular to the sheet. (c) Schematic of the boundary conditions, with springs at the proximal (k_{pro}) and at the distal (k_{dis}) ends; the circle (with radius L_{dam}) indicates the insult zone where a localized degradation of elastin is applied; the diameter d and the thickness along the same line are used to assess the initial distortions and displacements during the simulations. (d) Reconstructed geometry of the patient-specific aorta from the CT scan. In (a) and (b), the media is filled with north west lines and the adventitia with north east lines, in (c) the media is filled with dots and the adventitia with vertical black thick lines.

($\boldsymbol{X} = X_1\boldsymbol{e}_\Phi + X_2\boldsymbol{e}_R + X_3\boldsymbol{e}_\Theta$) reference frame (where $\boldsymbol{e}_\Theta$ refers to the poloidal or circumferential direction, and $\boldsymbol{e}_\Phi$ refers to the toroidal or longitudinal direction), Fig. 4.2b. However, it is necessary to consider regional variations of $\lambda^l_{h\Phi}(\boldsymbol{X}, t_0)$, $\lambda^l_{h\Theta}(\boldsymbol{X}, t_0)$ and $\lambda^l_{hR}(\boldsymbol{X}, t_0)$. For that, we assumed $\lambda^l_{h\Phi}(\boldsymbol{X}, t_0)$ only varying along the radial direction from the inner curvature to the outer curvature (Fig. 4.2b) such as

$$\lambda^l_{h\Phi}(R, t_0) = \lambda^l_{h\Phi-IC} + (\lambda^l_{h\Phi-OC} - \lambda^l_{h\Phi-IC})\frac{R - R_{IC}}{d}, \tag{4.9}$$

where d is the diameter of the tube and $R \in [R_{IC}, R_{OC}]$. Additionaly, the maximum $\lambda^l_{h\Phi}$ is set at the outer curvature ($\lambda^l_{h\Phi-OC}$) and is equal to the supposed *in vivo* axial stretch λ^{iv}, while the minimum stretch is updated iteratively at the inner curvature ($\lambda^l_{h\Phi-IC}$).
Therefore the circumferential prestretch, $\lambda^l_{h\Theta}(R, t_0)$, satisfies a similar expression and the radial prestretch is assigned to satisfy the local incompressibility condition, yielding

$$\lambda^l_{h\Theta}(R, t_0) = \lambda^l_{h\Theta-IC} + (\lambda^l_{h\Theta-OC} - \lambda^l_{h\Theta-IC})\frac{R - R_{IC}}{d}, \tag{4.10}$$

and

$$\lambda^l_{hR}(R, t_0) = (\lambda^l_{h\Theta}\lambda^l_{h\Phi})^{-1}. \tag{4.11}$$

Then, the two parameters $\lambda^l_{h\Theta-IC}$ and $\lambda^l_{h\Theta-OC}$ are found by solving Eq. 4.6 projected along the radial direction of the torus.

4.4.3.4 Assigning $\boldsymbol{F}^l_e(\boldsymbol{X}, t_0)$ in a patient-specific aortic arch

When Ω_R is not a perfectly toric tube, compatibility equations are not satisfied anymore if we assume that $\boldsymbol{F}^l_e(\boldsymbol{X}, t_0)$ is a diagonal tensor. However, the torus is still a first approximation of the aortic arch. Therefore, for patient-specific geometries, we developed an iterative approach starting from the solution of Eq. 4.9, and thereafter updating it iteratively to address the distortions induced by the incompatibility of the assigned prestretch. This consisted in updating the axial prestretch at the inner curvature ($\lambda^l_{h\Phi-IC}$), improving its values iteratively by reducing the thickness distortion (under the tolerance ϵ_t=3%), and then in updating the circumferential prestretch at the outer and inner curvatures ($\lambda^l_{h\Theta-OC}$ $\lambda^l_{h\Theta-IC}$, respectively) reducing the distortion of the diameter (under ϵ_d=6%), Fig. 4.3.

4.4.3.5 Time evolutions of $\boldsymbol{F}^j_{gr}(\boldsymbol{X}, t_0)$

The prestretch $\boldsymbol{F}^j_e(\boldsymbol{X}, t_0)$ at t_0 equals the inelastic deformation gradient $\boldsymbol{F}^j_{gr}(\boldsymbol{X}, t_0)$ of the constituents. This inelastic deformation gradient relates the natural stress-free configuration with an hypothetical traction-free configuration, which at t_0 is the reference configuration. During G&R the natural stress-free configuration continuously evolves due to the mass turnover and structure changes, see Appendix C, section C.3. Therefore, the inelastic deformation is continuously changing according to

$$\boldsymbol{F}^j_{gr}(t) = \boldsymbol{F}^j_{gr}(t_0) + \int_{t_0}^{t} \dot{\boldsymbol{F}}^j_{gr}(\tau)d\tau. \tag{4.12}$$

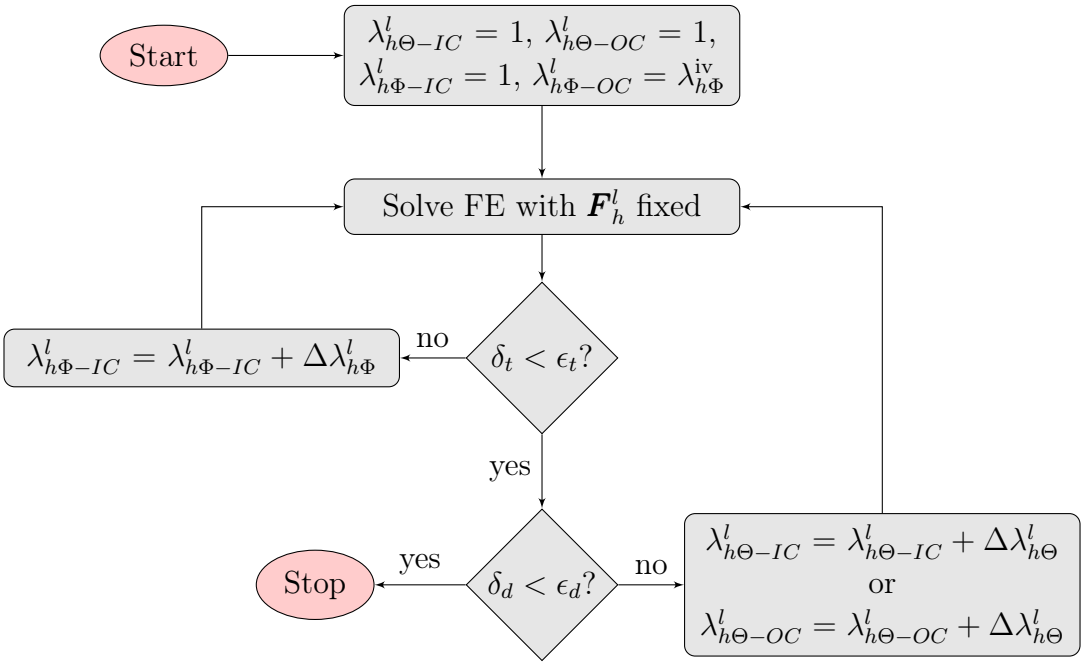

Figure 4.3 – Flowchart for the homeostatic prestretch algorithm, showing how the prestretch gradient is found iteratively by solving forward FE problems successively. In the forward FE model, the prestretch gradient is held constant. After each forward analysis, the axial prestretch gradient ($\nabla\lambda^l_{h\Phi}$) is updated if the thickness distortion (δ_t) is larger than the thickness tolerance (ϵ_t), or the circumferential prestretch gradient ($\nabla\lambda^l_{h\Theta}$) is updated if the diameter distortion (δ_d) is larger than the diameter tolerance (ϵ_d) [49].

4.4.4 Numerical implementation

The hCM model of G&R was implemented in an in-house research Finite-Element (FE) code based on Florence [66], [67] (written in Python/C++). We implemented new routines for the code and further modified existing Florence routines. At the core, a forward Euler (explicit) time integration scheme was created for the hCM, according to the formulation presented in Appendix C.3. Another new routine was developed to assign an assembly of multiple mixture materials in one body, as for instance a bi-layer arterial wall. We also developed routines to assign Robin elastic boundary conditions at both ends of the tube, as explained in Appendix C, section C.1. The meshes were generated using GMSH [91].

4.4.5 Verification

A simulation was performed on a cylinder. An insult was applied, corresponding to the same elastin degradation as the one considered previously by other authors [12], [24], [27], further written in Eq. 4.13. The purpose of this simulation was to verify our model, as reference results were previously published for such problem [27]. The geometry, load, mechanical properties, densities, initial prestrain and mass turnover are reported in Table 4.1. Different mass-gain parameters were tested ($k_\sigma^{c_i} = \{0.05, 0.09, 0.11, 0.15\}/T^{c_i}$) as in the reference results, the mass-parameters part of the G&R model introduced in detail in Appendix C.3. The mesh was hexaedral and composed of 2×15×60 elements (thickness×circumferential×length) in a quarter cylinder.
The temporal evolutions of the maximum radius predicted by our model were in good agreement with the reference results of [27], as shown in Fig. 4.4. In Fig. 4.4a, the comparison was performed against the three dimensional model of [27]. The relative error is between 3% and 9%. In Fig. 4.4b, the comparison was performed against the membrane model of [27]. The relative error is even lower, ranging between 1% to 4%. The error is estimated 15 years after the original insult. In Table 4.2, we also compare the stress and normalized reference mass density of collagen, showing a good agreement between [27] and our model.

4.4.6 Applications

Our new model was then applied to simulate G&R in different types of ATA geometries. For each case, we predicted temporal evolutions of the lumen diameter and of the wall thickness, as defined in Figure 4.2, following an initial insult. The material properties and initial densities were assigned as described in Appendix C, section C.4.

4.4.6.1 Initial insult for G&R

The G&R in the arterial model is triggered by either an initial insult consisting in a sharp spatial-temporal degradation of elastin (Eq. 4.13) or by the half-life

Symbol	Value	
Geometry and load		
radius	r	$10 - mm$
length	l	$90 - mm$
thickness	t	$1.41 - mm$
pressure	p	$100 - mmHg$
Mechanical properties		
neo-Hookean	μ^l	$72 - J/kg$
bulk-modulus	κ^l	$100 \times 72 - J/kg$
Fung-quadratic, collagen	$k_1^{c_i}$	$568 - J/kg$
	$k_2^{c_i}$	11.2
passive, SMC	k_1^m	$7.6 - J/kg$
	k_2^m	11.4
active, SMC	σ_{actmax}	$54 - kPa$
	λ_0^m	0.8
	λ_{max}^m	1.4
	λ_{act}	1.0
Density		
elastin	ϱ_{R0}^l	$241.5 - kg/m^3$
SMC	ϱ_{R0}^m	$157.5 - kg/m^3$
collagen(0 and $\pi/2$)	$\varrho_{R0}^{c_1} = \varrho_{R0}^{c_4}$	$65.1 - kg/m^3$
collagen($-\pi/4$ and $\pi/4$)	$\varrho_{R0}^{c_2} = \varrho_{R0}^{c_3}$	$241.5 - kg/m^3$
Initial remodeling (prestrain)		
elastin longitudinal	$\lambda_{rz}^l(t=0)$	1.25^{-1}
elastin circumferential	$\lambda_{r\theta}^l(t=0)$	1.34^{-1}
SMC	$\lambda_r^m(t=0)$	1.1^{-1}
collagen	$\lambda_r^{c_i}(t=0)$	1.062^{-1}
Turnover period		
collagen and SMC	$T^{c_i} = T^m$	$101 - days$
elastin	T^l	$101 - years$

Table 4.1 – Mechanical parameters used to verify our model against the results of [27] for the development of an aneurysm in an idealized cylindrical geometry.

		Literature [27]		This work		error	
		minimum	maximum	minimum	maximum	minimum	maximum
Stress	$k_\sigma = 0.05/T$	80-kPa	320-kPa	44-kPa	291-kPa	-45%	-9%
	$k_\sigma = 0.15/T$	80-kPa	120-kPa	95-kPa	105-kPa	19%	-12%
Collagen	$k_\sigma = 0.05/T$	0.8	6.1	0.73	5.03	-9%	-18%
	$k_\sigma = 0.15/T$	1.0	1.6	1.00	1.44	0%	-10%

TABLE 4.2 – Comparison of our results with results from [27] for the development of an aneurysm in an idealized cylindrical geometry following an initial insult (localized elastin degradation). Gain-parameter $k_\sigma = k_\sigma^m = k_\sigma^{c_i}$ and turnover time $T = T^m = T^{c_i}$ from the equation of rate mass degradation and deposition (details in Appendix C, section C.3).

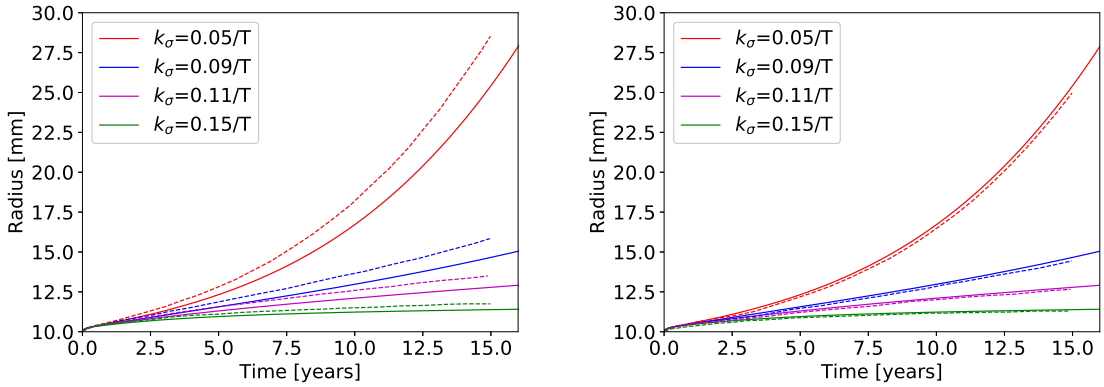

a b

FIGURE 4.4 – Evolution of the maximum radius for the cylinder benchmark case. 4.4a comparison between the radius predicted by our model (solid lines) with the three-dimensional model (dashed lines) of Braeu et al [27]. 4.4b comparison between the radius predicted by our model (solid lines) with the membrane hCM model of Braeu et al [27]

degradation of elastin (Eq. 4.14), such as,

$$\begin{aligned} \varrho^l_R(t) \quad &= \varrho^l_{R0} \exp\left(\frac{-t}{T^l}\right) + \varrho^l_{R0} \frac{D_{max}}{t_{dam}} \exp\left(-0.5 \left[\frac{X_d}{L_{dam}}\right]^2\right) \\ &\quad \frac{t_{dam} T^l}{t_{dam} - T^l} \left[\exp\left(\frac{-t}{T^l}\right) - \exp\left(\frac{-t}{t_{dam}}\right)\right] \end{aligned} \tag{4.13}$$

or

$$\varrho^l_R(t) = \varrho^l_{R0} \exp\left(\frac{-t}{T^l}\right), \tag{4.14}$$

where D_{max}=0.5, L_{dam}=10-mm, and t_{dam}=40-days are parameters related to elastin evolution, T^l is the half-life time of elastin, ϱ^l_R and ϱ^l_{R0} are the time and the initial elastin densities (per unit reference volume), respectively, and where the degradation in Eq. 4.13 is based on the distance X_d between a given position ($\vec{P}_x$) and the central degradation position ($\vec{P}_0$), according to

$$X_d = \begin{cases} ||\vec{P}_x - \vec{P}_0|| & \text{in the radial direction,} \\ \\ (\vec{P}_x - \vec{P}_0) \cdot \vec{v} & \text{in the axial direction,} \end{cases} \tag{4.15}$$

In this work, the G&R simulations are analysed with a forward Euler time integration scheme. To apply such method a discretization of time is needed, and with the purpose to keep stable evolution of the tissue we have taken equal time steps ten times smaller than the smallest turnover time (T^j), $\Delta t = T^j/10$.

4.4.6.2 Idealized ATA model

An idealized bi-layer model of an ATA, similar to the ones in [21] and [17], was defined as a first test case for the sake of simplicity, given the symmetries. The

model is bi-layered by equal distribution of the arterial tickness. The geometry was an eighth of a torus ($\phi = \pi/2$) of diameter d=36-mm and arch radius R=65-mm, Fig. 4.2b. Radial rollers with springs were used to ensure appropriate boundary conditions at both ends, as shown in Fig. 4.2c. This model is discretized in hexahedral elements with 4×12×48 (thickness×circumferential×length), two elements in media and adventitia tickness. The pressure, mechanical parameters and densities are reported in Tab. 4.3 with $\beta = 40$.

4.4.6.3 Patient-specific ATA model

A patient-specific geometry of an ATA was reconstructed from the CT scan of a patient harboring an aneurysm [17], as shown in Fig. 4.2d. Two layers were defined across the thickness, namely the media ($0.5t$) and the adventitia ($0.5t$). The boundary conditions at the proximal and distal ends were the same as for the idealized ATA, with radial rollers and springs, Fig. 4.2c. This model is discretized in hexahedral elements with 4×12×48 (thickness×circumferential×length), two elements in the thickness of media and adventitia. The pressure, mechanical parameters and densities are reported in Tab. 4.3, with $\beta = 20$.
Moreover, we also tested that our computational framework is capable to keep the homeostatic condition when there is no elastin degradation. The test was performed on the patient-specific geometry over a duration of 6000 days. The change of diameter was lower than 0.02%.

4.5 Results

4.5.1 Idealized ATA model

An initial prestretch was assigned for the elastin-matrix component as shown in Fig. 4.2b, with $\lambda^l_{h\Phi-IC} = 0.75$, $\lambda^l_{h\Phi-OC} = 1.3$ and $\lambda^l_{h\Theta-IC} = 1.45$, $\lambda^l_{h\Theta-OC} = 1.3$. The initial prestretch followed a linear distribution between the inner and the outer curvature. This permitted to reduce distortions below 2% in the diameter and 3% in the thickness, respect to the metrics shown in figure 4.2b. The stiffness of elastic boundaries, which also contribute significantly to reduce distortions, were set to 1-Pa/m and 0.2-Pa/m at the proximal and distal ends, respectively. These initial conditions eventually permitted to achieve G&R simulations for more than 10-years in this idealized ATA geometry.
In Figs. 4.5a and 4.5c, we show the influence of the gain-parameter on the rate of aneurysm growth obtained with this model. The lower the gain parameter values, the faster the diameter changes. Such parameter has also an influence on the thickness evolutions, as shown in Fig. 4.5b and 4.5d. The lower the gain parameter values, the faster the thickness decreases. When the gain-parameter values become too low, the G&R becomes unstable. In that case, the lumen diameter grows above 65-mm or 70-mm. The effect is amplified when G&R follows a localized lesion, as shown in Fig. 4.5c).

	Symbol	Value
Geometry and load		
thickness	t	$2.38 - mm$
pressure	p	$80 - mmHg$
Mechanical properties		
neo-hookean	μ^l	$80 - J/kg$
bulk modulus	κ^l	$\beta \times 80 - J/kg$
Fung-quadratic, collagen	$k_1^{c_i}$	$292.0 - J/kg$
	$k_2^{c_i}$	5.6
passive, SMC	k_1^m	$13.8 - J/kg$
	k_2^m	6.0
Density media		
elastin	ϱ_{R0}^l	$169.0 - kg/m^3$
SMC	ϱ_{R0}^m	$735.0 - kg/m^3$
collagen (0 and $\pi/2$)	$\varrho_{R0}^{c_1} = \varrho_{R0}^{c_4}$	$14.6 - kg/m^3$
collagen ($-\pi/4$ and $\pi/4$)	$\varrho_{R0}^{c_2} = \varrho_{R0}^{c_3}$	$58.4 - kg/m^3$
Density adventitia		
elastin	ϱ_{R0}^l	$565.0 - kg/m^3$
SMC	ϱ_{R0}^m	$0.0 - kg/m^3$
collagen (0 and $\pi/2$)	$\varrho_{R0}^{c_1} = \varrho_{R0}^{c_4}$	$48.5 - kg/m^3$
collagen ($-\pi/4$ and $\pi/4$)	$\varrho_{R0}^{c_2} = \varrho_{R0}^{c_3}$	$194.0 - kg/m^3$
Initial remodeling (prestretch)		
SMC	$\lambda_r^m(t=0)$	1.1^{-1}
collagen	$\lambda_r^{c_i}(t=0)$	1.1^{-1}
Turnover period		
collagen and SMC	$T^{c_i} = T^m$	$101 - days$
elastin	T^l	$101 - years$

Table 4.3 – Material parameters used in our models to simulate G&R in an idealized toric aortic arch and in a patient-specific ATA geometry. The parameters are introduced with their respective models in the Appendix C.2.

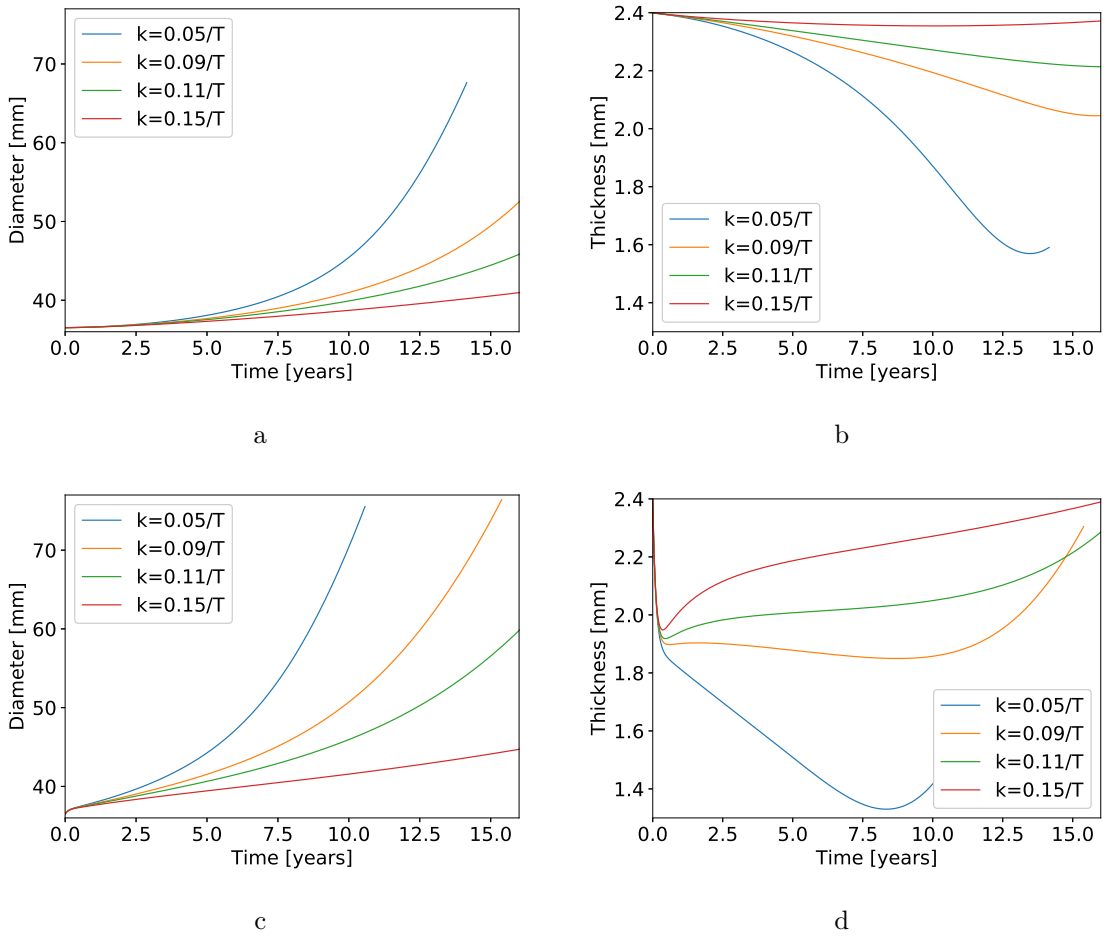

FIGURE 4.5 – Diameter (a) and thickness (b) evolution in the idealized ATA geometry in response to half-life elastin degradation. Diameter (c) and thickness (d) evolution of the idealized ATA in response to an initial insult (sharp elastin degradation).

Figs. 4.6a and 4.6b show the von Mises stress field for the two cases of elastin degradation (aging and insult, respectively). The stresses are higher for the localized elastin loss than for the long-term elastin degradation. There is still a similar stress distribution for both cases, as the larger stresses are in the IC of the arch and in the adventitia while the media does not exhibit major changes of stress distribution. The story is slightly different for the total collagen distribution, where the largest production of collagen occurs at the OC of the arch and in the adventitia, as shown in Fig. 4.6c and 4.6d.

4.5.2 Patient-specific ATA model

The initial prestretch of elastin was distributed with a linear gradient as shown in Fig. 4.2b with $\lambda^l_{h\Phi-IC} = 0.75$, $\lambda^l_{h\Phi-OC} = 1.3$ and $\lambda^l_{h\Theta-IC} = 1.5$, $\lambda^l_{h\Theta-OC} = 1.0$. Distortions lower than 6% were obtained in the diameter metric and below 3% in the thickness at IC and OC –the distortions are measured respect to the metrics shown in figure 4.2c–. We allowed more distortion in the homeostatic diameter as a trade-off between distortions and stability. Indeed, reducing initial distortions implied applying larger pre-tensions in the initial homeostatic state. Such large pre-tensions were systematically responsible for further instability in the G&R simulations. For instance, average stress values above 200 kPa for the homeostatic state were systematically responsible for a divergence of the FE analysis after 100 days of G&R. Spring stiffness values of 10 Pa/m and 0.5 Pa/m were assigned at the proximal and distal boundaries, respectively.

As the patient already harbored an ATA aneurysm, the reference homeostatic lumen diameter was 48 mm. Further diameter evolutions predicted by the model are shown in Figs. 4.7a and 4.7c. As for the idealized ATA, these evolutions depend on the gain parameter and on the type of insult (acute or long-term elastin loss). When the gain-parameter values become too low, the G&R becomes unstable after 60 mm diameter. Differences with respect to the idealized case are visible in the thickness evolution, as shown in Figs. 4.7b and 4.7d. For long-term elastin loss, the thickness decreases more slowly than with the acute insult, the latter showing a sharp decrease in the first year due to the acute elastin loss.

The stress distribution for the patient-specific ATA model shows a pattern of high stresses in the axial direction in both layers (media and adventitia). The largest stress values are found in the adventitia for both cases, as shown in Figs 4.8a and 4.8b. A very large stress concentration is obtained in the adventitia at the OC near the proximal edge. Despite the stress pattern and stress concentrations, collagen accumulates mainly in the adventitia at the OC and far from the boundaries for the long-term elastin loss, whereas collagen concentration is more pronounced in the elastin degradation zone for the acute insult, as shown in Figs. 4.8c and 4.8d.

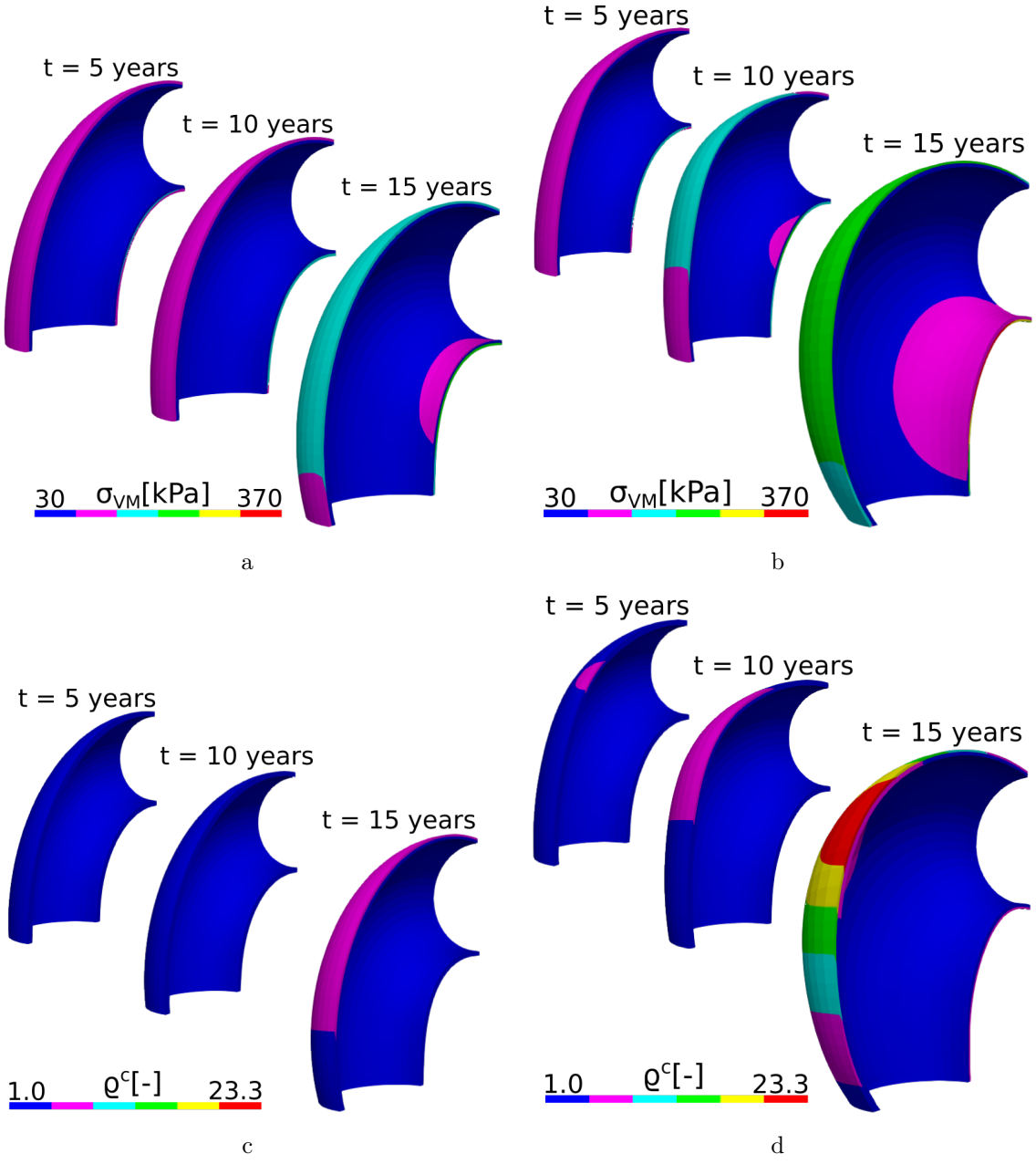

FIGURE 4.6 – Von Mises stress (σ_{VM}) evolution in response to half-life elastin degradation (a) and in response to an initial insult (sharp elastin degradation) (b) for the idealized ATA geometry. Normalized total collagen density (ρ^c) evolution in response to long-term elastin degradation (c) and localized elastin loss (d) for the idealized ATA geometry. Simulations were achieved with $k_\sigma = 0.09/T$

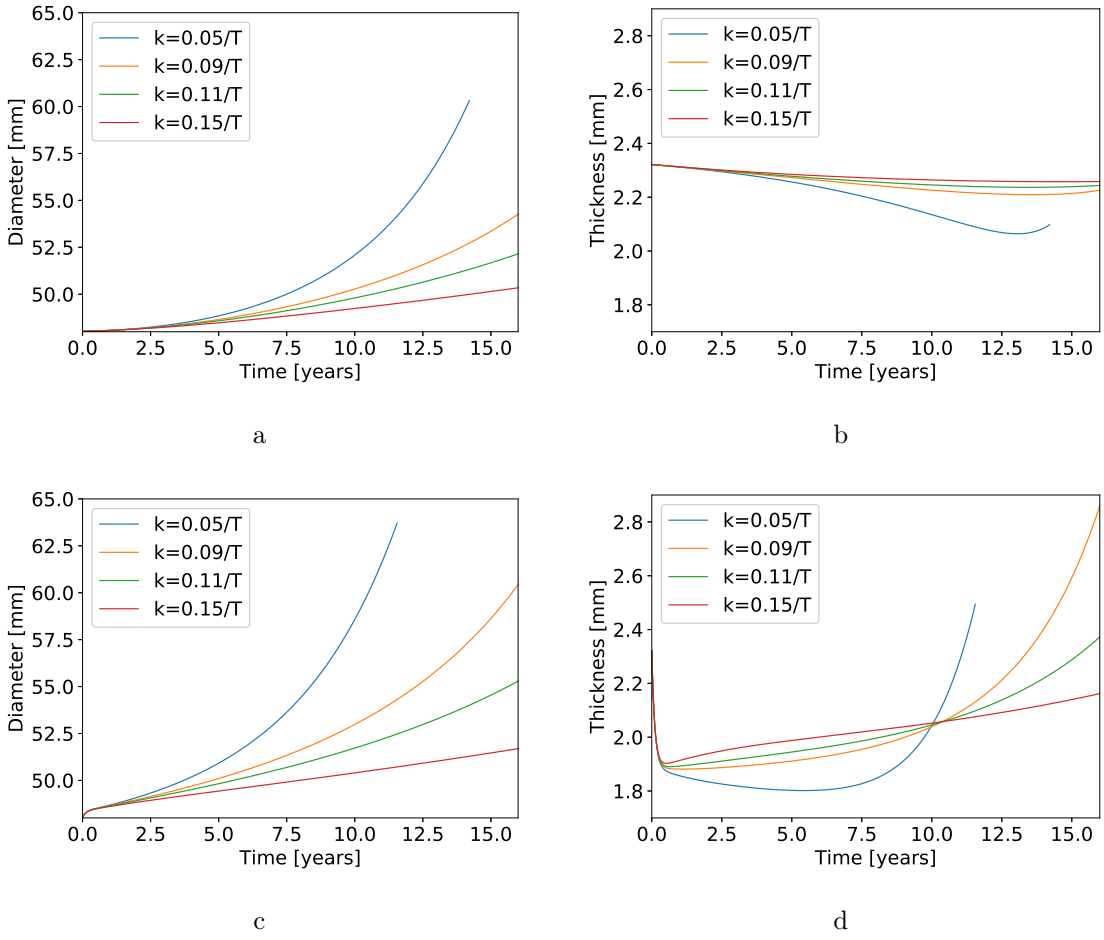

Figure 4.7 – Diameter (a) and thickness (b) evolution in the patient-specific ATA geometry in response to half-life elastin degradation. Diameter (c) and thickness (d) evolution of the patient-specific ATA in response to an initial insult (sharp elastin degradation).

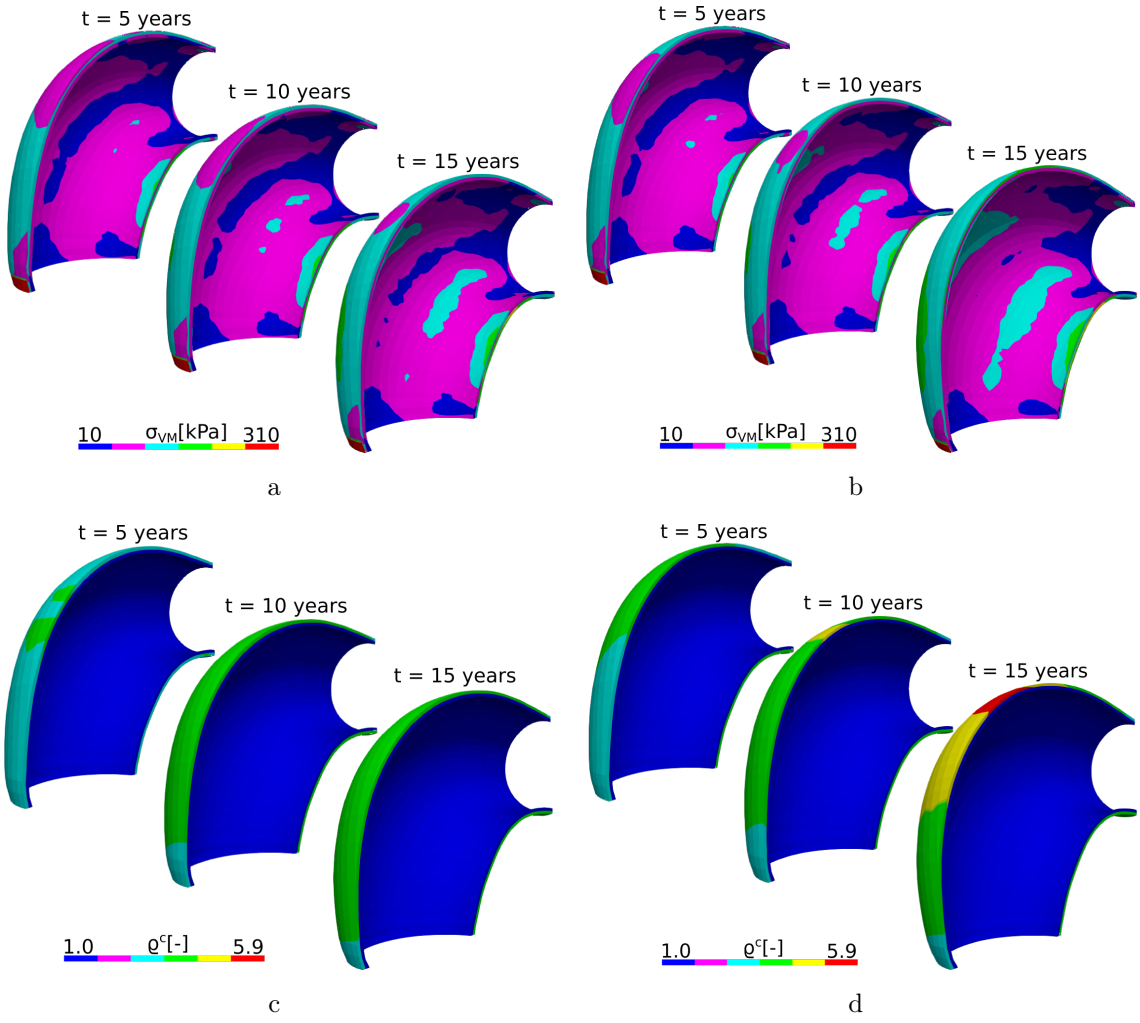

FIGURE 4.8 – Von Mises stress (σ_{VM}) evolution in response to half-life elastin degradation (a) and in response to an initial insult (sharp elastin degradation) (b) for the patient-specific ATA geometry. Normalized total collagen density (ρ^c) evolution in response to long-term elastin degradation (c) and localized elastin loss (d) for the patient-specific ATA geometry. Simulations were achieved with $k = 0.09/T$

4.6 Discussion

Mechanoregulation of collagen tension in soft tissues is essential in the progression of aortic aneurysms. In this work, we established a numerical model to simulate these effects in the thoracic aorta. The model is based on the constrained mixture theory, which requires that prestretches are assigned to each microstructural component of the arterial tissue. Although these prestretches actually exist even in the initial reference configuration, they have never been measured accurately and we need to make assumptions in order to assign them in computational models. They were previously assumed as homogeneous in idealized straight tubes, but in the present study, we investigated more elaborate prestretch distributions for curved arteries, with a special focus on a patient-specific ATA geometry.

We proposed to assign a prestretch gradient from the inner to the outer ATA curvature. This permitted to establish a compatible initial homeostatic state and to produce stable and long (above 10-years) simulations using our 3D FE implementation of G&R. This gradient was needed to compensate the different effects of the lumen pressure at the IC and OC in a curved vessel (Fig. 4.2c). This non-uniform prestretch is in agreement with the previous study of [21], who already considered a different axial prestretch at the IC and at the OC of an idealized toric aortic arch. Outside this study, the homeostatic deposition stretch of elastin was usually assigned as uniform in previously CM models dedicated to straight geometries [14], [16], [26]. Although a linear distribution of longitudinal and circumferential prestretches gives stability to G&R simulations, this remains a simplification for the sake of computational analyses. The current work suggests for the first time the existence of these spatial variations of prestretches in ATAs. However, the spatial distribution of prestretches could be more complex. For example, other distributions based on polynomial expressions could be defined to ATAs and optimized through sensitivity analyses [29]. Furthermore, the linear assumption has not been experimentally validated. Experimental investigations could consist in measuring the shortening of ATAs in the inner and outer curvature after excision. Nevertheless, [21] highlighted the difficulties to measure residual stresses. Therefore, the actual distribution of prestretches remains an open problem.

In addition to initial prestretches, other factors appeared to be critical to perform stable G&R simulations in curved arterial geometries. One of these factors is the boundary condition at the proximal and distal borders. We used radial rollers, as shown in Fig. 4.2c, and as detailed in Appendix C, section C.1. These boundary conditions are consistent with the actual conditions of an ATA, which is tethered elastically in the body, for instance to the heart. The elastic radial rollers also helped to reduce stress concentration at the proximal border in the patient-specific ATA simulations. Similar boundary conditions were previously used by [92] and [93] to model the external tissue support of the aorta (e.g. the surrounding organs), but our study is the first one dedicated to G&R.

Although we ensured that mechanical equilibrium was satisfied in the reference homeostatic configuration, our choice of the longitudinal prestretch remained ar-

bitrary [17], as it has never been characterized in human ATA. Even the linear gradient of prestretch in the radial direction and the parameters of Robin boundary conditions were chosen mostly for the sake of keeping stability in the simulations. There are always many constitutive parameters in G&R models, and more experimental data –especially on humans– are still necessary to set the parameter values more accurately.

Different models were previously used for the elastin in G&R simulations based on the CM model. We used a three-dimensional neo-Hookean nearly incompressible model, as detailed in Appendix C.2. This is a major difference with the model proposed by [27], where a combination of two- and three-dimensional formulations was implemented to ensure numerical stability. Although our model omitted the 2D part, we obtained still a very good agreement with their results in the verification case.

Our model captured aneurysm progression in the ATA, either with an idealized toric geometry or in a patient-specific geometry. For low gain parameters ($k_\sigma^j < 0.1/T^j$), the diameter reached 55 mm (Figs. 4.5 and 4.7), which is the threshold at which surgical repair is recommended, along with growing rates above 1.5 mm/year [44]. However, the respective von Mises stress values shown in Figs. 4.6b and 4.8b remained below 500 kPa [44], [94], [95]. Moreover, high gain parameters ($k_\sigma^j > 0.1/T^j$) induced less pronounced dilatations, with dimaters remaining below the 55 mm threshold and stabilization of aneurysm evolution.

In the patient-specific simulation modeling the aging effect, the gain parameters $k_\sigma^j = \{0.11, 0.15\}/T^j$ produced dilatation of 1.2-mm(3.7%) and 1.8-mm(2.5%) in the first decade, respectively. Such ATA diameter increases are in good agreement with previous observations made by [42] and [96], with progressions of 1.1-mm and 3% per decade, respectively. Aging is related with elastin fragmentation and possible fibrosis causing stiffening of the arterial wall [41], [63]. Our aging simulations captured well such effects by taking into account the half-life time of elastin in Eq. 4.14. Elastin degradation induced an accumulation of collagen, especially in the adventitia, which could be responsible for fibrosis and ATA stiffening. Unfortunately, we did not consider possible pressure increase due to hypertension that can be indirectly caused by the increased stiffness [42], [63]. Other effects remained neglected in our work, such as aortic unfolding, which is the natural increase of radius of curvature of the aortic arch with age [42]. Including this effect in the model would require updating the boundary conditions with time, especially at the aortic root. There is still a lack of knowledge about these effects and they should be investigated further in the future.

In the definition of the prestretch, we assumed a uniform wall thickness in the reference configuration [17]. Although the thickness of the aorta is not uniform, it is not possible to measure it accurately with currently available *in vivo* imaging modalities. [97] proposed a methodology for optimizing the thickness in the definition of the homeostatic state. Such optimization could be considered in a future work.

4.7 Conclusions

In this work, we implemented the homogenized constrained mixture model in a three-dimensional FE framework and we used this framework to simulate aneurysm development and progression in a patient-specific ATA, assuming that G&R works at maintaining a homeostatic level of tension in collagen fibers. We especially modelled aneurysm progression following localized elastin degradation in the ATA. As ATAs are curved arteries, heterogeneous initial prestretches had to be initially assigned to the constituents of the constrained mixture in order to satisfy equilibrium and set initial homeostatic conditions preceding the initial insult. It was critical to initiate G&R simulations with homeostatic conditions but these conditions also determine further aneurysm progression. This work highlighted the complexity of prestretches in FE models simulating G&R of the ATA based on tensional homeostasis. Such prestretches should actually reflect all the developmental history of each individual and future work will focus on identifying these prestretches *in vivo*.

Chapter 5

Extension of the model to chronic aortic dissections

Table of contents of the chapter

5.1 Résumé du chapitre en français. 111
5.2 Abstract of the chapter 112
5.3 The mechanical problem 112
5.4 Formulation of the interaction between layers. 113
5.5 Implementation 114
5.6 Simulations 116
5.7 Conclusion 118

5.1 Résumé du chapitre en français

La dissection aortique est une maladie grave qui peut conduire à la rupture de l'aorte. Par conséquent, le présent chapitre vise à développer un cadre mécanique pour les changements tissulaires qui se produisent dans une aorte disséquée. À cette fin, la dissection est analysée comme un problème mécanique où la paroi aortique est au moins composée de deux corps assemblés qui se désengagent dans le temps, selon un modèle de propagation de la fissure. L'idée est d'appliquer continuellement la théorie de la G&R sur le tissu aortique pour réaliser les adaptations dues aux charges et aux conditions changeantes. Cependant, le milieu doit initialement se comporter comme un seul corps unique. Pour cela, une condition spéciale est formulée pour maintenir les deux couches aortiques ensemble. Cette condition spéciale est gérée en interne par le code pour permettre la propagation de la dissection. Enfin, cette formulation est mise en œuvre dans le code tridi-

mensionnel par éléments finis présenté précédemment et une simulation test est finalement présentée pour cette nouvelle approche.

5.2 Abstract of the chapter

The aortic dissection is a catastrophic disease that could lead to the rupture of the aorta. Following this, the present chapter aims to develop a mechanical framework for tissue changes occuring in a chronic aortic dissection. For this purpose, the dissection is analysed as a mechanical problem where the aortic wall is at least composed of two assembled layers that separate after some time according to a model of dissection. The idea is to apply growth and remodeling on the aortic tissue to simulate the adaptations due to the changing loads and conditions. However, the assembly of the two layers needs to initially behave as a single body. Therefore, we formulated a special condition to keep two aortic layers tied together. This special condition was implemented in the three-dimensional finite-element code presented before in this thesis and a test simulation was eventually performed for the proof of concept.

5.3 The mechanical problem

We have already introduced aortic dissections in the background chapter (section 1.6.3). We described dissections as a disease originated by a tear in the intima that allows the blood to penetrate in the media and subsequently generate a fracture splitting the arterial wall, leaving an external wall (generally made of the external third of the media and of the adventitia), while the inner wall is then denominated as flap (which includes the inner two thirds of the media and the intima layer). This flap divides the arterial lumen in a true lumen and a false lumen. If the false lumen experiences big dilatation it may compromise the blood flow in the true lumen and the oxigenation to downstream organs.
The aortic dissection is usually produced in a matter of second or minutes and is further classified in acute or chronic due to the time the patient can hold it. The former does not present a real interest for the development of this work as it leads to death if emergency surgery is not achieved. The latter becomes more interesting for the present work as the patient can harbor the dissection for a longer period allowing the aorta to evolve and adapt to this new mechanobiologic conditions.
In this chapter we aim to establish a mechanical framework for the formation and subsequent progression of patient-specific chronic aortic dissections. In consequence, assumptions need to be taken for the model. An initial aortic wall is composed of two perfectly connected bodies, where the connection is lost during the formation of the dissection, Fig. 5.1. Additionally, where the connection is lost, a pressure can be applied. The initial aortic wall is assumed to be healthy and in its preferred state. Accordingly, it can be used as reference in the application of the growth and remodeling (G&R) models. Connectors are placed in the interface

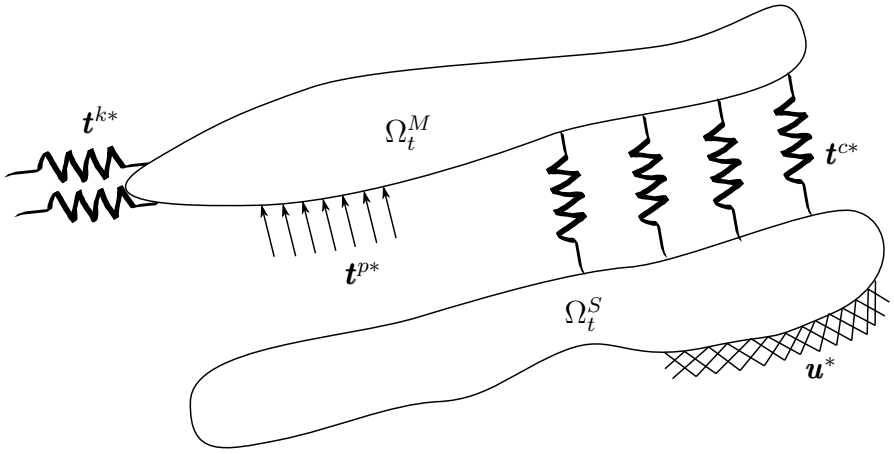

FIGURE 5.1 – The dissection model comprises two continuum bodies Ω_t^M and Ω_t^S, called the master and slave, respectively. Each body can have its own boundary conditions such as, pressure $\boldsymbol{t}^{p*}$, displacement impedance $\boldsymbol{t}^{k*}$ or imposed displacements $\boldsymbol{u}^*$. However, the two bodies share a special condition $\boldsymbol{t}^{c*}$ due to the connectors that keep the structure together.

between the two bodies (*e.g.* media and adventitia) and their failure produces a free surface where new pressure can be applied. A limitation is though that with those conditions the dissection plane is predefined.
Let Ω_t^M and Ω_t^S be two continuum bodies in the space $\mathbb{R}^3$, Fig. 5.1. The two bodies are connected by springs with a tension $\boldsymbol{t}^{c*}$. If the stiffness of the connectors (springs) is high enough the displacement of one body will be transmitted to the other body with low distortions. Additionally, if connectors are removed, the interaction of the two bodies will be partially lost, weakening the whole structure. The surface where connectors are removed is now free of interaction and other conditions can be assigned there, for example, a tension due to pressure $\boldsymbol{t}^{p*}$. The removal of the connectors would produce a change in the mechanical state of the structure composed by the two bodies. Such change can be considered as an alteration to perform further adaptations in the structure with G&R models.

5.4 Formulation of the interaction between layers

In the present work the connection of the two bodies is modeled by springs which are similar to the Robin boundary conditions. The difference lies in displacements of the spring. In the Robin boundary conditions, the displacement is assessed between the current and reference coordinates, while in the connector the spring displacement is assessed as the relative displacement between the slave and master bodies. The displacement of the master surface is $\boldsymbol{u}^M$ and the displacement of the slave surface is $\boldsymbol{u}^S$, with the current displacement defined in equation 1.4. Thereupon the virtual work in the connectors will be similar to the virtual work of the elastic Robin boundary conditions with the new relative displacement of

the spring,

$$\delta \mathcal{W}^{c}_{ext}(\boldsymbol{x}, \delta \boldsymbol{u}) = \int_{\partial \Omega_t} \delta(\boldsymbol{u}^S - \boldsymbol{u}^M) \cdot k(\boldsymbol{u}^S - \boldsymbol{u}^M) da \tag{5.1}$$

with the linearization of its virtual work due to the displacement increments,

$$\Delta\delta \mathcal{W}^{c}_{ext}(\boldsymbol{x}, \delta \boldsymbol{u}) \cdot \Delta \boldsymbol{u} = \int_{\partial \Omega_t} \delta(\boldsymbol{u}^S - \boldsymbol{u}^M) \cdot k\Delta(\boldsymbol{u}^S - \boldsymbol{u}^M) da. \tag{5.2}$$

If a finite-element (FE) method is considered, the domain of the continuum bodies is discretized. The discretization generates nodes and elements for the numerical resolution. Thereafter when the integral surface in the virtual work or its linearization (Eqs. 5.1 and 5.2, respectively) is computed, it is possible to perform the computation either in the faces of the elements (surface) or in the nodes of the interacting surfaces. Our approach does it in the nodes of the interactig surfaces for the sake of simplicity of the formulation. Therefore, the integrals become sums on the connectors, where each connector is defined by two nodes, one in the slave and another in the master surface. Let a denote the nodes of the connector. The displacement of the connector, its virtual work and the linearization of the virtual work are

$$\boldsymbol{u}^S - \boldsymbol{u}^M = \boldsymbol{u}^S_a - \boldsymbol{u}^M_a, \tag{5.3}$$

$$\delta \mathcal{W}^{ce}_{ext}(\boldsymbol{x}, \delta \boldsymbol{u}) = \sum_a \delta(\boldsymbol{u}^S_a - \boldsymbol{u}^M_a) \cdot k(\boldsymbol{u}^S - \boldsymbol{u}^M), \tag{5.4}$$

$$\Delta\delta \mathcal{W}^{ce}_{ext}(\boldsymbol{x}, \delta \boldsymbol{u}) \cdot \Delta \boldsymbol{u} = \delta(\boldsymbol{u}^S_a - \boldsymbol{u}^M_a) \cdot k\Delta(\boldsymbol{u}^S_b - \boldsymbol{u}^M_b). \tag{5.5}$$

The springs between the interacting surfaces are denominated connectors because they connect the nodes of the master surface with the slave surface one to one. This requires to predefine the corresponding nodes with the shortest distance between the slave and master surfaces. The formulation was developed in order to avoid using contact algorithms that could demand high implementing efforts and high computational resources.

5.5 Implementation

The interaction of the two bodies for the dissection model was implemented within the code of the Robin boundary conditions, Fig. 5.2. The computation of the connector tension was developed additionally to the computation of the tensions due to pressure and elastic boundaries. Accordingly, all the displacement-dependent tensions were managed in the same part of the code. Furthermore, the connectors implementation worked with "flags" on the faces of the interacting surfaces to assign the nodes with connectors and eventually remove the connector if needed. The computations for the connector forces and stiffness are managed in the routine `StaticConnectorAssmebler`. The procedure followed by this routine is represented in figure 5.3. The routine gives a global force vector assembled from the slave and master forces, $\boldsymbol{f}^S$ and $\boldsymbol{f}^M$; and a global stiffness matrix ($\boldsymbol{K}$) assembled from the stiffness of the connector element in its correspondent nodes a and b.

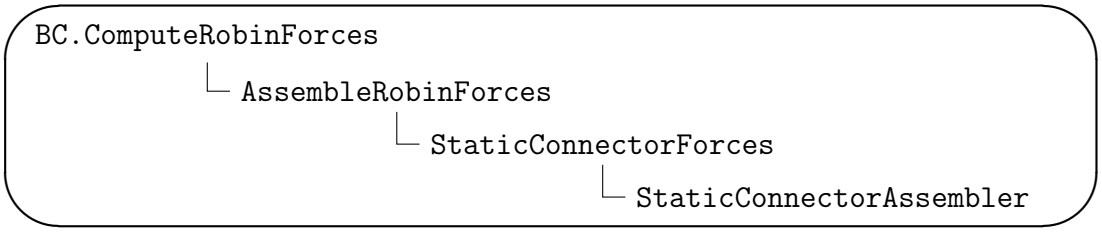

Figure 5.2 – Connector forces implementation within the Robin boundary conditions.

⋆ Loop on the connectors elements
- Assign the stiffnes k to the connector
- Find master and slave points in the connector
  $\boldsymbol{x}^M$ and $\boldsymbol{x}^S$
- Compute displacement of the connector
  $\boldsymbol{u}^S - \boldsymbol{u}^M$
- Compute local forces in the slave and master points
  $\boldsymbol{f}^S = k(\boldsymbol{u}^S - \boldsymbol{u}^M)$ for $\delta\boldsymbol{u}_a^S$
  $\boldsymbol{f}^M = -k(\boldsymbol{u}^S - \boldsymbol{u}^M)$ for $\delta\boldsymbol{u}_a^M$
- Compute the local stiffness matrix
  $\boldsymbol{k}_{ab}^{SS} = k$ for $(\delta\boldsymbol{u}_a^S, \Delta\boldsymbol{u}_b^S)$
  $\boldsymbol{k}_{ab}^{SM} = -k$ for $(\delta\boldsymbol{u}_a^S, \Delta\boldsymbol{u}_b^M)$
  $\boldsymbol{k}_{ab}^{MS} = -k$ for $(\delta\boldsymbol{u}_a^M, \Delta\boldsymbol{u}_b^S)$
  $\boldsymbol{k}_{ab}^{MM} = k$ for $(\delta\boldsymbol{u}_a^M, \Delta\boldsymbol{u}_b^M)$

⋆ Assemble global forces and stiffness
  $\boldsymbol{f}^S, \boldsymbol{f}^M \rightarrow \boldsymbol{f}$
  $\boldsymbol{k}_{ab}^{SS}, \boldsymbol{k}_{ab}^{SM}, \boldsymbol{k}_{ab}^{MS}, \boldsymbol{k}_{ab}^{MM} \rightarrow \boldsymbol{K}$

Figure 5.3 – Connector assembler.

⋆ Feed the routine with dissection spread parameters
d_{max} and T_{dis} maximum spread and time threshold, respectively
⋆ Compute the speed of spread of the dissection
$v_{dis} = d_{max}/T_{dis}$
⋆ Assign the spread of the dissection
$d_{dis} = v_{dis} \times t$, if $t < T_{dis}$
$d_{dis} = d_{max}$, if $t \geq T_{dis}$
⋆ Loop on connector elements
• If $x_z < d_{dis}$
∗ Vanish connector
∗ Activate pressure in the faces containing the node

FIGURE 5.4 – Connector assembler.

Additionally, within the G&R time integrator we included a routine to manage the propagation of the dissection in the arterial model, called `ComputeDissectionSpread`. Basically this routine shifts the "flags" of the connector and pressure in the Robin boundary conditions to remove connectors and assign pressure in the new free faces, Fig. 5.4.

5.6 Simulations

A test simulation was performed for the dissection problem. The artery was represented by two concentric cylinders with different inner radii. The inner cylinder has an inner radius of 10-mm and a thickness of 0.705-mm, while the outer cylinder has an inner radius of 10.715-mm and a thickness of 0.705-mm. The inner cylinder represents the media and the outer cylinder represents the adventitia. The dissection surface is defined between the surfaces generated by the outer radius of the media and the inner radius of the adventitia, and initially the two layers are completely connected at this surface. The dissection is then produced up to 10-mm in the axial direction within 40-days. A pressure of 80-mmHg is applied on the newly created surfaces, while in the true lumen the pressure is always kept as 100-mmHg. The mechanical properties used for the arterial wall are the same ones as Braeu et al [27].

Figures 5.5 and 5.6 show the planes XZ and XY of the dissection in the cylinder after 100-days of mechanobiological adaptation. The two layers disengage according to the dissection parameters while G&R of the tissue is still effective. The new conditions produce a reduction of the diameter of the media in the dissected zone, and the increase of the diameter of the adventitia.

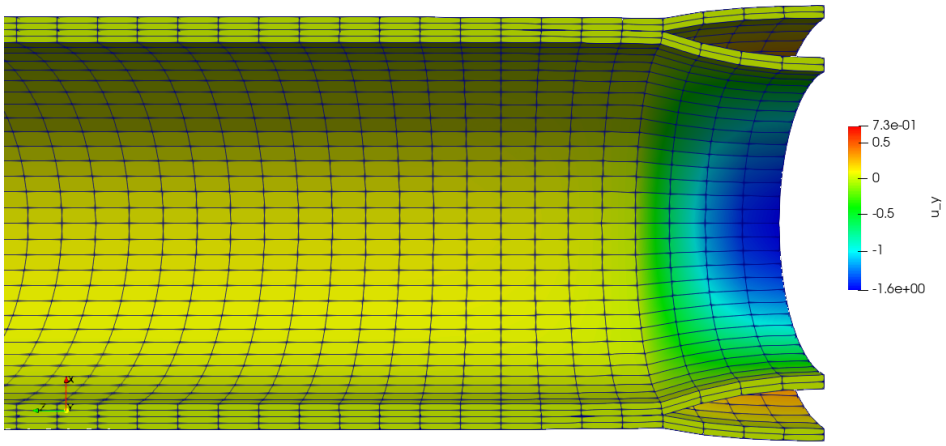

Figure 5.5 – View of the XZ plane of the dissected cylinder.

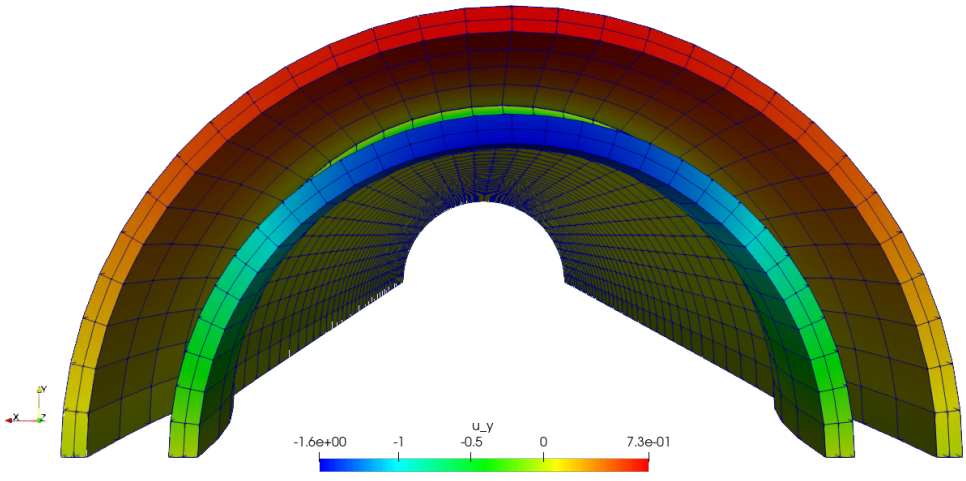

Figure 5.6 – View of the XY plane of the dissected cylinder.

5.7 Conclusion

The formulation presented in this chapter allowed to simulate the evolutions of the aortic wall after the propagation of a dissection. Eventually this approach could help to estimate the dimensional changes occurring in a dissected aorta and consequently evaluate the risks for a given patient.
The model of the artery was made of two concentric cylinders representing the media and adventitia, given the mechanical relevance of these two layers. The two cylinders have initially a small gap but behave as a single layer with reduced distortions. The two cylinders are connected through special conditions applied between the two surfaces.
This formulation permitted to avoid contact elements between the two surfaces. This avoided the nonlinearities and the long resolution times due to the search of interacting nodes in the contact. Consequently this method offered a simple interaction of the two arterial layers, which are assumed to be perfectly tied in healthy conditions. Moreover, the connectors were uni-dimensional elements (springs or bars) with high stiffness to reduce the distortions between the two layers. The connector could be seen as a penalty method penalizing the motion of one layer with respect to another.
In the approach developed here, the dissection propagated along an assigned surface and it was managed by a temporal function. Eventually this work could be completed with cohesive fracture models [98]–[100] in an attempt to relate the stress with the propagation of the dissection.
The dissection surface was initially defined. This may represent a major limitation if one would like to predict the dissection process. But our goal here was to simulate the evolution of a chronic dissection at the long term. Nevertheless, future challenges will be to enhance this model with cohesive fracture for the initial development of the dissection [98], [100]. Moreover, our implementation could be coupled with extended FE using energy dissipation [101], [102]. Such model would allow to propagate the dissection without the limitation of predefining the fracture surface.

Conclusion Générale en français

Synthèse

La paroi aortique a une structure et une composition complexes, elle est composée de la matrice extracellulaire (ECM) et des cellules qui y sont intégrées. L'ECM est une structure qui maintient les cellules en place, mais de la même manière, l'ECM est entretenue par les cellules, qui évaluent et synthétisent les protéines de l'ECM. De plus, les cellules et l'ECM sont organisées en différentes couches dans l'artère, avec des fonctions spécifiques. Dans ce travail, la paroi aortique a été abordée en incluant deux couches ou phases mécaniques pertinentes: la média et l'adventice. L'intima est négligée car elle n'a pas de pertinence mécanique. On considère que chaque phase est composée de cellules et d'ECM, l'ECM étant constitué d'élastine (supposée isotrope) et de fibres de collagène. Dans le cadre de la mécanique des milieux continus, on suppose que tous les matériaux (cellules, élastine et collagène) de la paroi aortique sont parfaitement mélangés en chaque point.

En outre, les adaptations du tissu aortique ont été modélisées par les modèles de croissance et de remodelage (G&R). Dans ce travail, on utilise spécifiquement le modèle de mélange contraint homogénéisé (hCM) pour ses facilités d'implémentation et sa consommation réduite en ressources de calcul, par rapport aux modèles de mélange contraint classique. La sélection de ce modèle permet de modéliser les déformations inélastiques en référence à l'état homéostatique, lié à l'état préférentiel du tissu. En effet, les modèles constitutifs des déformations inélastiques dépendent de la différence entre la contrainte actuelle et la contrainte homéostatique. Néanmoins, les déformations inélastiques peuvent également être induites par des variations des contraintes ou de la rigidité, par exemple dans le cas des modèles d'étirement de recrutement pour la G&R.

Au début du travail de mise en œuvre, plusieurs complications sont apparues lors de l'implémentation du modèle hCM dans un solveur d'éléments finis (FE) tridimensionnel, tel qu'`ABAQUS`. À ce moment-là, il était également difficile de comprendre toute la portée de la G&R appliquée aux trois dimensions. Il a donc été décidé de laisser de côté `ABAQUS` pendant un certain temps et de travailler dans un code bidimensionnel dans le but de mieux comprendre les effets de la G&R dans les artères en effectuant plusieurs simplifications dans le modèle. Cela a abouti à l'écriture d'un code `FORTRAN` pour les éléments de coque axisymétriques. Le développement de ce code permet de réduire l'analyse des quantités tensorielles

à leurs directions principales et de réduire le temps de calcul pour les simulations de G&R dans les artères cylindriques.
Avec le code axisymétrique développé dans cette thèse, il a été possible d'exécuter trois cas de simulation, par exemple, l'élargissement de l'anévrisme, le déploiement d'une endoprothèse et l'élargissement de l'anévrisme avec la pose ultérieure d'une endoprothèse. L'agrandissement de l'anévrisme est l'analyse typique réalisée avec les modèles G&R. Elle commence par une dégradation brutale de l'élastine dans la paroi artérielle qui, à moyen terme, entraîne la croissance d'un anévrisme. Pour la première fois, les effets G&R produits dans une artère après la pose d'une endoprothèse ont été étudiés. Le surdimensionnement du stent augmente la contrainte dans la longeur du segment de l'endoprothèse et à son bord, ce qui provoque un remodelage de l'artère. Le dernier cas analysé correspond à l'élargissement d'un anévrisme dans l'aorte dû à une forte dégradation initiale de l'élastine avec la pose d'une endoprothèse après quelques années de développement de l'anévrisme. L'endoprothèse modifie les charges sur l'artère et réduit finalement la taille de l'anévrisme comme prévu. Enfin, après la mise en place d'une endoprothèse, le modèle tend à relâcher la contrainte dans l'artère, en fonction de paramètres G&R adéquats, tels que le taux d'ajout de collagène.
De toute évidence, après la mise en œuvre réussie du code bidimensionnel, l'étape suivante de ce travail a consisté à développer un solveur d'éléments finis tridimensionnel pour le G&R. Dans ce cas, le modèle hCM a été implémenté dans un solveur FE open-source disponible sur `GitHub` [30] et développé à l'université de Swansea [66], [67]. Le programme est écrit en `Python` et `C++` et ses routines sont clairement commentées ce qui permet une compréhension facile du code et facilite les modifications ultérieures. Les modifications apportées à ce code ont pour objectif l'implémentation de la G&R pour l'analyse vasculaire. Par conséquent, les routines ont été construites pour le modèle hCM et pour le matériau de mélange pour la paroi artérielle, de plus, il était nécessaire de créer les routines pour les charges dépendantes des déformations, telles que, la pression et les limites élastiques des conditions limites de Robin.
Avec cette dernière implémentation de G&R dans le solveur FE tridimensionnel, il a été possible d'exécuter des simulations dans des formes cylindriques, toriques et spécifiques au patient. Une fois encore, la forme cylindrique est la simulation de référence pour l'implémentation des modèles G&R avec une forte dégradation initiale de l'élastine ; elle est utilisée pour comparer les résultats fournis par le code développé ici avec les résultats de la littérature [27]. Par la suite, les simulations pour le tore et la forme spécifique du patient ont représenté une difficulté supplémentaire, car nous avons constaté que la mise en place de la configuration homéostatique nécessite une attention particulière dans ce type de formes. La mise en place de la configuration homéostatique a été résolue par l'utilisation d'un préétirement non uniforme pour réduire les distorsions par rapport à la configuration de référence. En fin de compte, cette approche permet de maintenir les contraintes homéostatiques dans la plage des contraintes normales pour une artère *in vivo*. Sa dernière conséquence est la stabilisation des simulations G&R dans les géométries

courbes et permet une longue durée de simulation (+10 ans).
Enfin, la dissection aortique s'est révélée être une application intéressante du modèle G&R développé dans ce travail. Le travail a commencé avec des modèles d'artères disséquées, mais comme une artère disséquée pourrait ne pas être considérée comme un état homéostatique nous avons commencé à mettre en œuvre un modèle de propagation de la dissection dans le solveur EF. Il n'a pas été possible d'aller plus loin dans ce projet en raison de contraintes temporelles liées au développement de cette thèse. Ainsi, le modèle de propagation et de G&R subséquent dans la dissection aortique est simplement implémenté dans le solveur et les applications plus poussées à des géométries spécifiques au patient font l'objet de travaux futurs.

Limites

L'une des premières limites du travail présenté ici est que la pression luminale augmente avec l'âge en l'espace de quelques décennies dans l'aorte. Cependant, de tels effets ont été négligés dans ce travail, bien que les simulations aient été effectuées sur des échelles de temps de l'ordre d'une ou deux décennies. En fait, il s'agit d'un élément qui peut être ajouté à la simulation de la G&R. Dans la littérature [63], cette augmentation de la pression dans les artères est attribuée à l'augmentation de la rigidité de la paroi artérielle avec le changement des dimensions de l'aorte qui, à terme, nécessiterait des efforts plus importants de la part du cœur pour pousser le sang dans tout le système.
Dans ce travail, la présence de l'intima dans le modèle aortique a été négligée. En effet, l'intima est généralement supposée ne pas avoir d'effets mécaniques importants sur l'ensemble de la structure. Ainsi, dans les simulations effectuées dans ce travail, on a généralement supposé que la paroi aortique ne comportait que la média et l'adventice. En outre, chaque couche comporte plusieurs types de cellules et de protéines qui composent l'ensemble du tissu. Au moins ici, on a supposé que les modèles contiennent de l'élastine, du collagène et des cellules musculaires lisses comme constituants les plus appréciables. Malgré cela, il existe d'autres matériaux intégrés dans la structure qui sont ici considérés comme faisant partie de la structure de l'élastine. L'élastine est considérée comme un matériau isotrope malgré son organisation en fibres élastiques organisées en lamines élastiques concentriques. De plus, dans le modèle hCM, les constituants sont réduits à un point infiniment petit où ils sont parfaitement mélangés ; néanmoins, dans une paroi aortique réelle, le milieu est organisé en couches concentriques successives de lamelles élastiques et de cellules musculaires lisses, sans mélange parfait des constituants dans un espace plus petit que les cellules.
Ce que l'on appelle l'état homéostatique est lié à l'état préféré (généralement mesuré par le stress) dans lequel les cellules sont à l'aise pour leur fonction, sans qu'il y ait de définition rigoureuse. Normalement, l'état homéostatique est défini à partir d'une contrainte moyenne comprise entre 100 kPa et 150 kPa, qui correspond

à la contrainte dans une artère dans des conditions normales de pression (80 mmHg à 120 mmHg) et des conditions normales du tissu artériel. Malheureusement, la pression et le tissu changent dans le temps et il serait difficile de sélectionner un âge de référence pour la géométrie, la structure du tissu et les conditions de charge. Enfin, dans le cas de géométries spécifiques au patient (obtenues à partir du scanner), on suppose que l'image actuelle du patient se trouve dans un état homéostatique et que la G&R est effectuée à partir de ce point, indépendamment du fait que le patient soit déjà porteur d'une maladie. Cet obstacle serait plus clair dans le cas du scanner d'une aorte disséquée où la configuration de l'aorte avant la dissection est totalement inconnue et où l'image du scanner ne peut pas être considérée comme la cible homéostatique des adaptations dans le cadre de la G&R.
Il a été prouvé que les modèles de la G&R capturent la régénération du tissu dans la paroi aortique. Néanmoins, le modèle hCM comprend trois modèles constitutifs pour la déformation inélastique (remodelage et croissance) et les densités, et chaque équation a ses propres paramètres à définir. Le taux net de densité de masse est principalement contrôlé par le paramètre de gain qui contrôle la vitesse à laquelle un constituant est déposé dans le tissu et il est particulier à chaque constituant. Le remodelage utilise la demi-vie du constituant comme paramètre et il est également particulier à chaque constituant. La mesure de ces paramètres peut être compliquée à obtenir car la demi-vie et la vitesse à laquelle les matériaux sont déposés peuvent être particulières à chaque patient et il peut être difficile de les mesurer chez un patient vivant. On dispose de quelques données sur la demi-vie des constituants de la paroi aortique, mais elles se situent dans une fourchette très large [2], [12].
Les programmes développés dans ce travail contiennent encore quelques problèmes. Par exemple, le code de coque axisymétrique n'a pas réussi la comparaison avec le cas de référence pour les modèles G&R, mais dans ce cas particulier, cela est dû à la mise à jour des densités constitutives. Cela a été réglé dans la dernière version du code publiée. Les simulations tridimensionnelles présentent des problèmes liés au module de masse (κ^e) pour l'incompressibilité de l'élastine qui doit être faible pour assurer la convergence du modèle, ce problème peut être attribué à la croissance due aux changements de volume et de forme. Un autre problème survient dans le cas spécifique d'un patient où il y a une concentration de contraintes dans une limite qui peut être attribuée à la géométrie irrégulière obtenue du patient ou à la nature des conditions aux limites, en fait, les conditions aux limites appliquées dans ce cas sont la réaction élastique parce qu'elle réduit la contrainte dans cette limite par rapport aux rouleaux radiaux ou aux conditions d'encastrement.

Contributions

Les contributions de ce travail par rapport à la littérature sont listées ici:

- un code de coque axisymétrique a été écrit à partir de zéro pour résoudre

G&R pour les artères cylindriques, qui peut fournir des résultats rapides après avoir pris en compte plusieurs simplifications [70] ;

- avec le modèle de coque bidimensionnel ont été calculés pour la toute première fois les effets du déploiement d'un stent dans une artère et l'évolution du tissu autour;
- un code tridimensionnel plus général a été modifié pour inclure la G&R pour les problèmes de mécanique vasculaire et il est open-source et disponible dans `GitHub` [30] ;
- dans ce travail ont été effectuées des simulations G&R dans un patient spécifique obtenu à partir du scanner, même si cela est dans la littérature, les simulations ici sont moins contraintes pour assurer la convergence;
- la G&R dans le cas spécifique du patient a été possible à travers un préétirement non uniforme dans la direction longitudinale et circonférentielle pour trouver un état homéostatique compatible;
- il est proposé ici une formulation pour la propagation de la dissection aortique et pour la première fois un modèle G&R est appliqué sur une dissection chronique;
- premier auteur de l'article "A new finite element shell model for arterial growth and remodeling after stent implantation", publié dans *Internatial Journal for Numerical Methods in Biomedical Engineerging* [69] ;
- co-auteur d'article "3D finite-element modelling of vascular adaptation after endovascular aneurysm repair", accepté dans *International Journal for Numerical Methods in Biomedical Engineering* [103] ;
- premier auteur de l'article "About prestretch in homogenized constrained mixture models: simulating growth and remodeling in patient-specific aortic geometries", accepté dans *Biomechanics and Modeling in Mechanobiology*, maintenant en révision [104].

Perspectives

Malgré les nombreuses simulations de G&R présentées dans cette thèse, la validation expérimentale des modèles fait toujours défaut. Car jusqu'à présent, les modèles G&R ont été utilisés pour analyser le développement d'anévrismes dans des modèles d'artères [16] et pour étudier le concept de stabilité mécanobiologique lié à l'homéostasie [8]. En outre, Mousavi et al [18] ont comparé les résultats de G&R avec un modèle statistique pour la croissance des anévrismes. De plus, dans ce travail, il a été possible d'appliquer un modèle G&R à une géométrie spécifique au patient. Par conséquent, il pourrait être possible de suivre les aortes d'une cohorte de patients pendant plusieurs années (10 ans environ) pour recueillir

des données expérimentales sur l'élargissement des anévrismes qui pourraient être comparées aux résultats donnés par les modèles G&R, et finalement ajuster les paramètres liés à la demi-vie et aux taux de renouvellement des constituants du tissu.
Des données expérimentales peuvent également être recueillies pour les dissections aortiques. À partir du modèle de dissection, on peut suivre la propagation de la dissection dans l'artère. Et avec le modèle de G&R, il est possible de modéliser les adaptations des tissus après la dissection, puis de comparer l'évolution du modèle avec les images temporelles de l'aorte disséquée du patient pour ajuster les paramètres du moèdel de G&R. Au final, cela permettrait de proposer un outil pour estimer les changements géométriques, ainsi que le stress et la rigidité de l'aorte, qui pourrait être utilisé pour prendre des décisions concernant l'application ou non de la chirurgie chez un patient. Il s'agit d'un travail pourquivi par Shaojie Zhang, actuellement post au laboratoire.
Dans la simulation de l'aorte thoracique ascendante spécifique à un patient, il a été déduit que la pré-tension peut être non uniforme dans l'état homéostatique afin de répondre aux exigences de compatibilité pour la G&R et de maintenir les contraintes dans une plage "normale" (entre 100-kPa et 150-kPa). Cependant, cette hypothèse doit être prouvée expérimentalement en mesurant les déformations entre les configurations *in vivo* et *ex vivo* de l'aorte. Cela peut présenter plusieurs difficultés en raison de la nécessité d'effectuer des mesures sur le patient vivant et d'autres mesures une fois que l'aorte n'est plus dans le patient (par exemple lors d'une intervention chirurgicale). Une autre option pourrait être le développement d'une méthode dans laquelle les mesures *in vivo* peuvent fournir toutes les informations nécessaires au calcul de l'étirement ou de la précontrainte.
Une analyse supplémentaire peut être proposée pour les simulations de déploiement de stent réalisées dans cette thèse. Après l'implémentation du solveur tridimensionnel, l'analyse du stent peut être étendue à la paroi artérielle épaisse. Le stent peut être modélisé en évitant les modèles de contact en utilisant une approche similaire à celle utilisée ici dans le modèle bidimensionnel. Un bon point de départ serait d'écrire quelques modifications dans les routines pour les conditions aux limites élastiques afin d'imiter le placement du stent. En fait, cette recherche correspond au travail entrepris par Shaojie Zhang, post-doc au laboratoire, et elle a conduit à la publication d'un article.
Aujourd'hui, les modèles G&R ont trouvé un autre domaine de développement dans la conception de matériaux d'ingénierie tissulaire pour les prothèses dans les vaisseaux sanguins (artères et veines) ou les valves cardiaques. Le matériau d'ingénierie tissulaire peut être ajouté à la bibliothèque du code tridimensionnel avec sa formulation correspondante adaptée au modèle G&R. De cette manière, le modèle hCM mis en œuvre dans le code peut modifier le matériau en fonction des adaptations qui se produisent dans le tissu sur une longue échelle de temps. Cette ligne correspond également à une recherche entreprise dans le projet SimInSitu (http://www.siminsitu.eu/), dans le cadre duquel Felipe Sempertegui a démarré un post-doc au laboratoire pour poursuivre les développements.

Un problème artériel généralement négligé dans le développement de la maladie est la formation de la plaque d'athérome (collée à l'intima). Cela qui peut être implémenté dans le solveur tridimensionnel avec l'écriture d'un nouveau matériau qui considère les propriétés de la plaque dans le mélange. Il pourrait être nécessaire de supposer un modèle à trois couches pour la paroi artérielle, de sorte que les propriétés de la plaque soient simplement attribuées à d'intima. De plus, dans le modèle, on peut considérer la contrainte de cisaillement pariétal due au flux sanguin comme une entrée pour une fonction qui détermine les régions avec formation de plaque.
Enfin, le code tridimensionnel prend encore beaucoup de temps pour réaliser des simulations dans une géométrie spécifique au patient. Pour le travail futur dans le code, les routines pourraient être améliorée pour rendre les calculs plus rapides ; le passage de certaines routines –comme la routine de croissance et de remodelage– d'un langage de haut niveau à un langage de bas niveau pour diminuer le temps de calcul. Enfin, l'adaptation des routines au calcul parallèle, permettrait que le code utilise toute la performance d'un ordinateur multi-tâches.

General Conclusion

Overview

The aortic wall has a complex structure and composition, it is composed by the extracellular matrix (ECM) and cells embedded in it. The ECM is a scaffold that keeps the cells in place and simultaneously the ECM is maintained by the cells, which assess their environment and synthesize proteins to modify it. Additionally the cells and the ECM are organized in different layers within the artery with specific functions. In order to model these evolutions in the aorta, it is necessary to develop a model distinguishing the layers as a composite material. In this work, the aortic wall was modelled including two relevant mechanical layers or phases, the media and adventitia, whereas the intima was neglected. The tissue was modelled as a mixture made of cells and of the ECM, the ECM comprising an isotropic matrix (which includes the contribution of elastin) reinforced by collagen fibres. We assumed that these different components of the tissue (cells, elastin and collagen) are perfectly mixed together.

Furthermore, the aortic tissue adaptations were modeled with the Growth and Remodeling (G&R) theory. More specifically in this work, we used the homogenized Constrained Mixture (hCM) model for the reduced computational resources needed, compared to the traditional Constrained Mixture models. The selection of this approach permitted to model the inelastic deformations with reference to the homeostatic state, which is introduced as the preferred state of the tissue. Indeed the constitutive models of the inelastic deformations depend on the difference between the current stress and the homeostatic stress.

We solved several challenges related to the implementation of the hCM model in a three-dimensional finite-element (FE) solver. We first worked on a two-dimensional code with the aim to embrace the G&R effects in arteries by performing several simplifications in the model. This ended up in writing a `FORTRAN` code from scratch for the axisymmetric shell elements. The development of this code allowed to reduce the analysis of the tensorial quantities to their principal directions and reduce the computation time for G&R simulations in cylindrical arteries.

With this code, it was possible to execute three simulation cases, namely, aneurysm enlargement, stent-graft deployment, and aneurysm enlargement with subsequent stent-graft placement. The aneurysm enlargement is a typical analysis performed

with G&R models [12], [16], [27], starting with a sharp degradation of elastin in the arterial wall (insult) that in the long term induces aneurysm growth. For the first time ever, the G&R effects produced in an artery after the placement of a stent-graft were simulated numerically. We showed that the oversizing of the stent-graft can provoke remodeling in the artery. Regarding aneurysm enlargement due to initial sharp elastin degradation, we showed also that it can be stopped after placing the stent-graft as the stress in the aortic wall are eventually decreased.
We also developed a thee-dimensional FE solver for G&R. In this case the hCM model was implemented within an open-source FE solver available in `GitHub` [30] and developed initialy at Swansea University [66], [67]. The program is written in `Python` and `C++` and its routines are clearly commented which allows an easy understanding of the code and facilitate further modifications. The modifications done in this code were the implementation of G&R for vascular analysis. For that, we built the routines for the hCM model and for the mixture material of the arterial wall. Moreover, we created routines for deformations-dependent boundary conditions, such as, the pressure and elastic boundaries from the Robin boundary conditions.
With the latter G&R implementation in the three-dimensional FE solver, it was possible to execute simulations in cylindrical, toric and patient-specific aortic models. Again the cylindrical shape is the benchmark simulation for G&R models implementation. It was used to compare our results against previous results of the literature [27]. Thereafter, the simulations for the torus and patient-specific aortic models had to overcome another challenge related to assigning the homeostatic configuration. The setup of the homeostatic configuration was solved with the use of non-uniform prestretch to reduce the distortions with respect to the reference configuration. Ultimately this approach keeps the homeostatic stresses within the range of normal stresses for an *in vivo* artery. Another positive consequence is the stabilization of the G&R simulations in curved geometries for long simulations (>10 years).
Finally, the aortic dissection emerged as an interesting application to the G&R model developed in this work. As a dissected artery might not be considered as the homeostatic state, we started the implementation of a dissection propagation model within the FE solver. The model for propagation and subsequent G&R in aortic dissections has just been implemented in the solver and further applications to patient-specific geometries are in progress.

Limitations

One of the first limitations of the work presented here is that the average luminal pressure changes with age in the aorta. However such effects were neglected in this work. This is something that can be added to the G&R simulations in the future. In the literature [63] this change of pressure in the arteries is attributed to the increasing stiffness of the arterial wall and to the change of dimensions of

the aorta, requiring increasingly higher efforts from the heart to pump the blood into the system.
In this work we neglected the presence of the intima in the aortic model, as the intima is usually assumed to have marginal mechanical effects in the whole structure. We assumed that the aortic wall can be modeled with 2 layers, the media and the adventitia. Furthermore, each layer has a different structure with different cells and proteins composing the tissue. We assumed that the tissue comprises elastin, collagen and smooth muscle cells as the constituents with the most significant contribution to the mechanical behaviour. Other constituents such as proteoglycans embedded in the structure have been omitted. The elastin was modeled as embedded in an isotropic material despite its fibrous organization in concentric laminas. Additionally, in the hCM model the constituents are reduced to a infinitesimally small point where they are perfectly mixed. This may not be the case in an actual aortic wall where the media is organized in subsequent concentric layers of elastic lamina and smooth muscle cells, which is actually not a perfect mixture.
The so called homeostatic state related to the preferred state (usually expressed with a preferred stress) in which the cells are comfortable for their function lack of a rigorous definition. Normally the homeostatic state is defined from an average circumferential stress between 100-kPa to 150-kPa, which is the circumferential stress in an artery under normal conditions of pressure (80-mmHg to 120-mmHg) and normal conditions of the arterial tissue. Unfortunatelly the pressure and the tissue change in time and it would be difficult to select an age for the reference of the geometry, tissue structure and loading conditions. Finally in the case of patient-specific geometries (obtained from CT scans) it is assumed that the patient is in the homeostatic state. The G&R is intialized from this point on, independently if the patient is already harboring a disease. This problem is exacerbated for dissected aorta where the configuration of the aorta before dissection is completly unknown and the CT scan cannot be considered as the homeostatic target of the adaptations under G&R.
The G&R models have proved to be useful in the modeling of tissue regeneration [9]. Nonetheless, the hCM model includes three constitutive models for the inelastic deformation (remodeling and growth) and densities, and each equation have its own parameters to define. The net rate of mass density is mainly controled by the gain parameter that controls the speed in which some constituent is deposited in the tissue and it is particular to each constituent. The remodeling uses the half-life of the constituent as a parameter and it is also particular to each constituent. The measurement of such parameters can be challenging to obtain as the half-life and the speed at which the materials are deposited. They can be specific to each patient and they may be difficult to measure. There are some data available related to the half-life of the constituents in the aortic wall but they are in a very wide range [2], [12].
In this work the production of collagen depends on the extant collagen and on the difference between current and homeostatic stresses. Nonetheless, in the arterial wall the production of collagen is controlled by the cells (SMCs and fibroblasts),

this establish a dependence of the rate of collagen production with the amount of cells in the neighborhood. Hence, the production of collagen might also depend on the amount of cells to represent feasible values that an actual artery can handle.

In this work, it has been taken an homogenized approach for the increments of mass of the constituents in the tissue. Such homogenization of the mass increments produce a perfect combination of the newly produced collagen with the extant collagen, this is, after the addition, the collagen is one material with averaged properties. Hence the model does not distinguish the newly produced collagen from the extant one. The homogenized model is then not able to have increments of collagen produced at different times with different properties, for instance, different prestretch. Another limitation due to the non-differentiation of collagen is the lack of a description for the aging of the newly produced collagen. By not having a description of the aging of collagen, the model is neglecting changes on the stiffness of each increment of collagen in time.

By having a thrombus attached to the arterial wall, it already means non-healthy conditions. In this case the artery may not be considered in a stable state and such conditions does not suit to the definition of homoestasis. Consequently, some assumptions of the shape and state of the artery previous to the thrombus formation might be needed, unfortunately, such state would be fictitious.

In an actual arterial wall the production of collagen is driven by the SMCs with synthetic function. However, in this work the production of collagen has not been related to the amount of synthetic SMCs present in the neighborhood and the SMCs has been considered with its passive behavior, active behavior of SMCs was just considered for the cylinder case. Consequently, in this work the mechanical model does not distinguish synthetic cells from contractile cells. Furthermore, the production of collagen have not dependence on the amount of SMCs for this model. This is then different from the process of production of collagen in the arterial wall and it may represent a limitation with the feasible levels of collagen production in an artery and the actual stress in the cells. Furthermore, by assuming a switch of the cells in their phenotypes, there will be a continuous evolution of the feasible levels of collagen production and active stress in the artery.

The codes developed in this work can still be improved. For example the axisymmetric shell code did not agree accurately with the benchmark case for G&R models, but this was due to the update of constituent densities. The bug was fixed in the latest version of the code. The three-dimensional simulations had issues related to the bulk modulus (κ^e) for incompressibility of elastin, which has to remain low enough in order to ensure the convergence of the model. This problem was attributed to the changes in volume and shape. Another problem arose in the patient-specific case where there was a concentration of stress in one boundary. This may be attributed to the irregular geometry obtained from the patient or from the nature of the boundary conditions. Actually, the boundary conditions applied in this case were the elastic reactions as this reduced the stress in such boundary with respect to radial rollers or clamping conditions.

Contributions

The contributions of this work with respect to the state of the art are listed here:

- an axisymmetric shell code was written from scratch to solve G&R for cylindrical arteries, which can provide fast results after taking into account several simplifications [70];
- with the two-dimensional shell model we computed for first time ever the effects of stent-graft deployment on the evolution of the aneurysm;
- a more general three-dimensional FE code was modified to include G&R for vascular mechanics problems. It is open-source and available in `GitHub` [30];
- in this work we performed G&R simulations in a patient-specific aortic geometry obtained from a CT scan;
- G&R in the patient-specific case was possible after introducing non-uniform prestretches in the longitudinal and circumferential directions to find a compatible homeostatic state;
- we proposed a formulation for the propagation of aortic dissections and a G&R model was applied for the first time to simulate the evolution of a chronic dissection;
- first author of the article "A new finite element shell model for arterial growth and remodeling after stent implantation", published in Internatial Journal for Numerical Methods in Biomedical Engineerging [69];
- co-author of the article "3D finite-element modelling of vascular adaptation after endovascular aneurysm repair", accepted in International Journal for Numerical Methods in Biomedical Engineering [103];
- first author of the article "About prestretch in constrained mixture models: simulating growth and remodeling in patient-specific aortic geometries", currently in review in Biomechanics and Modeling in Mechanobiology [104];

Future work

One of the major challenge for future work is related to the experimental validation of the models. Until this point the G&R models have been used to analyse the development of aneurysms in models of arteries [16] and the concept of mechanobiological stability related to homeostasis [8]. Furthermore, Mousavi et al [18] compared G&R results with a statistical model for the growth of aneurysms. Moreover, in this work it was possible to apply a G&R model to a patient-specific geometry. Consequently, it might be possible to follow up the aortas of a cohort of patients for several years (10 approximately) to collect experimental data for

the enlargement of aneurysms that can be compared with the results given by the G&R models, and ultimately identify parameters such as the half-life and the rate of constituents turnover.
Experimental data can also be collected for aortic dissections, for instance by tracking the evolution of the dissected aorta of the patient to fit the G&R parameters. Eventually this would enable to estimate geometrical changes along with stress and stiffness in the aorta. The work on aortic dissections is still on going with Shaojie Zhang, currently post-doc in our group.
In the simulation of patient-specific Ascending Thoracic Aorta we deduced that the prestretch can be non-uniform in the homeostatic state to meet the compatibility requirements for G&R and keep the stresses in a normal range (between 100-kPa to 150-kPa). However, this hypothesis should be proved experimentally by measuring the deformations between the *in vivo* and *ex vivo* configurations of the aorta. This may represent several challenges due to the need to carry out measurements into a living patient before collecting the aorta, for instance after a surgery.
A further analysis can be proposed for stent-graft deployment after the simulations performed in this thesis. After the implementation of the three-dimensional solver the analysis of the stent-graft can be extended to thick arterial walls. The stent can be modeled avoiding contact models by using a similar approach as the one introduced in chapter 3. A good starting point would be to write some modification in the routines for elastic boundary conditions to model the stent placement. Actually this research has been undertaken by Shaojie Zhang, who is a post-doc in our group, and it has been published recently.
Nowadays, G&R models have also found another area of development in the design of tissue engineered materials for prosthesis in blood vessels (arteries and veins) or heart valves. The tissue engineered material can be added to the library of the three-dimensional code with its adequate formulation adapted to G&R. Like this the hCM model implemented in the code can simulate the changes in the material according to the adaptations taking place in the tissue in the long time scale. This is the aim of the SimInSitu project (http://www.siminsitu.eu/), funded by the EU. Currently, Felipe Sempertegui who is a post-doc in our group, is working on this project.
An arterial issue which is usually neglected in the development of disease is the atherosclerotic plaque between the intima and the media. This is something that can be eventually implemented within our three-dimensional solver by introducing of a new material that considers the properties of the plaque in the mixture. It might be needed to set up a three-layer model for the wall of atherosclerotic arteries. Moreover, the wall shear stress induced by the blood flow could be introduced as an input for plaque formation.
Another feature to include in future work is the discretization of time employed in the G&R simulations. Eventually with the use of adaptative time step methods is possible to reduce the computation time of the simulations. Given the nature of the G&R model employed in this work, an appropiate measure to perform the time step adaptation is the difference between the current stress and the reference

homeostatic stress ($\Delta\boldsymbol{\sigma}$) used to drive the turnover of mass and the remodeling. Finally it is still a challenge to speed up the computations. Switching some routines from high level language to low level language should diminish the time of computation. Based in the experience of switching the order of the material models which reduces the computation time in 10 times. Moreover, parallel computing is another option to increase the performance of our code.

Appendix A

Appendix of the Chapter 2

Table of contents of the chapter

A.1 Reference configuration tensors 135
A.2 Matrices for shell elements formulation 136

A.1 Reference configuration tensors

In this section are introduced the second Piola-Kirchhoff stress tensor and the reference elasticity tensor produced by the linearization of the stress, $\Delta \boldsymbol{S} = \mathbb{C} : \Delta \boldsymbol{E}$.

$$\boldsymbol{S} = 2\frac{\partial W}{\partial \boldsymbol{C}} = \phi^e(\boldsymbol{S}^e_{vol} + \boldsymbol{S}^e_{iso}) + \phi^m(\boldsymbol{S}^m_{act} + \boldsymbol{S}^m_{pas}) + \sum_{i=1}^{4} \phi^{c_i} \boldsymbol{S}^{c_i} \tag{A.1}$$

$$\boldsymbol{S}^e_{vol} = \kappa^e J^e_e (J^e_e - 1)\boldsymbol{C}^{-1} \tag{A.2}$$

$$\boldsymbol{S}^e_{iso} = \mu^e J_e^{e-2/3} \left(\boldsymbol{C}^{e\ -1}_{gr} - \frac{1}{3}\mathrm{tr}(\boldsymbol{C}^e_e)\boldsymbol{C}^{-1} \right) \tag{A.3}$$

$$\boldsymbol{S}^m_{pas} = 2k^m_1(\lambda^{m2}_e - 1)\exp(k^m_2(\lambda^{m2}_e - 1)^2)\frac{\boldsymbol{a}^m_0 \otimes \boldsymbol{a}^m_0}{||\boldsymbol{F}^m_{gr}\boldsymbol{a}^m_0||^2} \tag{A.4}$$

$$\boldsymbol{S}^m_{act} = \frac{\sigma_{actmax}}{\varrho_R(0)\lambda} \left(1 - \frac{(\lambda_m - \lambda_{act})^2}{(\lambda_m - \lambda_0)^2} \right) \boldsymbol{a}^m_0 \otimes \boldsymbol{a}^m_0 \tag{A.5}$$

$$\boldsymbol{S}^{c_i} = 2k^{c_i}_1(\lambda^{c_i 2}_e - 1)\exp(k^{c_i}_2(\lambda^{c_i 2}_e - 1)^2)\frac{\boldsymbol{a}^{c_i}_0 \otimes \boldsymbol{a}^{c_i}_0}{||\boldsymbol{F}^{c_i}_{gr}\boldsymbol{a}^{c_i}_0||^2} \tag{A.6}$$

$$\mathbb{C} = 2\frac{\partial \boldsymbol{S}}{\partial \boldsymbol{C}} = \phi^e(\mathbb{C}^e_{vol} + \mathbb{C}^e_{iso}) + \phi^m(\mathbb{C}^m_{act} + \mathbb{C}^m_{pas}) + \sum_{i=1}^{4} \phi^{c_i} \mathbb{C}^{c_i} \tag{A.7}$$

$$\mathbb{C}^e_{vol} = \kappa^e J^e_e((2J^e_e - 1)\boldsymbol{C}^{-1} \otimes \boldsymbol{C}^{-1} - 2(J^e_e - 1)\boldsymbol{C}^{-1} \odot \boldsymbol{C}^{-1}) \tag{A.8}$$

$$\begin{aligned}\mathbb{C}^e_{iso} = \; & \tfrac{2}{3}\mu^e J_e^{e-2/3}\left(\mathrm{tr}(\boldsymbol{C}^e_e)\boldsymbol{C}^{-1}\odot\boldsymbol{C}^{-1} + \tfrac{1}{3}\mathrm{tr}(\boldsymbol{C}^e_e)\boldsymbol{C}^{-1}\otimes\boldsymbol{C}^{-1}\right.\\ & \left. -\boldsymbol{C}^{e}_{gr}{}^{-1}\otimes\boldsymbol{C}^{-1} - \boldsymbol{C}^{-1}\otimes\boldsymbol{C}^{e}_{gr}{}^{-1}\right)\end{aligned} \tag{A.9}$$

$$\mathbb{C}^m_{pas} = 4k^m_1(1+2k^m_2(\lambda^{m2}_e-1)^2)\exp(k^m_2(\lambda^{m2}_e-1)^2)\frac{\boldsymbol{a}^m_0\otimes\boldsymbol{a}^m_0\otimes\boldsymbol{a}^m_0\otimes\boldsymbol{a}^m_0}{||\boldsymbol{F}^m_{gr}\boldsymbol{a}^m_0||^4} \tag{A.10}$$

$$\mathbb{C}^m_{act} = \frac{-2\sigma_{actmax}}{\varrho_R(0)\lambda^2}\left(1-\frac{(\lambda_m-\lambda_{act})^2}{(\lambda_m-\lambda_0)^2}\right)\boldsymbol{a}^m_0\otimes\boldsymbol{a}^m_0\otimes\boldsymbol{a}^m_0\otimes\boldsymbol{a}^m_0 \tag{A.11}$$

$$\mathbb{C}^{c_i} = 4k^{c_i}_1(1+2k^{c_i}_2(\lambda^{c_i2}_e-1)^2)\exp(k^{c_i}_2(\lambda^{c_i2}_e-1)^2)\frac{\boldsymbol{a}^{c_i}_0\otimes\boldsymbol{a}^{c_i}_0\otimes\boldsymbol{a}^{c_i}_0\otimes\boldsymbol{a}^{c_i}_0}{||\boldsymbol{F}^{c_i}_{gr}\boldsymbol{a}^{c_i}_0||^4} \tag{A.12}$$

A.2 Matrices for shell elements formulation

In this section are introduced the matrices for the virtual work and its linearization after discretization in the implementation of the shell elements framework, section 2.6. Where $\boldsymbol{B}^{mb}$ is the membrane-bending matrix, $\boldsymbol{B}^{pen}$ is the penalization matrix for the virtual shear strain, $\boldsymbol{G}^z$ results from the linearization of the longitudinal virtual strain, $\boldsymbol{G}^\theta$ results from the linearization of the tangential virtual strain, $\boldsymbol{G}^{pen}$ results from the linearization of the shear virtual strain and $\boldsymbol{K}^p_{ab}$ are the stiffness matrices at nodes a and b due to the incremental forces for incremental displacements.

$$\begin{aligned}
B^{mb}_{11} &= ((1+u_{,s})-\xi\beta_{,s}\cos\beta)N_{a,s}\\
B^{mb}_{12} &= (w_{,s}-\xi\beta_{,s}\sin\beta)N_{a,s}\\
B^{mb}_{13} &= \xi(((1+u_{,s})\sin\beta - w_{,s}\cos\beta)\beta_{,s}N_a - ((1+u_{,s})\cos\beta + w_{,s}\sin\beta)N_{a,s})\\
B^{mb}_{21} &= \frac{1}{R}((1+e_\theta)\cos\theta + \xi\frac{1}{R}\cos\theta\sin(\theta-\beta))N_a\\
B^{mb}_{22} &= \frac{1}{R}((1+e_\theta)\sin\theta + \xi\frac{1}{R}\sin\theta\sin(\theta-\beta))N_a\\
B^{mb}_{23} &= -\xi\frac{1}{R}(1+e_\theta)\cos(\theta-\beta)N_a
\end{aligned}$$

$$\begin{aligned}
B^{pen}_1 &= -\sin\beta N_{a,s}\\
B^{pen}_2 &= \cos\beta N_{a,s}\\
B^{pen}_3 &= -((1+u_{,s})\cos\beta + w_{,s}\sin\beta)N_a
\end{aligned}$$

$$
\begin{aligned}
G^z_{11} &= N_{a,s}\, N_{b,s} \\
G^z_{12} &= 0 \\
G^z_{13} &= \xi(N_{a,s}\, N_b \beta_{,s} \sin\beta - N_{a,s}\, N_{b,s} \cos\beta) \\
G^z_{21} &= 0 \\
G^z_{22} &= N_{a,s}\, N_{b,s} \\
G^z_{23} &= -\xi(N_{a,s}\, N_b \beta_{,s} \cos\beta + N_{a,s}\, N_{b,s} \sin\beta) \\
G^z_{31} &= \xi(N_a N_{b,s}\, \beta_{,s} \sin\beta - N_{a,s}\, N_{b,s} \cos\beta) \\
G^z_{32} &= -\xi(N_a N_{b,s}\, \beta_{,s} \cos\beta + N_{a,s}\, N_{b,s} \sin\beta) \\
G^z_{33} &= \xi(N_a N_b (1+u_{,s})\beta_{,s} \cos\beta + N_a N_b w_{,s}\, \beta_{,s} \sin\beta + N_a N_{b,s}\, (1+u_{,s}) \sin\beta \\
&\quad -N_a N_{b,s}\, w_{,s} \cos\beta + N_{a,s}\, N_b (1+u_{,s}) \sin\beta - N_{a,s}\, N_b w_{,s} \cos\beta)
\end{aligned}
$$

$$
\begin{aligned}
G^\theta_{11} &= \frac{1}{R^2} N_a N_b \cos^2\theta \\
G^\theta_{12} &= \frac{1}{R^2} N_a N_b \cos\theta \sin\theta \\
G^\theta_{13} &= -\xi \frac{1}{R^2} N_a N_b \cos\theta \cos(\theta-\beta) \\
G^\theta_{21} &= \frac{1}{R^2} N_a N_b \cos\theta \sin\theta \\
G^\theta_{22} &= \frac{1}{R^2} N_a N_b \sin^2\theta \\
G^\theta_{23} &= -\xi \frac{1}{R^2} N_a N_b \sin\theta \cos(\theta-\beta) \\
G^\theta_{31} &= -\xi \frac{1}{R^2} N_a N_b \cos\theta \cos(\theta-\beta) \\
G^\theta_{32} &= -\xi \frac{1}{R^2} N_a N_b \sin\theta \cos(\theta-\beta) \\
G^\theta_{33} &= -\xi \frac{1}{R} N_a N_b (1+e_\theta) \sin(\theta-\beta)
\end{aligned}
$$

$$
\begin{aligned}
G^{pen}_{11} &= 0 \\
G^{pen}_{12} &= 0 \\
G^{pen}_{13} &= -N_{a,s}\, N_b \cos\beta \\
G^{pen}_{21} &= 0 \\
G^{pen}_{22} &= 0 \\
G^{pen}_{23} &= -N_{a,s}\, N_b \sin\beta \\
G^{pen}_{31} &= -N_a N_{b,s} \cos\beta \\
G^{pen}_{32} &= -N_a N_{b,s} \sin\beta \\
G^{pen}_{33} &= -(1+u_{,s}) N_a N_b \sin\beta - w_{,s}\, N_a N_b \cos\beta
\end{aligned}
$$

$$\boldsymbol{K}_{11}^{p} = \begin{bmatrix} 0 & 2r_1(3p_1+p_2)-2r_2p_1 \\ -r_1(3p_1+p_2)-r_2(p_1+p_2) & (z_2-z_1)(3p_1+p_2) \end{bmatrix} + \begin{bmatrix} (r_1-r_2)(3r_1+r_2)p_{,u} & (r_1-r_2)(3r_1+r_2)p_{,w} \\ (z_2-z_1)(3r_1+r_2)p_{,u} & (z_2-z_1)(3r_1+r_2)p_{,w} \end{bmatrix} \tag{A.13}$$

$$\boldsymbol{K}_{12}^{p} = \begin{bmatrix} 0 & -2r_1p_1-2r_2(p_1+p_2) \\ r_1(3p_1+p_2)+r_2(p_1+p_2) & (z_2-z_1)(p_1+p_2) \end{bmatrix} + \begin{bmatrix} (r_1-r_2)(r_1+r_2)p_{,u} & (r_1-r_2)(r_1+r_2)p_{,w} \\ (z_2-z_1)(r_1+r_2)p_{,u} & (z_2-z_1)(r_1+r_2)p_{,w} \end{bmatrix} \tag{A.14}$$

$$\boldsymbol{K}_{21}^{p} = \begin{bmatrix} 0 & 2r_1(p_1+p_2)+2r_2p_2 \\ -r_1(p_1+p_2)-r_2(p_1+p_2) & (z_2-z_1)(p_1+p_2) \end{bmatrix} + \begin{bmatrix} (r_1-r_2)(r_1+r_2)p_{,u} & (r_1-r_2)(r_1+r_2)p_{,w} \\ (z_2-z_1)(r_1+r_2)p_{,u} & (z_2-z_1)(r_1+r_2)p_{,w} \end{bmatrix} \tag{A.15}$$

$$\boldsymbol{K}_{22}^{p} = \begin{bmatrix} 0 & 2r_1p_2-2r_2(p_1+3p_2) \\ r_1(p_1+p_2)+r_2(p_1+3p_2) & (z_2-z_1)(p_1+3p_2) \end{bmatrix} + \begin{bmatrix} (r_1-r_2)(r_1+3r_2)p_{,u} & (r_1-r_2)(r_1+3r_2)p_{,w} \\ (z_2-z_1)(r_1+3r_2)p_{,u} & (z_2-z_1)(r_1+3r_2)p_{,w} \end{bmatrix} \tag{A.16}$$

Appendix B

Appendix of the Chapter 3

Table of contents of the chapter

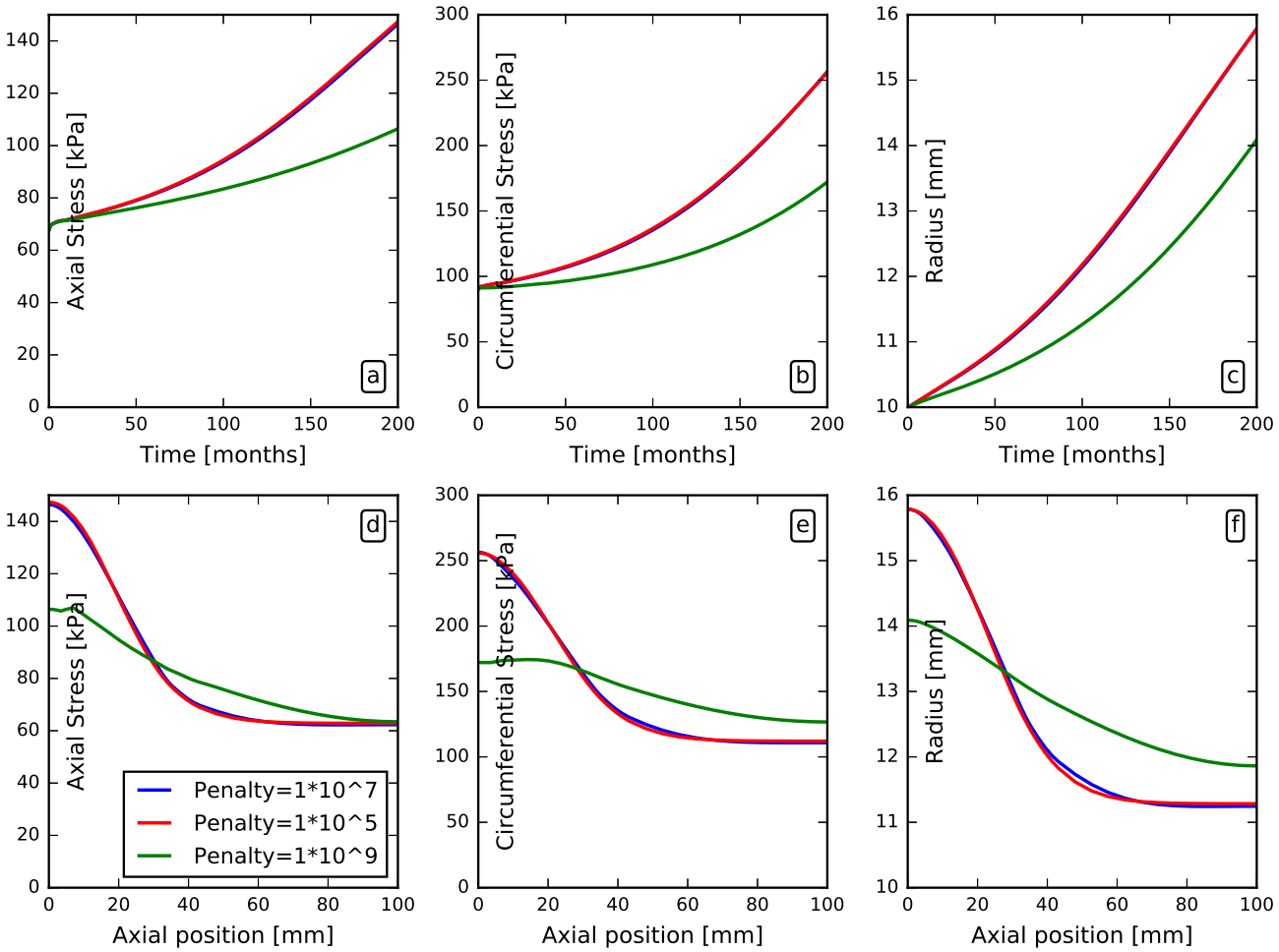

FIGURE B.1 – Effects of different penalties on the aneurysm development of arterial wall due to elastin loss. a, b and c are plotted in the center of the arterial wall ($Z = 0$) versus the time. d, e and f are plotted for the last time step (after 199 months) along the arterial axial direction.

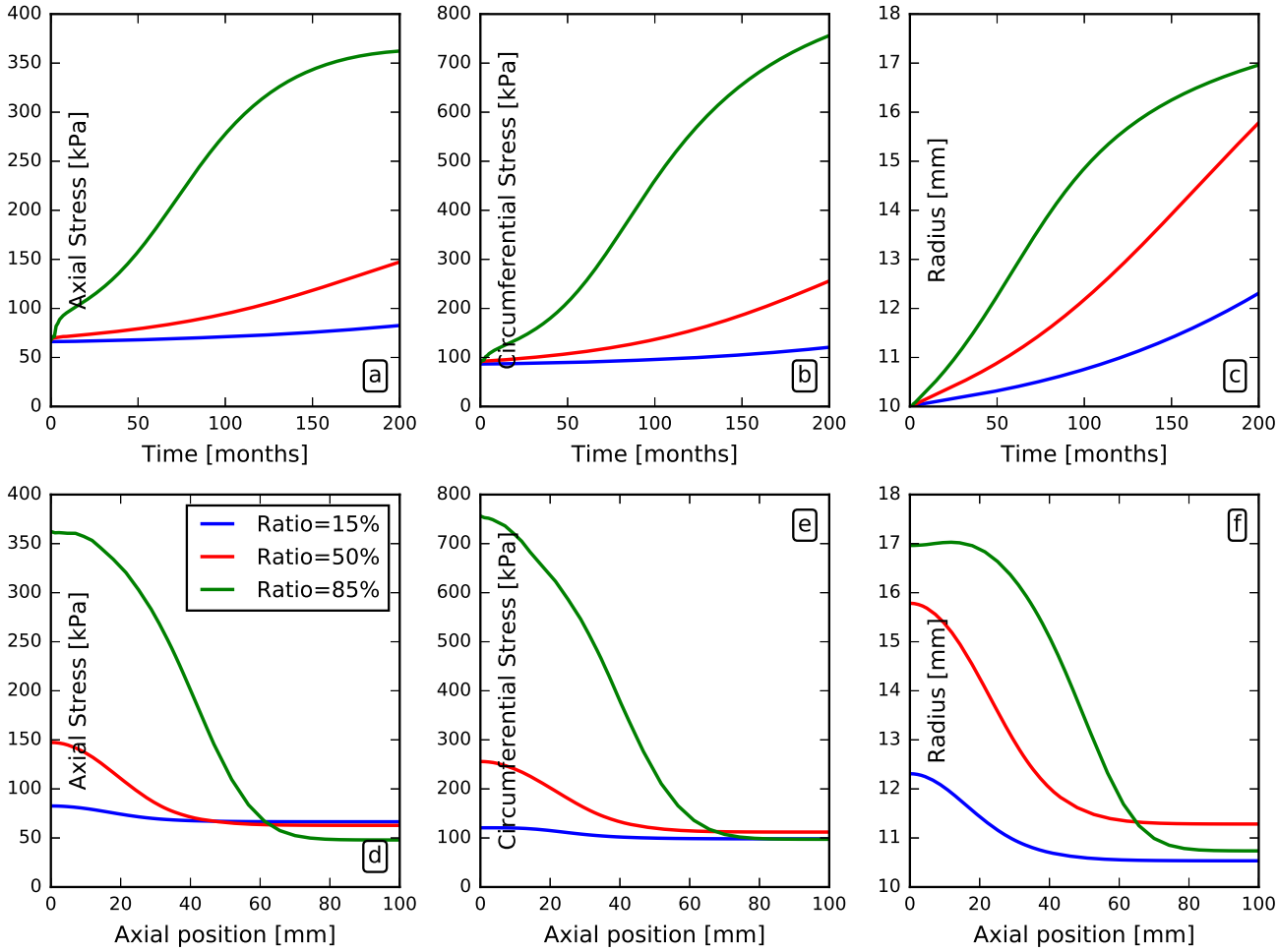

Figure B.2 – Effects of different media-adventitia ratio on the aneurysm development of arterial wall due to elastin loss. a, b and c are plotted in the center of the arterial wall ($Z = 0$) versus the time. d, e and f are plotted for the last time step (after 199 months) along the arterial axial direction.

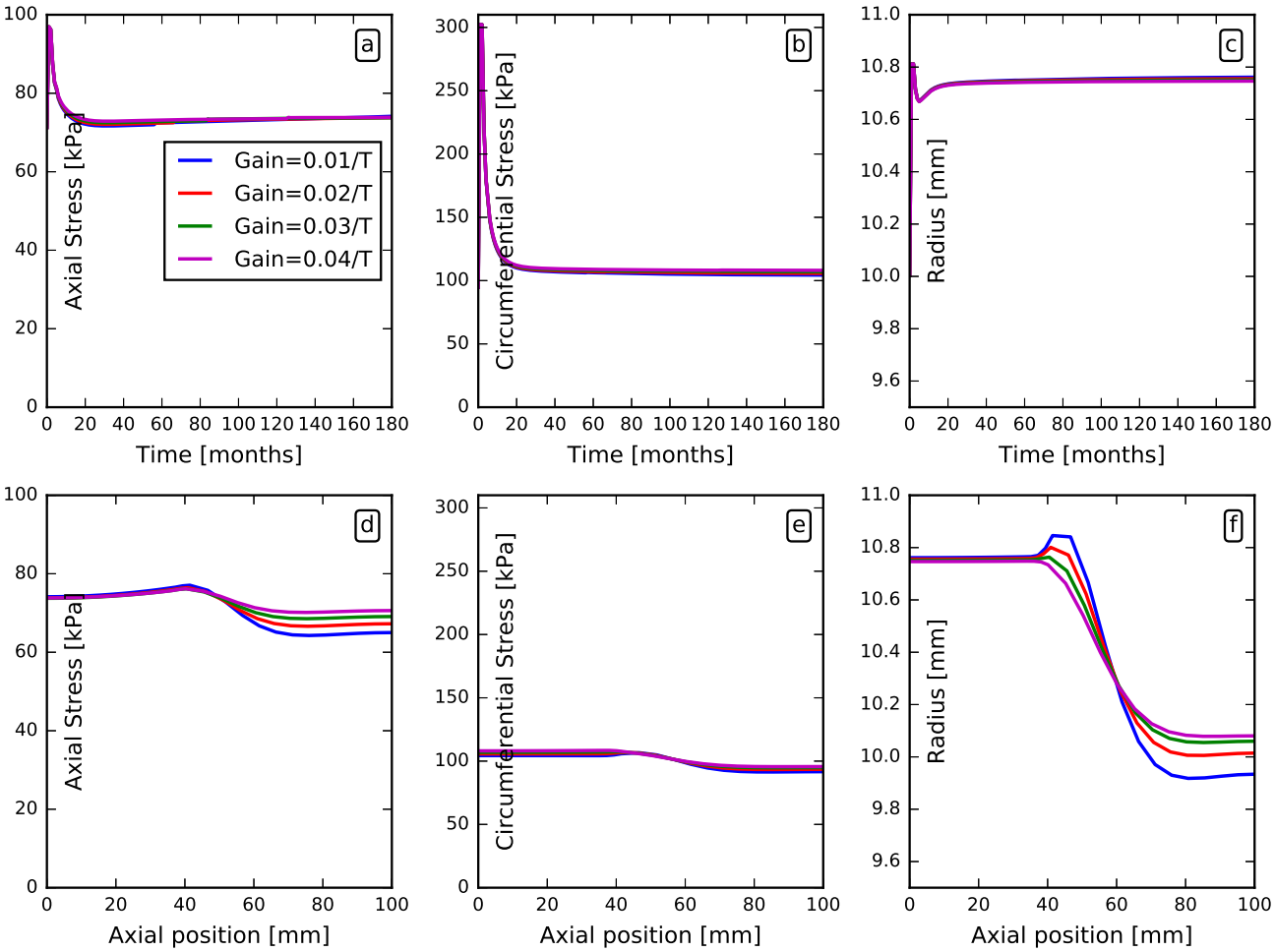

FIGURE B.3 – Effects of gain parameters on the arterial wall G&R due to stent deployment. a, b and c are plotted in the center of the arterial wall ($Z = 0$) versus the time. d, e and f are plotted for the last time step (after 180 months) along the arterial axial direction.

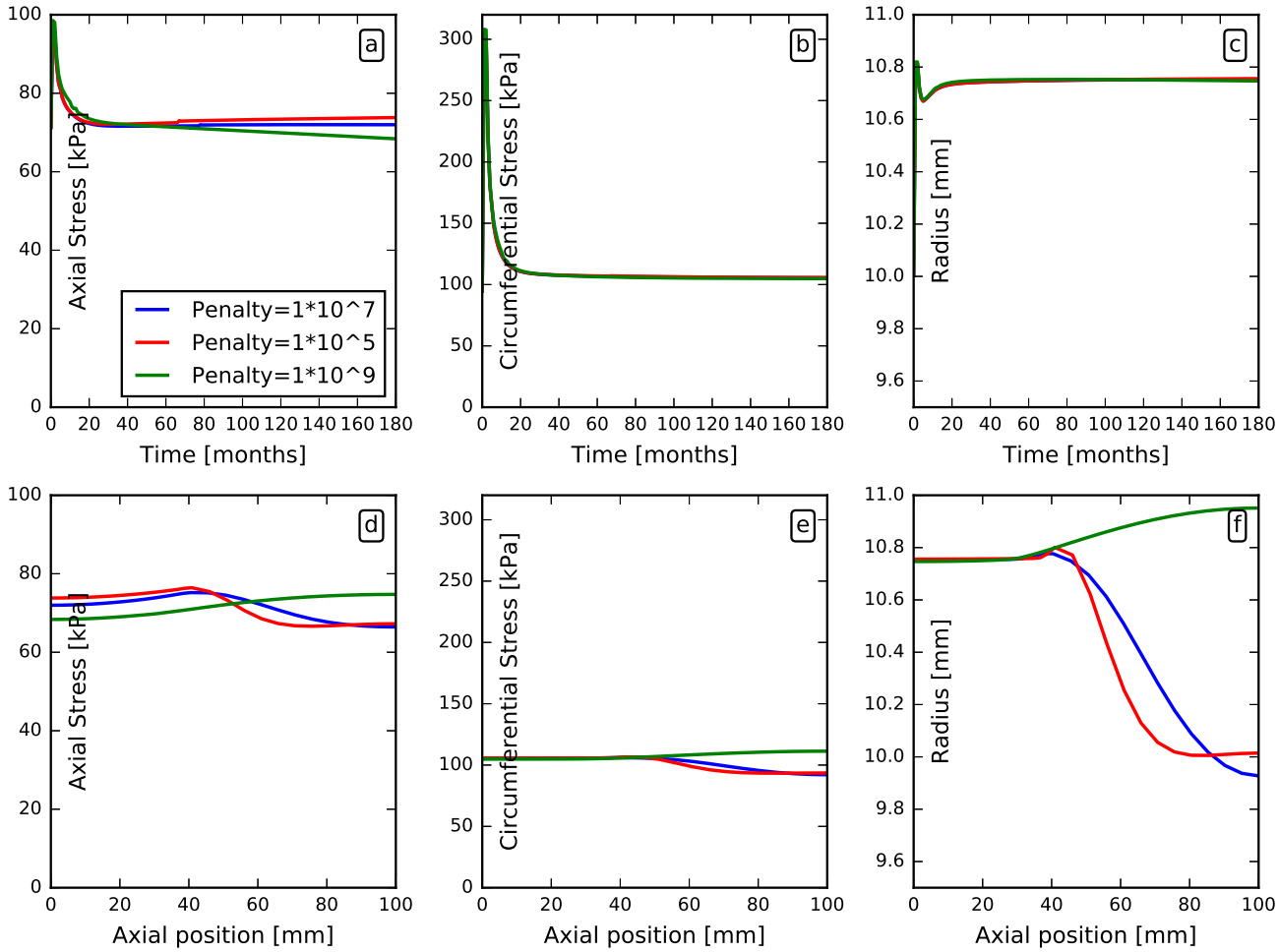

Figure B.4 – Effects of different penalties on the arterial wall G&R due to stent deployment. a, b and c are plotted in the center of the arterial wall ($Z = 0$) versus the time. d, e and f are plotted for the last time step (after 180 months) along the arterial axial direction.

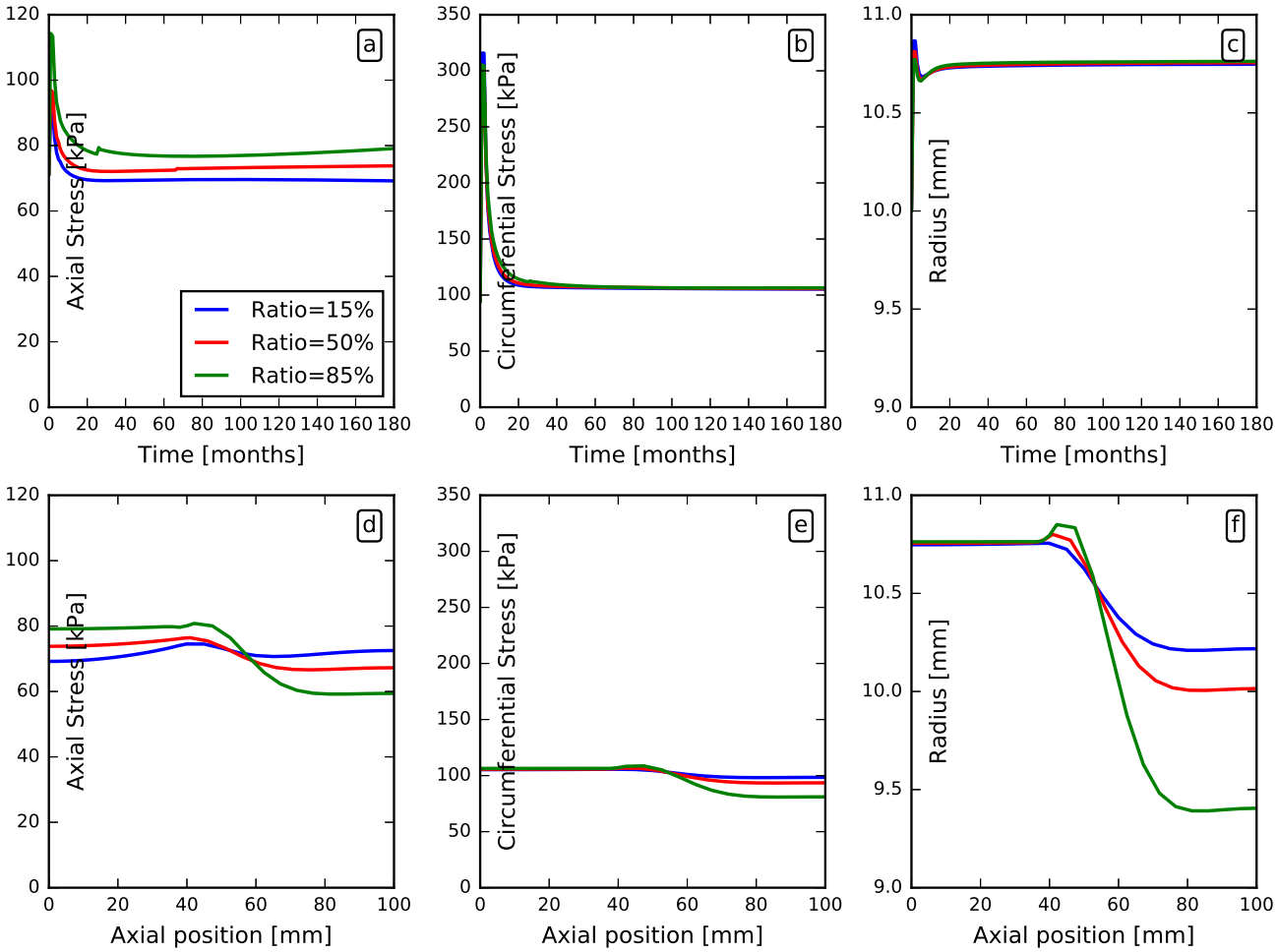

FIGURE B.5 – Effects of media-adventitia ratios on the arterial wall G&R due to stent deployment. a, b and c are plotted in the center of the arterial wall ($Z = 0$) versus the time. d, e and f are plotted for the last time step (after 180 months) along the arterial axial direction.

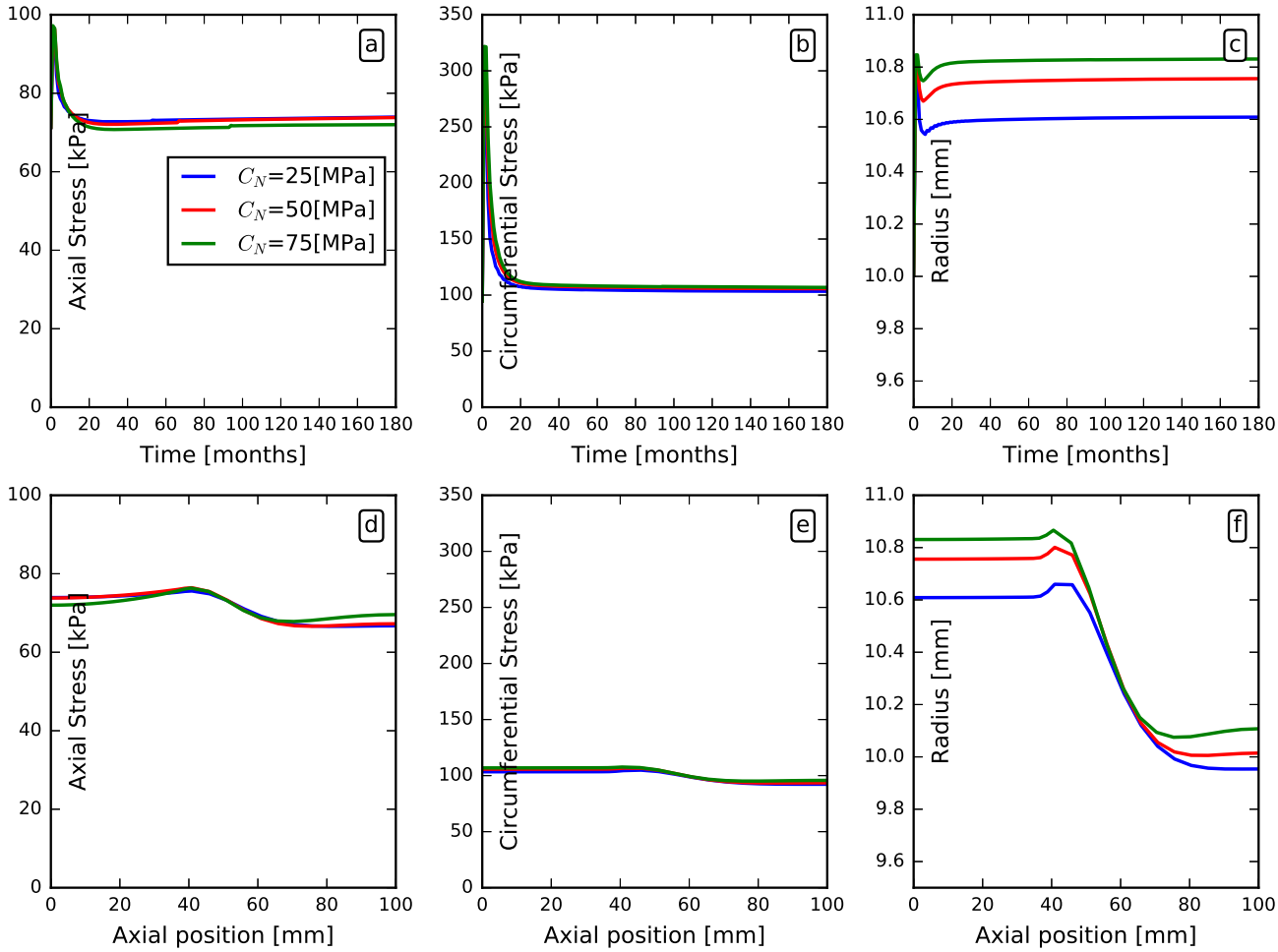

Figure B.6 – The effect of the stent stiffness on the G&R of the arterial wall. a, b and c are plotted in the center of the arterial wall ($Z = 0$) versus the time. d, e and f are plotted for the last time step (after 180 months) along the arterial axial direction.

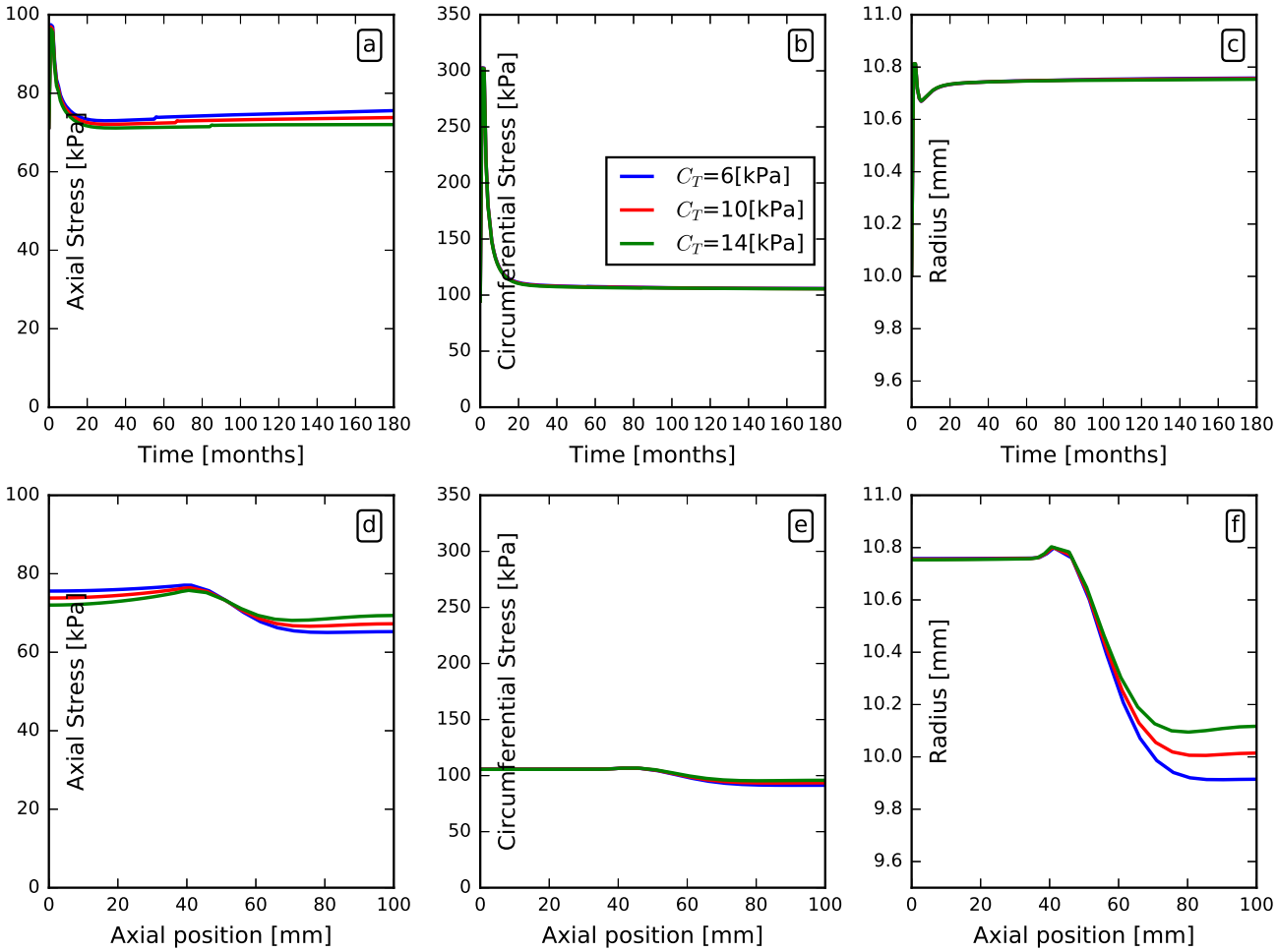

FIGURE B.7 – The effect of the stent tangential coefficients on the G&R of the arterial wall. a, b and c are plotted in the center of the arterial wall ($Z = 0$) versus the time. d, e and f are plotted for the last time step (after 180 months) along the arterial axial direction.

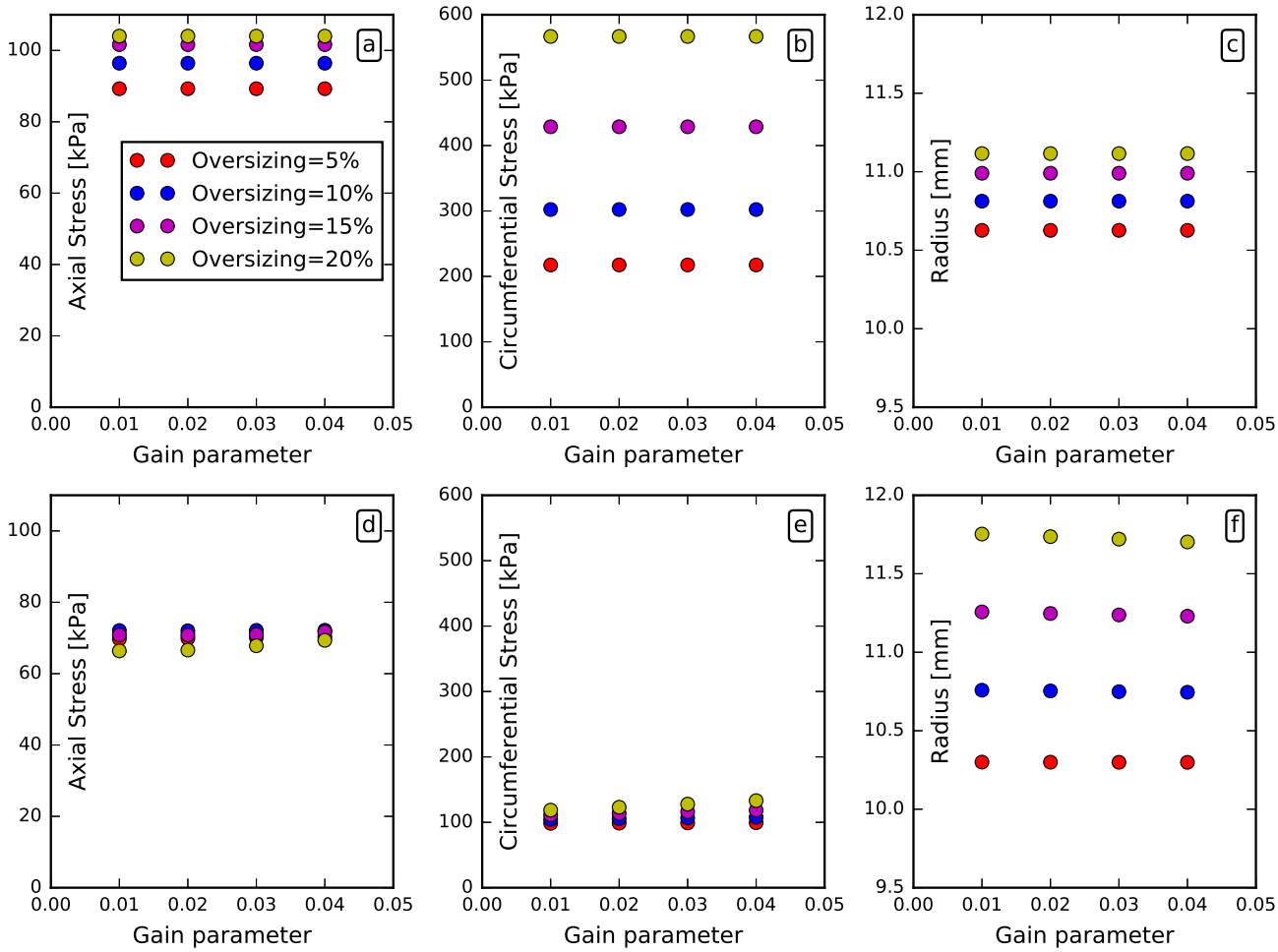

Figure B.8 – The effect of the stent over-sizing and gain parameters on the G&R of the arterial wall. a, b and c are plotted in the center of the arterial wall ($Z = 0$) versus the time. d, e and f are plotted for the last time step (after 180 months) along the arterial axial direction.

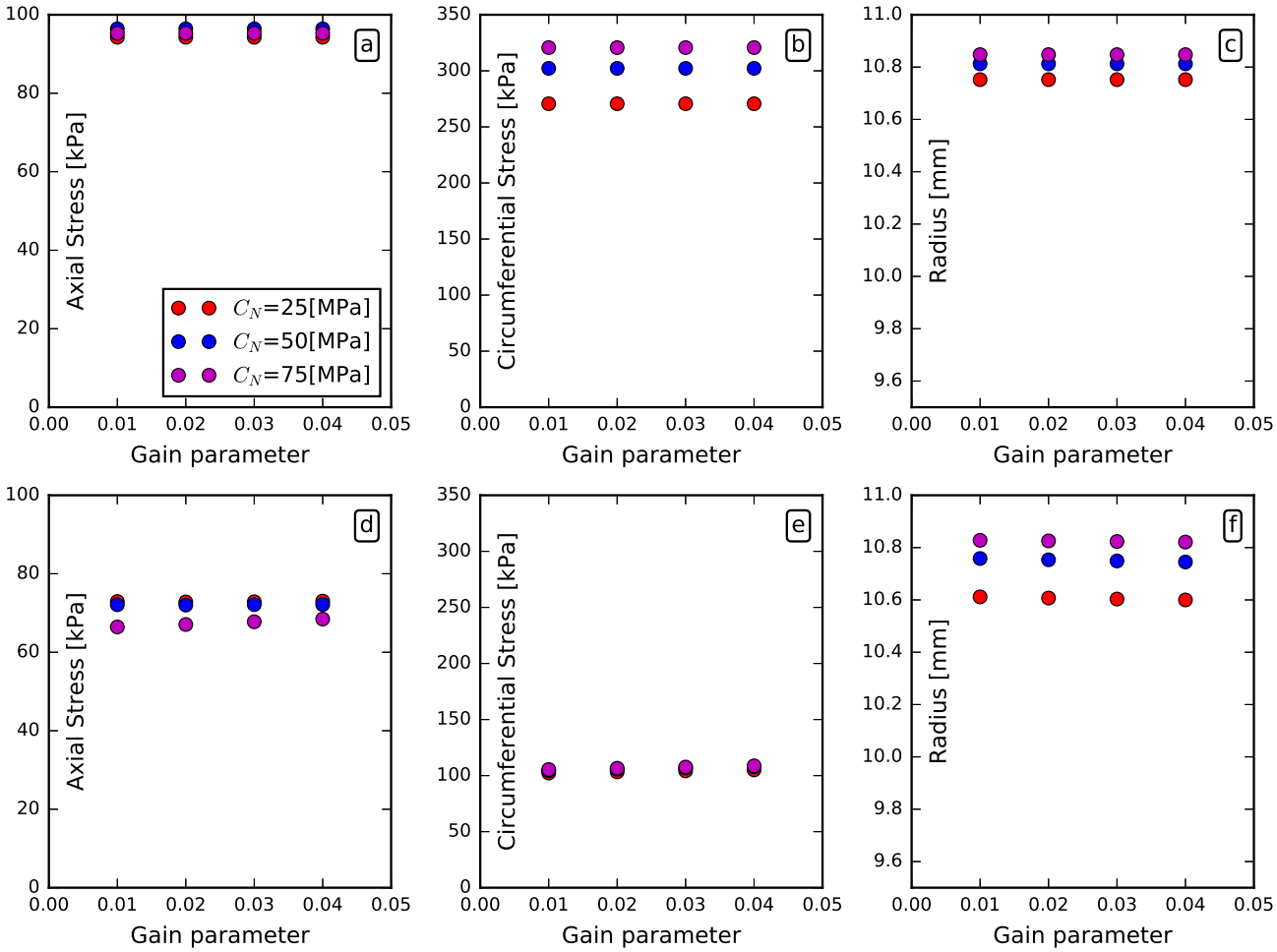

FIGURE B.9 – The effect of the stent stiffness and gain parameters on the G&R of the arterial wall. a, b and c are plotted in the center of the arterial wall ($Z = 0$) versus the time. d, e and f are plotted for the last time step (after 180 months) along the arterial axial direction.

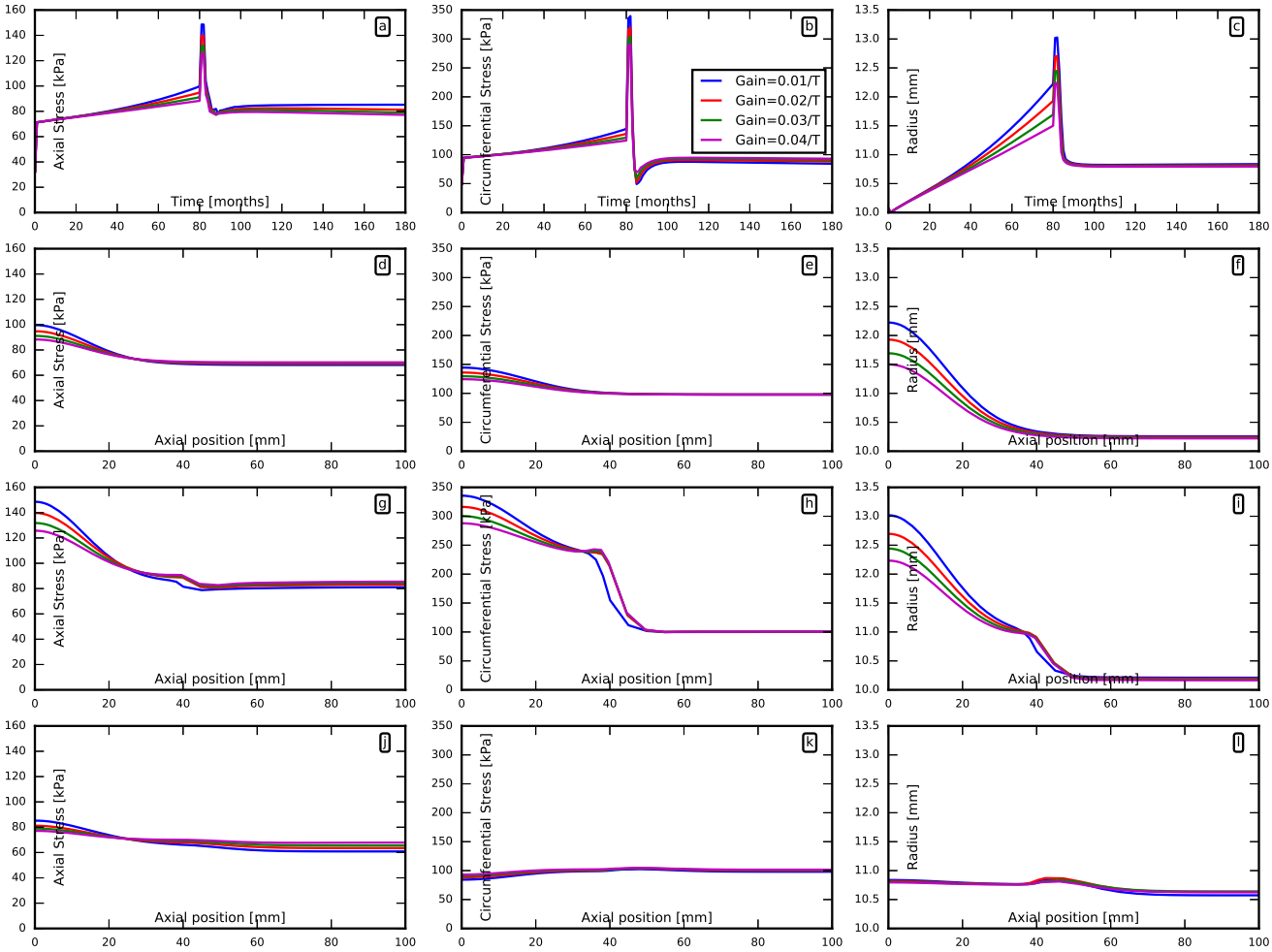

Figure B.10 – The effect of gain parameters on the behavior of the arterial wall before and after stent deployment for an arterial wall undergone several years of G&R. a, b and c are plotted in the center of the arterial wall ($Z = 0$) versus the time. d, e and f are plotted for the instant just before stent deployment (t=80 months) along the arterial axial direction. g, h and i are plotted for the instant just after stent deployment (t=80 months) along the arterial axial direction. j, k and l are plotted after 100 months of the stent deployment along the arterial axial direction.

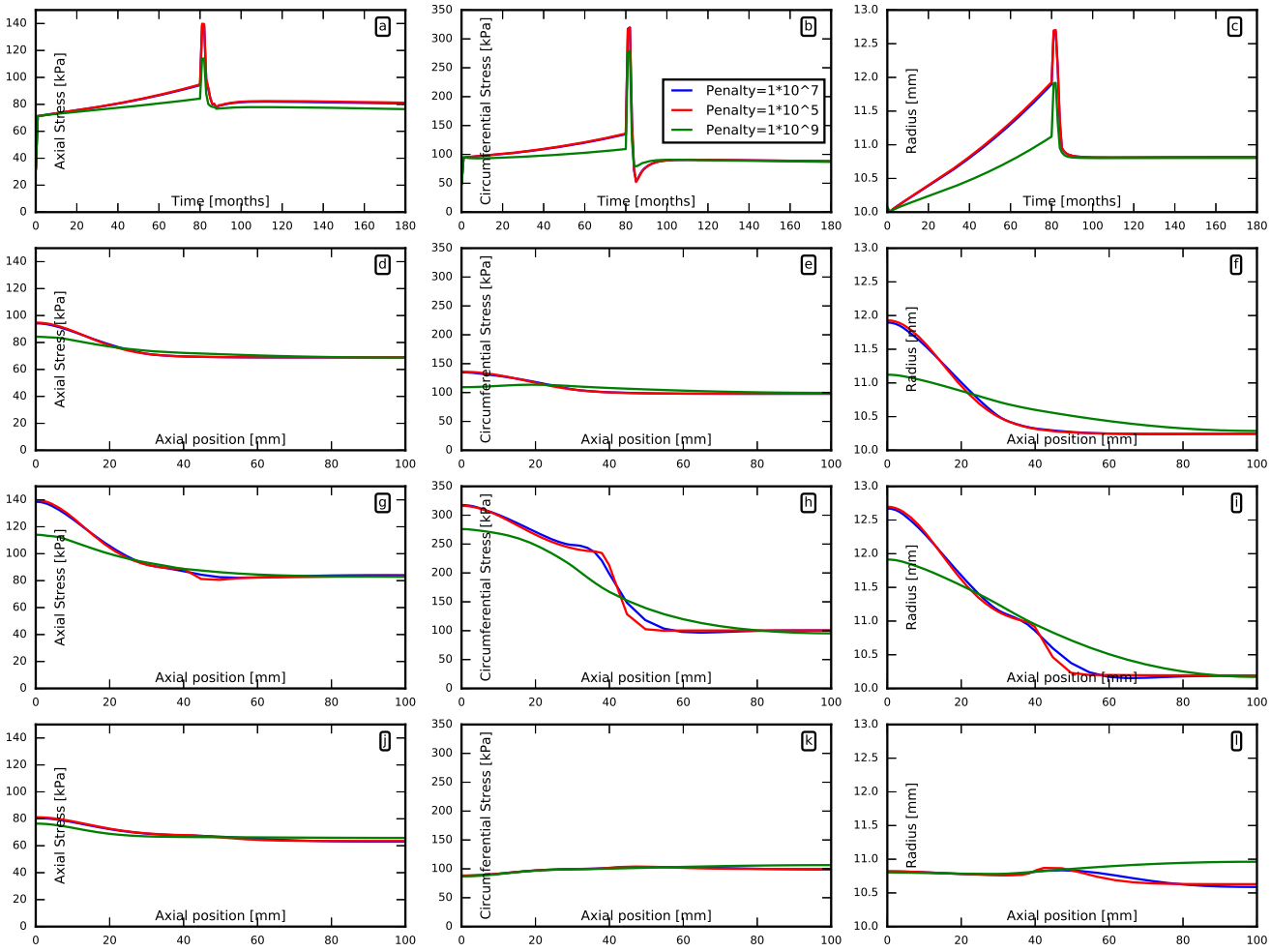

FIGURE B.11 – The effect of different penalties on the behavior of the arterial wall before and after stent deployment for an arterial wall undergone several years of G&R. a, b and c are plotted in the center of the arterial wall ($Z = 0$) versus the time. d, e and f are plotted for the instant just before stent deployment (t=80 months) along the arterial axial direction. g, h and i are plotted for the instant just after stent deployment (t=80 months) along the arterial axial direction. j, k and l are plotted after 100 months of the stent deployment along the arterial axial direction.

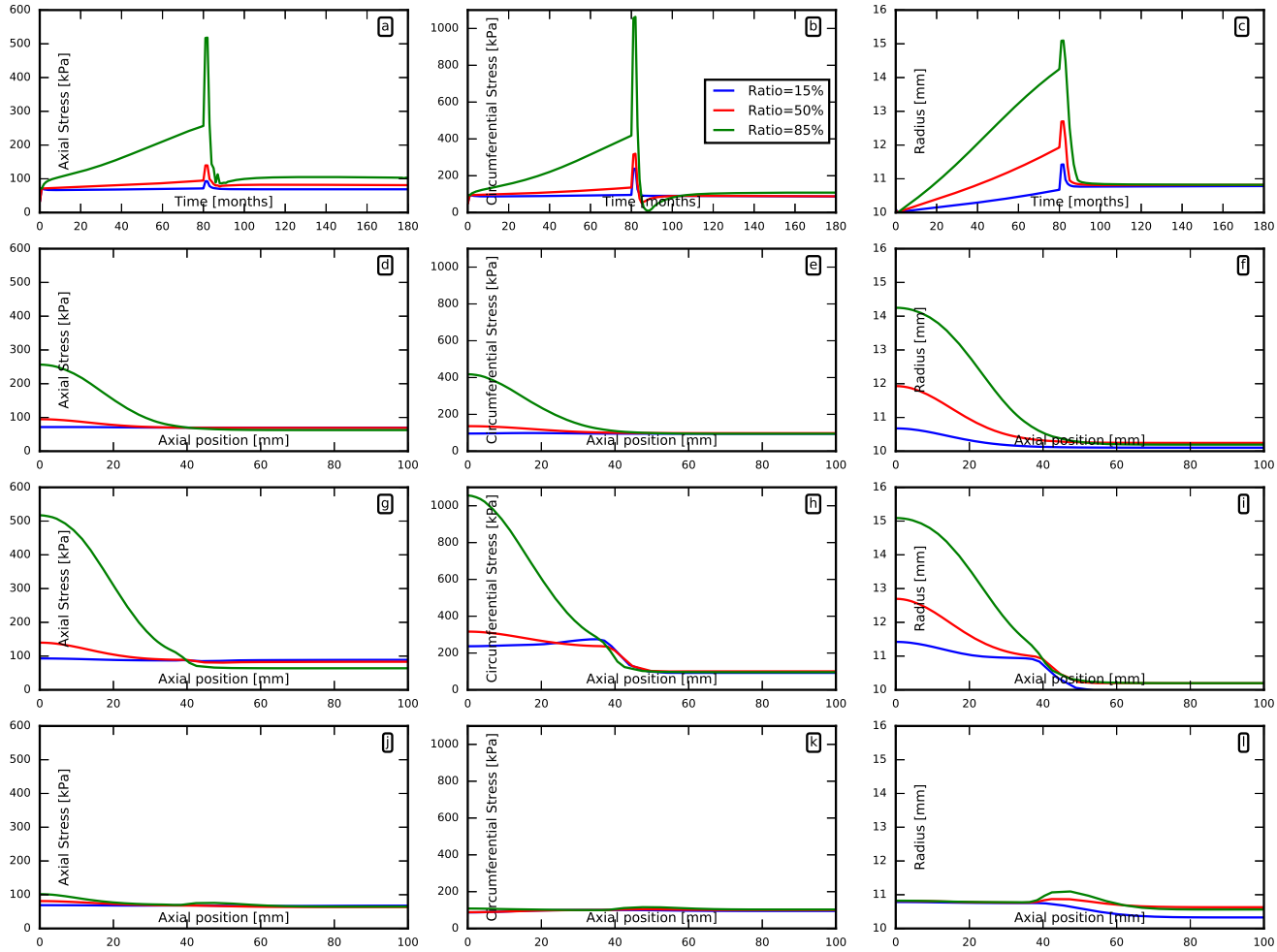

Figure B.12 – The effect of media-adventitia ratios on the behavior of the arterial wall before and after stent deployment for an arterial wall undergone several years of G&R. a, b and c are plotted in the center of the arterial wall ($Z = 0$) versus the time. d, e and f are plotted for the instant just before stent deployment (t=80 months) along the arterial axial direction. g, h and i are plotted for the instant just after stent deployment (t=80 months) along the arterial axial direction. j, k and l are plotted after 100 months of the stent deployment along the arterial axial direction.

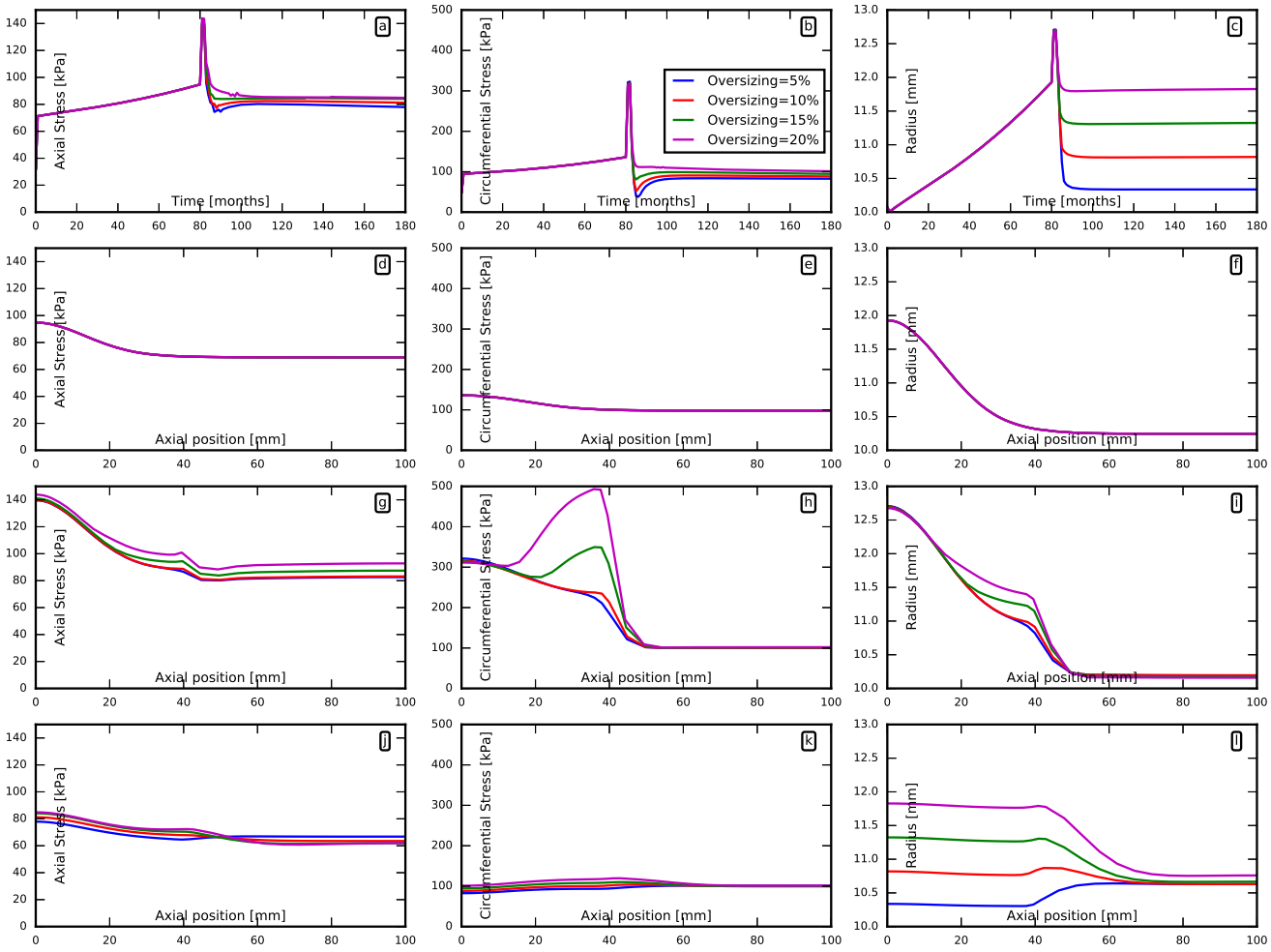

FIGURE B.13 – The effect of stent over-sizing on the behavior of the arterial wall before and after stent deployment for an arterial wall undergone several years of G&R. a, b and c are plotted in the center of the arterial wall ($Z = 0$) versus the time. d, e and f are plotted for the instant just before stent deployment (t=80 months) along the arterial axial direction. g, h and i are plotted for the instant just after stent deployment (t=80 months) along the arterial axial direction. j, k and l are plotted after 100 months of the stent deployment along the arterial axial direction.

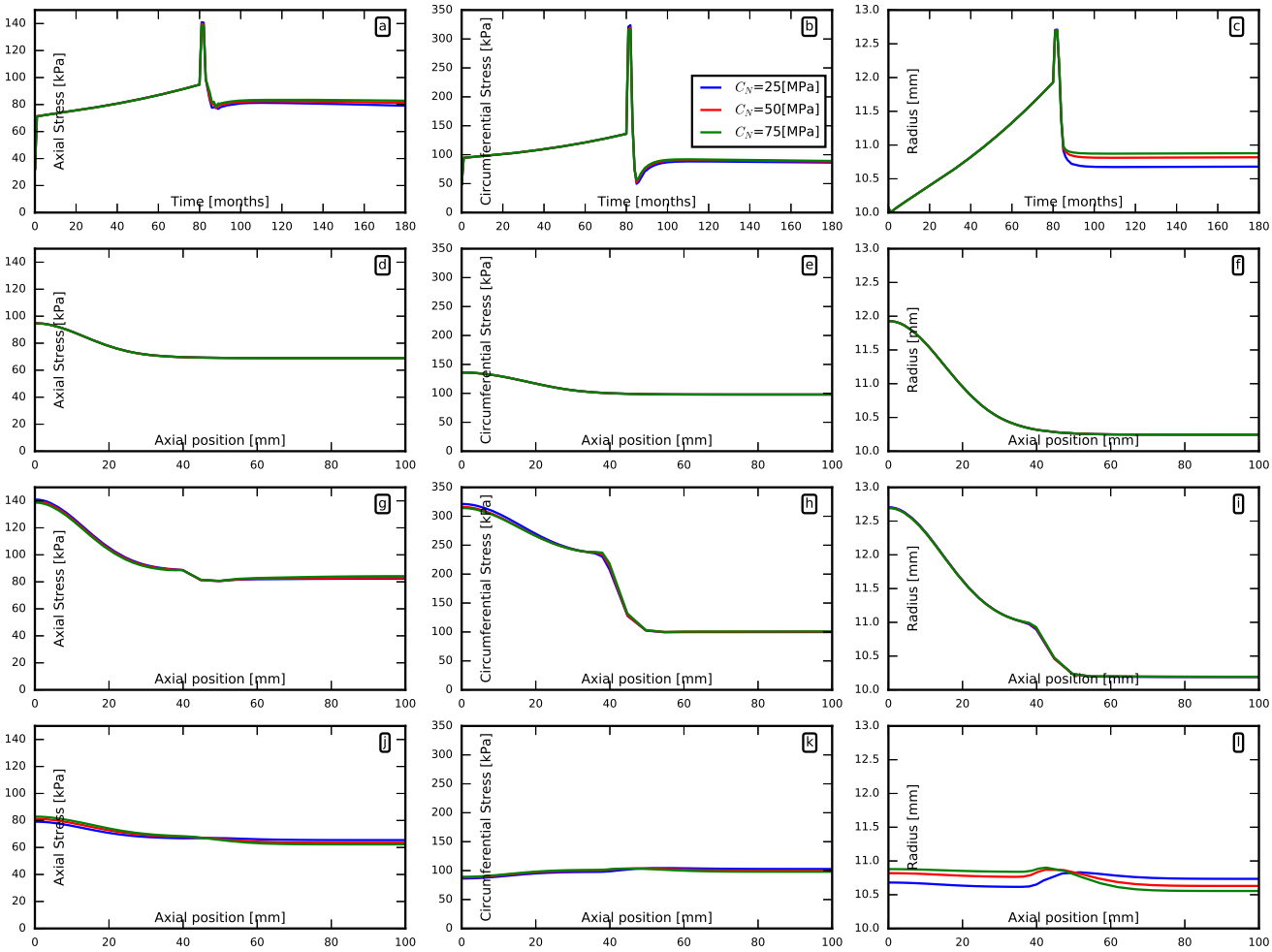

Figure B.14 – The effect of stent normal coefficient on the behavior of the arterial wall after stent deployment for an arterial wall undergone several years of G&R. a, b and c are plotted in the center of the arterial wall ($Z = 0$) versus the time. d, e and f are plotted for the instant just before stent deployment (t=80 months) along the arterial axial direction. g, h and i are plotted for the instant just after stent deployment (t=80 months) along the arterial axial direction. j, k and l are plotted after 100 months of the stent deployment along the arterial axial direction.

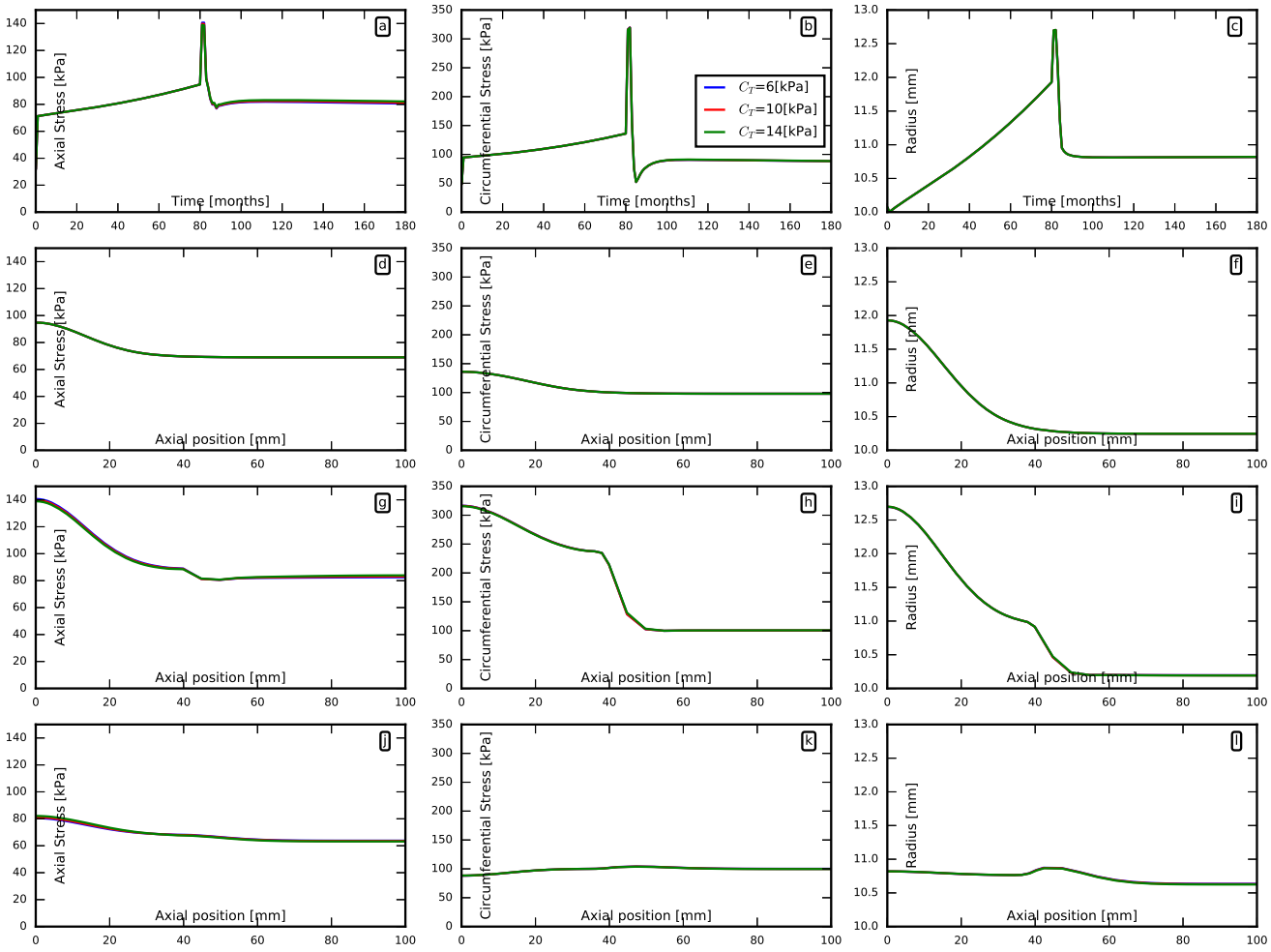

FIGURE B.15 – The effect of stent tangential coefficient on the behavior of the arterial wall after stent deployment for an arterial wall undergone several years of G&R. a, b and c are plotted in the center of the arterial wall ($Z = 0$) versus the time. d, e and f are plotted for the instant just before stent deployment (t=80 months) along the arterial axial direction. g, h and i are plotted for the instant just after stent deployment (t=80 months) along the arterial axial direction. j, k and l are plotted after 100 months of the stent deployment along the arterial axial direction.

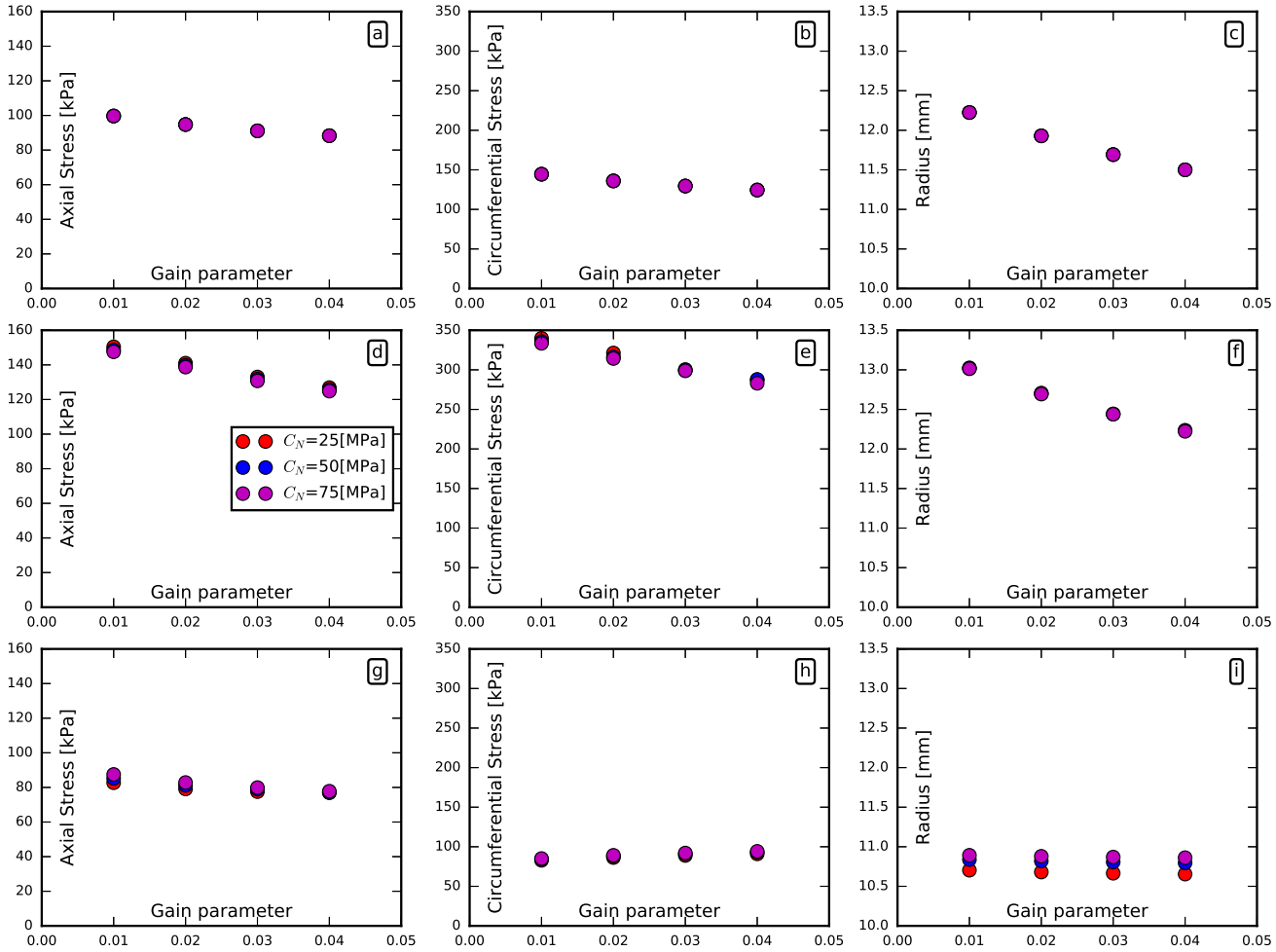

Figure B.16 – The effect of gain parameters and stent stiffness on the behavior of the arterial wall after stent deployment for an arterial wall undergone several years of G&R. a, b and c are plotted in the center of the arterial wall ($Z = 0$) versus the time. d, e and f are plotted for the instant just before stent deployment (t=80 months) along the arterial axial direction. g, h and i are plotted for the instant just after stent deployment (t=80 months) along the arterial axial direction. j, k and l are plotted after 100 months of the stent deployment along the arterial axial direction.

Appendix C

Appendix of the Chapter 4

Table of contents of the chapter

C.1 Theoretical framework 157
C.2 Constitutive Models 159
C.3 Growth and Remodeling 160
C.4 Material properties 161

C.1 Theoretical framework

Let us consider a material mixture composed by several constituents ($j = 1, 2, ..., n$) in its hypothetical traction-free reference configuration $\boldsymbol{\Omega}_R \subset \mathbb{R}^3$ and subsequently deformed into a loaded configuration $\boldsymbol{\Omega}_t \subset \mathbb{R}^3$ at time $t \geq 0$ (Fig. 4.1). The deformation map $\chi : \mathbb{R}^+ \times \boldsymbol{\Omega}_R \to \mathbb{R}^3$ which maps a material point $\boldsymbol{X} \in \boldsymbol{\Omega}_R$ to the corresponding spatial point $\boldsymbol{x} = \chi(\boldsymbol{X}, t) \in \boldsymbol{\Omega}_t$ produces a deformation gradient of the mixture defined as

$$\boldsymbol{F} = \frac{\partial \boldsymbol{x}}{\partial \boldsymbol{X}}, \tag{C.1}$$

where this total deformation incorporate an elastic and inelastic deformation for each jth constituent in the mixture, equation 1.
It is assumed that the material mixture is hyperelastic and depends only on the elastic deformation of each constituent, *i.e.* on the elastic Cauchy-Green tensor

$$\boldsymbol{C}_e^j = [\boldsymbol{F}_{gr}^j]^{-T} \boldsymbol{C} [\boldsymbol{F}_{gr}^j]^{-1}, \tag{C.2}$$

where $\boldsymbol{C} = \boldsymbol{F}^T \boldsymbol{F}$ is the Cauchy-Green tensor related to the deformation gradient defined in Eq. 1. Thus, from the equations 3 and C.2 is possible to define stress

in the jth constituent as,

$$\boldsymbol{S}^j = 2\frac{\varrho_R^j}{\phi^j}\frac{\partial \Psi^j}{\partial \boldsymbol{C}} \tag{C.3}$$

where the sum of the all individual stresses give the second Piola-Kirchhoff stress of the whole mixture ($\sum_j^n \phi^j \boldsymbol{S}^j$), with the constituent mass fraction $\phi^j = \frac{\varrho_R^j}{\varrho_R}$ and the density of the mixture ($\varrho_R = \sum_j^n \varrho_R^j$). The $\boldsymbol{S}^j$ can be mapped to the spatial configuration by the push-forward transformation

$$\boldsymbol{\sigma}^j = \frac{1}{J}\boldsymbol{F}\boldsymbol{S}^j\boldsymbol{F}^T \tag{C.4}$$

with $J = \det \boldsymbol{F}$.
During G&R the tissue is continously adapting and consequently is changing its structure with depositon/removal of mass of the constituents, for instance, elastin degradation, SMCs apoptosis/proliferation or collagen production by fibroblasts/SMCs. The mass changes in the mixture can be written like,

$$\dot{m} = \frac{D}{Dt}(\varrho_R V) = \frac{D}{Dt}(\varrho v), \tag{C.5}$$

where $\dot{m}$ is the depositon/removal of mass in the mixture, $\varrho_R V$ is the density times the volume in reference configuration, ϱv is the density times the volume in spatial configuration. The reference volume V does nont change, the spatial density is constant in time and homogeneous, and with the relation between the volumes $v = JV$ ($\varrho_R = \varrho J$), we can write the mass changes in reference and spatial configurations as it follows [23],

$$\frac{\partial \varrho_R}{\partial t} = J\varrho \mathrm{div}\boldsymbol{v}, \tag{C.6}$$

then, the reference density (per unit reference volume) change over time $\varrho_R = \varrho_R(t)$ [24], [27]. Furthermore, G&R occurs at slow time scales, then it can be assumed that it is quasi-static and the linear momentum balance equals zero,

$$\frac{D}{Dt}(\varrho \boldsymbol{v}) = \mathrm{div}\boldsymbol{\sigma} + \boldsymbol{f} = 0 \tag{C.7}$$

where $\boldsymbol{v}$ is the velocity of the system, $div\boldsymbol{\sigma}$ is the diveregence of the mixture Cauchy stress $\boldsymbol{\sigma}$ and the force $\boldsymbol{f}$, in the spatial configuration.
At the surface of the body the conditions can be, given deformations (Dirichlet), external loads applied on the body surface (Neumann) or deformation-dependent forces (Robin, [92], [93]). The Robin boundary conditions are introduced by the following expression:

$$\boldsymbol{\sigma} \cdot \boldsymbol{n} = p\boldsymbol{n} + k\boldsymbol{u}, \tag{C.8}$$

where p denotes the pressure, $\boldsymbol{n}$ the normal to the surface, the elastic forces with stiffness k and displacement $\boldsymbol{u}$. This forces are appropriate for the modelization of the lumen pressure in blood vessels due to the blood flow, and the elastic forces are usefull to give flexible and stable boundary displacements.

C.2 Constitutive Models

At the equation 2 is assumed that the mixture strain energy W per unit reference volume is the sum of the constituents strain energies Ψ^j per unit mass. Therefore, we consider our material to be vascular tissue composed by three constituents such as, elastin, SMCs and collagen. The elastin is assumed to be isotropic; the smooth muscle have an active, $(\bullet)_{act}$, and a passive ,$(\bullet)_{pas}$, behavior; and the collagen is composed by four fibre families aligned in circumferential, longitudinal and two diagonal directions, respectively. The total strain energy may be written such as

$$W = \varrho_R^l \Psi^l + \varrho_R^m (\Psi_{pas}^m + \Psi_{act}^m) + \sum_{i=1}^{4} \varrho_R^{c_i} \Psi^{c_i}, \tag{C.9}$$

for each component we assumed a strain energy to represent the corresponding hyperelastic behavior. We modeled the elastin with a Neo-Hookean hyperelastic model as in [65], [79]

$$\Psi^l = \frac{\mu^l}{2} \left(\boldsymbol{I} : \bar{\boldsymbol{C}}_e^l - 3 \right) + \frac{\kappa^l}{2} \left(J_e^l - 1 \right)^2 \tag{C.10}$$

where μ^l and κ^l are stress-like material parameters (shear and bulk modulus), while $\bar{\boldsymbol{C}}_e^l$ and J_e^l are the elastic isochoric right Cauchy-Green tensor and the elastic jacobian of elastin, respectively. The isochoric right Cauchy-Green tensor is related to the right Cauchy-Green tensor by $\bar{\boldsymbol{C}}_e^l = (J_e^l)^{2/3} \boldsymbol{C}_e^l$ and the elastin elastic jacobian is $J_e^l = \det(\boldsymbol{F}_e^l)$.
We modeled the collagen fibre families by an anisotropic Fung-type exponential function such as

$$\Psi^{c_i} = \frac{k_1^{c_i}}{2k_2^{c_i}} \left(\exp(k_2^{c_i} (\lambda_e^{c_i 2} - 1)^2) - 1 \right) \tag{C.11}$$

where $k_1^{c_i}$ and $k_2^{c_i}$ are a stress–like and dimensionless material parameters, respectively, while $\lambda_e^{c_i}$ is the elastic stretch contribution of the collagen fibre obtained as

$$\lambda_e^{c_i} = \frac{\lambda^{c_i}}{\lambda_r^{c_i}} \text{ with } \lambda^{c_i} = \sqrt{\boldsymbol{C} : (\boldsymbol{a}_0^{c_i} \otimes \boldsymbol{a}_0^{c_i})} \text{ and } \lambda_r^{c_i} = \| \boldsymbol{F}_{gr}^{c_i} \cdot \boldsymbol{a}_0^{c_i} \| \tag{C.12}$$

where λ^{c_i} and $\lambda_r^{c_i}$ are the total and remodeling stretch (cf. 1) of the fibre, respectively. We also modeled the passive behavior of SMCs by an anisotropic Fung-type exponential function such as

$$\Psi_{pas}^m = \frac{k_1^m}{2k_2^m} \left(\exp(k_2^m (\lambda_e^{m2} - 1)^2) - 1 \right) \tag{C.13}$$

where k_1^m and k_2^m are stress–like and dimensionless material parameters, respectively, λ_e^m is the elastic contribution of SMCs calculated such as

$$\lambda_e^m = \frac{\lambda^m}{\lambda_r^m} \text{ with } \lambda^m = \sqrt{\boldsymbol{C} : (\boldsymbol{a}_0^m \otimes \boldsymbol{a}_0^m)} \text{ and } \lambda_r^m = \| \boldsymbol{F}_{gr}^m \cdot \boldsymbol{a}_0^m \| \tag{C.14}$$

where λ^m and λ^m_r are the total and remodeling stretch (cf. 1) of the fibre, respectively. While we modeled its active behavior according to Braeu et al [27],

$$\Psi^m_{act} = \frac{\sigma_{actmax}}{\varrho_{R0}} \left(\lambda_{act} + \frac{(\lambda^m_{max} - \lambda_{act})^3}{3(\lambda^m_{max} - \lambda^m_0)^2} \right) \tag{C.15}$$

with σ_{actmax} the maximal active Cauchy stress, λ_{act} is the active stretch in the fibre direction, λ^m_0 and λ^m_{max} are the zero and maximum active stretches and ϱ_{R0} denotes the total mixture density in the homeostatic reference configuration.

C.3 Growth and Remodeling

The idea of the hCM models is to pool all the sequential mass additions within one single change using temporal homogenization (Fig. 1). To do so, three assumptions are made: (i) the mechanical properties are changed by G&R, (ii) survival mass (mass turnover) functions are exponential and (iii) inelastic deformations, $\boldsymbol{F}^j_{gr} = \boldsymbol{F}^j_g \boldsymbol{F}^j_r$, are in turn decomposed into growth-related, $\boldsymbol{F}^j_g$, and remodeling-related (turnover-related), $\boldsymbol{F}^j_r$, contributions. In this model a single local average inelastic deformation gradient $\boldsymbol{F}^j_{gr}$ is defined by constituent. The model can handle isotropic or anisotropic growth, the latter being more relevant for arteries and manifesting with thickening or thinning effects [80].
We assumed that G&R is a stress mediated process which tends to minimize deviations between the current stress and a reference stress metrics named homeostatic stress ($\boldsymbol{\sigma}_h$). Therefore, the rate of mass degradation and deposition at time t for the jth constituent is expressed as

$$\dot{\varrho}^j_R = \varrho^j_R k^j_\sigma \frac{\sigma^j - \sigma^j_h}{\sigma^j_h} + \dot{D}^j \tag{C.16}$$

where ϱ^j_R is the mass density (per unit reference volume) of the jth constituent at time t, k^j_σ denotes a mass-gain parameter, σ^j is the spatial stress along the fibre ($\sigma^j = (\boldsymbol{a}^j_0 \otimes \boldsymbol{a}^j_0) : \boldsymbol{\sigma}^j$, cf C.4), $\dot{D}^j$ includes any additional mass deposition or degradation governed by non-mechanical effects (for instance the effect of a drug). Equation C.16 is related to the equation C.6 through the addition of constituents mass $\sum_j \varrho^j_R = \varrho_R$. A more general form of this equation is presented by Braeu et al [27], using a tensorial representation and possibly considering wall shear stress stimuli [25], [81]. The wall shear stress effects induced by the blood flow are neglected in our work here.
Braeu et al [27] assumed that growth captures local change of volume induced by mass variations of each constituent, and that all components of the mixture share the same growth deformation: $\boldsymbol{F}^j_g = \boldsymbol{F}_g$. Then, the growth is measured from the changes of the reference mass density (ϱ_R) respect to the initial ($t_0 = 0$) reference mass density (ϱ_{R0}) through

$$\det(\boldsymbol{F}_g) = \frac{\varrho_R}{\varrho_{R0}}, \tag{C.17}$$

noting that the mixture volume changes are measured by the determinant of the deformation gradient $J = \det(\boldsymbol{F})$ and assuming the elastic and remodeling processes are isochoric ($\det(\boldsymbol{F}_e^j) = \det(\boldsymbol{F}_r^j) = 1$), so, the mixture volume changes remains equal to the growth $J = \det(\boldsymbol{F}_g)$. If the growth is assumed to be anisotropic and along the thickness direction ($\boldsymbol{a}_0^\perp$), can be expressed in tensorial form as

$$\boldsymbol{F}_g = \boldsymbol{I} + \frac{\varrho_R}{\varrho_{R0}} \boldsymbol{a}_0^\perp \otimes \boldsymbol{a}_0^\perp - \boldsymbol{a}_0^\perp \otimes \boldsymbol{a}_0^\perp \tag{C.18}$$

where $\boldsymbol{I}$ is the identity second order tensor. Therefore, due to the continuous mass deposition and removal, the traction-free configuration change during G&R (Fig. 1), even if there is a balance between mass deposition and removal ($\dot{\varrho}_R^j = 0$), this occur with a prestress which is different from the current stress at which mass is removed or deposited. Altogether leads to changes of tissue microstructure referred as remodeling. Therefore, assuming that remodeling occurs at a constant volume and along a fibre in the direction $\boldsymbol{a}_0^j$, the evolution of the remodeling of the jth constituent at time t is expressed such as [24]

$$\dot{\lambda}_r^j = \left(\frac{\dot{\varrho}_R^j}{\varrho_R^j} + \frac{1}{T^j} \right) \frac{\lambda^j}{(\lambda_e^j)^2} \left(\frac{\partial \sigma^j}{\partial \lambda_e^j} \right)^{-1} \times \left(\sigma^j - \sigma_{pre}^j \right). \tag{C.19}$$

where subscript "pre" indicates prestress, $\dot{\lambda}_r^j$ denotes the remodeling velocity and T^j is the average turnover time during which old mass increment is degraded and replaced by a new mass increment. According to proposition 1 from Cyron and Humphrey [8], the prestress σ_{pre}^i is equal to the homeostatic stress σ_h^i. The remodeling of the fibre can be represented in tensorial form as

$$\boldsymbol{F}_r^j = \lambda_r^j \boldsymbol{a}_0^j \otimes \boldsymbol{a}_0^j + \frac{1}{\sqrt{\lambda_r^j}} (\boldsymbol{I} - \boldsymbol{a}_0^j \otimes \boldsymbol{a}_0^j), \tag{C.20}$$

finally, from equations C.18 and C.20 is possible to get the inelastic deformation tensor or growth and remodeling for a fibre as

$$\boldsymbol{F}_{gr}^j = \lambda_r^j \boldsymbol{a}_0^j \otimes \boldsymbol{a}_0^j + \frac{1}{\sqrt{\lambda_r^j}} (\boldsymbol{I} - \boldsymbol{a}_0^j \otimes \boldsymbol{a}_0^j + \frac{\varrho_R}{\varrho_{R0}} \boldsymbol{a}_0^\perp \otimes \boldsymbol{a}_0^\perp - \boldsymbol{a}_0^\perp \otimes \boldsymbol{a}_0^\perp) \Longrightarrow \boldsymbol{F}_{gr}^j \cdot \boldsymbol{a}_0^j = \lambda_r^j \boldsymbol{a}_0^j. \tag{C.21}$$

To calculate the G&R deformation gradient over time we solved the system composed of Eqs. C.16, C.17 and C.19 by performing temporal integration, this is applied in a precedure to carry-out G&R simulation within a FE code, figure C.1.

C.4 Material properties

The mechanical properties of the patient-specific model are fitted from data available in the literature [79] (bulge test). For this issue we assume that the material in the bulge have bi-tangential deformation ($\boldsymbol{F} = \mathrm{diag}[\lambda_{\theta 1}\, \lambda_{\theta 2}\, \lambda_r]$) and it is incompressible ($\det \boldsymbol{F} = 1$). The computation of the experimental measures as stretch and stress are made in base of the formulation presented in [105], from where we

⋆ Initialize state variables
$\varrho_R^j(0)$ and $\boldsymbol{F}_{gr}^j(0)$
⋆ Set boundary conditions
⋆ Assemble the internal stiffness matrix $\mathbf{K}_{int}$
⋆ Let the time flow n years
- If $t \neq 0$. Update state variables (G&R) and internal stiffness matrix $\mathbf{K}_{int}$
  $\varrho_R^j(t+1) = \varrho_R^j(t) + \dot{\varrho}_R^j \Delta t$ and $\boldsymbol{F}_{gr}^j(t+1) = \boldsymbol{F}_{gr}^j(t) + \dot{\boldsymbol{F}}_{gr}^j \Delta t$
  $\dot{\varrho}_R^j = \dot{\varrho}_R^j(\sigma^j, \sigma_h^j)$ and $\dot{\boldsymbol{F}}_{gr}^j = \dot{\boldsymbol{F}}_{gr}^j(\boldsymbol{F}, \boldsymbol{F}_e^j, \sigma^j, \sigma_h^j)$
- Update external forces $\mathbf{F}_{ext}$ and residual $\mathbf{R}$
  $\mathbf{R} = -\mathbf{F}_{ext}$
- Newton-Raphson loop, until $\mathbf{R} \approx 0$
  * Solve the equilibrium system, if first iteration $\mathbf{K} = \mathbf{K}_{int}$
    $\mathbf{K} \cdot \boldsymbol{\Delta} = \mathbf{R}$
  * Compute current coordinates
    $\boldsymbol{x}(t+1) = \boldsymbol{x}(t) + \boldsymbol{\Delta}$
  * Compute internal stiffness matrix $\mathbf{K}_{int}$ and internal forces $\mathbf{T}_{int}$
  * Compute external stiffness matrix $\mathbf{K}_{ext}$ and external forces $\mathbf{F}_{ext}$
  * Update stiffness matrix $\mathbf{K}$ and residual $\mathbf{R}$
    $\mathbf{K} = \mathbf{K}_{int} + \mathbf{K}_{ext}$ and $\mathbf{R} = \mathbf{T}_{int} - \mathbf{F}_{ext}$
- Update total displacements
  $\boldsymbol{\delta}(t+1) = \boldsymbol{x}(t+1) - \boldsymbol{X}$
- Compute CMM measures
  $\sigma^j(t+1) = \boldsymbol{\sigma}^j : (\boldsymbol{a}_0^j \otimes \boldsymbol{a}_0^j)$
- If $t = 0$. Stock constituent measures. $t = 0$ is the homeostatic step
  $\sigma_h^j = \sigma^j(t=0)$

FIGURE C.1 – Implemented algorithm of the hCM model with forward Euler integration. Time $t = 0$ is the homestatic step and defines its constituent stress metrics for the G&R evolution.

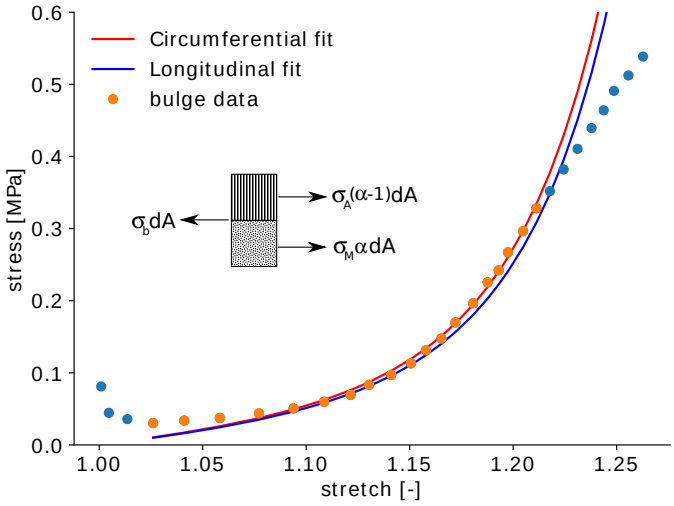

Figure C.2 – Patient axial and circumferential stress-stretch curves fitted from data available in the literature [79] (bulge test). The tangential stress (σ_b) distributed within the layers, with σ_M and σ_A the media and adventitia stress, respectively, and α is the media thickness ratio in the total arterial wall.

distribute the tangential stress σ_b within the specific-layer stresses σ_M and σ_A, media and adventitia, respectively, with α as the media thickness ratio, Fig. C.2. The definition of the constituent densities is made in base of the histological observation showed in [34], where the thoracic aorta is composed by 35% of SMCs, 35% of elastin and 30% of collagen, according to our approach of three constituent in the arterial wall. After we place the constituents ratios in a unit square (left square in Fig. C.3), and from the new constituent rectangles is possible to get their vertical and horizontal dimensions. The next step is to draw two new unit squares subjected to the media/adventitia (50%/50%) ratio; so the media gets 70% of muscle, 16.2% of elastin and 13.8% of collagen; while the adventitia gets 53.8% of elastin and 46.2% of collagen. Finally, the constituent areas (or proportion) are multiplied by the mixture density, for instance, $\varrho_{R0} = 1050[kg/m^3]$, which either correspond to the whole arterial wall or to each layer, Fig. C.3.

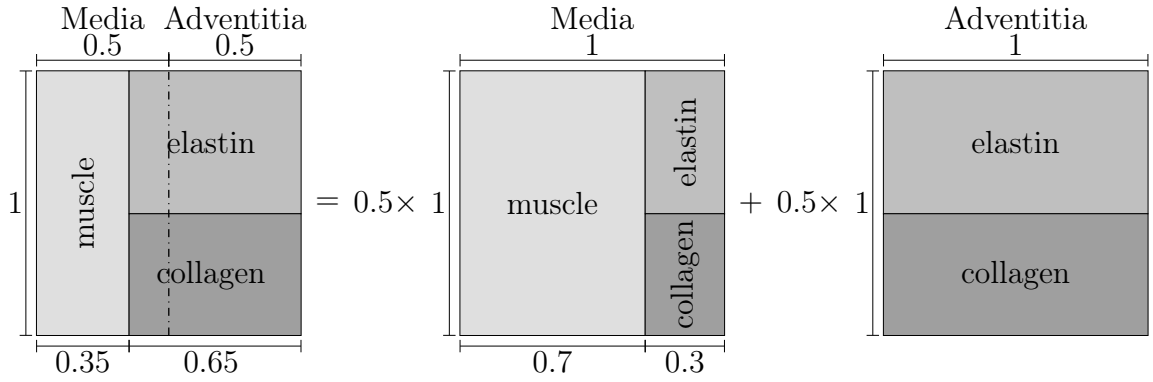

FIGURE C.3 – The first unit square at the left represents the whole arterial wall divided in the mixture constituents, which is split into two new unit squares according to the media/adventitia ratio, each one with its corresponding mixture constituents.

Bibliography

[1] P. Aaronson, J. Ward, and M. Connolly, *The Cardiovascular System at a Glance*. John Wiley and Sons, 2012.

[2] J. D. Humphrey, M. A. Schwartz, G. Tellides, and D. M. Milewicz, "Role of mechanotransduction in vascular biology", *Circulation Research*, vol. 116, no. 8, pp. 1448–1461, 2015. DOI: 10.1161/CIRCRESAHA.114.304936. eprint: https://www.ahajournals.org/doi/pdf/10.1161/CIRCRESAHA.114.304936. [Online]. Available: https://www.ahajournals.org/doi/abs/10.1161/CIRCRESAHA.114.304936.

[3] A. Caulk, G. Tellides, and J. Humphrey, "Chapter 7 - vascular mechanobiology, immunobiology, and arterial growth and remodeling", in *Mechanobiology in Health and Disease*, S. Verbruggen, Ed., Academic Press, 2018, pp. 215–248.

[4] E. Ladich, J. Butany, and R. Virmani, "Chapter 5 - aneurysms of the aorta: Ascending, thoracic and abdominal and their management", in *Cardiovascular Pathology (Fourth Edition)*, L. M. Buja and J. Butany, Eds., Fourth Edition, San Diego: Academic Press, 2016, pp. 169–211, ISBN: 978-0-12-420219-1. DOI: https://doi.org/10.1016/B978-0-12-420219-1.00005-7. [Online]. Available: https://www.sciencedirect.com/science/article/pii/B9780124202191000057.

[5] L. Hiratzka, G. Bakris, J. Beckman, R. Bersin, V. Carr, D. Casey, K. Eagle, L. Hermann, E. Isselbacher, E. Kazerooni, N. Kouchoukos, B. Lytle, D. Milewicz, D. Reich, S. Sen, J. Shinn, L. Svensson, and D. Williams, "2010 accf/aha/aats/acr/asa/sca/scai/sir/sts/svm guidelines for the diagnosis and management of patients with thoracic aortic disease", *Journal of the American College of Cardiology*, vol. 55, no. 14, e27 –e129, 2010, ISSN: 0735-1097. DOI: https://doi.org/10.1016/j.jacc.2010.02.015. [Online]. Available: http://www.sciencedirect.com/science/article/pii/S0735109710007151.

[6] J. A. Elefteriades and E. A. Farkas, "Thoracic aortic aneurysm: Clinically pertinent controversies and uncertainties", *Journal of the American College of Cardiology*, vol. 55, no. 9, pp. 841–857, 2010, ISSN: 0735-1097. DOI: https://doi.org/10.1016/j.jacc.2009.08.084. [Online].

Available: https://www.sciencedirect.com/science/article/pii/S0735109709040753.

[7] T. E. o. E. Britannica, *Encyclopedia britannica: Homeostasis*, https://www.britannica.com/scienc Accessed 14 June 2021.

[8] C. Cyron and J. Humphrey, "Vascular homeostasis and the concept of mechanobiological stability", *Int J Eng Sci*, vol. 52, pp. 645–664, 2016.

[9] ——, "Growth and remodeling of load-bearing biological biological soft tissues", *Meccanica*, vol. 52, pp. 645–664, 2016.

[10] S. Baek, K. Rajagopal, and J. Humphrey, "A theoretical model of enlarging intracranial fusiform aneurysms", *J Biomech Eng*, vol. 128(1), pp. 142–149, 2006.

[11] P. Texakalidis, A. Sweid, N. Mouchtouris, E. Peterson, C. Sioka, L. Rangel-Castilla, J. Reavey-Cantwell, and P. Jabbour, "Aneurysm formation, growth, and rupture: The biology and physics of cerebral aneurysms", *World Neurosurgery*, vol. 130, pp. 277 –284, 2019, ISSN: 1878-8750. DOI: https://doi.org/10.1016/j.wneu.2019.07.093. [Online]. Available: http://www.sciencedirect.com/science/article/pii/S1878875019319990.

[12] J. Wilson, S. Baek, and J. Humphrey, "Importance of initial aortic properties on the evolving regional anisotropy, stiffness and wall thickness of human abdominal aortic aneurysms", *J R Soc Interface*, vol. 9, no. 74, pp. 2047–2058, 2012.

[13] P. Watton and N. Hill, "Evolving mechanical properties of a model of abdominal aortic aneurysm", *Biomech Model Mechanobiol*, vol. 8(1), pp. 25–42, 2009.

[14] W. Lin, M. Iafrati, R. Peattie, and L. Dorfmann, "Growth and remodeling with application to abdominal aortic aneurysms", *J Eng Math*, vol. 109(1), pp. 113–137, 2017.

[15] S. Zeinali-Davarani, A. Sheidaei, and S. Baek, "A finite element model of stress-mediated vascular adaptation: Application to abdominal aortic aneurysms", *Comput Methods Biomech Biomed Eng*, vol. 14, no. 9, pp. 803–817, 2011.

[16] N. Horvat, L. Virag, G. A. Holzapfel, J. Sorić, and I. Karšaj, "A finite element implementation of a growth and remodeling model for soft biological tissues: Verification and application to abdominal aortic aneurysms", *Computer Methods in Applied Mechanics and Engineering*, vol. 352, pp. 586 – 605, 2019, ISSN: 0045-7825. DOI: https://doi.org/10.1016/j.cma.2019.04.041. [Online]. Available: http://www.sciencedirect.com/science/article/pii/S0045782519302518.

[17] S. Mousavi, S. Farzaneh, and S. Avril, "Patient-specific predictions of aneurysm growth and remodeling in the ascending thoracic aorta using the homogenized constrained mixture model", *Biomech Model Mechanobiol*, vol. 18, pp. 1895–1913, 2019. DOI: https://doi.org/10.1007/s10237-019-01184-8.

[18] S. Jamaleddin Mousavi, R. Jayendiran, S. Farzaneh, S. Campisi, M. Viallon, P. Croisille, and S. Avril, "Coupling hemodynamics with mechanobiology in patient-specific computational models of ascending thoracic aortic aneurysms", *Computer Methods and Programs in Biomedicine*, vol. 205, p. 106 107, 2021, ISSN: 0169-2607. DOI: https://doi.org/10.1016/j.cmpb.2021.106107. [Online]. Available: https://www.sciencedirect.com/science/article/pii/S0169260721001826.

[19] C. Bellini, J. Ferruzzi, S. Roccabianca, E. D. Martino, and J. Humphrey, "A microstructurally motivated model of arterial wall mechanics with mechanobiological implications", *Ann Biomed Eng*, vol. 42(3), pp. 488–502, 2014.

[20] L. Taber and J. Humphrey, "Stress-modulated growth, residual stress, and vascular heterogeneity", *J Biomech Eng*, vol. 123, no. 6, pp. 528–535, 2001.

[21] P. Alford and L. Taber, "Computational study of growth and remodelling in the aortic arch.", *Comput Methods Biomech Biomed Engin*, vol. 11, no. 5, pp. 525–38, 2008, ISSN: 1025-5842. [Online]. Available: http://www.biomedsearch.com/nih/Computational-study-growth-remodelling-in/18792831.html.

[22] J. Humphrey and K. Rajagopal, "A constrained mixture model for growth and remodeling of soft tissues", *Math Models Methods Appl Sci*, vol. 12(3), pp. 407–430, 2002.

[23] E. Rodriguez, A. Hoger, and A. McCulloch, "Stress-dependent finite growth in soft elastic tissues", *J Biomech*, vol. 27, pp. 455–467, 1994.

[24] C. Cyron, R. Aydin, and J. Humphrey, "A homogenized constrained mixture (and mechanical analog) model for growth and remodeling of soft tissue", *Biomech Model Mechanobiol*, vol. 15, pp. 1389–1403, 2016.

[25] C. Figueroa, S. Baek, C. Taylor, and J. Humphrey, "A computational framework for fluid–solid-growth modeling in cardiovascular simulations", *Comput. Methods Appl. Mech. Engrg.*, vol. 198, no. 45, pp. 3583 –3602, 2009.

[26] A. Valentín, J. Humphrey, and G. Holzapfel, "A finite element-based constrained mixture implementation for arterial growth, remodeling, and adaptation: Theory and numerical verification", *Int J Numer Method Biomed Eng*, vol. 29(8), pp. 822–49, 2013.

[27] F. Braeu, A. Seitz, R. Aydin, and C. Cyron, "Homogenized constrained mixture models for anisotropic volumetric growth and remodeling", *Biomech Model Mechanobiol*, vol. 16(3), pp. 889–906, 2017.

[28] C. Cyron, J. Wilson, and J. Humphrey, "Mechanobiological stability: A new paradigm to understand the enlargement of aneurysms?", *J. R. Soc. Interface*, vol. 11, p. 20 140 680, 2014.

[29] S. Brandstaeter, S. L. Fuchs, J. Biehler, R. C. Aydin, W. A. Wall, and C. J. Cyron, "Global sensitivity analysis of a homogenized constrained mixture model of arterial growth and remodeling", *Journal of Elasticity*, 2021. DOI: https://doi.org/10.1007/s10659-021-09833-9.

[30] *Kuru: Finite-element open-source library*, https://github.com/jdlaubrie/Kuru, Accessed 14 July 2021.

[31] M. Labrosse, *Cardiovascular Mechanics*. Sep. 2018, ISBN: 9781315280295. DOI: 10.1201/b21917.

[32] E. Teo and E. Isselbacher, "34 - diseases of the aorta", in *Essential Echocardiography*, S. Solomon, J. Wu, and L. Gillam, Eds., Elsevier, 2019, 354 – 368.e1.

[33] J. D. Humphrey, *Cardiovascular Solid Mechanics: Cells, Tissues, and Organs*, 1st ed. Springer, 2002. DOI: 10.1007/978-0-387-21576-1.

[34] J. Humphrey and G. Holzapfel, "Mechanics, mechanobiology, and modeling of human abdominal aorta and aneurysms", *Journal of Biomechanics*, vol. 45, no. 5, pp. 805 –814, 2012, Special Issue on Cardiovascular Solid Mechanics, ISSN: 0021-9290. DOI: https://doi.org/10.1016/j.jbiomech.2011.11.021. [Online]. Available: http://www.sciencedirect.com/science/article/pii/S0021929011007032.

[35] D. C. Iliopoulos, E. P. Kritharis, A. T. Giagini, S. A. Papadodima, and D. P. Sokolis, "Ascending thoracic aortic aneurysms are associated with compositional remodeling and vessel stiffening but not weakening in age-matched subjects", *The Journal of thoracic and cardiovascular surgery*, vol. 137, no. 1, 101—109, 2009, ISSN: 0022-5223. DOI: 10.1016/j.jtcvs.2008.07.023. [Online]. Available: http://intl-jtcs.ctsnetjournals.org/cgi/content/full/137/1/101.

[36] S. Pasta, J. A. Phillippi, T. G. Gleason, and D. A. Vorp, "Effect of aneurysm on the mechanical dissection properties of the human ascending thoracic aorta", *The Journal of Thoracic and Cardiovascular Surgery*, vol. 143, no. 2, pp. 460–467, 2012, ISSN: 0022-5223. DOI: https://doi.org/10.1016/j.jtcvs.2011.07.058. [Online]. Available: https://www.sciencedirect.com/science/article/pii/S0022522311008348.

[37] H. K. Siddiqi, P. Libby, and P. M. Ridker, "Covid-19 – a vascular disease", *Trends in Cardiovascular Medicine*, vol. 31, no. 1, pp. 1–5, 2021, ISSN: 1050-1738. DOI: https://doi.org/10.1016/j.tcm.2020.10.005. [Online]. Available: https://www.sciencedirect.com/science/article/pii/S1050173820301286.

[38] J. Xu and G.-P. Shi, "Vascular wall extracellular matrix proteins and vascular diseases", *Biochimica et Biophysica Acta (BBA) - Molecular Basis of Disease*, vol. 1842, no. 11, pp. 2106–2119, 2014, ISSN: 0925-4439. DOI: https://doi.org/10.1016/j.bbadis.2014.07.008. [Online]. Available: https://www.sciencedirect.com/science/article/pii/S0925443914002191.

[39] M. Thiriet and K. H. Parker, "Physiology and pathology of the cardiovascular system: A physical perspective", in *Cardiovascular Mathematics: Modeling and simulation of the circulatory system*, L. Formaggia, A. Quarteroni, and A. Veneziani, Eds. Milano: Springer Milan, 2009, pp. 1–45, ISBN: 978-88-470-1152-6. DOI: 10.1007/978-88-470-1152-6_1. [Online]. Available: https://doi.org/10.1007/978-88-470-1152-6_1.

[40] S. Sherifova and G. A. Holzapfel, "Biomechanics of aortic wall failure with a focus on dissection and aneurysm: A review", *Acta Biomaterialia*, vol. 99, pp. 1–17, 2019, ISSN: 1742-7061. DOI: https://doi.org/10.1016/j.actbio.2019.08.017. [Online]. Available: https://www.sciencedirect.com/science/article/pii/S1742706119305641.

[41] M. O'Rourke, A. Farnsworth, and J. O'Rourke, "Aortic dimensions and stiffness in normal adults", *JACC: Cardiovascular Imaging*, vol. 1, no. 6, pp. 749 –751, 2008, ISSN: 1936-878X. DOI: https://doi.org/10.1016/j.jcmg.2008.08.002. [Online]. Available: http://www.sciencedirect.com/science/article/pii/S1936878X08003744.

[42] A. Redheuil, W.-C. Yu, E. Mousseaux, A. A. Harouni, N. Kachenoura, C. O. Wu, D. Bluemke, and J. A. Lima, "Age-related changes in aortic arch geometry: Relationship with proximal aortic function and left ventricular mass and remodeling", *Journal of the American College of Cardiology*, vol. 58, no. 12, pp. 1262–1270, 2011, ISSN: 0735-1097. DOI: https://doi.org/10.1016/j.jacc.2011.06.012. [Online]. Available: https://www.sciencedirect.com/science/article/pii/S0735109711022789.

[43] K. Garg, C. B. Rockman, V. Lee, T. S. Maldonado, G. R. Jacobowitz, M. A. Adelman, and F. F. Mussa, "Presentation and management of carotid artery aneurysms and pseudoaneurysms", *Journal of Vascular Surgery*, vol. 55, no. 6, pp. 1618–1622, 2012, ISSN: 0741-5214. DOI: https://doi.org/10.1016/j.jvs.2011.12.054. [Online]. Available: https://www.sciencedirect.com/science/article/pii/S0741521411031028.

[44] O. Trabelsi, F. Davis, J. Rodriguez-Matas, A. Duprey, and S. Avril, "Patient specific stress and rupture analysis of ascending thoracic aneurysms", *J Biomech*, vol. 10, pp. 1836–1843, 2015.

[45] I. Sultan, J. E. Bavaria, and W. Y. Szeto, "Chapter 27 - thoracic endovascular aortic repair for descending thoracic aortic and aortic arch aneurysms", in *Atlas of Cardiac Surgical Techniques (Second Edition)*, F. W. Sellke and

M. Ruel, Eds., Second Edition, Elsevier, 2019, pp. 455–476, ISBN: 978-0-323-46294-5. DOI: https://doi.org/10.1016/B978-0-323-46294-5.00027-3. [Online]. Available: https://www.sciencedirect.com/science/article/pii/B9780323462945000273.

[46] A. Mitsis, X. Yuan, I. Akin, and C. A. Nienaber, "Acute aortic syndromes", *Medicine*, vol. 46, no. 9, pp. 560–565, 2018. DOI: https://doi.org/10.1016/j.mpmed.2018.06.011.

[47] N. A. Orabi, L. E. Quint, K. Watcharotone, B. Nan, D. M. Williams, and K. M. Kim, "Distinguishing acute from chronic aortic dissections using ct imaging features", *The International Journal of Cardiovascular Imaging*, vol. 34, pp. 1831–1840, 2018, ISSN: 1573-0743. DOI: 10.1007/s10554-018-1398-x. [Online]. Available: https://doi.org/10.1007/s10554-018-1398-x.

[48] A. G. Sherrah, S. M. Grieve, R. W. Jeremy, P. G. Bannon, M. P. Vallely, and R. Puranik, "Mri in chronic aortic dissection: A systematic review and future directions", *Frontiers in Cardiovascular Medicine*, vol. 2, p. 5, 2015, ISSN: 2297-055X. DOI: 10.3389/fcvm.2015.00005. [Online]. Available: https://www.frontiersin.org/article/10.3389/fcvm.2015.00005.

[49] S. A. Maas, A. Erdemir, J. P. Halloran, and J. A. Weiss, "A general framework for application of prestrain to computational models of biological materials", *Journal of the Mechanical Behavior of Biomedical Materials*, vol. 61, pp. 499–510, 2016, ISSN: 1751-6161. DOI: https://doi.org/10.1016/j.jmbbm.2016.04.012. [Online]. Available: https://www.sciencedirect.com/science/article/pii/S1751616116300765.

[50] A. Holzapfel, C. Gasser, and R. Ogden, "A new constitutive framework for arterial wall mechanics and a comparative study of material models", *J Elast*, vol. 61, pp. 1–48, 2000.

[51] J. Bonet and R.D.Wood, *Nonlinear Continuum Mechanics for Finite Element Analysis*, 2nd ed. Cambridge University Press, 2008. DOI: 10.1017/CBO9780511755446.

[52] J. Marsden and T. Hughes, *Mathematical Foundations of Elasticity*, ser. Dover Civil and Mechanical Engineering Series. Dover, 1994, ISBN: 9780486678658.

[53] G. Holzapfel, *Nonlinear Solid Mechanics: A Continuum Approach for Engineering*, 2nd ed. Wiley, 2000, ISBN: 9780471823193.

[54] L. Malvern, *Introduction to the mechanics of a continuous medium*. Prentice-Hall, 1969.

[55] P. Wriggers, *Nonlinear Finite Element Methods*. Springer Science & Business Media, 2008.

[56] E. de Souza Neto, E. Neto, D. Peric, D. Owen, and D. Owen, *Computational Methods for Plasticity: Theory and Applications*. Wiley, 2008, ISBN: 9780470694527.

[57] P. Watton, N. Hill, and M. Heil, "A mathematical model for the growth of the abdominal aortic aneurysm", *Biomech Model Mechanobiol*, vol. 3(2), pp. 98–113, 2004.

[58] T. Eriksson, P. Watton, X. Luo, and Y. Ventikos, "Modelling volumetric growth in a thick walled fibre reinforced artery", *J Mech Phys Solids*, vol. 73, pp. 134–150, 2014.

[59] M. Latorre and J. Humphrey, "Critical roles of time-scales tissue growth and remodeling", *APL Bioeng*, vol. 2(2), p. 026 108, 2018.

[60] M. Latorre and J. D. Humphrey, "Fast, rate-independent, finite element implementation of a 3d constrained mixture model of soft tissue growth and remodeling", *Computer Methods in Applied Mechanics and Engineering*, vol. 368, p. 113 156, 2020, ISSN: 0045-7825. DOI: https://doi.org/10.1016/j.cma.2020.113156. [Online]. Available: https://www.sciencedirect.com/science/article/pii/S0045782520303418.

[61] J. Wilson, S. Baek, and J. Humphrey, "Parametric study of effects of collagen turnover on the natural history of abdominal aortic aneurysms", *Proc Math Phys Eng Sci*, vol. 469(2150), p. 20 120 556, 2013.

[62] J. S. Wilson and J. Humphrey, "Evolving anisotropy and degree of elastolytic insult in abdominal aortic aneurysms: Potential clinical relevance?", *Journal of Biomechanics*, vol. 47, no. 12, pp. 2995–3002, 2014, ISSN: 0021-9290. DOI: https://doi.org/10.1016/j.jbiomech.2014.07.003. [Online]. Available: https://www.sciencedirect.com/science/article/pii/S0021929014003832.

[63] C. Vlachopoulos, M. O'Rourke, and W. Nichols, *McDonald's Blood Flow in Arteries: Theoretical, Experimental and Clinical Principles*. CRC Press, 2011, ISBN: 9781444128789. [Online]. Available: https://books.google.fr/books?id=byrSBQAAQBAJ.

[64] C. Bellini, N. Kristofik, M. Bersi, T. Kyriakides, and J. Humphrey, "A hidden structural vulnerability in the thrombospondin-2 deficient aorta increases the propensity to intramural delamination", *Journal of the Mechanical Behavior of Biomedical Materials*, vol. 71, pp. 397–406, 2017, ISSN: 1751-6161. DOI: https://doi.org/10.1016/j.jmbbm.2017.01.045. [Online]. Available: https://www.sciencedirect.com/science/article/pii/S1751616117300504.

[65] J. Mousavi and S. Avril, "Patient-specific stress analyses in the ascending thoracic aorta using a finite-element implementation of the constrained mixture theory", *Biomech Model Mechanobiol*, vol. 16, pp. 1765–1777, 2017.

[66] R. Poya, A. Gil, R. Ortigosa, R. Sevilla, J. Bonet, and W. Wall, "A curvilinear high order finite element framework for electromechanics: From linearised electro-elasticity to massively deformable dielectric elastomers", *Computer Methods in Applied Mechanics and Engineering*, vol. 329, pp. 75 –117,

2018, ISSN: 0045-7825. DOI: https://doi.org/10.1016/j.cma.2017.09.020. [Online]. Available: http://www.sciencedirect.com/science/article/pii/S0045782517306503.

[67] R. Poya, A. Gil, and R. Ortigosa, "A high performance data parallel tensor contraction framework: Application to coupled electro-mechanics", *Computer Physics Communications*, vol. 216, pp. 35 –52, 2017, ISSN: 0010-4655. DOI: https://doi.org/10.1016/j.cpc.2017.02.016. [Online]. Available: http://www.sciencedirect.com/science/article/pii/S0010465517300681.

[68] O. Zienkiewicz, R. Taylor, and D. Fox, *The Finite Element Method for Solid and Structural Mechanics*. Elsevier, 2014.

[69] J. Laubrie, S. Mousavi, and S. Avril, "A new finite-element shell model for arterial growth and remodeling after stent implantation", *International Journal for Numerical Methods in Biomedical Engineering*, vol. 36, Nov. 2019. DOI: 10.1002/cnm.3282.

[70] *Shell element code*, https://github.com/jdlaubrie/shell-elem, Accessed 15 July 2021.

[71] W. Wagner, "A finite element model for non-linear shells of revolution with finite rotations", *Int J Numer Methods Eng*, vol. 29, pp. 1455–1471, 1990.

[72] *Florence: Finite-element open-source library*, https://github.com/jdlaubrie/florence, Accessed 14 July 2021.

[73] A. Cocciolone, J. Hawes, M. Staiculescu, E. Johnson, M. Murshed, and J. Wagenseil, "Elastin, arterial mechanics, and cardiovascular disease", *Am J Physiol Heart Circ Physiol*, vol. 315(2), H189–H205, 2018.

[74] H. Hosseini, K. Garcia, and L. Taber, "A new hypothesis for foregut and heart tube formation based on differential growth and actomyosin contraction", *Development*, vol. 144(13), pp. 2381–91, 2017.

[75] H. Hosseini and L. Taber, "How mechanical forces shape the developing eye", *Prog Biophys Mol Biol*, pp. 1–12, 2018.

[76] N. Famaey, J. Vastmans, H. Fehervary, L. Maes, E. Vanderveken, F. Rega, S. Mousavi, and S. Avril, "Numerical simulation of arterial remodeling in pulmonary autografts", *Z Angew Math Mech*, pp. 1–19, 2018.

[77] A. Valentín and G. Holzapfel, "Constrained mixture models as tools for testing competing hypotheses in arterial biomechanics: A brief survey", *Mech Res Commun*, vol. 42, pp. 126–33, 2012.

[78] A. Valentín, J. Humphrey, and G. Holzapfel, "A multi-layered computational model of coupled elastin degradation, vasoactive dysfunction, and collagenous stiffening in aortic aging", *Ann Biomed Eng*, vol. 39(7), pp. 2027–45, 2011.

[79] S. Mousavi, S. Farzaneh, and S. Avril, "Computational predictions of damage propagation preceding dissection of ascending thoracic aortic aneurysms", *Int J Numer Method Biomed Eng*, vol. 34(4), e2944, 2018.

[80] T. Matsumoto and K. Hayashi, "Response of arterial wall to hypertension and residual stress", in *Biomechanics*, 1996, pp. 93–119.

[81] L. Taber, "A model for aortic growth based on fluid shear and fiber stresses", *J Biomech Eng*, vol. 120, no. 3, pp. 348–354, 1998.

[82] W. V. Maltzahn, D. Besdo, and W. Wiemer, "Elastic properties of arteries: A nonlinear two-layer cylindrical model", *J Biomech*, vol. 14, no. 6, pp. 389–397, 1981.

[83] A. Rachev, "Theoretical study of the effect of stress-dependent remodeling on arterial geometry under hypertensive conditions", *J Biomech*, vol. 30, no. 8, pp. 819–827, 1997.

[84] A. Pérez-Martin, I. Aïchoun, and M. D. Rienzo-Ambrozkiewicz, "Chapitre 2 - rappels physiologiques: Organisation générale et régulation du système artériel et de l'endothélium", in *Maladies Artérielles*, Paris: Elsevier Masson, 2016, pp. 9 –26.

[85] A. de Préville, D. Fabre, J. Sobocinski, R. Spear, A. Hertault, T. Martin-Gonzalez, R. Azzaoui, and S. Haulon, "Chapitre 27 - anévrismes de l'aorte thoracique", in *Maladies Artérielles*, Paris: Elsevier Masson, 2016, pp. 313 –317.

[86] G. Holzapfel and T. Gasser, "Computational stress-deformation analysis of arterial walls including high-pressure response", *Int J Cardiol*, vol. 116, no. 1, pp. 78 –85, 2007.

[87] H. Kitahara, K. Okada, T. Kimura, P. Yock, A. Lansky, J. Popma, A. Yeung, P. Fitzgerald, and Y. Honda, "Impact of stent size selection on acute and long-term outcomes after drug-eluting stent implantation in de novo coronary lesions", *Circ Cardiovasc Interv*, vol. 10, no. 10, e004795, 2017.

[88] D. Chamié, H. Bezerra, G. Attizzani, H. Yamamoto, T. Kanaya, G. Stefano, Y. Fujino, E. Mehanna, W. Wang, A. Abdul-Aziz, M. Dias, D. Simon, and M. Costa, "Incidence, predictors, morphological characteristics, and clinical outcomes of stent edge dissections detected by optical coherence tomography", *JACC: Cardiovasc Interv*, vol. 6, no. 8, pp. 800 –813, 2013.

[89] H. García-García, N. Gonzalo, S. Tanimoto, E. Meliga, P. de Jaegere, and P. Serruys, "Characterization of edge effects with paclitaxel-eluting stents using serial intravascular ultrasound radiofrequency data analysis: The betax (beside taxus) study", *Rev Esp Cardiol*, vol. 61, no. 10, pp. 1013–1019, 2008.

[90] L. Hornỳ, T. Adámek, and M. Kulvajtová, "A comparison of age-related changes in axial prestretch in human carotid arteries and in human abdominal aorta", *Biomechanics and modeling in mechanobiology*, vol. 16, no. 1, pp. 375–383, 2017.

[91] C. Geuzaine and J.-F. Remacle, "Gmsh: A 3-d finite element mesh generator with built-in pre- and post-processing facilities", *International Journal for Numerical Methods in Engineering*, vol. 79, no. 11, pp. 1309–1331, 2009. DOI: 10.1002/nme.2579. eprint: https://onlinelibrary.wiley.com/doi/pdf/10.1002/nme.2579. [Online]. Available: https://onlinelibrary.wiley.com/doi/abs/10.1002/nme.2579.

[92] N. Nama, M. Aguirre, J. D. Humphrey, and C. A. Figueroa, "A nonlinear rotation-free shell formulation with prestressing for vascular biomechanics", *Scientific Reports*, vol. 10, no. 1, p. 17 528, 2020, ISSN: 2045-2322. DOI: https://doi.org/10.1038/s41598-020-74277-5.

[93] P. Moireau, N. Xiao, M. Astorino, C. Figueroa, D. Chapelle, C. Taylor, and J. Gerbeau, "External tissue support and fluid–structure simulation in blood flows", *Biomechanics and Modeling in Mechanobiology*, vol. 11, pp. 1 –18, 2012. DOI: https://doi.org/10.1007/s10237-011-0289-z.

[94] A. Duprey, O. Trabelsi, M. Vola, J.-P. Favre, and S. Avril, "Biaxial rupture properties of ascending thoracic aortic aneurysms", *Acta Biomaterialia*, vol. 42, pp. 273 –285, 2016, ISSN: 1742-7061. DOI: https://doi.org/10.1016/j.actbio.2016.06.028. [Online]. Available: http://www.sciencedirect.com/science/article/pii/S1742706116303051.

[95] X. He, S. Avril, and J. Lu, "Prediction of local strength of ascending thoracic aortic aneurysms", *Journal of the Mechanical Behavior of Biomedical Materials*, vol. 115, p. 104 284, 2021, ISSN: 1751-6161. DOI: https://doi.org/10.1016/j.jmbbm.2020.104284. [Online]. Available: http://www.sciencedirect.com/science/article/pii/S1751616120308201.

[96] J. Sugawara, K. Hayashi, T. Yokoi, and H. Tanaka, "Age-associated elongation of the ascending aorta in adults", *JACC: Cardiovascular Imaging*, vol. 1, no. 6, pp. 739 –748, 2008, ISSN: 1936-878X. DOI: https://doi.org/10.1016/j.jcmg.2008.06.010. [Online]. Available: http://www.sciencedirect.com/science/article/pii/S1936878X08003689.

[97] S. Zeinali-Davarani, L. G. Raguin, D. A. Vorp, and S. Baek, "Identification of in vivo material and geometric parameters of a human aorta: Toward patient-specific modeling of abdominal aortic aneurysm", *Biomechanics and Modeling in Mechanobiology*, vol. 10, no. 5, pp. 689–699, 2011. DOI: https://doi.org/10.1007/s10237-010-0266-y.

[98] T. Gasser and G. Holzapfel, "Modeling the propagation of arterial dissection", *European Journal of Mechanics A-solids*, vol. 25, pp. 617–633, 2006.

[99] A. Ferrara and A. Pandolfi, "A numerical study of arterial media dissection process", *International Journal of Fracture*, vol. 166, no. 1, pp. 21–33, 2010. DOI: https://doi.org/10.1007/s10704-010-9480-y.

[100] J. Brunet, B. Pierrat, E. Maire, J. Adrien, and P. Badel, "A combined experimental-numerical lamellar-scale approach of tensile rupture in arterial medial tissue using x-ray tomography", *Journal of the Mechanical Behavior of Biomedical Materials*, vol. 95, pp. 116–123, 2019, ISSN: 1751-6161. DOI: https://doi.org/10.1016/j.jmbbm.2019.03.028. [Online]. Available: https://www.sciencedirect.com/science/article/pii/S1751616118316655.

[101] L. Wang, S. M. Roper, X. Y. Luo, and N. A. Hill, "Modelling of tear propagation and arrest in fibre-reinforced soft tissue subject to internal pressure", *Journal of Engineering Mathematics*, vol. 95, pp. 249–265, 2015. DOI: https://doi.org/10.1007/s10665-014-9757-7.

[102] J. Brunet, B. Pierrat, and P. Badel, "A parametric study on factors influencing the onset and propagation of aortic dissection using the extended finite element method", *IEEE Transactions on Biomedical Engineering*, pp. 1–1, 2021. DOI: 10.1109/TBME.2021.3056022.

[103] S. Zhang, J. Laubrie, S. Mousavi, and S. Avril, "3d finite-element modelling of vascular adaptation after endovascular aneurysm repair", *International Journal for Numerical Methods in Biomedical Engineering*, 2021.

[104] J. Laubrie, S. Mousavi, and S. Avril, "About prestretch in constrained mixture models: Simulating growth and remodeling in patient-specific aortic geometries", *Biomechanics and Modeling in Mechanobiology*, 2021.

[105] F. Rossi, F. Fumagalli, A. Ruiz-Moreno, P. Moilanen, and P. Hähner, "Membrane bulge test rig for irradiation-assisted stress-corrosion cracking", *Nuclear Instruments and Methods in Physics Research Section B: Beam Interactions with Materials and Atoms*, vol. 479, pp. 80 –92, 2020, ISSN: 0168-583X. DOI: https://doi.org/10.1016/j.nimb.2020.06.012. [Online]. Available: http://www.sciencedirect.com/science/article/pii/S0168583X20302883.

École Nationale Supérieure des Mines
de Saint-Étienne

NNT: 2021LYSEM036

Author: Joan D. Laubrie Soto

Title: Finite-element modeling and patient-specific prediction of aortic aneurysm progression

Speciality: Mechanics and Engineering

Keywords: Growth and Remodeling, patient-specific, aorta, aneurysm, dissection, stent, homeostasis

Abstract

The aortic wall as other biological systems have adaptations with the purpose to maintain its stability. This stability depends on the cell assessing the state of the aorta. Eventually a disturbed activity of the cells may lead to maladaptations and progression of diseases. Thus, the objective of this thesis is to implement a mechanical approach for the adaptations in a numerical solver and apply it to patient-specific aortas. First, the mechanical approach is included in a two-dimensional axisymmetric shell method. Where the growth and remodeling (G&R) of the tissue is triggered from mass removal or load changes. The load changes are produced by the placement of a stent into the artery and produce further remodeling in it. Second, the G&R model is included within a three-dimensional thick solver. In the new code the adaptation is triggered from mass removal, but in this case the simulations are performed on cylinder, torus and patient-specific shapes. From those simulation is deduced the need for non-uniform prestretch in non-cylindrical geometries. Third, in the three-dimensional solver is included a routine for the analysis of aortic dissection propagation under G&R.

École Nationale Supérieure des Mines
de Saint-Étienne

NNT: 2021LYSEM036

Auteur: Joan D. Laubrie Soto

Titre: Modélisation éléments finis et prédiction personnalisées de la progression de l'anévrisme aortique

Spécialité: Mécanique et Ingénierie

Mots-Clefs: Croissance et Remodelage, patient, aorte, anévrisme, dissection, stent, homéostasie

Résumé

La paroi aortique, comme d'autres systèmes biologiques, présente des adaptations visant à maintenir sa stabilité. Cette stabilité dépend de l'évaluation de l'état de l'aorte par la cellule. A terme, une activité perturbée de les cellules peut conduire à des inadaptations et à la progression de maladies. Ainsi, l'objectif de cette thèse est d'implémenter une approche mécanique des adaptations dans un solveur numérique et de l'appliquer à des aortes spécifiques aux patients. Tout d'abord, l'approche mécanique est incluse dans une méthode de coque axisymétrique bidimensionnelle. La croissance et le remodelage (G&R) du tissu sont déclenchés par l'élimination de la masse ou les changements de charge. Les changements de charge sont produits par le placement d'un stent dans l'artère et produisent un remodelage supplémentaire de celle-ci. Deuxièmement, le modèle G&R est inclus dans un solveur épais tridimensionnel. Dans le nouveau code, l'adaptation est déclenchée à partir de la suppression de la masse, mais dans ce cas, les simulations sont effectuées sur des formes cylindriques, toriques et spécifiques au patient. De ces simulations, on déduit la nécessité d'un pré-étirement non uniforme dans les géométries non cylindriques. Troisièmement, le solveur tridimensionnel comprend une routine pour l'analyse de la propagation d'une dissection aortique dans le cadre de G&R.